UNIVERSITÀ
DEGLI STUDI
FIRENZE

UNIVERSITY OF FLORENCE
DEPARTMENT OF INDUSTRIAL ENGINEERING (DIEF)
CURRICULUM: INDUSTRIAL AND RELIABILITY ENGINEERING

A THESIS PRESENTED FOR THE DEGREE OF DOCTOR OF PHILOSOPHY

———————————

AN INNOVATIVE DATA-DRIVEN RELIABILITY LIFE CYCLE FOR COMPLEX SYSTEMS

CANDIDATE:
Dr. Gabriele Patrizi

SUPERVISORS:
Prof. Marcantonio Catelani
Prof. Lorenzo Ciani

PHD COORDINATOR:
Prof. Giampaolo Manfrida

ACADEMIC DISCIPLINE: ING - INF/07

———————————

CYCLE XXXIV   YEARS: 2018-2022

University of Florence, Department of Industrial Engineering (DIEF)

To my family,

with love.

ACKNOWLEDGEMENTS

CONTENTS

ABSTRACT

In the last few years, the reliability assessment acquired a fundamental role in many advanced technology applications. System downtime and unexpected failures massively affect the productivity of a system/product/plant. As a consequence, the Reliability, Availability, Maintainability, and Safety (RAMS) disciplines, together with diagnostics and prognostics tools are becoming more and more essential for several application fields, especially in case of complex industrial systems where environment, personnel, and equipment safety are mandatory features.

Several works in recent literature deal with design for reliability methods that integrates one or more reliability tasks during the early phase of the design. However, all-around Reliability Life Cycle procedures that takes into account the complete system life cycle (from design and development to actual implementation) are rarely dealt with. Another fundamental aspect that is barely taken into account by recent literature is the importance of measurements and data within the context of a reliability life cycle approach. Usually, reliability parameters are estimated using probabilistic approaches, failure and degradation models, statistical analysis and failure data included in handbooks. However, instrumentation and measurements technologies could remarkably improve and optimize several different RAMS methodologies introducing suitable data analysis in spite of handbook data and probabilistic approaches. Trying to fill these gaps, the main aim of this work is to extend the classical idea of Design for Reliability introducing an innovative data-driven reliability life cycle procedure that integrates different RAMS techniques to optimize the reliability of complex industrial systems during both design and operational phases. However, it is not enough to simply provide a reliability procedure based on a set of different techniques without a thorough and structured study of the state-of-the art of each method. Therefore, the second aim of this project is the optimization of the techniques included in the proposed Reliability Life Cycle in order to overcome the major drawbacks highlighted by the literature review of each method. Firstly, the work deals with Failure Modes, Effects and Criticality

Analysis (FMECA) providing a statistical comparison of the alternative approaches found in literature and applying all of them to the risk analysis of a real case study (Ventilation system for high-speed trains). Furthermore, the work shows how the FMECA could be integrated in the context of a data-driven approach. Then, an innovative method to easily and effectively estimate a risk threshold is presented and tested using the design of a control system for wind turbine as a case study. Reliability Allocation plays a central role in the proposed Reliability Life Cycle. In this point of view, this work presents an innovative method able to overcomes all the initial hypotheses required by the other approaches and test it on three complex systems (a numerical example, a sensor unit for railway systems and a lubrication system for gas turbines). The work also presents two test plans with the aim of characterize components and equipment by both system performance and system reliability point-of-views. The results of the experimental measurement campaigns provide significant information to improve the RAMS parameters and the electrical and metrological performances of the components under analysis (Inertial Measurement Units and DC-Dc converters for diagnostic devices). Furthermore, this research also proposes a new customized diagnostic-oriented decision-making diagram for maintenance management and apply it to maintenance planning of a wind turbine. Moreover, a new diagnostic method based on a data-driven Condition Monitoring tool is presented to efficiently monitor the health and detect damages in the wind turbine by means of measurements of critical parameters of the tested system. Finally, the work also deals with data-driven remaining useful life (RUL) estimation of Lithium-Ion batteries proposing a hybrid approach based on both condition monitoring and physic degradation model where a state-space estimation is used to generate a big dataset for the training of the proposed Recurrent neural Network. The application on a real battery dataset proves the superiority of the proposed degradation model and the effectiveness of the estimation with respect to the state of the art.

LIST OF FIGURES

LIST OF TABLES

ABBREVIATIONS & ACRONYMS

AF	Acceleration Factor
AGREE	Advisory Group on Reliability of Electronic Equipment
AHP	Analytic Hierarchy Process
AHRS	Attitude and Heading Reference Systems
AI	Artificial Intelligence
ALARP	As Low As Reasonably Practicable
ALT	Accelerated Life Test
AR	AutoRegressive
ARINC	Aeronautical Radio Incorporation
ARPN	Alternative Risk Priority Number
ART	Adaptive Resonance Theory
ARW	Angular Random Walk
ASD	Acceleration Spectral Density
ATTF	Accelerated Time-To-Failure
AWM	Averaging Weighted Method
BMS	Batteries Management System
CBM	Condition-Based Maintenance
CBPM	Condition-Based Prognostic Maintenance
CFM	Critical Flow Method
CM	Condition Monitoring
D	Detection
DEMATEL	DEcision-MAking Trial and Evaluation Laboratory
DESN	Deep Echo State Network
DfR	Design for Reliability
DMM	Digital Multimeter
DUT	Device Under Test
EE	Estimation Error
E/E/PE	Electrical/Electronic/Programmable Electronic
EKF	Extended Kalman Filter
EOL	End of Life
ERPN	Exponential Risk Priority Number

ESD	Electrostatic discharge
ESN	Echo State Network
ESS	Environmental Stress Screening
FF	Failure Finding
FHIA	FMECA and HAZOP Integrated Analysis
FMA	Function-Movement-Action
FMEA	Failure Modes and Effects Analysis
FMECA	Failure Modes, Effects and Criticality Analysis
FOO	Feasibility-Of-Objectives
FPMH	Failure Per Million Hours
FTH	Failure Threshold
GA	Genetic Algorithm
GPR	Gaussian Process Regression
HASS	Highly Accelerated Stress Screening
HAWT	Horizontal-Axis Wind Turbine
HAZOP	HAZard and OPerability analysis
HVAC	Heating, Ventilation and Air Conditioning
IEC	International Electrotechnical Commission
IFM	Integrated Factors Method
IGBT	Insulated Gate Bipolar Transistor
IMU	Inertial Measurement Unit
IoT	Internet of Things
IRPN	Improved risk priority Number
ISO	International Organization for Standardization
KF	Kalman Filter
K-M	Kaplan-Meier
LCC	Life Cycle Cost
LDA	Life data Analysis
LIB	Lithium-Ion Battery
LIT	Level Indicating Transmitter
LRPN	Logarithmic Risk priority Number
LSB	Least significant bit
MCU	Micro Controller Unit
MEMS	Micro-Electro-Mechanical System
MEOWA	Maximal Entropy Ordered Weighted Averaging
MEMVOWA	Maximum Entropy Minimal Variance Ordered Weighting Averaging
MIT	Massachusetts Institute of Technology
MLE	Maximum Likelihood Estimation

MONESN	Monotonic Echo State Network
MPPT	Maximum Power Point Tracking
MSE	Mean Square Error
MVOWA	Minimal Variance Ordered Weighting Averaging
O	Occurrence
ODR	Output Data Rate
OWA	Ordered Weighting Averaging
OWGA	Ordered Weighted Geometric Averaging
O&M	Operation&Maintenance
PDF	Probability Density Function
PDIT	Pressure Differential Indicating Transmitter
PCV	Pressure Control Valve
PF	Particle Filter
PFC	Power Factor Correction
PHA	Preliminary Hazard Analysis
PHM	Prognostic and Health Management
PIT	Pressure Indicating transmitter
PWM	Pulse Width Modulation
PROMETHEE	Preference ranking organization method for enrichment evaluation
PSM	Pulse Skipping Modulation
PSV	Pressure Safety valve
PVST	Partial Valve Stroke Test
QUALIFLEX	Qualitative Flexible Multiple Criteria Method
RA	Reliability Allocation
RAMS	Reliability, Availability, Maintainability and Safety
RAV	Risk Assessment Value
RBD	Reliability Bock Diagram
RCA	Root Cause Analysis
RCM	Reliability Centred Maintenance
RFID	Radio-Frequency IDentification
RLC	Reliability Life Cycle
RMS	Root Mean Square
RMSE	Root Mean Square Error
RNN	Recurrent Neural Network
RPN	Risk Priority Number
RR	Rank Regression
RSS	Reliability Stress Screening
RTD	Resistance Temperature Detector

RUL	Remaining Useful Life
RVM	Relevance Vector Machine
S	Severity
SAEL	Safety Automation Equipment List
SC	Service Condition
SCADA	Supervisory Control and Data Acquisition
SIL	Safety Integrity Level
SIS	Safety Instrumented System
SNR	Signal to Noise Ratio
SOC	State of Charge
SOH	State-of-Health
SRS	Safety Related System
SVM	Support Vector Machine
TCV	Temperature Control Valve
TIT	Temperature Indicating Transducer
TODIM	Portuguese acronym of interactive and multiple attribute decision making
TOPSIS	Technique for Order of Preference by Similarity to Ideal Solution
TRI	Toyota Research Institute
TTF	Time-To-Failure
UAV	Unmanned Aerial Vehicle
UKF	Unscented Kalman Filter
UPF	Unscented Particle Filter
URPN	Universal Generating Function based RPN
VIKOR	Serbian acronym of Multicriteria Optimization and Compromise Solution
WSN	Wireless Sensor network
WMN	Wireless Mesh Network
WT	Wind Turbine

CHAPTER 1

INTRODUCTION

This chapter provides a general overview of the themes analyzed in this thesis outlining the importance of every topic. The aim of this section is to provide enough background information so that the reader can understand the context in which the research sits. More in detail, this chapter discusses the gaps that this research aims to fill. The research questions are properly outlined, and the problems addressed by this study are extensively explained. The second part of the section illustrates the main contributions that this work will provide to the body of knowledge. The key element of novelties is thoroughly stressed to emphasize the importance of the thesis within the context of the RAMS disciplines and more in detail within the topic of Instrumentation and Measurements to Improve Diagnostics, Prognostic and Reliability.

1.1. Research questions and objectives of the work

Reliability engineering is the discipline of ensuring that a product will be as reliable as possible when operated under predetermined and well-defined conditions. To put it simple, the function of reliability engineering is to avoid failures. In reality, failures are inevitable; a product will fail sooner or later and thus, design countermeasures and maintenance operations should be planned accordingly.

Nowadays, the interest in reliability engineering is growing fast worldwide in every industrial and technological field since it has grown to cover areas such as risk management and maintenance planning. Energy production systems such as Oil&Gas, nuclear, wind and solar plants, railway infrastructure, aerospace applications, automotive and self-driving vehicles, robotics, bioengineering and manufacturing industries are examples of application fields which constantly integrates reliability engineering within the product/system/plant design cycle.

1.1.1. Design for Reliability

Reliability engineering is implemented by taking structured and feasible actions that maximize reliability and minimize the effects of failures. In general, two major steps are necessary to accomplish this objective. The first step of reliability engineering should be performed during the design and development phases of the product to maximize its reliability performances before the production. Parameters such failure rate, probability of failure at fixed time, acceptable risk level of a possible failure, safety impact in case of hazardous event, reliability to be allocated to each subunit are just few examples of reliability requirements that are more and more included in the overall product design requirements in every industrial and technological field. This first step is usually called Design for Reliability (DfR) and it could be implemented using a variety of techniques (reliability prediction, reliability allocation, fault tree analysis, failure modes and effects analysis, Weibull analysis, reliability testing just to cite a few).

Design for Reliability is not a new concept, but it has begun to receive a great deal of attention in recent years. Specifically, Design for Reliability describes the entire set of tools that support product and process design (typically from early in the concept stage all the way through to product design and

development) to ensure that customer expectations in terms of reliability are fully met throughout the life of the product with low overall life-cycle costs.

In other words, DfR is a systematic, streamlined, concurrent engineering program in which reliability engineering is weaved into the total development cycle. lt relies on an array of reliability engineering tools along with a proper understanding of when and how to use these tools throughout the design cycle [1]–[4].

DfR aims to understand, identify, and prevent underlying failures before the devices are built. In designing a product, engineers usually miss the following characteristics:

    a.   Key failure modes and failure rate of the product.
    b.   Key failure modes that may be present in the service environment.
    c.   Usable life of the product.
    d.   Cost of maintenance required to sustain the inherent reliability.
    e.   Availability, and rigorous testing.

Essentially, DfR is a process that ensures that a product, or system, performs a specified function within a given environment over the expected lifetime. The complexities of today's technologies make DfR more significant and valuable than ever before. Some of these reasons include:

- Product differentiation: As electronic technologies reach maturity, there are fewer opportunities to set products apart from the competition through traditional metrics, like price and performance.
- Reliability assurance: Advanced circuitry, sophisticated power requirements, new components, new material technologies and less robust parts make ensuring reliability increasingly difficult.
- Cost control: 70% of a project's budget is allocated to design.
- Preserving profits: Products get to market earlier, preventing erosion of sales and market share.

The design for reliability process encompasses a variety of tools and practices and describes the overall order of deployment that an organization needs to follow in order to design reliability into its products.

There are many techniques that could be applied during design phase to estimate and to improve reliability (and more generally all RAMS) performances of the product. A well-defined and standardized procedure that takes into account such aspects is currently not available. However, there are many different DfR procedures that integrates several RAMS methodologies.

The most common methods implemented in DfR processes are:
- Failure Modes and Effects Analysis
- Reliability Block Diagram
- Fault Tree Analysis
- Physics of Failure
- Accelerated Test
- Screening procedures
- Weibull Analysis

1.1.2. From Design for Reliability to Life Cycle Reliability

Once a product is deployed and its life cycle is started, the second step of reliability engineering could be implemented. Appropriate maintenance operations should be initiated to alleviate performance degradation and prolong product life. Adequate data-driven reliability evaluation and condition-based maintenance operation should be put in practice to optimize the performance of the system by a reliability and availability point of view.

Bearing all these aspects in mind, it is essential to develop and implement appropriate and adequate reliability programs that synthesize these individual reliability techniques.

Currently, there are several design for reliability methods available in literature that integrates different reliability tasks. However, all-around Reliability Life Cycle (RLC) procedures that takes into account the complete system life cycle (from design and development to disposal) are seldom available.

Another fundamental aspect that is barely taken into account by recent literature is the importance of measurements and data within the context of a reliability life cycle approach. Usually, reliability parameters are estimated using probabilistic approaches, failure and degradation models, statistical analysis and failure data included in handbooks. However, the size and number of available datasets has grown rapidly in the last few years since lots of devices are now capable of collect and store more and more information. Mobile devices, Internet of Things (IoT) technologies, smart and remote sensing, wireless sensor networks and radio-frequency identification (RFID) readers are some examples of innovation technologies that allows to acquire enormous amount of data about the life cycle of a monitored system/plant.

In this point of view, instrumentation and measurements technologies could remarkably improve the reliability life cycle of a product/system introducing suitable data analysis to optimize the reliability tasks.

1.1.3. Objectives of the work

Trying to fill all the above-mentioned gaps and trying to answer the research questions described above, the main objective of this work is to extend the classical idea of Design for Reliability introducing an innovative data-driven reliability life cycle procedure that integrates different RAMS (Reliability, Availability, Maintainability and Safety) techniques to optimize the reliability of complex industrial systems during both design and operation phases.

The proposal of an all-around reliability life cycle procedure aims at identifying an optimal solution to manage the RAMS requirements of a complex systems during its life cycle regardless the application field. This is the reason why this work is not built upon a single case study, but several applications have been considered in the different sections of this project.

Furthermore, it is also extremely important to optimize each single method that is included in the overall procedure in order to achieve the best outcomes of the methodology and guarantee high RAMS performances of the developed system.

For this reason, the second objective of this work is a thorough and structured study of some of the techniques included in the proposed data-driven reliability life cycle procedure analyzing the state-of-the art of each method and providing one or more improvements to solve the major drawbacks found in literature.

The RAMS techniques that have been studied and optimized in this work are the following:

- FAILURE MODES AND EFFECTS ANALYSIS (FMEA): the major shortcomings of this method have been studied in Section 3. After a comprehensive literature review of the alternative FMEAs available in literature, the objective of the work is a critical comparison of the approaches proposed in literature by a statistic point of view in order to evaluate what alternative method provides the most suitable and accurate results. After that, another aim of the work is to show how FMEA could be integrated in the context of a data-driven approach highlighting the importance of measurements to estimate the FMEA parameters during product life cycle.

- RISK THRESHOLD ESTIMATION: the problem of the identification of a risk threshold to distinguish negligible failure modes and critical failure modes in the context of risk assessment for complex systems is dealt with in Section 4. Just few methods are currently available to solve this problem, and all of them have severe drawbacks. As a consequence, the aim of the research is to propose a RPN (Risk Priority Number)

threshold estimation method that could be objective and repeatable, easy and practical, accurate and cost-effective.

- RELIABILITY ALLOCATION (RA): the state of the art of RA methods presented in Section 5 shows that all the approaches available in literature to allocate reliability performances to components and subunits require two initial assumptions: functional series configuration of the system architecture and exponential failure distribution of each component making up the system. Bearing these limitations in mind, the objective of this work is to propose a general high-level RA procedure that will allow designers to overcome the initial hypothesis and consequently apply each allocation method available in literature also to redundant complex systems that includes component characterized by Weibull, Lognormal, Gamma or any other failure distribution.

- ENVIRONMENTAL STRESS SCREENING (ESS): two ESS-based test plans are presented in Section 6 with the aim of characterize components and equipment by both system performance and system reliability point-of-views. In this context, the major objective of the work is to present how an effective ESS test plan could be used during design phase to characterize the performances of the developed system under harsh operating contexts typical of the real scenarios in which the system will be installed. The results of the experimental measurement campaigns provide significant information to improve the RAMS parameters of the system under analysis.

- CONDITION MONITORING (CM) AND CONDITION-BASED MAINTENANCE (CBM): the importance of CM and CBM during the system life cycle are shown in Section 7. The scope of the research is to reduce subjectivity in maintenance task selection with respect to the current international standard that regulate this issue. Furthermore, the procedure aims at reducing cost by optimizing maintenance decisions and by making the projects more cost-efficient and cost-effective. Moreover, the work also aims at proposing a new diagnostic method based on a data-driven condition monitoring system to efficiently monitor the health and detect damages in the system by means of measurements of critical parameters.

- REMAINING USEFUL LIFE (RUL): Section 8 deals with data-driven RUL estimation. The aim of this work is to introduce a hybrid approach based on both condition monitoring and physic degradation model to improve the accuracy and precision of RUL estimation for Lithium-Ion

batteries by means of Artificial Intelligence (AI) tools such Recurrent Neural Network (RNN) trained by innovative degradation models and hybrid approaches.

Simultaneously, another objective of this works is to spread the idea of components and systems characterized by a non-constant failure rate to the product complete life cycle, taking this aspect into consideration in the various RAMS methods included in the proposed Reliability Life Cycle.

Furthermore, the proposed approach aims at integrates data-driven methodologies within the classical concepts of reliability estimation to improve the RAMS assessment based on real data in spite of handbooks data and reliability models.

An overview of the major objectives of this work is represented in Fig. 1.1 emphasizing the four different aspects: introduction of a Reliability Life Cycle, optimization of RAMS methods, non-constant failure rate assumption extended to the complete procedure and data-driven methodologies to improve RAMS performances.
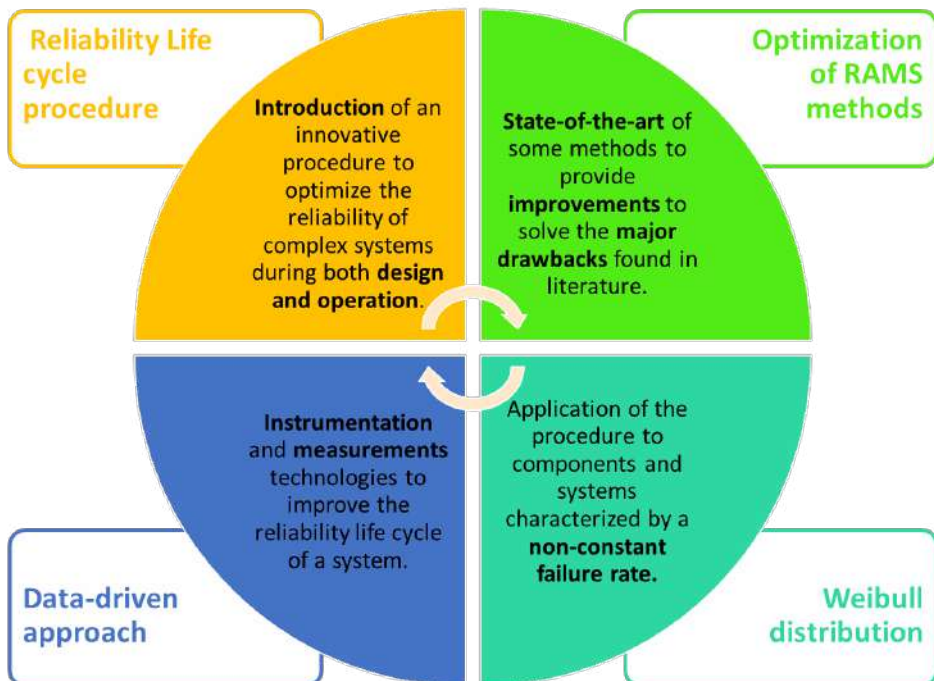
Fig. 1.1. Overview of the major objectives of this work.

1.2. List of major contributions

This subsection aims at illustrates the key element of novelties and the major contributions to the body of knowledge brought by this work. Hereinafter is reported a list of all the novel concepts introduced in this thesis and in the international publications (both conferences and peer-reviewed journals) related to it:

- Introduction of an all-around data-driven reliability life cycle procedure that extend the concept of the classical Design for Reliability methods supporting by a reliability point of view the complete life cycle of a complex industrial system, from design and development up to installation, operation, maintenance and disposal.

- Definition of an innovative accurate, well-structured data-driven procedure that integrates different reliability tasks that are usually performed on its own (see Section 9) to optimize the RAMS parameters of the system under analysis.

- Integration of safety requirements and SIL evaluation within the concept of a broadened DfR that is not usually taken into account by literature.

- Development of a critical analysis of alternative RPNs by a statistical point of view to emphasize the best solution carrying out a Failure Modes, Effects and Criticality Analysis.

- Proposal of measurements integration within the context of a FMECA assessment during product life cycle.

- Introduction of an innovative approach based on a statistical analysis and a boxplot to separate negligible and critical failure modes as the outcome of a FMECA. The proposed methodology is an easy, practical and repeatable solution which represents the optimal trade-off between cost and risk reduction level suffering no subjectivity in threshold definition.

- Unlike the other methods available in literature, the proposed RPN threshold estimation methodology introduces the ALARP (As Low As Reasonably Practicable) concept as intermediate level between negligible and critical failure modes.

- Proposal of an innovative reliability allocation methodology that overcomes the initial hypothesis of functional series configuration required by every other method that has been found in recent literature.

- Integration of the reliability allocation method within the concept of DfR together with accelerated life test to overcome also the second

hypothesis required by all the allocation approaches available in literature (i.e. the exponential failure distribution). Adequate accelerated test plans can be performed right after the allocation procedure on the most critical components to allow extension of the methodology also to failure distributions other than the exponential one (e.g. 2-parameter Weibull, 3-parameter Weibull, Lognormal, Gaussian, Gamma, etc).

- Proposal of both a suitable testbed and customized Environmental Stress Screening test plan for performance and reliability analysis of Inertial Measurement Units (IMU) under vibration and temperature conditions.

- Characterization of DC-DC converters under harsh environmental conditions including cold temperature, high temperature, high humidity levels and wideband random vibrations by means of a customized Reliability Stress Screening test plan.

- Introduction of an innovative diagnostic-oriented decision-making diagram within the concept of maintenance planning to decrease subjectivity of task selection and to improve the reliability and availability performances of the complex industrial system under analysis using data coming from monitoring and diagnostic units.

- Proposal of a data-driven condition monitoring tool to detect damages in a wind turbine by means of measurements of critical parameters.

- Use of a hybrid approach which integrates condition monitoring and physical degradation model to enhance the condition-based maintenance of Lithium-Ion batteries.

- Integration of an Artificial Intelligence estimation method with a state space estimation to evaluate the Remaining Useful Life of Lithium-Ion batteries. The state space estimation allows to generate a big dataset used for the training of an Echo State Network accurately customized introducing additional deep layers (used to ensure an accurate estimation of nonlinear trends) and a genetic algorithm (used to optimize the performance of the neural network).

- Introduction of a single exponential degradation model for Lithium-Ion batteries which is an alternative to the widely known empirical double exponential model. The proposed model provided comparable results with lower parameters and lower complexity ensuring the same accuracy.

1.3. Impact of measurements within this work

Although measurements and data are used to improve every step of the proposed reliability life cycle procedure, their major impact could be summarized as:

- DURING PRODUCT DESIGN: Introduction of a system characterization by a reliability point of view using different testing procedures such as Environmental and Reliability Stress Screening. These methods allow to evaluate the reliability performance by adequate experimental measurements setup used to simulate the real operating conditions of the system during its life cycle. Recent literature does not adequately consider how the actual operating conditions can affect the performance and reliability of a system. This kind of analysis is called context-awareness assessment because it considers the real scenario in which the system is operating, which could be characterized by the presence of significant temperature, humidity, vibrations, mechanical shocks and so on. Take all these stress sources into account during the system design by means of adequate measurements setup allow to achieve a considerable improvement of the system reliability estimation.

- DURING PRODUCT OPERATION: design of adequate condition-based maintenance and prognostic analysis which uses data coming from suitable diagnostic units to precisely estimate the Remaining Useful Life (RUL) of the system and consequently to plan the required maintenance operation based on the actual health state of the system. This will allow to save Operation&Maintenance (O&M) cost, to optimize system productivity and availability and to minimize the system downtime.

Chapter 2

Systems under analysis

This chapter provides a brief description of the complex systems taken as case study in the various sections of this work. In particular, six different systems have been used to test the performances of the methodologies introduced in the other chapters and included in the proposed Reliability Life Cycle. The chapter describes the basic features of a wind turbine (with specific reference to the control system and the yaw unit), an HVAC unit for railway applications, an Inertial Measurement Unit for automotive and low-cost aeronautical applications, a lithium-ion battery, a lubrication system for gas turbines and a customized self-made DC-DC converter.

2.1. Wind Turbine

Wind energy is one of many renewable energy sources that offer an alternative to burning fossil fuels [5] and is now one of the most widely used sources of renewable energy [6]. Wind energy is popular because of the lower investment cost and well-developed technology compared to the other renewable energy sources [7]. In compliance with WindEurope, (i.e. the Association for Wind Energy in Europe), the European Union (EU) is moving toward renewable energy sources, with hundreds of billions invested in renewable energy development and many new installations [8].

The inevitable power fluctuations represent one of the greatest drawbacks of wind energy, as they introduce serious technical challenges into the electric power grid, such as power system quality and reliability, system protection, and power flow control [7]. Moreover, compared to other electricity generation systems, wind turbines (WTs) have relatively higher failure rates because of the harsher operation conditions and higher maintenance costs due to their relative inaccessibility [9]. These are the reasons why WTs have been taken as cases study in this work.

A wind turbine (WT) is a device that converts the wind's kinetic energy into electrical energy. It has evolved from generating a few kilowatts in the 1980s to several megawatts today [10], [11]. WTs are generally placed together (wind farm) to produce electricity. The international standard IEC 61400 define Horizontal-axis wind turbine (HAWT) as a wind turbine system whose rotor axis is substantially parallel to the wind flow [12]. HAWT have the main rotor shaft and electrical generator at the top of a tower within an enclosure called nacelle. The nacelle, and consequently the rotor, must be pointed toward the wind direction to maximize the WT productivity.

A wind turbine must grasp the mechanical energy from wind and convert it to electrical energy. So, it has both mechanical components and electrical components. The main components making up a wind turbine are illustrated in Fig. 2.1.

By a mechanical point of view, a WT primarily consists of a tower, a nacelle, a rotor (i.e. a hub and three blades), and a foundation. The blades are connected to a central hub, which rotates with them. The whole assembly is called rotor. The rotor is mechanically isolated from the rest of the turbine that does not rotate with wind. The blades and hub rotate the main shaft, which goes inside an enclosed space on the top of the tower. This enclosed space is called the nacelle. The nacelle houses the gearbox, generator, and all the other necessary components such as heat exchangers, coolers and heaters, other motors and gears and so on.
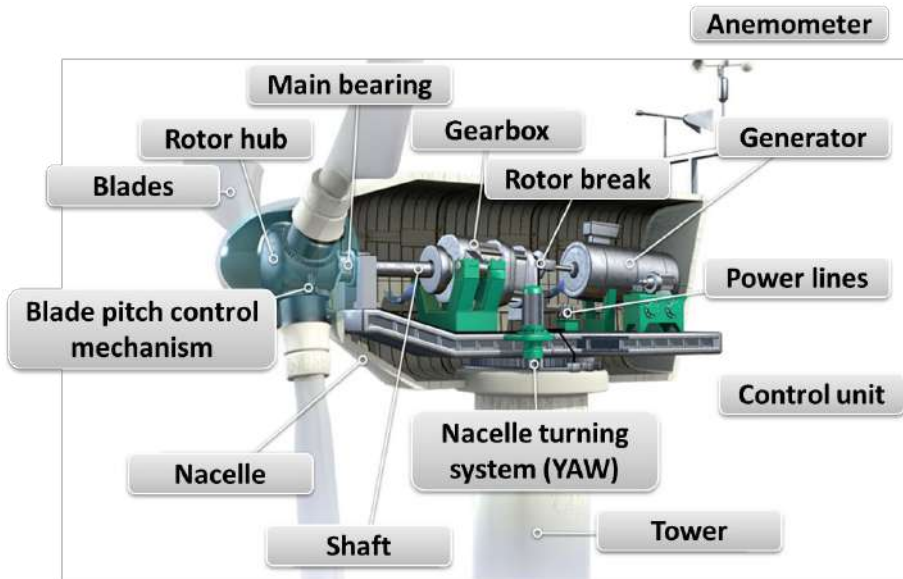
Fig. 2.1. Main components included in the Wind Turbine under analysis.

By an electrical/electronic point of view, the major components of a WT are the generator and the transformer. There are many other electrical components for various functions, such as motors for yaw motion, motors for blade pitch motion, motors for oil circulation pumps, space heaters for winter time warming inside the nacelle, lighting, various sensors, UPS, I/O board and a central processor or a PLC.

The nacelle of the WT represents the intermediate part between the rotor and the tower. It does not rotate with the rotor, but it must rotate with respect to the tower. This rotating motion, called yaw, is necessary for directing the turbine toward the wind stream. This motion is provided by the yaw system, which comprises yaw motors and a yaw gears [13], [14].

The yaw system is a key concern in new wind turbine installation since wind direction is a highly unstable physical quantity, as highlighted in Fig. 2.2. The graph shows the wind direction measured by an anemometer located on a 2 MW Spanish onshore wind turbine during one day of operation. Moving the WT towards the wind direction is mandatory to maximize the energy production [15].

Fig. 2.3 shows the yaw axis and the direction of the movement obtained with the yaw system.
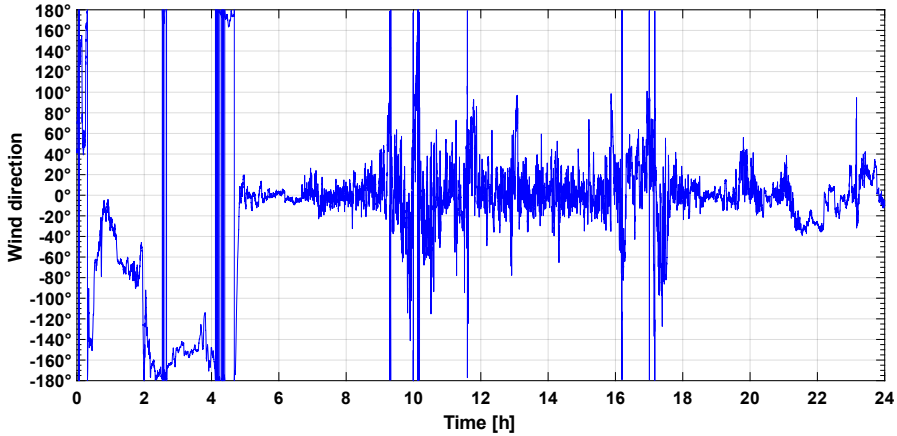
Fig. 2.2. Wind direction acquired by the control system of a 2 MW Spanish onshore WT during one day of operation.
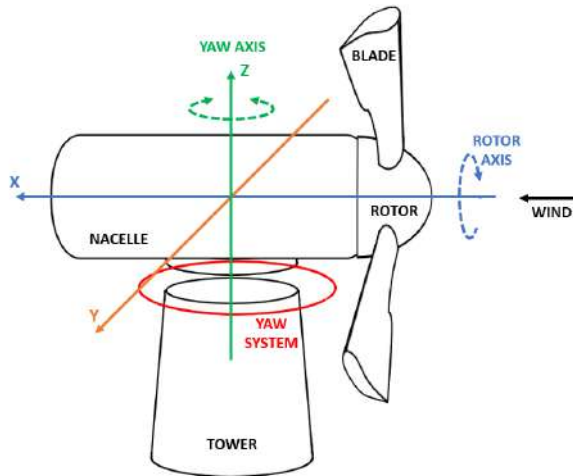
Fig. 2.3. Schematic representation of the axis in a wind turbine.

The WT under test is a 2MW wind turbine from the "LA PLANA 1" wind farm, located about 20km southwest of Zaragoza, in the region of Aragon, Spain. This wind farm consists of 5 WTs used to perform Research and Development (R&D) in wind energy. More in detail, the WT under test is a G80/2000 machine manufactured by "Gamesa Corporación Tecnológica", it is characterized by an 80 m rotor diameter mounted on the top of a 60 m tubular tower by "Vestas wind systems".

In this work, three different subsystems have been detailed analyzed as part of several case studies in the following sections:

- YAW system. The turbine of interest has two active motion subsystems in redundant configuration: an hydraulic unit and an electromechanical unit.
- Control system. It is a very critical unit characterized by several purposes. It has to collect information coming from the SCADA (Supervisory Control and Data Acquisition) system and from the other external sensors. These data must be transferred to the operating center, but they are also processed and used to manage all the turbine functionalities.
- The electrical equipment unit is a generic subsystem containing all the electrical components in the turbine, including a power converter integrating an IGBT module, a rectifier bridge, a crowbar system, a system used to improve the power factor (PFC), a soft starter, transformers, contactors, relays and so on.

2.2. HVAC system

Heating, ventilation, and air conditioning (HVAC) is the technology of indoor and vehicular environmental comfort. The objectives of HVAC systems are to provide an acceptable level of occupancy comfort and process function, to maintain good indoor air quality, and to keep system costs and energy requirements to a minimum [16], [17].

With hundreds of commuters often crowded onto train carriages during peak hours, passenger comfort is a major concern for operators around the world. While train carriages can mitigate some of the misery of overcrowding with good design and punctual service, an efficient heating, ventilation and air conditioning system (HVAC) is the best way of regulating temperature and air quality on crowded trains [18], [19]. Furthermore, one of the main objective of HVAC is to ensure emergency ventilation and sufficient air exchange [20]–[22]. In summary, HVAC has to ensure four functionalities: cooling capacity, heating capacity, ventilation capacity and emergency ventilation. The HVAC system installed in each train car consists of an air equipment conditioning, a control rack, extractor box, heater and floor heaters, convectors, the necessary probes to control the temperature of the different enclosures of the car, a pressure wave control and a control panel in each cabin. More specifically, the main components of the HVAC under analysis are:

- Heat exchanger.
- Condenser fan and motor assemblies.
- Semi-hermetic compressor.
- Liquid tanks.
- Air and liquid filters.
- High and low pressure switches.
- Temperature, moisture and liquid indicators.
- Evaporator blower.
- Expansion valves
- Outdoor air temperature sensor
- Control panel.

The basic diagram of the HVAC under test is illustrated in Fig. 2.4.
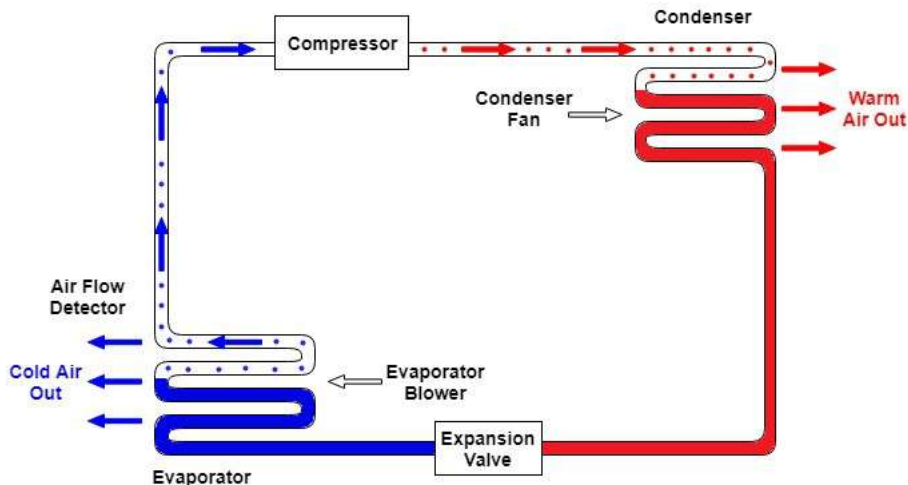
Fig. 2.4. HVAC functional diagram including the main components of the unit.

The refrigeration/heating cycle of the HVAC under test uses four essential elements, namely compressor, condenser, expansion valve and evaporator blower. At the inlet of a compressor, the refrigerant inside the system is in a low pressure, low temperature, gaseous state. The compressor pumps the refrigerant gas up to a high pressure and temperature. From there it enters a heat exchanger (sometimes called a condensing coil or condenser) where it loses heat to the outside, cools, and condenses into its liquid phase. An expansion valve regulates the refrigerant liquid to flow at the proper rate.

The liquid refrigerant is returned to another heat exchanger where it is allowed to evaporate, hence the heat exchanger is often called an evaporating coil or evaporator blower.

As the liquid refrigerant evaporates it absorbs heat from the inside air, returns to the compressor, and repeats the cycle. In the process, heat is absorbed from indoors and transferred outdoors, resulting in cooling of the train.

2.3. Inertial Measurement Unit

Today, Inertial Measurement Units (IMUs) are widespread in many application contexts. Cellular phones, cars, human motion, robotics, self-driving vehicles, navigation in transportation vehicles, military and aviation represent only a part of frameworks in which these kinds of devices are more and more employed (see for instance but not only [23]–[28]). One of the reasons for such expansion is that in many practical situations, IMUs represents an optimal trade-off to achieve the design requirements and implement effective and efficient diagnostic [29], [30].

According to the complexity, costs, size and weight constraints of the specific application, IMUs could integrate different kind of sensors. The most common are: triaxial accelerometers (used for measuring the linear acceleration towards the three axes), triaxial gyroscopes (used for measuring the angular rate toward the three axes) and triaxial magnetometers (used for measuring the static magnetic field toward the three axes) or only a subset of them.

From a practical point of view, the common solutions available today on the market, are low-cost low-power unit based on Micro Electro-Mechanical Systems (MEMS) devices [31]–[33]. MEMS-based IMUs have great performances in terms of accuracy, stability integration capability and cost-efficiency. Furthermore, thanks to their small size, MEMS-based IMUs are easily integrated in many systems and they can provide measurement information for algorithms of positioning, localization and tracking just to cite a few [34]–[36].

The Inertial platform analyzed in this work is the LSM9DS1 iNEMO inertial module by ST Microelectronics. This IMU is a MEMS device which integrates a 3-axial accelerometer, a 3-axial gyroscope, a 3-axial magnetometer and a temperature transducer. The key features of the considered device are the following:

- 3 acceleration channels, 3 angular rate channels, 3 magnetic field

channels.
- 9-axes degree of freedom.
- $\pm 2/\pm 4/\pm 8/\pm 16$ g linear acceleration full scale.
- $\pm 4/\pm 8/\pm 12/\pm 16$ gauss magnetic full scale.
- $\pm 245/\pm 500/\pm 2000$ dps angular rate full scale.
- 16-bit data output.
- SPI and I2C serial interfaces.
- Analog supply voltage 1.9 V to 3.6 V.
- Embedded temperature sensor.
- Embedded FIFO.
- Position and motion detection functions.
- Guaranteed to operate over an extended temperature range from -40 °C to +85 °C.
- Typically adopted in several applications as indoor navigation, smart user interfaces, advanced gesture recognition and automotive.

The LSM9DS1 is a system-in-package usually integrated within simple evaluation board required to easily integrates the unit within more complex systems. In this case, the STEVAL-MKI159V1 adapter board from ST Microelectronics has been used. An image of the adapter board with the LSM9DS1 MEMS-based IMU is reported in Fig. 2.5.

Fig. 2.5. STEVAL-MKI159V1 adapter board from ST Microelectronics used to host the LSM9DS1 MEMS-based IMU.

Furthermore, a suitable Printed Circuit Board (PCB) has been specifically designed and realized for hosting the IMU and connectors needed for powering the device and allowing digital data exchange with the required external Micro Controller Unit (MCU).

The LSM9DS1 inertial platform has been configured to have a full scale of 16 g for the accelerometer, a full scale of 2000 dps for the gyroscope and a full scale of   16 gauss for the magnetometer. Such full scales allow to achieve a sensitivity of 0.732 mg/LSB, 0.43 mgauss/LSB, and 70 mdps/LSB respectively.

To acquire data from the IMU the SPI serial standard interface has been used. An STM32 Nucleo-64 boards by ST Microelectronics is used to retrieve the data coming from the IMU through a ribbon cable using an SPI communication configured to work at 10 kHz.

More in detail, the Nucleo-64 board integrates a STM32F401RE microcontroller which is based on a high-performance ARM®Cortex® -M4 32-bit RISC architecture. It is used to manage the configuration and communication over I2C interface with the inertial platform and sends the acquired data through USB to a laptop.

The firmware of the STM32 Nucleo-64 handles the data acquisition doing polling of the LSM9DS1 data-ready register.

A summary of the proposed acquisition chain is illustrated in Fig. 2.6.

MEMS-based IMU

Triaxial Accelerometer
- Full scale ±16 g
- Sensitivity 0.732 mg/LSB

Triaxial Gyroscope
- Full scale ±2000 dps
- Sensitivity 70 mdps/LSB

Triaxial Magnetometer
- Full scale ±16 gauss
- Sensitivity 0.58 mgauss/LSB

Nucleo 64 board

To initialize and set all the DUT functionalities.

To acquire data coming from the MEMS sensors using I2C communication.

To transfer data to a PC using USB communication interface (ODR = 119 Hz)

Laptop

Responsible for collecting and storing the data measured by the IMUs.

Fig. 2.6. Summary of the IMU acquisition chain including a MEMS-based platform, a MCU-based Nucleo 64 board and a laptop.

The primary purposes of the STM32 Nucleo-64 boards are the following:

- To initialize and set all the DUT functionalities.
- To acquire data coming from the MEMS sensors. The communication between the DUT and the microcontroller is based on the I2C communication bus, which operates at 400 kHz.
- To transfer the acquired data to a PC through the USB communication interface, which implements a virtual COM port service operating at 115200 bps. The output data rate (ODR) selected for this application is 119 Hz since it is a classical choice for many positioning algorithms [25]. In this case, an analog antialiasing filter of 50 Hz is automatically introduced on each axis and on each sensor.

2.4. Lithium-Ion batteries

In everyday life people use electrical energy to power most of their devices, leading to a great necessity of stored electrical energy. Nearly all of the electricity is generated at large power plants, then it is delivered to buildings through transmission lines, transformers and cables. The energy is at this point available on demand via wall outlets [37].

Batteries are a valid alternative to electricity distribution through grids which remarkably allows more freedom.

The energy of chemical compounds acts as a storage medium, and during discharge a chemical process generates energy. For some batteries this process can be reversed, thus the battery can be recharged. This allows a differentiation of batteries into two main categories: Primary and Secondary [38]:

- Primary batteries convert chemical energy into electrical energy only once.
- Secondary batteries are reversible energy converters and can be charged and discharged a fixed amount of time.

During the last forty years Lithium batteries have gained a central role in the battery market. Lithium batteries are used in many complex critical systems such as pacemakers and bioengineering device, mission-critical defense and space systems, portable radio transceivers, mobile phones and laptops, the majority of miniaturized electronic devices and many others.

Most lithium batteries have a cell voltage range of 1.5 - 4.0 V. Since lithium is a lightweight material, these batteries have a high energy content by weight.

Other advantages of using lithium as battery anodes are: Flat and stable discharging current, wide temperature range (e.g. from -10 °C up to +55 °C), long shelf life (over 10 years), more environmentally friendly with respect to batteries that use metals such as nickel and cadmium.

Lithium battery got its name from the metal of the anode (negative electrode), which is the most lightweight metal and the third element of the periodic system. In primary batteries the electrolyte is made from an organic solvent and a salt solved in it, the salt usually is a lithium salt. The cathode material can be solid or fluid (some examples are Thionyl chloride SOCl2 or Copper Monosulfide CuS). However, Lithium batteries are mainly known as secondary batteries. Many cells have been developed starting from primary ones. For example, a widely used secondary Lithium cell is based on an anode made of lithium-aluminum alloy with manganese and chromium additions and a manganese dioxide cathode. The electrolyte of this cell is made of a salt mixed with ethylene carbonate (EC). This battery can last up to 500 cycles with a depth of discharge of 10%. Many other examples could be made, but the most important secondary battery is the Lithium-ion battery commercialized by Sony in 1991. The anode of these batteries can be made of carbon in graphitic form and contains lithium in the charged state. The cathode is made from cobalt oxide (CoO2) which is able to build lithium-cobatl oxide(LiCoO2) during discharge phase. Lithium ions migrate back and forth during cycling between the two host lattices, Carbon (C) and cobalt oxide (CoO2).

Since 1991 lithium-ion batteries technology have been considerably improved to achieve higher standards in terms of eco-sustainability, cost and useful life leading to the development of solid-state batteries with polymeric electrolyte.

The internal structure of a cylindric Lithium-Ion battery is illustrated in Fig. 2.7.

Despite several improvements, some shortcomings related to the use of Lithium-Ion batteries still remain. First of all, Lithium-ion batteries represent complex electrochemical-mechanical systems in which various degradation mechanisms are possible. These degradation mechanisms reduce the charge capability of the battery over its life, resulting in capacity drop and internal resistance increase (which lead to a rapid decrease of the battery useful life). Other shortcomings are related to the temperature excursion. While low temperature significantly decreases their performances, high temperature could lead to severe failure and risk of explosion.
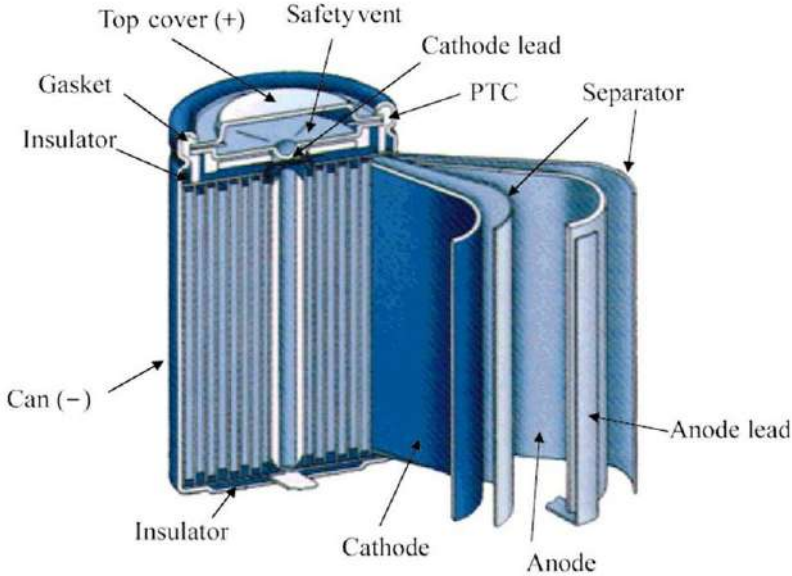
Fig. 2.7. Internal structure of a cylindric Lithium-Ion battery.

2.5. Lube Oil Console for Gas Turbine

A gas turbine is a turbomachinery that converts thermal energy into mechanical energy. The standard set-up of a gas turbine is an upstream rotating compressor coupled to a combustion chamber and a downstream turbine. Gas turbines work in a continuous thermodynamic cycle and the basic operation is described in the following. Atmospheric air flows through a compressor that brings it to higher pressure, than a fuel is added into the air to create a high-temperature flow after ignition in combustion chamber. This way the chemical energy of the air mixture (air and fuel) is converted in thermal energy. The high-temperature and high-pressure gas enters the turbine: here it expands down to the exhaust pressure and produces mechanical energy. The output of the process is the turbine shaft work that is used to drive the compressor and other devices coupled to the shaft (e.g. electric generator).

The proper working of the turbomachinery is ensured by the gas turbine auxiliary systems such as starting system, lubrication system and control system, as it is possible to see in the functional diagram in Fig. 2.8.
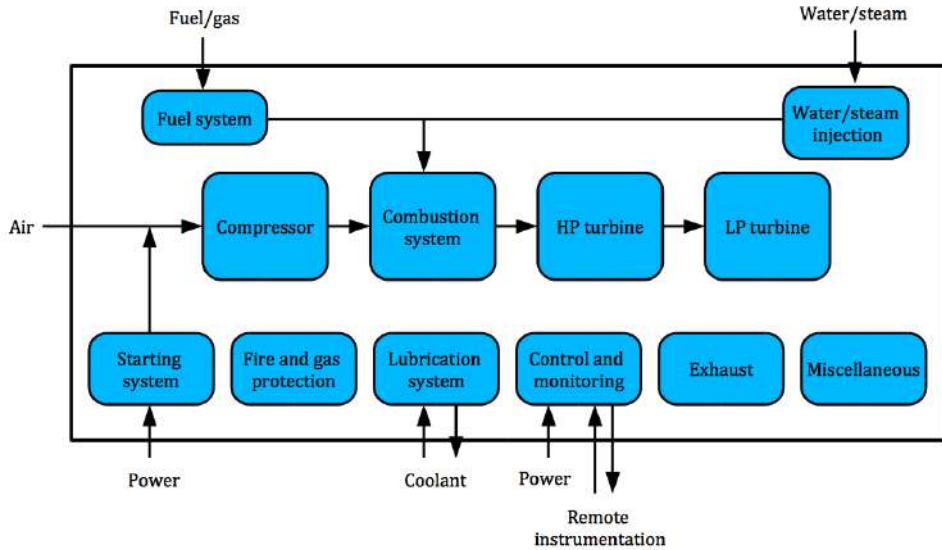
Fig. 2.8. Functional diagram of a gas turbine.

One of the most important auxiliary unit is the lubrication system, also known as lube oil console.

A lube oil console is used to reduce friction and fatigue between moving surfaces in mechanical equipment. The main aims of the mineral lube oil console are the following [39], [40]:

- Take the oil from a tank.
- Regulate the hydraulic parameters of the oil (such as pressure, temperature, density, viscosity and flow rate).
- Provide clean oil to the components that require it at the proper pressure, temperature, density, viscosity and flow rate.

In compliance with [40], the complete Reliability Block Diagram (RBD) of the Lube Oil under analysis is illustrated in Fig. 2.9 highlighting redundancies using different colors. The 2oo3 configuration is illustrated using a grey box, while the parallel configuration is highlighted by red color. The standby redundancies are characterized by their own symbols: a green box represents a warm standby (i.e. the standby unit is powered and ready to operate on demand) while cold standby configurations (i.e. the standby unit is completely disconnected and it cannot fail when the main unit is activated) are illustrated using yellow.

A specific description of the functionalities of each block included in the RBD in Fig. 2.9 is included in the following.
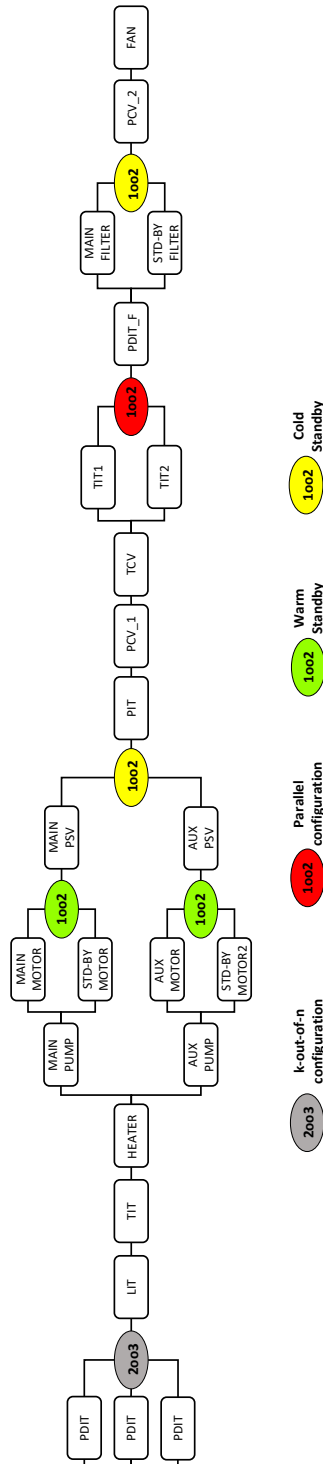
Fig. 2.9. Reliability Block Diagram of the Mineral Lube Oil Console under analysis.

The tank is equipped with a temperature sensor (TIT - Temperature Indicating Transducer), three identical differential pressure sensors (PDIT - Pressure Differential Indicating Transmitter) in 2-out-of-3 configuration (simply called 2oo3 in the following), a level transducer (LIT - Level Indicating Transmitter) and an electric heater which are submerged in the oil.

A "Pumps unit" composed by two redundant branches called "Pump unit 1" and "Pump unit 2" is used to take the oil from the tank and to send it to the temperature regulation system.

Each pump unit is composed by a pump which is driven using two redundant electric motors to ensure high continuity of service. The main motor and the standby motor supply the main pump in the unit 1, while the auxiliary motor and the standby motor 2 supply the auxiliary pump in the unit 2. A Pressure Safety valve (PSV) is installed along with each pump.

A Pressure Indicating transmitter (PIT) and a Pressure Control Valve (PCV) are installed to monitor and regulate the pressure of the oil outcoming from the pump, while the temperature of the oil is monitored and regulated using two redundant TITs and a Temperature Control Valve (TCV).

The final stage of the system is a filtering unit composed by two redundant filters (called Main filter and Standby filter) along with a PDIT and a PCV used to identify when a filter is dirty, and it requires to be replaced.

The system includes also a fan to guarantee air exchange.

2.6. DC-DC converter

A DC-DC converter is a system used in power supply unit to convert a DC voltage value into a greater/lower DC voltage value. The DC-DC converter under analysis is a customized unit used for power supply of a sensor node in the context of WSN-based diagnostic units for industrial complex systems. However, the same sensor node could also be used for several purposes, such as smart farming monitoring system, IoT infrastructure, health monitoring, non-destructive control, etc. The developed power supply is composed of a battery pack, regulated through a buck converter. Additional integrated sensors of current and voltage (power meters) are equipped on the input and output of the DC-DC converter. The electric circuit of the Buck converter under study is shown in the electrical schematic in Fig. 2.10. A synchronous topology has been selected since it avoids the conduction losses on the diode due to the forward voltage with consequent increment of conversion efficiency.

25
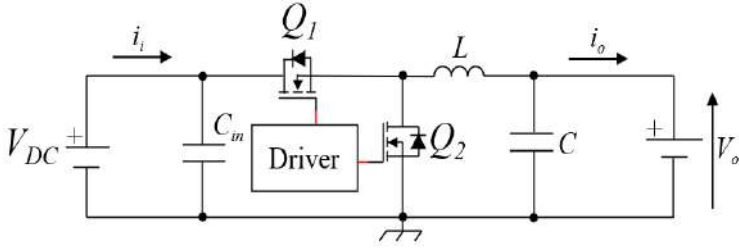
Fig. 2.10. Topology of the Buck converter under analysis.

The electrical parameters of the developed Buck converter are reported in TABLE II. I.

TABLE II. I
PARAMETERS OF THE DC-DC CONVERTER UNDER ANALYSIS.

PARAMETER	VALUE
Input Voltage V_{in}	18 V
Input Current I_{in}	170 mA
Output Voltage V_{out}	9 V
Output current I_{out}	350 mA
Load R_L	25 Ω

The prototype of the developed diagnostic system is illustrated in Fig. 2. 11 highlighting the main components of the DC-DC converter and the ESP32 microcontroller used to drive the converter, to acquire data from condition monitoring sensors and transmit the data to a central hub for elaboration and storage purposes. A summary of the main components included in the customized PSM-based Buck DC-DC converter is reported in TABLE II. *II*.

To achieve the best performance regardless of the operating conditions, the use of Pulse Skipping Modulation (PSM) has been evaluated. As known, the most used modulation technique for power converters is the Pulse Width Modulation (PWM) which operates at a constant frequency and variable duty cycle [41], [42]. The switching losses of a PWM converter are approximately constant independently from the load since the operating frequency is fixed. Thus, the conversion efficiency is usually maximum at heavy-load but decreases dramatically at light-loads. For this reason, the PSM has been used to increase the conversion efficiency also at light load. This modulation operates at fixed duty cycle and period, but some cycles are skipped to adjust the output power. The advantage of this modulation is the reduction of switching loss for light load with consequent increment of DC-DC conversion efficiency cycle [41], [42].
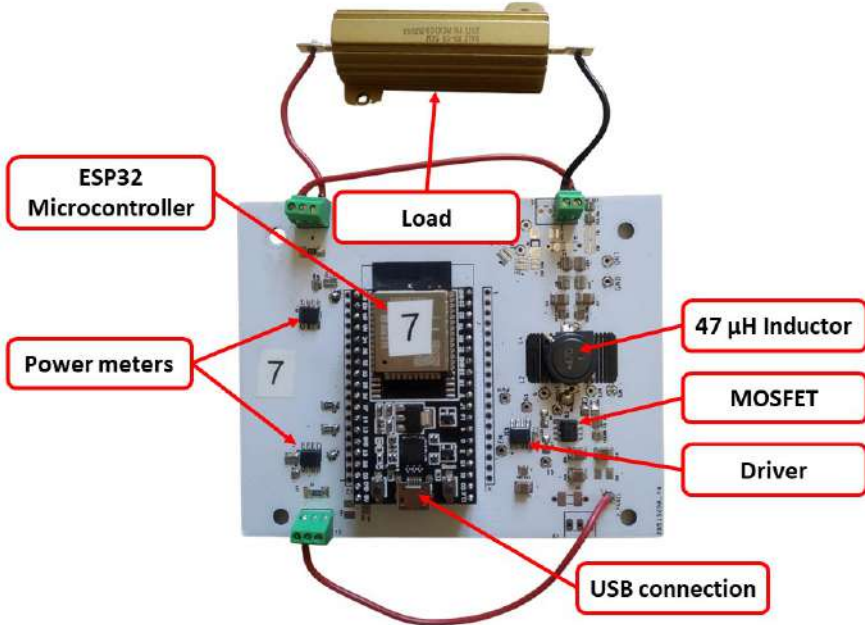
Fig. 2. 11. Prototype of the power supply under analysis. The main components of the DC-DC converter are highlighted with red boxes.

Table II. II

Main components of the developed DC-DC converter including model, manufacturer and main parameters.

Component	Model and Manufacturer	Main Parameters
Inductor	NS12575T470MN By Taiyo Yuden	L = 46.3 µH r_L = 62.3 mΩ @1 MHz
Output Capacitor	GRM32ER7YA106KA By Murata	C = 9.84 µF r_C = 12.2 mΩ @1 MHz
MOSFETs	BSO150N03 By Infineon	r_{DS} = 18.2 mΩ
Driver	TPS28226DRBR By Texas instrument	Sink current I_{max} = 4 A Max frequency 2 MHz
Power Meters	INA219 By Texas Instrument	12 BIT ADC Conversion time 532 µs

CHAPTER 3

FAILURE MODES AND EFFECTS ANALYSIS: A CRITICAL REVIEW

Failure Modes, Effects and Criticality Analysis (FMECA) plays a central role in many Design for Reliability procedure. This chapter provides an overview about FMECA according to the international standard IEC 60812 (2018). The base theory, the aim and the methodology of the classical FMECA are presented along with an extensive state of the art. All the alternative Risk Priority Numbers that do not completely revolutionized the base idea of the IEC 60812 have been taken into account in order to identify the optimal FMECA procedure to be included in the proposed Reliability Life Cycle. The final part of the chapter implements the classical FMECA along with some alternative approaches to the most critical component of an HVAC system for railway applications. [1,2]

---

[1] The literature review included in this chapter has been published as "L. Ciani, G. Guidi, and G. Patrizi, "Fuzzy-based approach to solve classical RPN drawbacks for railway signaling systems," *IEEE Intelligent Transportation System Magazine*, Article in Press, 2021 ".

[2] The part of this chapter related to the alternative Risk Priority Numbers has been published as: L. Ciani, G. Guidi, and G. Patrizi, "A Critical Comparison of Alternative Risk Priority Numbers in Failure Modes, Effects, and Criticality Analysis," *IEEE Access*, vol. 7, pp. 92398–92409, 2019.

3.1. Introduction on FMEA and FMECA methods

Failure Modes and Effects Analysis (FMEA) was firstly introduced in 1950s by U.S. Military Standard MIL-STD 1629: "Procedures for Performing a Failure Mode Effect and Criticality Analysis" [43]. After that, it was developed and applied by NASA, in 1960s, to verify reliability of space programs. In the late 1970s, the Ford Motor Company introduced FMEA to the automotive industry for safety and regulatory consideration. By 1990s, many international standards were published for different applications of FMECA. Nowadays, it becomes one of the most powerful methods used for risk assessment and maintenance management [44].

FMEA is a systematic procedure for the analysis of a system to identify the potential failure modes, their causes and effects on system performance (performance of the immediate assembly and the entire system or a process). Here, the term system is used as a representation of hardware, software (with their interaction) or a process [45]. The analysis is successfully performed preferably early in the development cycle so that removal or mitigation of the failure mode is most cost effective. This analysis can be initiated as soon as the system is defined enough to be presented as a functional block diagram where performance of its elements can be defined. FMEA timing is essential; if done early enough in the development cycle, then incorporating the design changes to overcome deficiencies identified by the FMEA may be more cost-effective. It is therefore essential that the FMEA task and its deliverables be incorporated into the development plan and schedule. Thus, FMEA is an iterative process that takes place coincidentally with design process. The FMEA is also an iterative process that is updated as the design develops. Design changes will require that relevant parts of the FMEA be reviewed and updated [46], [47].

FMEA is applicable at various levels of system decomposition from the highest level of block diagram down to the functions of discrete components or software commands. Therefore, application of FMEA have to be preceded by a hierarchical decomposition of the system into its more basic elements. It is useful to employ simple block diagrams to illustrate this decomposition. The analysis then starts with lowest level elements. A failure mode effect at a lower level may then become a failure cause of a failure mode of an item in the next higher level. The analysis proceeds in a bottom-up fashion until the end effect on the system is identified.

FMEA generally deals with individual failure modes and the effect of these failure modes on the system. Each failure mode is treated as independent. The

procedure is therefore unsuitable for consideration of dependent failures or failures resulting from a sequence of events. To analyze these situations other methods and techniques, such as Markov analysis or fault tree analysis may be required.

The reasons for undertaking Failure Mode Effects Analysis may include [47]:

- To identify those failures which have unwanted effects on system operation, e.g. preclude or significantly degrade operation or affect the safety of the user.
- To satisfy contractual requirements of a customer, as applicable.
- To allow improvements of the system's reliability or safety (e.g. by design modifications or quality assurance actions).
- To allow improvement of the system's maintainability (by highlighting areas of risk or nonconformity for maintainability).

Traditionally there have been wide variations in the manner in which FMEA is conducted and presented. The analysis is usually done by identifying the failure modes and failure mechanisms, their respective causes and immediate and final effects. The analytical results can be presented on a worksheet that contains a core of essential information for entire system and details developed for that specific system. It shows the ways the system could potentially fail, the components and their failure modes that would be the cause of system failure, and the cause(s) of occurrence of each individual failure mode.

FMECA (Failure Modes, Effects and Criticality Analysis) is an extension to the FMEA to include a means of ranking the criticality of the failure modes to allow prioritization of countermeasures [47]. It is widely considered an effective and efficient methodology for risk assessment, failure analysis and maintenance decision-making. It is a powerful and effective tool that could be easily applied to estimate the risk associated to every failure of a safety-critical system [15], [39], [48]. It adds to the FMEA worksheet the frequency of occurrence rank (O), the severity measure rank (S) and the detection of each failure mode (D). According to the International Standard IEC 60812 (2018) [47], these three parameters are combined in order to calculate a criticality rank called Risk Priority Number (RPN), as follow:

$$RPN = O \cdot S \cdot D \qquad (3.1)$$

Occurrence (O) is an index that measures the probability that a failure mode will happen, where the greater the index the greater the frequency of occurrence. Severity (S) measures the impact of the failure effects on the system

functionalities, low values of S stand for negligible failures, while greater values of S stand for catastrophic failures with safety implication. Detection (D) represents the probability that the failure mode will be diagnosed before its effects are manifested on the system. Detection is ranked in a reverse order compared to the previous parameters, the higher the D, the lower the possibility of detecting the failure [49]–[51]. The international standard IEC 60812 [47] suggest to use only integer number in a 1-to-10 scale to assess the values of O, S and D. Consequently, the RPN can assume values within the range [1; 1000].

3.2.   Drawbacks of classical RPN

The classical RPN formula in Equation 3.1 is very simple and intuitive, but its use for the criticality analysis of the system/process failure modes has highlighted many drawbacks [51]–[58]:

- Gaps in the Range: The RPN values are not continuous but have only a few unique values. If a 10 values scale is used, 88% of the range is empty; the largest number is 1000, but 900 is the second largest followed by 810, 800, 729, and 720.

- Duplicate RPNs: Different values of the parameters may generate identical RPN values. For example, the RPN numbers 60, 72, and 120 can be formed from 24 different combinations of S, O, and D. However, the hidden risk implications of the three events may be very vastly different because of the different severities of the failure modes.

- High Sensitivity to Small Changes: Multiplying the numbers comprising the RPN is intended to magnify the effects of high-risk factors. For above mention example, if O and D are both 8, then a 1- point difference in severity rating results in a 64 quantitative grade difference in the RPN. It is very evident RPN value varying sensitivity to small changes.

- Inadequate Scale of RPN, in fact the relative importance among O, S and D is not taken into consideration. The three factors are assumed to have the same importance. This may not be the case when applying to a practical FMECA. For example, the RPN1 with 3, 4, and 5 as S, O, and D, respectively, gives the value of 60, whereas the RPN2 with 3, 5, and 5 gives 75. In fact, in RPN2 the failure mode has the twice the occurrence, but the RPN value is not doubled. This explains that the RPN values cannot be compared linearly.

- O, S, D are defined in very subjective way, in fact the three factors are difficult to precisely determine. Much information in FMECA can be expressed in a linguistic way such as moderate, remote or very high. Anyway, people who express these judgements should presumably be experts in the field where FMECA is performed, and these experts represent the most reliable source of information. In spite of that, experts' knowledge is often uncertain and incomplete so that FMECA analysis is to performed by the support of methods able to properly manage such uncertainty of input data.

- Dispersion of RPNs: All the possible RPN values are scattered among the full range, in fact there is a high concentration of multiple value in the left side of the scale and a low concentration in the right side.

Fig. 3.1 shows the numbers formed by the RPN and the relative problems expressed below. The most intuitive drawback is the presence of "holes" in the scale between the numbers. In fact, greater part of the numbers is concentrated in the left side of the scale. Another evident problem shown by the figure is the multiplicity of some values, for example there are 24 different combinations for obtaining some specific RPN values.
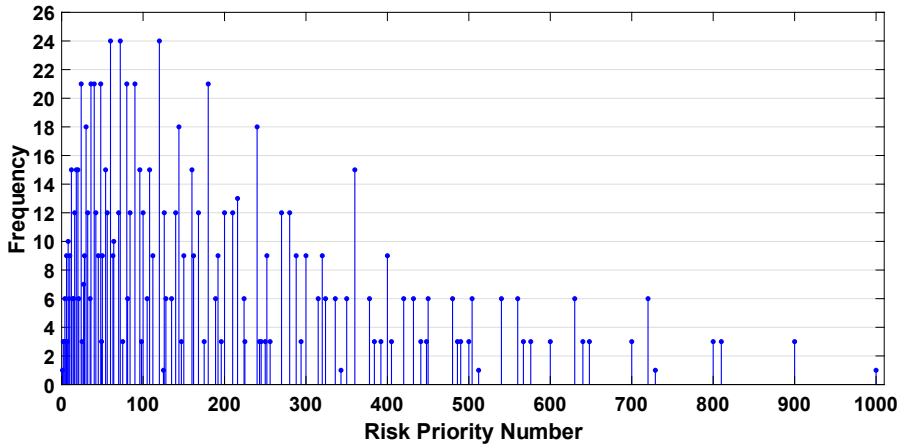
Fig. 3.1. Histogram of all the possible values of Risk Priority Number.

3.3. Review of innovative FMECA approaches

Many works in recent literature try to propose different methodologies to overcome the problems associated to the classical RPN. Braband [59] proposes to assess the new IRPN as the sum of the Occurrence, Severity and Detection using logarithmic scale to evaluate the indexes (more detail about this approach are given in section 3.4.1). This method is the only alternative RPN included in the international standard IEC 60812 [47]. Chang et al. [60] propose an exponential RPN called ERPN given by the sum of three exponential functions, one for each of the indexes. This approach is enhanced in [61] using the product of occurrence and detection that stand as probability, and severity plays a role as value in power (more detail about these two exponential methods are given in section 3.4.2). In this way a higher weight to Severity is assessed compared to Occurrence and Detection. Several papers propose different RPN formulations introducing innovative coefficients and parameters. These solutions could solve at least two of the RPN drawbacks: the duplicate issue and the relative importance of the parameters. For instance, in [62] an alternative RPN is proposed by considering the associated quality cost and the capability of failure detection system as additional terms to optimize the prioritization of each failure mode. Carmignani [63] introduces a priority-cost FMECA calculating the priority of every potential design fault and the profitability in accomplishing the corrective design actions. In [64] the Root Cause Analysis (RCA) is used to assess sub-criterion weight and significant coefficient for Occurrence, Severity and Detection. Tang et al. [65] proposes an innovative approach considering the ambiguity measure of the experts that carried out the assessment of O, S and D to mitigate the subjectivity issue. Chang [66] suggests to use a method that integrates the ordered weighted geometric averaging (OWGA) operator and the decision-making trial and evaluation laboratory (DEMATEL) approach in order to a achieve an efficient and effective algorithm in risk analysis. In [67] a simple approach is proposed defining a new metric called RAV (Risk Assessment Value) as the product of Occurrence and Severity divided by Detection. In [68] Severity is obtained by summing different parameters related to safety, environment, costs, customer satisfaction and mission goal. In [69] a data-driven RPN calculation is introduced based on quantitative measures and sizable datasets to obtain a more formal and objective risk evaluation. Giardina [70] introduces a FMECA and HAZOP (hazard and operability analysis) integrated analysis called FHIA to improve risk analysis of complex system. In [71] a method based on minimum cut set is

proposed to take into account multiple failure modes and to extend the RPN definition by multiplying it with a weight parameter which characterize the importance of the failure causes within the system.

A widely used technique to overcome the RPN problems is the fuzzy logic [72]. Fuzzy theory was firstly introduced by Professor Lotfi A. Zadeh in 1965 [73] to handle the concept of partial-truth values between "completely true" and "completely false". A fuzzy set A is usually expressed in terms of its membership function μ_A which maps domain elements (x) in their respective degrees of belonging in the interval from 0 to 1 [74], [75]:

$$A = \{(x, \mu_A(x)) \mid x \in X\} \tag{3.2}$$
$$\mu_A(x) : X \to [0, 1] \tag{3.3}$$

The strength of fuzzy is intrinsically correlated to Equation 3.2, in fact the possibility of assessing a degree of membership that is not fixed to 0 or 1, but could varies within a range between "false" to "true" allows to achieved several advantages in reliability engineering.

Fuzzy is flexible and conceptually easy to understand, it introduces linguistic terminology and it allows to work with approximate values as well as incomplete or ambiguous data [76], [77].

Fuzzy theory was applied to FMECA procedure in many different industrial fields, such as nuclear power plant [78], traditional power plant [79], power electronic components [80], satellite [55], agriculture [81], Oil&Gas [82], tunneling operation [83] and many others. Fuzzy FMECA could be conducted in many different ways depending on the drawbacks that the procedure wants to overcome. In many paper the fuzzy "If-Then principle" is implemented because it is far too easy the assessment of O, S and D using linguistic terms (see for instance [84]–[89]). All papers that use the fuzzy if-then to solve the FMECA drawbacks start representing Occurrence, Severity and Detection through linguistic variables that are associated to fuzzy membership functions [90]–[93]. Using a set of fuzzy inference rules, a fuzzy RPN assessment is obtained [94]–[99]. All the If-then FMECA procedures in literature are based on one of the following three types of fuzzy inferences to solve the if-then rules. The Mamdani inference firstly proposed in [100] results in an aggregation of fuzzy sets that must be defuzzied to achieve the crisp RPN. In the Sugeno inference [101] the results of the if-then rule provides a polynomial that must be solved to obtain the RPN. The last one is the Tsukamoto inference [102] which is a hybrid approach based on Mamdani and Sugeno inferences which is not widely used in literature. The

main disadvantages of all the if-then approaches is the number of rules that must be assessed.

If-Then FMECA is not the only way to introduce fuzzy theory inside the classical FMECA procedure. In [103] an approach based on convex normalized fuzzy number is introduced using the degree of match to estimate the matching between the expert judgments and the fuzzy number. Keskin et al. [104] proposes to use the fuzzy Adaptive Resonance Theory (fuzzy ART) to assess the Risk Priority Number. In [105] the fuzzy RPN is calculated using alpha-level sets and linear programming models through the weighted geometric means of the fuzzy number assessed for Occurrence, Severity and Detection. In [106] a fuzzy approach integrating weighted least square method is used to achieve robustness RPN results in term of uncertainty. In [107] a consensus-based group decision-making framework has been proposed based on possibilistic hesitant fuzzy linguistic information. The integration of fuzzy theory with TOPSIS (Technique for Order of Preference by Similarity to Ideal Solution) method was firstly proposed by Chen [108], and then applied in many papers such as Braglia et al. [109], Carpitella et al. [110] or Mangeli et al. [111] to solve FMECA drawbacks. In [112] the analytic hierarchy process (AHP) was used to integrate inside the classical FMECA some economic aspects. This approach was enhanced in [113] combining fuzzy TOPSIS and AHP method. Other papers integrate fuzzy logic with different approaches, such as TODIM (a Portuguese acronym of interactive and multiple attribute decision making) [114], VIKOR (a Serbian acronym of Multicriteria Optimization and Compromise Solution) [115], PROMETHEE (Preference ranking organization method for enrichment evaluation) [116] and QUALIFLEX (Qualitative flexible multiple criteria method) [117].

3.4.   Alternative RPNs: a critical analysis

Several papers propose different approaches to overcome the limits associated to RPN. As extensively illustrated in the previous subsection, literature is plenty of papers that suggest integrating fuzzy theory in FMECA to optimize the RPN calculation.

Despite these papers provides significant results in terms of RPN prioritization, the introduction of many different approaches within the classical FMECA drastically increase the complexity of the procedure. In fact, in many of these works, fuzzy is combined with other mathematical theory or with advanced approaches, consequently the complexity of the technique rapidly increases.

Moreover, in almost all of the already proposed fuzzy-FMECA the concept of the classical RPN defined in the international standard IEC 60812 is completely missing. The risk is not achieved by the multiplication of the three above-mentioned indexes, but with different complex procedures that are not fully compatible with the policy of many companies that looks at easy and fast procedure to assess the risk analysis.

As a consequence, the rest of the work takes into account only the alternative RPNs which propose powerful solution to solve the drawbacks included in Section 3.2 without increasing the computational complexity of the method and remaining coherent to the classical idea included in the standard IEC 60812 [47].

TABLE III.I summarizes the main proposed approaches for each of the individual problem [51]. The first column of TABLE III.I contains the RPN drawbacks, while the second one contains the main methods suggested in literature to solve them.

TABLE III.I
POSSIBLE APPROACHES TO SOLVE COMMON RPN ISSUES.

ISSUES	POSSIBLE APPROACH
Holes	- Sum O, S and D.
Duplicate RPNs	- Introduction of corrective factors. - Using exponentiation or exponential function. - Scale reduction. - Fuzzy theory.
High sensitivity	- Sum O, S and D.
Importance O, S, D	- Introduction of corrective factors. - Different formulation of RPN. - Fuzzy theory.
Subjectivity O, S, D	- Fuzzy theory. - Measurements
Dispersion	- Logarithmic equation. - Sum O, S and D. - Scale compression.

3.4.1. Sum of the indexes

Braband et al. [59], [118] proposes an alternative equation for the RPN assessment, using the sum of the three metrics, called IRPN - Improved Risk Priority Number. The international standard IEC 60812 (2018) [47] recognizes the alternative RPN method proposed by Braband (called ARPN - Alternative

Risk Priority Number - instead of IRPN) as the only admissible modified version of the commonly used RPN with the aim of providing a more consistent assessment of criticality when parameters can be quantified on a logarithmic scale. Equation 2 shows how to assess the Alternative Risk Priority Number:

$$ARPN \; = \; IRPN \; = \; O + S + D \tag{3.4}$$

Considering a [1; 10] range of integer values for the three parameters O, S and D, Fig. 3.2 shows the numbers formed by the IRPN and the relative repetition frequency. The IRPN is a powerful solution for most the problems explained above because it results in a continuous scale delating the value dispersion, as shown in Fig. 3.2.

In fact, IRPN assumes all the integer values in the interval from 3 to 30, therefore the IRPN scale has no gaps.

Moreover, it solves the sensitivity problem because small variations in one ranking have the same effects on the IRPN, independently of the values of the other factors. Despite these advantages, the problem of the duplicate IRPNs is highly accentuated, with the maximum repetition frequency of 75, three times bigger than the classical RPN. This problem is clearly evident considering that the percentage number of unique values is only 2.8% comparing to the 12% of the classical RPN.
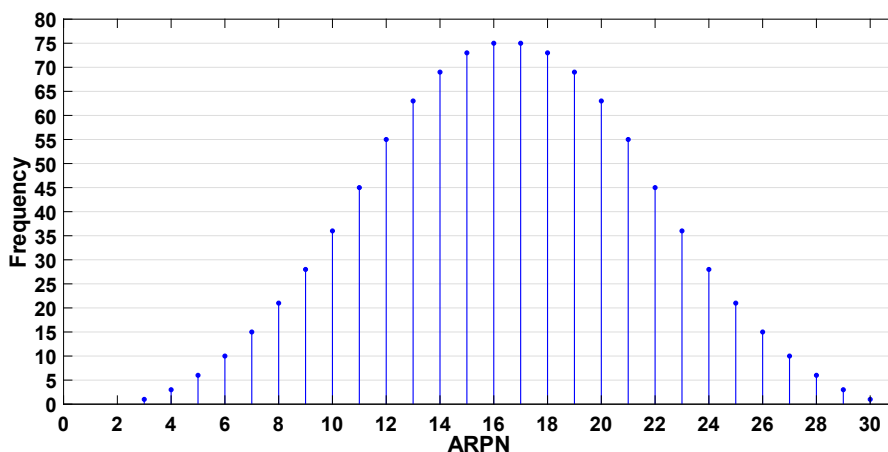
Fig. 3.2. Histogram of all the possible values of ARPN (or IRPN).

3.4.2. Exponential alternatives to the RPN

Chang et al. [60] proposed an exponential RPN (ERPN) as Equation 3.3. In this method, the number of unique values for risk evaluation of failures has been increased, reducing the number of duplicates RPNs (see Fig. 3.3).

$$ERPN(x) = x^{W_S \cdot S} + x^{W_O \cdot O} + x^{W_D \cdot D} \tag{3.5}$$

Where:

- x is a positive integer, and $x \geq 2$;
- O, S and D are integer values between 1 and 10;
- W_S, W_O, W_D are weights for severity, occurrence and detection respectively.

Chang proved that the optimal choice is x=3, leading to 220 different unique values.
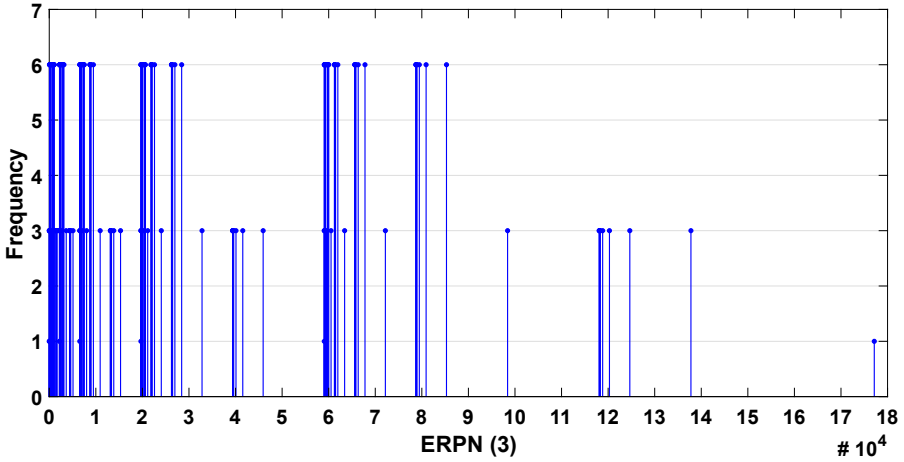
Fig. 3.3. Histogram of all the possible values of ERPN(3).

Khorshidi et al. [61] proposed another exponential alternative modifying Equation 3.3, as the product of occurrence and detection standing as probability, and severity plays a role as value in power, as follow:

$$URPN(z) = (O \cdot D) \cdot z^S \tag{3.6}$$

Where z is a real number, and $z \geq 1$. According to Khorshidi, the choice that leads to the maximum number of unique values is $z = e$ (see Fig. 3.4).
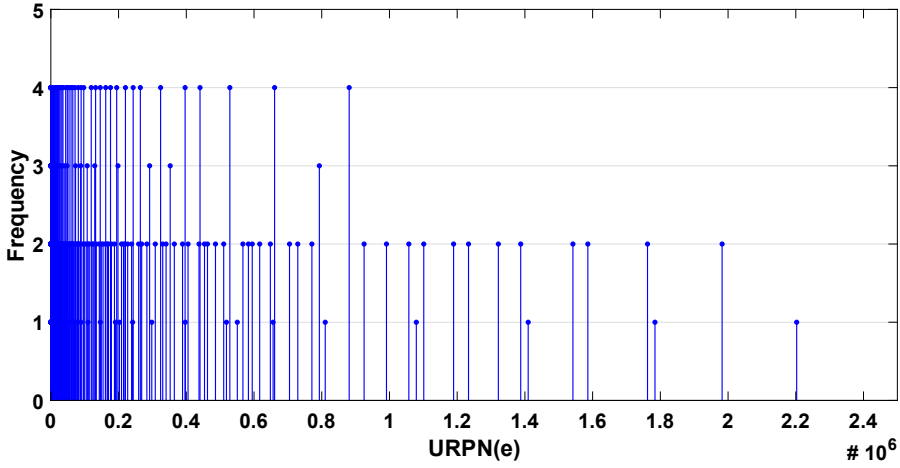
Fig. 3.4. Histogram of all the possible values of URPN(e).

Both ERPN and URPN solve very well the problem of duplicate values and of different importance between O, S and D. However, both approaches amplify the problems of the "holes" and the dispersion issue because the maximum possible values are respectively 2 and 3 order of magnitude larger than the classical RPN.

3.4.3. Logarithmic RPN

The application of logarithm in the classical RPN equation compress the scale of possible RPN to a 0-3 range (if base-10 is used), as shown in Fig. 3.5.
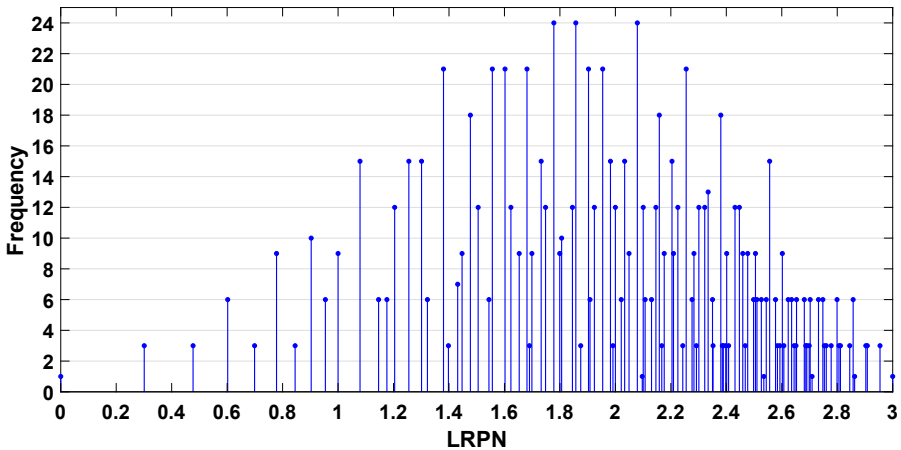
Fig. 3.5. Histogram of all the possible values of LRPN.

$$LRPN = log(O \cdot S \cdot D) \qquad (3.7)$$

The logarithmic RPN reduces the dispersion and the "holes" in the scale, but it has no effects on duplicates issue and on the importance of the three factors. For these reasons it is not an optimal method and in literature there is not any documentation that applies this equation on real systems.

3.4.4. Scale adjustments

Many papers (see for instance but not only [68], [69], [119]–[121]) suggest to reduce the number of O, S and D levels because in many applications it is difficult to evaluate the parameters in ten different levels. According to these works, the choice of only 5 levels is optimal in several manufacturing fields. The standard IEC 60812 (2006) [122] proposed a 10-level approach and a reference guide to how assess these values. The 2018 new version of the standard [47] revises the reference guide table and it lets the designers free to assign the O, S and D values personalizing their own tables.

For instance, the assessment of the occurrence rank is strictly related to the item failure rate and usually the failure rates of the components that make up a generic system varying in few orders of magnitude. Therefore, the use of a 5 or less different occurrence values is recommended in order to cover the failure rates range in an optimal way. The consequences of a failure mode influence the severity assessment. In many applications it is not possible to define ten different levels of failure consequences, therefore the severity ranks are merged in sublevels with two or three individual level together. The same considerations are valid also for the detection range because usually the diagnostic information is not completely available during the design phase. For these reasons, a 5 or less levels evaluation is optimal also for severity and detection.

Two examples of the application of a 1-5 scale of the O, S and D parameters for classical RPN and for IRPN are illustrated respectively in Fig. 3.6 and Fig. 3.7. ERPN and URPN using 1 to 5 scale are both the best solutions in term of duplicate issues, but the range of possible values has little significance even in this case, as it is possible to see in Fig. 3.8 in case of the URPN(e) approaches is applied using a reduced scale.

Overall, all the proposed approaches maintain each related drawback, but the adjustment of the scale using only five different values allow to mitigate these limits, making every technique more suitable for industrial and manufacturing applications.

Fig. 3.6. Histogram of all the possible RPN using a 1-5 scale of O, S and D parameters.

Fig. 3.7. Histogram of all the possible IRPN using a 1-5 scale of O, S and D parameters.

Fig. 3.8. Histogram of all the possible URPN(e) using a 1-5 scale of the O, S and D parameter.

3.4.6. Statistical comparison

The associated statistics of different alternative Risk Priority Numbers (e.g. mean, median, minimum value and maximum value) have been evaluated and included in TABLE III.II. The table also includes the maximum repetition frequency of a single risk value (called "Max Rep"), the number of different unique values and the percentage of unique values, considering that the possible different combinations of three factors expressed in a 10-point scale is 10^3.

The IRPN proposed by Braband [59], [118] is characterized by a very compressed range from 3 to 30, with mean value and median coincident with the midpoint of the range. These parameters highlight that this method can easily overcome the "holes" and the dispersion issues. At the same time, the duplicate problem is amplified, as it is clearly identified considering that the percentage number of unique values is only 2.8% comparing to the 12% of the classical RPN. Indeed, it is characterized by the highest "most frequency", representing the main problem related to this approach. Quite the opposite, ERPN and URPN solve very well the duplicates drawback with the maximum repetition frequencies of 6 and 4 respectively, and the related percentages of unique values of 22% and 42% respectively. Despite these advantages, both these methods have a limited use because of the range of possible values that is extremely broadened. Indeed, the mean value and the median of ERPN and URPN are shifted toward high numbers, producing results very difficult to interpret. The logarithmic RPN is characterized by a very compressed and dense scale with the same number of unique values of the classical RPN. The worst issue of this method is the shape of the distribution, that is moved toward the highest values of the range (i.e. right side of the plot), as it is possible to see in Fig. 3.5.

The statistical demonstration of this sentence is provided by the LRPN median, that is the only value in the column higher than the midpoint of the range. In this case, the shape of the distribution and the high median value make the definition of the RPN threshold very challenging, because lots of RPN are concentrated in the final section of the range. Finally, TABLE III.II also highlights that all the alternative approaches proposed above have advantages and disadvantages, and no one can solve at the same time all the RPN drawbacks without introducing other limitations. Therefore, in many real cases, the classical RPN is still suitable, and the choice of alternative method depend on the analytical cost that a company can support. TABLE III.III compares the application of a scale adjustment on the classical RPN and on the alternative Risk Priority Numbers analyzed in this section. Obviously, the identification of

just 5 different values mitigates the duplicate issue, as it is possible to see comparing the percentages of unique values in TABLE III.II. and TABLE III.III.

TABLE III.II

COMPARISON BETWEEN STANDARD RPN AND DIFFERENT ALTERNATIVE RISK PRIORITY NUMBER APPROACHES USING A 1 TO 10 SCALE.

FUNCTION	MEAN	MEDIAN	MAX REP	NUMBER OF UNIQUE VALUES	% UNIQUE VALUES	MIN	MAX
RPN 1-10 scale	166	105	24	120	12%	1	1,000
IRPN 1-10 scale	16.5	16.5	75	28	2.8%	3	30
ERPN(3) 1-10 scale	26,572	13,203	6	220	22%	9	177,147
URPN(e) 1-10 scale	105,402	4,877.5	4	420	42%	e	2,202,646.6
LRPN 1-10 scale	1.9679	2.0212	24	120	12%	0	3

.

TABLE III.III

COMPARISON BETWEEN STANDARD RPN AND DIFFERENT ALTERNATIVE RISK PRIORITY NUMBER APPROACHES USING A 1 TO 5 SCALE.

FUNCTION	MEAN	MEDIAN	MAX REP	NUMBER OF UNIQUE VALUES	% UNIQUE VALUES	MIN	MAX
RPN 1-5 scale	27	20	9	30	24%	1	125
IRPN 1-5 scale	9	9	19	13	10.4%	3	15
ERPN(3) 1-5 scale	217.8	189	6	35	28%	9	729
URPN(e) 1-5 scale	419.77	147.78	3	70	56%	e	3.710,33
LRPN 1-5 scale	1.78	1.86	9	30	24%	0	3

3.5. Case study: HVAC system

In order to compare advantages and disadvantages of the alternative risk priority numbers described above, a FMECA for Heating, Ventilation and Air Condition (HVAC) system in railway application has been developed in this work. The critical analysis of the comparison can provide recommendations and suggestions regarding the choice of the alternative RPN basing on the type of application.

This study focuses on the failure modes, effects and criticality analysis of some of the most critical components that make up the HVAC: compressor, evaporator blower and air flow detector.

The compressor draws in the cold gases exiting the evaporator battery at low pressure and compresses them, so it comes out as gas at high pressure and overheated. The motor compressor is fitted with an electromagnetic valve to vary the capacity according to the demands of refrigeration load at any time.

Blowers are used to compress the water vapor for the purpose of raising its pressure and saturation temperature. This produces the desired heat transfer in the main heat exchanger for recycling the energy in the vapor, which greatly improves energy efficiency.

Air flow detector, due to the interaction with the streaming fluid, generates an electrically measurable signal for determination of the total flow of the fluid. The air flow sensor can alert to HVAC cooling system failures, or it can be used to ensure there is air flow through the cabins all times.

3.5.1. Risk assessment using 1 to 10 scale

TABLE III.IV includes all the items failure modes, the causes and the effects of each mode. The latter are divided in "Local effects" (i.e. effects on compressor), "Global effects" (i.e. effects on the upper classification-level) and "Effects on train" (i.e. effects on the global system). The occurrence O, severity S and detection D of each mode were provided by three reliability experts in order to quantitatively consider the criticality of the components. The average results of the assessment are included in table V. O, S and D parameters can assume value in the 1-10 scale, the assessment follows the rules proposed in the international standard IEC 60812.

The occurrence values are assessed considering the failure rate of each failure mode (provided by the manufacturer), while the failure effects influence the severity values.

TABLE III.IV

FMEA of the Most critical items included in a HVAC.

FAILURE MODES	CAUSES OF FAILURE	LOCAL EFFECTS	GLOBAL EFFECTS	EFFECTS ON TRAIN
COMPRESSOR				
FM1 - Motor does not start on demand	Motor seize up. Blocked compressor. Damage winding.	Loss of pumping capacity.	Loss of cooling function.	Loss of cooling capacity.
FM2 – Incorrect signal from thermostat	Overheating of compressor. Thermostat dirty.	Loss of protection	Possible damage of compressor.	Possible loss of cooling capacity.
FM3 – Pump gas leakage	Mechanical failure. Fretting compressor.	Loss of refrigerant pumping.	Loss of cooling function.	Loss of cooling capacity.
FM4 – Sticking internal valve	Internal failure. Valve dirty.	Pressure doesn't increase.	Loss of cooling function.	Loss of cooling capacity.
FM5 - Internal overload motor protection	Short circuit. Electric overload. Compressor motor protection failure.	Loss of pumping capacity. Short circuit of compressor.	Loss of cooling function.	Loss of cooling capacity.
EVAPORATOR BLOWER				
FM6 – Incorrect signal from thermostat	Vibrations over specification. Aging.	Motor does not work.	No ventilation Low pressure switch will cut off.	Loss of ventilation, cooling and heating capacity.
FM7 – Fails to run	Internal failure. Coil in short-circuit. Lifetime of the motor (aging).	Motor does not work.	No ventilation in evaporator coil. The pressure will increase.	Loss of ventilation, cooling and heating capacity.
FM8 - Mechanical crack	Lack of oil. Bearings deteriorated. Lifetime of the motor (aging).	Motor does not work.	No ventilation in evaporator coil. The pressure will increase.	Loss of ventilation, cooling and heating capacity.
AIR FLOW DETECTOR				
FM9 – It doesn't detect air flow when there is.	Internal failure.	The heating coil and the compressor are stopped.	Loss of heating or cooling function.	Loss of cooling and heating capacity.
FM10 - It detects air flow when there is no supply air	Internal failure.	There is no detection of air flow.	Possible damage of the system.	No effect

TABLE III.V is divided into six sections:

1. Occurrence, Severity and Detection assessment for each failure mode.
2. Classical RPN assessment ("value" column) and its decreasing prioritization ordering of the modes ("rank" column). The highest the rank, the highest the criticality related to this failure mode.
3. IRPN assessment ("value" column) and its decreasing prioritization ordering of the modes ("rank" column).
4. ERPN assessment using base $x = 3$ and identical weights (set as 1) for the factors ("value" column) and its decreasing prioritization ordering of the modes ("rank" column).
5. URPN assessment using $z = e$ ("value" column) and its decreasing prioritization ordering of the modes ("rank" column).
6. LRPN assessment ("value" column) and its decreasing prioritization ordering of the modes ("rank" column).

The criticality assessment using the classical method leads to RPN values which vary in the first half of the admissible range (i.e. from 1 to 1000). The results are quite distant from each other: this leads to an easy prioritization of the mode from the highest RPN (most critical) to the lowest (least critical).

TABLE III.V

FAILURE MODE OF AN HVAC IN RAILWAY APPLICATION RANKED USING CLASSICAL AND ALTERNATIVE RISK PRIORITY NUMBERS.

	O	S	D	RPN		IRPN		ERPN (3)		URPN (e)		LRPN	
				VALUE	RANK	VALUE	RANK	VALUE	RANK	VALUE	RANK	VALUE	RANK
FM1	8	6	7	336	3	21	2	9,477	4	22,592	5	2.527	3
FM2	3	5	4	60	10	12	10	351	10	1,780	9	1.778	10
FM3	6	6	7	252	6	19	6	3,645	7	16,944	6	2.401	6
FM4	5	6	5	150	7	16	8	1,215	8	10,085	7	2.176	7
FM5	4	6	5	120	9	15	9	1,053	9	8,068	8	2.079	9
FM6	8	8	4	256	5	20	5	13,203	3	95,390	3	2.408	5
FM7	9	8	6	432	1	23	1	26,973	1	160,971	1	2.636	1
FM8	8	8	5	320	4	21	2	13,365	2	119,238	2	2.505	4
FM9	7	7	7	343	2	21	2	6,561	5	53,735	4	2.535	2
FM10	7	3	7	147	8	17	7	4,401	6	984	10	2.167	8

A threshold value which distinguishs the group of the most dangerous modes from the set of the least critical one could be identified comparing the data or by different mathematical approaches (more detail about the determination of the thresholds is reported in the next subsections.

The IRPN scores vary in a limited range, leading to two main problems: item with the same values (e.g. Despite different O, S and D index FM1, FM8 and FM9 have the same IRPN=21) and difficulty in the definition of a RPN threshold rate due to a very compressed scale of admissible results.

Both ERPN(3) and URPN(e) provide outcomes hardly comparable with the classical formulation because of the very wide admissible range. For the same reason the interpretation of the criticality related to these numbers is quite hard.

The LRPN is the only one that maintains the same prioritization ordering of the classical formulation. The results are irrational numbers compressed in a very small range.

Fig. 3.9 illustrates the results obtained from the analysis of TABLE III.V highlighting how the different approaches provide different prioritization orders. The chart shows ten different groups composed by five bars with different colors where the groups stand for the analyzed failure mode, the colors represent the different techniques, and the height of the bars identifies the criticality of the mode. The height of a bar depends on the priority associated to that mode with the specified method: the higher the bar and more critical is the mode, therefore higher is the rank.
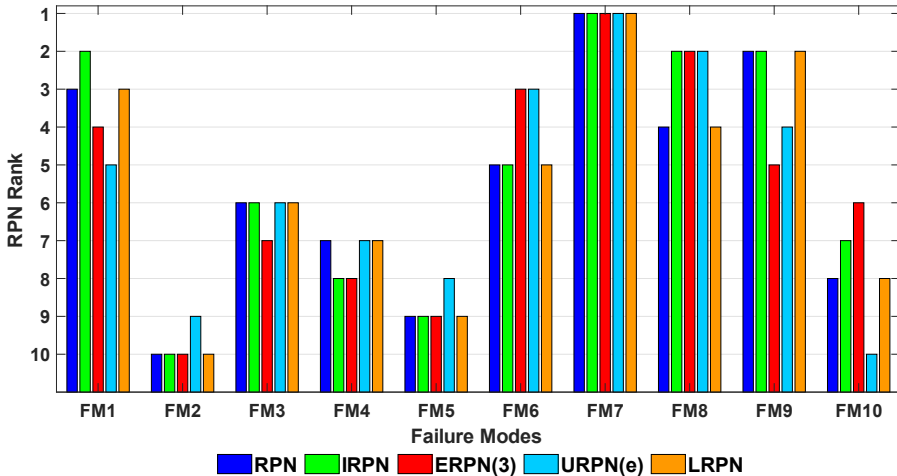
Fig. 3.9. Bar plot of the classical and alternatives RPN ranking for each failure mode.

What is striking about Fig. 3.9 and TABLE III.V is that the different approaches provide different ordering despite they consider the same O, S and D dataset. The most evident finding to emerge from the IRPN analysis is the duplicate issue, consequently the IRPN prioritization is meaningless because it is impossible to distinguish the more critical modes in presence of many identical values. The ERPN amplifies the importance of higher values of O, S and D; for instance, FM8 moves from the fourth rank in the classical RPN prioritization to the second position in the ERPN rank, due to the very high value of O and S. In some circumstances, giving high priority to higher O, S and D values could be positive. The disadvantages are evident when only one value of O, S and D is close to 10: in this case the exponential formulation of the higher parameter is dominant making the other one negligible. The URPN amplifies the importance only of the severity, therefore if the severity is very high the mode will definitely be critical. For example, using this method FM6, FM7 and FM8 have the maximum priority because they are characterized by the highest severity of the system (S=8).

In summary, these results show that the most reasonable prioritization order is the one provided by the classical Risk Priority Number.

3.5.2. Risk assessment using 1 to 5 scale

After the risk assessment of the previous section, the occurrence O, severity S and detection D rates of the identified failure modes were evaluated again considering a scale adjustment in order to test and validate the advantages and disadvantages of the 1 to 5 scale applied to the classical Risk Priority Number. The new O, S and D score are collected in TABLE III.VI.

TABLE III.VI

O, S AND D ASSESSMENT FOR THE FAILURE MODE OF AN HVAC USING A 1 TO 5 SCALE.

FAILURE MODE	O	S	D
FM1	5	3	5
FM2	1	2	2
FM3	3	3	5
FM4	2	3	3
FM5	1	3	3
FM6	5	5	2
FM7	5	5	4
FM8	5	5	3
FM9	4	4	5
FM10	4	1	5

TABLE III.VII
COMPARISON OF THE RANKS USING 1 TO 5 SCALE AND 1 TO 10 SCALE APPLIED TO
CLASSICAL RISK PRIORITY NUMBER.

FAILURE MODE	1-10 SCALE RPN		1-5 SCALE RPN	
	VALUE	RANK	VALUE	RANK
FM1	336	3	75	3
FM2	60	10	4	10
FM3	252	6	45	6
FM4	150	7	18	8
FM5	120	9	9	9
FM6	256	5	50	5
FM7	432	1	100	1
FM8	320	4	75	3
FM9	343	2	80	2
FM10	147	8	20	7

TABLE III.VII includes a comparison between the results of the classical RPN assessment obtained using the standard scale and the reduced scale. As the table shows, there is not a significant difference between the rank provided by the two approaches. There are only two small differences between the two datasets:

   a) The rank of the failure modes FM4 and FM10 are inverted: using the 1-10 scale FM4 and FM10 are the 7th and the 10th most critical modes respectively, instead the rank are swaped when the 1-5 scale are used.
   b) The failure modes FM1 and FM8 are characterized by the same RPN when the 1-5 scale are used: it results in two modes with the same rank.

The difference a) is negligible because affect two modes characterized by low Risk Priority Number. In fact, FM4 and FM10 are considered not critical mode, therefore the difference in the rank provided by the two approaches is not significant. Quite the opposite, the difference b) is very relevant because highlights that the scale reduction could involves in a duplicates problem.
This result is somewhat counterintuitive. The most surprising aspect of this difference is that the percentage of unique value using the 1-5 scale is doubled respect to use the 1-10 scale. Theoretically, reducing the scale, the number of duplicates decrease. Actually, the use of a small scale involves more duplicates in the O, S and D assessment, consequently the possibility of a duplicate in RPN evaluation increase.

The probability of a duplicate generated by the same combination of O, S, D increases using 1-5 scale while the probability of a duplicate generated by different combination of O, S, D decreases.

Taken together, these results suggest that there is a benefit in the use of a reduced scale in term of unique values, but it is very important to pay specific attention to the Occurrence, Severity and Detection assessment in order to cover the complete admissible range of the parameter and reduce the possibility of a duplicate in the Risk Priority Number.

The results obtained in TABLE III.VII are summarized in Fig. 3.10, using a bar plot illustrating ten different groups composed by two bars with different colors. The different groups stand for the analyzed failure modes, the blue bar represents the 1-10 scale assessment, and the red bar stands for the 1-5 scale evaluation. The higher the bar, the higher the rank associated to that mode (i.e more critical is the failure modes).

Fig. 3.11 shows another comparison of the Risk Priority Numbers obtained in the previous assessments, where the height of the bars stands for the relative RPN, expressed as the ratio between the Risk Priority Number of that mode divided by the maximum RPN of the analysis.

Considering the critical failure mode (i.e. the mode characterized by high relative RPN) no significant differences were found between the two approaches. Quite the opposite, analyzing the modes with low Risk Priority Number there was a significant difference between the two method. This means that, in proportion, the reduced scale affects more the assessment of the lower Risk Priority Numbers compared to the higher Risk Priority Numbers.
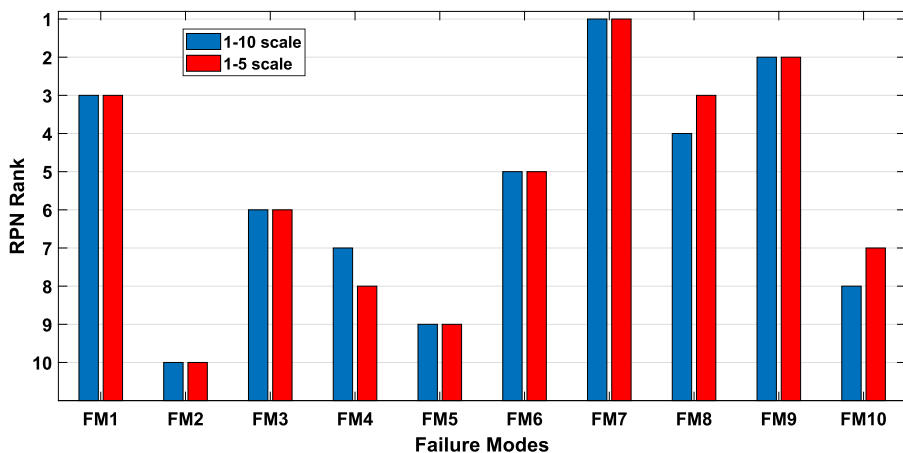
Fig. 3.10. Bar plot of the RPN ranking using 1-10 scale (blue bars) and 1-5 scale (red bars) for each failure mode.
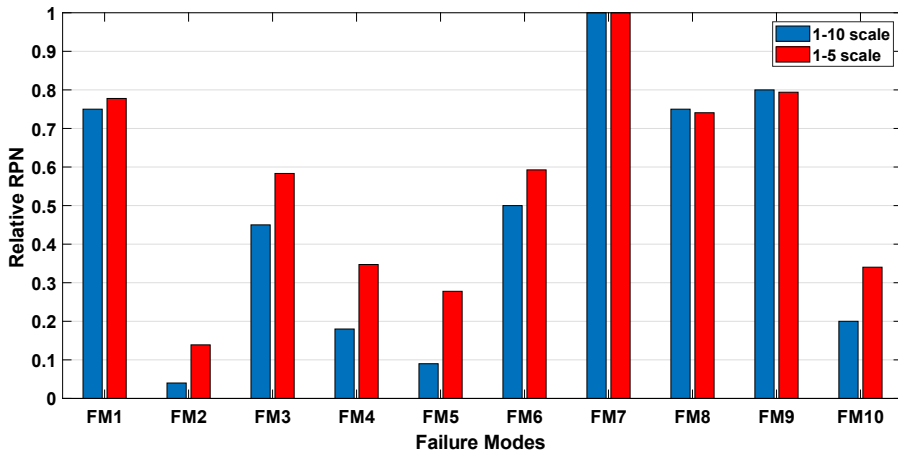
Fig. 3.11. Bar plot of the relative Risk Priority Number obtained using the classical RPN approach (blue bars) and the 1-5 scale RPN (red bars).

3.6. Measurements to improve FMECA during product life cycle

The proper implementation of FMECA during the different steps of the product life cycle (design, development, manufacturing and maintenance) allows to identify and possibly solve potentially critical problems. It can be readily perceived that the information provided by the FMECA can be useful during the definition of the operative constraints, as well as during the preventive maintenance operations.

The main aim of this thesis is to provide a general Data-Driven Reliability Life Cycle procedure that could be implemented to any kind of complex system. From this perspective, FMECA plays a central role within the procedure. But, how measurements (and more generally data) could improve the performances of FMECA procedure?

If FMECA is properly integrated within the approach the answer to the previous question is quite straightforward. The first part of the FMECA worksheet is a qualitative analysis that includes the report of failure modes and mechanisms, causes of failure and failure effects. The second part of the worksheet includes the quantitative part of the procedure with the assessment of Occurrence, Severity and Detection. As seen before in section 3.2. one of the greatest drawbacks of the FMECA is the evaluation of these criticality indexes that could be extremely subjective and mainly influenced by the experience of

the analyst. A possible solution is to assess O, S and D by means of dedicated measurements to delete the subjectivity issue. The solution proposed in this work to improve FMECA reducing subjectivity of the assessment by means of measured data are reported in the following paragraphs.

3.6.1. Occurrence assessment by means of Accelerate Test

The occurrence O could be estimated using the results of Accelerated Life Test (ALT) on the specific components. ALT technique allows to achieve information about the component reliability based on the results of tests performed subjecting a product to conditions above the nominal service operations [123], [124]. Stresses such as temperature excursion, high voltage and severe mechanical shocks are able to discover faults in a short amount of time with respect to the nominal conditions [125]–[127]. ALT is particularly useful in case of electronic devices because the wear-out of such components usually occurs after an extended amount of time. Therefore, it is essential to speed up the test since testing a population of electronic devices in normal conditions would yield few or no failures in a reasonable time even if a large sample is tested. An online monitoring of the device during the test allows to achieve information about the Accelerated Time-To-Failure (ATTF) of the items under test. Obviously, these data must be properly processed before they can be used to assess Occurrence. The complete procedure is illustrated in Fig. 3.12.

First of all, the Time-To-Failure (TTF) in standard conditions must be evaluated using the proper Acceleration Factor (AF). Depending on the stress test used to accelerate the failure mechanisms, different models can be implemented to estimate the AF. When estimating acceleration due to temperature, the Arrhenius degradation model is usually implemented. It is used to express both a single failure mechanism's sensitivity to temperature and also a product's thermal acceleration factor. The accelerating factor AF_{Arr} of the Arrhenius model is given by [128]:

$$AF_{Arr} = exp\left[\frac{E_a}{K_B}\left(\frac{1}{T_0} - \frac{1}{T_{test}}\right)\right]$$
(3.8)

Where T_0 is the reference temperature (i.e. operating temperature of the item in standard conditions), T_{test} is the exposition temperature during the test, $K_B = 8.617 \times 10^{-5}\ eV/K$ is Boltzmann's constant and E_a is the activation energy of the failure mechanisms, expressed in eV.
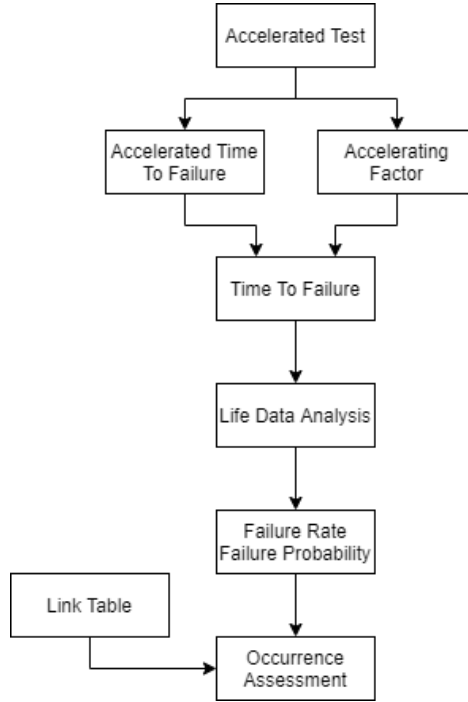
Fig. 3.12. Proposed procedure to assess Occurrence O by means of measured data during accelerated test.

Regarding the humidity stress, one of the most common models is the Peck's law, introduced by D.S. Peck in 1989. The accelerating factor AF_{Peck} considering Peck's law is written as [128]:

$$AF_{Peck} = \left(\frac{RH_{test}}{RH_0}\right)^p \tag{3.9}$$

Where RH_0 is the percentage reference humidity, RH_{test} is the percentage humidity during the stress test and p is the accelerating power for this stress (usually set equal to 2.7).

Another common acceleration factor is used in case of vibration stress, as follow [123]:

$$AF_{vib} = \left(\frac{W_{test}}{W_0}\right)^m \tag{3.10}$$

Where W_0 is the reference vibration in standard conditions, W_{test} is the vibration endured during the stress test and m is the accelerating power for this stress (usually set equal to 4). For other AF models, see [123], [128].

Once the TTF is obtained using the proper AF model, a statistical analysis called Life Data Analysis (LDA) could be used to achieve information on the failure rate and on the probability of failure of the device [129]–[131]. Finally, a link table could be used to associate the estimated failure rate or the probability of failure to the occurrence levels. An example of link table used to assess O in case of 1-to-5 scale is illustrated in TABLE III.VIII. The devices under test are electronic components.

TABLE III.VIII

EXAMPLE OF LINK TABLE USED TO ASSESS OCCURRENCE BY MEANS OF MEASURED DATA DURING ACCELERATED TEST IN CASE OF 1-TO-5 SCALE.

OCCURRENCE	RATING	FAILURE PROBABILITY
Remote	1	$< 1 \cdot 10^{-9}$
Low	2	$1 \cdot 10^{-9} \div 1 \cdot 10^{-8}$
Moderate	3	$1 \cdot 10^{-8} \div 5 \cdot 10^{-7}$
Possible	4	$5 \cdot 10^{-7} \div 1 \cdot 10^{-6}$
High	5	$> 1 \cdot 10^{-6}$

3.6.2. Severity assessment

The assessment of the Severity S is one of the most challenging tasks of a complete FMECA report. It is extremely difficult to precisely estimate S since it must rate the severity of the potential effect of the considered failure mode. Usually, a predetermined severity scale must be established and then the FMEA team assess the severity ranking of each failure based on the agreed-upon scale. Thus, unfortunately, it is not possible to improve the severity assessment based on available data coming from the product life cycle.

3.6.3. Detection assessment by means of online diagnostic

The assessment of the Detection rate D is strictly related to the presence of diagnostic systems able to identify the failure of a component before its effects are manifested on the system.

Instrument on-board diagnostics is performed directly on the component in question to assess its working/failure status. This makes it necessary to introduce a dedicated on-board monitoring and diagnosis system to be installed near the analyzed component. Notwithstanding the increase of the system complexity and its cost, the introduction of diagnostic units allows to achieve several requirements extensively described in Section 7.

Among others, data coming from diagnostic units could be used to precisely estimate the detection rate D within the FMECA process. Consequently, it is possible to continuously improve the FMECA during the product life cycle using the data of the diagnostic unit.

3.7. Final Remarks

The aim of this section was twofold:

- Contextualize the FMEA procedure within the concept of Data-Driven Reliability life Cycle.
- Examine the different approaches presented in literature regarding the evaluation of alternative risk priority numbers.

Several methods currently exist for the risk assessment of failure modes during a FMECA. These alternative approaches try to compensate the multiple issues related to the classical RPN interpretation, such as the presence of holes within the RPN range, the presence of duplicates, the values dispersion, the subjectivity of the assessment etc. The work focuses only on the techniques which do not introduce additional corrective factors or do not completely distort the formulation of the RPN with the introduction of new analytical theory.

The analyzed approaches are: the standard RPN, IRPN (consists of the sum of O, S, D), ERPN (based on the exponentiation of O, S, D), URPN (consists on the product of O, D and S as power) and LRPN (based on the logarithm of the product of O, S, D).

The advantages and disadvantages of each technique are evaluated by using a chart of all the possible values obtained combining O, S, D according to each procedure. This study has identified that no one method succeeds to solve all the issues and the solution of one problem involves the worsening of the other drawbacks.

The previous methods have been analyzed also considering a reduced O, S, D scale from 1 to 5. This reduction does not solve the problems but mitigates all of them, therefore it represents a trade-off through easiness of implementation, accuracy of results, flexibility to different application field, solution of the issues.

In order to test and validate these assumptions, a FMECA was developed for the critical components of a HVAC system used in railway applications. These results show that the RPN is the most trustworthy equation because it provides the most reasonable prioritization order of the failure modes, especially when a 1-to-5 scale is involved.

Finally, some considerations regarding the subjectivity of the O, S and D assessment are presented. This work proposes to solve the problem assessing the parameters by means of data measured during the product life cycle (accelerated test for Occurrence evaluation and Diagnostic units for Detection assessment).

CHAPTER 4

A PROPOSAL FOR RPN THRESHOLD ESTIMATION

This chapter analyze the RPN threshold estimation methods available in literature. However, the available procedures suffer many drawbacks. Trying to fill this need, this section proposes a new approach for the Risk Priority Number threshold estimation based on a statistical analysis and compares the proposed method with the other quantitative prioritization techniques found in literature. The goal of the chapter is to introduce an innovative methodology that effectively identify the most critical component of the system under test, which is a fundamental aspect of the proposed Reliability Life Cycle procedure. The proposed approach has been applied to the electrical and electronic components included in a Spanish 2 MW onshore wind turbine. [1]

---

[1] The part of this chapter related to the innovative RPN threshold estimation method has been published as: M. Catelani, L. Ciani, D. Galar, and G. Patrizi, "Risk Assessment of a Wind Turbine: A New FMECA-Based Tool With RPN Threshold Estimation," IEEE Access, vol. 8, pp. 20181–20190, 2020.

4.1. The problem of RPN threshold estimation

This part of the work deals with the problem of the evaluation of a threshold risk value, which can distinguish negligible and critical failure modes. In fact, the components covered by the FMECA procedure are usually very different from a risk value point of view. The most critical failure modes, characterized by high RPN values, should be separated from those characterized by a significantly lower RPN value. The selection of "high priority" failure modes is a very critical issue for the development of corrective action plans and for the Operation&Maintenance decision-making process. Thus, the question is: "How such separation can be performed?"

4.2. Literature review of RPN threshold estimation methods

Usually, companies define the RPN threshold using questionnaires to take into account the judgement of multiple experts in a qualitative manner. Alternatively, some companies apply corrective actions in a hierarchical order starting from the most critical components. Then, countermeasures are applied until the budget allows it. The major flaw of this cost-oriented approach is that some critical risk could not be mitigated. For some kind of applications this approach is still valuable, quite the opposite in case of safety related applications (e.g. railway systems, energy production plant, aerospace field etc.) a more precautionary point of view is required. Consequently, it is extremely important to identify which components are critical and which are not by means of a risk threshold.

The international standard IEC 608212 [47] that define and regulate the FMECA technique misses to consider a method to identify a risk threshold and consequently to divide the failure modes in critical modes and negligible modes. Quite the same, also the Military Standard MIL-STD 1629A [43] does not take into account this aspect. Furthermore, only few papers in recent literature deals with this issue.

Some papers set the RPN threshold subjectively by the judgement of multiple experts in the matter (see for instance but not only [68], [132]–[134]), and only few papers propose their own approaches for the threshold value.

Bluvband et al. [135], [136] highlight for the first time that RPNs follows a particular trend and recommend a graphical tool for RPN analysis. This tool

creates a graph of ordered RPN values called Scree Plot which requires a preliminary ordering of RPN values by size, from smallest to largest. The calculated RPNs ordered by size usually form a right-skewed distribution, with a first tail on the left (negligible risk values) and a second tail on the right (critical risk values representing "outliers" from the distribution analysis point of view). The left part of the plot is characterized by a gradual increase of the RPN values, usually fit by means of a straight line $f_1(x)$ with a slight slope. The RPN values scattered around this line should be considered a kind of "information noise", as they do not require immediate attention. The short uppermost part of the Scree Plot is characterized by a very steep increase of the RPN values (RPN jumps), in the form of a straight-line $f_2(x)$ with a very strong slope. The RPN values scattered around this line are related to the most critical issues of FMECA and must be dealt with promptly. The threshold value is determined in a qualitative way by evaluating the ordinate of the intersection between the two fit lines. The method proposed by Bluvband [135], [136] is an intuitive and simple graphical tool. The idea at the basis of this approach seems to be very interesting. The main concern of the method is related to the subjectivity for the division of the two datasets characterized by different slopes.

Zhao et al. [137] propose a method to obtain a more objective and accurate RPN analysis, as follow:

- Create Scree plot, following the rules explained by the Bluvband method.
- Fit the RPN plot with a polynomial approximation of the first order using the linear regression method.
- Plot the confidence bound of the linear regression.
- Determine the threshold value of RPN from the turning point of the confidence level.

This approach is based on a simple linear approximation method, but in many practical cases the RPNs do not follow a linear trend. Therefore, the approximation of the values with a single straight line provides a significant error.

The use of the 80:20 Pareto principle is one of the most established approaches in reliability analysis to rank failure modes according to their RPN value and to optimize corrective actions for critical components. The Pareto diagram is helpful to visualize the differences between the rankings for the failures and effects. The 80:20 principle can be explained as follow: 80% of the total Risk Priority Numbers calculated during the FMECA procedure comes from only the 20% of the potential failure modes.

Pareto analysis starts with the prioritization of failure modes by ranking them

in order, from the highest risk priority number to the lowest. The Pareto chart combines a bar graph with a cumulative line graph; the bars are placed from left to right in descending order, while the cumulative line distribution shows the percent contribution of all preceding failures. The combined chart uses the 80:20 rule to indicate where the engineering effort should be focused more [138]–[144]. Unfortunately, Pareto chart is not suitable for some kind of risk-assessment applications because it is not always verified that the 80% of the criticalities arise from 20% of the causes, or in other words that the 80% of the RPNs represents the 20% of the failure modes.

4.3. Proposed approach: Boxplot analysis

A new approach has been introduced in this work to overcome the limits of the previous methodologies. The proposed procedure consists of the following steps:

1) Calculation of the Risk Priority Numbers according to the guidelines provided by the FMECA standard (a scale adjustment as in Section 3.4.4 could be implemented in order to minimize the RPN drawbacks achieving an optimal assessment).
2) Identification of the main statistical parameters of the RPN dataset (i.e. 25th percentile, mean value, median value, 75th percentile, outliers, minimum and maximum value).
3) Generation of the boxplot of all the assessed Risk Priority Numbers.
4) The negligible modes are all the failure modes with RPNs below the median value.
5) The critical modes are all the failure modes with RPNs above the 75th percentile.
6) The interval between the median value and the 75th percentile is considered ALARP ("as low as reasonably practicable") region.

As the acronyms suggests, the ALARP region refers to reducing risk to a level that is as low as reasonably practicable. In practice, this means that the operator has to show through reasoned and supported arguments that there are no other practicable options that could reasonably be adopted to reduce risks further [145].
If a failure mode is characterized by an RPN value that falls inside the ALARP zone, then designers have to analyze possible countermeasures to reduce the risk bearing in mind the benefits resulting from its acceptance and taking into

account the costs of any further reduction. Then designers could choose to apply countermeasures or not based on the previous consideration. The upper and lower limits of the ALARP region must be considered as low as reasonably practicable too.

Instead, if the RPN is above the 75th percentile then the risk is treated as intolerable and cannot be justified in any ordinary circumstance, so corrective actions must be implemented.

The introduction of an ALARP region in the process of setting a RPN threshold is one of the main strengths of the proposed method allowing to analytically identify not only a region of maximum criticality but also a set of failure modes with intermediate level of risk. This aspect is well-known in the risk assessment theory, however there are no procedure available in literature that allows to identify objectively and analytically an RPN threshold value for critical modes along with an ALRP region.

4.4. Case study: Electronic components of a Wind Turbine

This study focuses on the (E/E/PE) components (i.e. electrical/electronic/programmable electronic items) inside the wind turbine described in section 2.1. The components are summarized in the low-level taxonomy in Fig. 4.1 (control system) and Fig. 4.2 (Electrical unit).
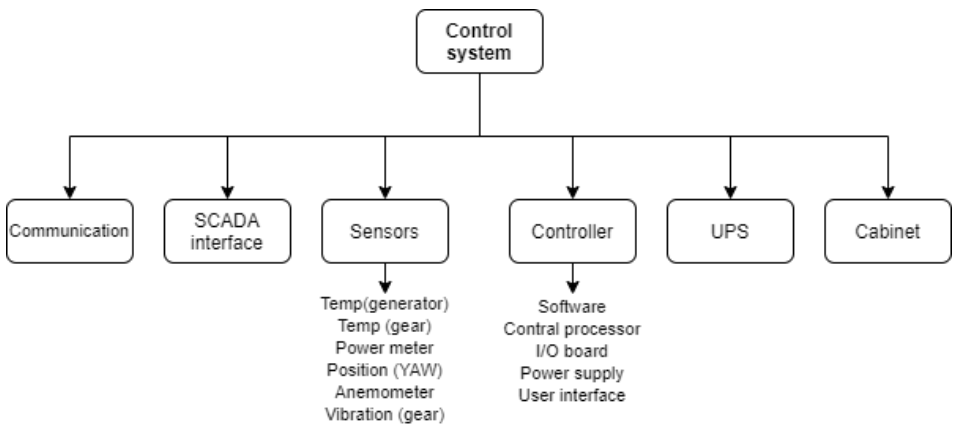
Fig. 4.1. Low-level taxonomy of the WT under test: control system classification.
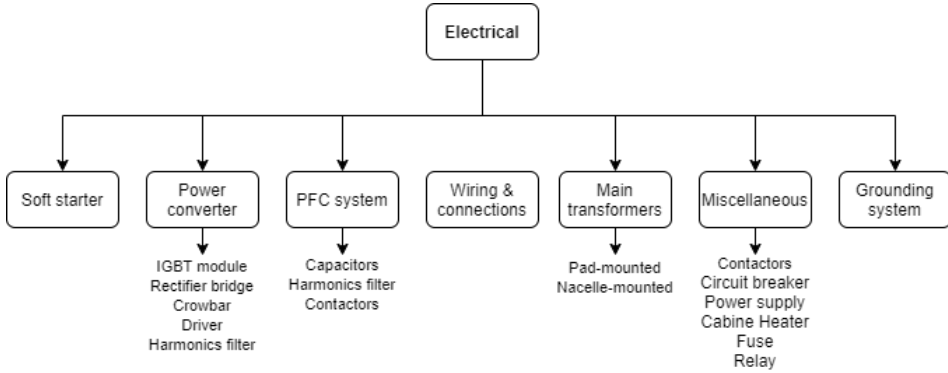
Fig. 4.2. Low-level taxonomy of the WT under test: Electrical unit classification.

TABLE IV.I shows an extract of the FMECA assessed for the E/E/PE components of the G80/2000 WT under test. The complete report includes 100 different failure modes: 38 modes refer to the control system, while 62 modes refer to the electrical subunit.

Since there are no specific standards or handbooks containing failure data of WT, then some generic handbooks are used to carry out the functional failure analysis of the G80/2000 WT tested in this work. The main sources are: HDBK-217plus (2015) [146], Telcordia SR-332 Issue 4 (2016) [147], MIL-HDB 338B (1998) [148], Siemens SN 29500-1 (2013) [149] and IEC 61709 (2017) [150].

The first section of Table V gives an overview of the studied components. The "Upper level taxonomy" column includes the higher hierarchical levels; the "Classification" column shows the current taxonomy level; the "Taxonomy" column identifies the components, and the "Function" column explains the objective of the studied item. The table has a second section for the standard FMEA procedure including the "Failure Mode", "Failure Cause," and a detailed explanation of the failure effects. The local effects describe the consequences of a failure mode on the operation, function, or status of the specific item under consideration, while the global effects stand for the consequences on the operation, function, or status of the higher-level taxonomy categorization (in this work, it refers to the effects on the nacelle and the whole wind turbine.).

In addition, some useful parameters are included in the third section of TABLE IV.I. More in detail, this section includes the failure rate of the considered item, the failure mode probability expressed by α and the mode failure rate which is used to evaluate the Occurrence rate. Considering λ the failure rate of the component, then the mode failure rate $\lambda^{(M)}$ is given by:

$$\lambda^{(M)} = \alpha \cdot \lambda \tag{4.1}$$

TABLE IV.I
FMECA EXTRACT OF THE E/E/PE COMPONENTS OF THE WT.

ITEM OVERVIEW			STANDARD FMEA				USEFUL PARAMETER					RISK			
Upper level taxonomy	Taxonomy	Function	Failure modes	Failure causes	Local effects	Global effects	Turbine functionality	Safety loss	Failure rate λ_i	α [%]	Mode failure rate	O	S	D	RPN
WT Control system	SCADA Interface	Monitor and control local equipments, store the data in a specific database	No data stored due to HW error	Processor halt / Workstation PC fault / Server PC fault	No data logging, no information about process state	No impact only if the other sensors are working, otherwise inoperative WT	Strongly reduced	YES	3,00E-07	66,7	2,00E-07	6	9	3	162
			No data stored due to SW error	Incorrect input data / Intruder attack / Design fault	Incorrect operation, system crash	No impact only if the other sensors are working, otherwise inoperative WT	Strongly reduced	YES		33,3	1,00E-07	5	9	3	135
WT Control system Controller	Central processor	Elaborate data and manage all the turbine facilities	Input Open	Electrical Failure / Welding failure	Partial reduction of the control system functionality	Partial WT functionality loss	Strongly reduced	YES		36,0	7,20E-08	5	9	2	90
			Output Open	Electrical Failure / Loss of power supply / Welding failure	Impossibility to manage the actuator	Nacelle can't move	Strongly reduced	YES		36,0	7,20E-08	5	9	2	90
			Supply Open	Power supply damage / Facility blackout	Control system can't work	Inoperative WT	Doesn't work	NO	2,00E-07	12,0	2,40E-08	4	8	2	64
			Output Stuck Low	SW error / Nearby welding / RF interface	Impossibility to manage the actuator	Nacelle can't move	Strongly reduced	YES		9,0	1,80E-08	4	9	2	72
			Output Stuck High	SW error / Nearby welding / RF interface	Impossibility to manage the actuator	Nacelle can't move	Strongly reduced	YES		8,0	1,60E-08	4	9	2	72
WT Control system Sensors	Anemometer	Measure the speed and the direction of the wind	Erratic Output	Reduced signal level / Impedance mismatch / A/D conversion error / Noise	Nacelle can't be oriented according to the wind direction	Turbine can't work at maximum available power	Reduced	NO	5,00E-07	66,7	3,34E-07	6	3	3	54
			Corrosion	Integrity failure due to the weather / Overvibration	Nacelle can't be oriented according to the wind direction	Turbine can't work at maximum available power	Reduced	NO		33,3	1,67E-07	6	3	2	36
WT Electrical PFC	Harmonics filter	Pass current only at center frequency	Center Frequency Drift	Deterioration / HF parasitic component	Filter passes current at different frequency, power factor decrease	WT efficiency reduction	Reduced	NO	1,20E-08	80	9,60E-09	3	3	3	27
			No Output	Electrical Failure / Damage due to Overvoltage / Damage of the welding	Current can't pass the filter, no output power	Turbine can't provide output voltage	Strongly reduced	NO		20	2,40E-09	2	6	3	36
WT Electrical Component	Motor contactor	Transmit the electrical current to the motor	All contacts remain in the energized position when the coil is de-energized	Jam / Deterioration / Error in control signal	Impossible to disconnect the motor	Possible damage of the other equipments	Strongly reduced	NO	1,25E-07	25	3,13E-08	4	6	3	72
			All contacts remain in the de-energized position when the coil is energized	Jam / Deterioration / Error in control signal	Impossible to connect the motor	Turbine can't work	Doesn't work	NO		25	3,13E-08	4	8	3	96
			Contacts will not open/close	Dust / Jam / Deterioration	Impossible to connect/disconnect the motor	Turbine can't work	Doesn't work	NO		20	2,50E-08	4	8	3	96
			Short circuit	Dust / Electrical Failure / Deterioration	Motor can't work	Turbine can't work	Doesn't work	NO		20	2,50E-08	4	8	3	96
			Simultaneous closing of normally open and normally closed contacts	Electrical Failure / Error in control signal	No effects on the motor functionality	-	No impact	NO		10	1,25E-08	4	1	3	12
WT Electrical Power conv	Crowbar system	Prevent an overvoltage condition of a power supply	Fail high/low	Electrical Failure / Overheating	Possible over voltage or under voltage condition	Possible control system damage	Doesn't work	YES	3,40E-07	53	1,80E-07	6	10	3	180
			No Output	Electrical Failure	Power converter can't work	Control system can work only if UPS is working	Strongly reduced	NO		47	1,60E-07	6	6	3	108

Furthermore, the third section of TABLE IV.I also includes two effective parameters such as the "Turbine functionality" and the "Safety loss" to evaluate the risk level of the modes and facilitate the Severity assessment:

- Turbine functionality: this parameter gives the turbine operational status after the failure:
  - No impact: the turbine continues its work although the failure mode has occurred.
  - No impact in the short term: initially the turbine continues its work with all functionality, but a maintenance action in short term is needed.
  - Reduced: Redundancy and auxiliary systems allow the turbine essential functionality; the turbine continues to provide electricity and only few operations/functionalities are not available.
  - Strongly reduced: Most operations/functionalities are not available; the turbine continues to provide electricity with lower efficiency.
  - Doesn't work: The turbine can't produce electricity and thus the emergency brake is activated.

- Safety loss: This parameter indicates if the failure modes could reduce the safety level of the turbine under analysis, with a consequent risk for the environment, the operator, or the turbine itself. It is a binary parameter which could be either "Yes" or "No".

The final section of the table illustrates the risk evaluation carried out assessing the Risk Priority Number using the Occurrence, Severity and Detection indexes.

Since only few information about diagnostic systems was available, detection has been classified on a 3-value scale, from 1 (best case) to 3 (worst case), where 2 represents the partially detectable scenario. A 1-to-10 scale has been set for the Occurrence rate, where the higher the mode failure rate, the higher the O rate. Quite the same, a 1-to-10 scale has been set also for the Severity rate, where the assessment is based on the Turbine functionality and Safety loss sections included in the FMECA report. TABLE IV.II includes the rules used to assess severity based on the two above-mentioned parameters: turbine functionality and safety loss.

Fig. 4.3 summarizes the complete results of the RPN values assessment for the E/E/PE components of the G80/2000 WT under study.

TABLE IV.II

EVALUATION CRITERIA TO ASSESS SEVERITY FOR THE WT.

SEVERITY	TURBINE FUNCTIONALITY	SAFETY LOSS	RATING
None	No impact	NO	1
	No impact in short term	NO	2
	Reduced	NO	3
Moderate	No impact	YES	4
	No impact in short term	YES	5
	Strongly reduced	NO	6
High	Reduced	YES	7
	Turbine doesn't work	NO	8
Hazardous	Strongly reduced	YES	9
	Turbine doesn't work	YES	10
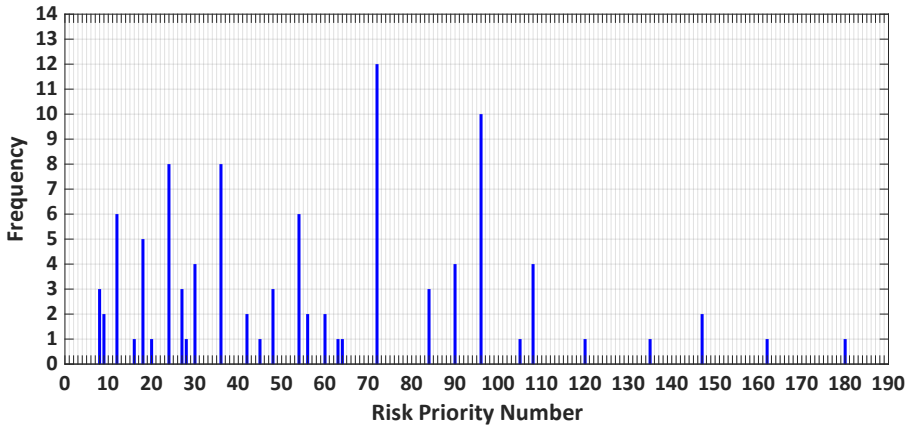
Fig. 4.3. Number of occurrences of each RPN assessed for the turbine under test.

The results of the FMECA reports have been used as case study to test the performancs of the proposed methodology. The following subsections includes the application of the quantitative methods available in literature and a comparison with the proposed Boxplot-based analysis.

4.4.1. Bluvband method

This subsection reports the analysis of the RPN threshold carried out using the Bluvband method [135], [136] on the Risk Priority Number dataset evaluated in the FMECA of the E/E/PE components that compose the WT under analysis. The aim is to determine the most hazardous failures and identify a threshold level that represenst the limit above which countermeasures on critical failures are required.

The "Curve Fitting Tool" by MATLAB could be used to implement the linear regression method and to evaluate the algebraic description of the straight lines $f_1(x)$ and $f_2(x)$. The coefficients in the following equation are evaluated at a 95% confidence level:

$$f_1(x) = p_1 \cdot x + p_2 \qquad \Rightarrow \qquad \begin{cases} p1 = 1.101 \\ p2 = -0.748 \end{cases} \qquad (4.2)$$

$$f_2(x) = p'_1 \cdot x + p'_2 \qquad \Rightarrow \qquad \begin{cases} p'_1 = 7.391 \\ p'_2 = -572.3 \end{cases} \qquad (4.3)$$

Note that the slopes of the two straight lines $f_1(x)$ and $f_2(x)$ are remarkably different from each other. In particular, the line that fits the uppermost part of the plot is almost seven times greater than the other line.

$$\Delta_{slope} = \frac{p'_1}{p_1} = \frac{7.391}{1.101} = 6.7130 \qquad (4.4)$$

The results of the proposed method are illustrated in the Scree Plot in Fig. 4.4.
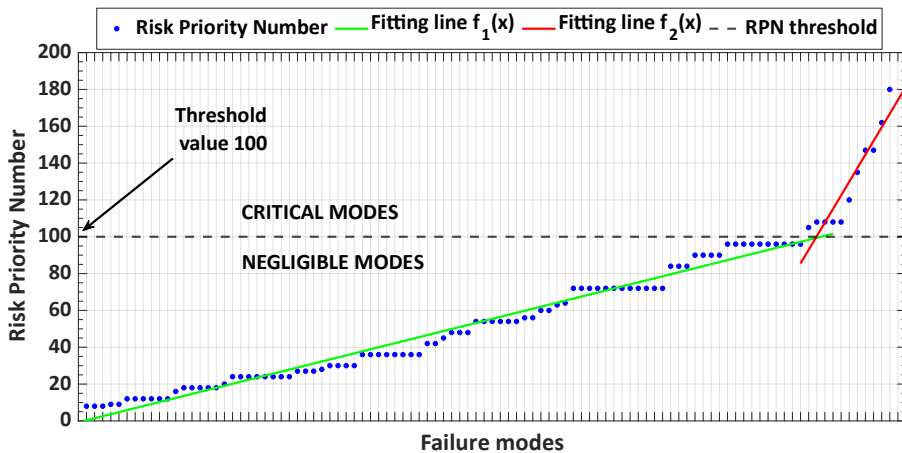
Fig. 4.4. Evaluation of RPN threshold using Bluvband method.

Analyzing the Scree Plot in Fig. 4.4 it is possible to define an RPN threshold value that represents the division between the negligible failure modes and the critical failure modes from the risk value point of view. The threshold can be identified by evaluating the ordinate of the intersection between the two fitting lines in Fig. 4.4, and the result is approximately 100.

4.4.2. Zhao method

This subsection reports the analysis of the RPN threshold carried out using the method proposed by Zhao et al. [137] on the RPN dataset evaluated in the FMECA of the E/E/PE components that compose the wind turbine under analysis.

Also in this case, the "Curve Fitting Tool" by MATLAB could be used to implement the linear regression method and to evaluate the algebraic description of the straight lines $f_{Zhao}(x)$ used to fit the RPN dataset. The 1st-degree polynomial fitting curve obtained from the analysis of the data is the following:

$$f_{Zhao}(x) = p_1^z \cdot x + p_2^z \qquad \Rightarrow \qquad \begin{cases} p1 \ = 1.262 \\ p2 \ = -6.024 \end{cases} \qquad (4.5)$$

The results of the procedure considering a 95% confidence bound of the straight fitting line are illustrated in the Scree Plot in Fig. 4.5.
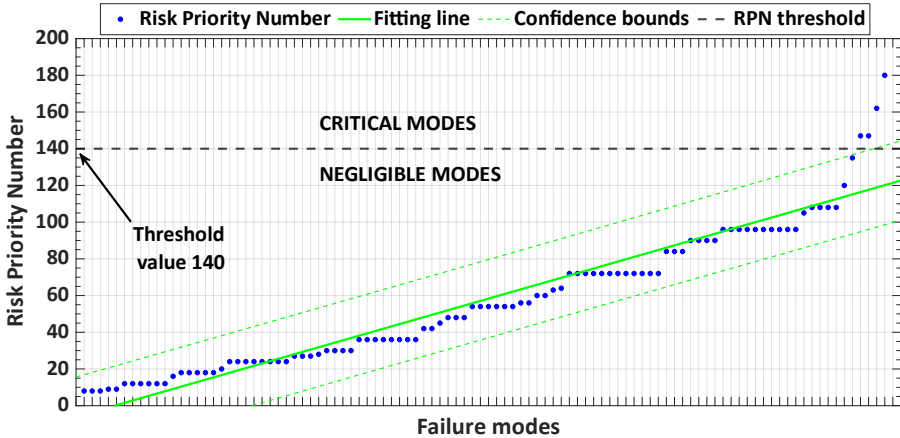
Fig. 4.5. Evaluation of RPN threshold using Zhao method.

4.4.3. 80:20 Pareto method

This subsection reports the analysis of the RPN threshold carried out using the 80:20 Parreto principle method in comliance with [138]–[144] on the RPN dataset evaluated in the FMECA of the E/E/PE components that compose the wind turbine under analysis.

The results of the analysis are illustrated in the Pareto chart in Fig. 4.6. Each light purple bar stands for the RPN assessment of the corresponding failure mode (y-scale on the left side of the chart), while the continuous blue line represents the cumulative percentage distribution of the Risk Priority Number (y-scale on the right side of the chart).

According to the 80:20 Pareto principle, the Risk Priority Number threshold of the dataset under analysis is approximately 48. The evaluation of the threshold level using Pareto method is highlighted in Fig. 4.6. The first step is the identification of the 80% of the cumulative distribution of the Risk Priority Numbers (highlighted using a red dot in the figure). Subsequently, the RPN threshold value is given by the value of the Risk Priority Number of the failure mode linked to the 80% of the cumulative percentage (highlighted using a red bar in the figure).
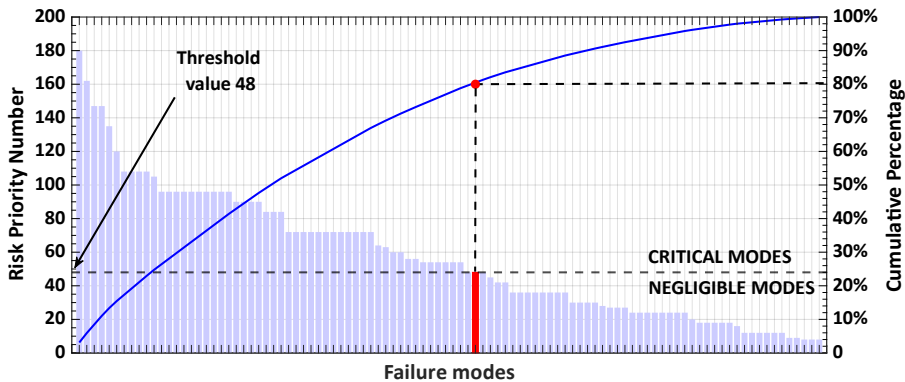
Fig. 4.6. Evaluation of RPN threshold using Pareto chart and 80:20 principle.

4.4.4. Critical comparison

The three procedures analyzed provide quite different results. The Zhao technique suggests considering only four failure modes inside the group of the most critical failure modes (threshold equal to 140), whereas the Bluvband approach recommends considering 11 failure modes inside this group (threshold

equal to 100), and the Pareto chart indicates that 55 failure modes are critical (threshold equal to 48).

Analyzing in detail the obtained results, it is clear that all the previous techniques have some critical drawbacks. For instance, according to the 80:20 rule of the Pareto method, 80% of the criticality should arise from 20% of the causes. The results obtained in this work suggested that this principle does not fit very well with this kind of application. As a matter of fact, 80% of the RPNs of the E/E/PE components in the wind turbine represent 55% of the failure modes. The Pareto chart cannot be considered a powerful technique to identify the RPN threshold of a system, actually the principle used to select the numerical value of the threshold should be reviewed and specifically defined for each kind of application. In this case, it is absolutely not reasonable select a threshold of 48 indicating that more than half of the failure modes are critical. Quite the opposite, the Zhao method suggests for the system under test that only four failure modes are critical. More generally, this technique provides untrustworthy results for many applications because of the manner in which the threshold is evaluated. In fact, using this procedure very few risk priority numbers overpass the 95% confidence bound falling in the critical modes group. The Bluvband method provides interesting results, both threshold value and number of modes considered critical is reasonable. Anyway, the procedure for the threshold evaluation is vague and extremely subjective. According to the authors, the calculated RPNs form a right-skewed distribution, with a first tail on the left and a second tail on the right with very different slopes, but no information about how to divide the distribution in two sections are given. As a consequence, the identification of the threshold is dependent on the judgment of the designer that carry out the procedure.

4.5. Application of the proposed Boxplot analysis to estimate the RPN threshold

The proposed Boxplot-based approach introduced in Section 4.3. has been applied to the case study described in Section 4.4 in order to estimate the RPN threshold of the E/E/PE components included in the wind turbine under analysis. The objective of this section is to test and validate the performances of the proposed method with the aim of identifying the optimal RPN threshold in terms of criticality identification, risk reduction, cost of the countermeasures and easiness of implementation.

The results of the statistical analysis are the following:

- Range of admissible values: [1; 300]
- Minimum: 8
- Maximum: 180
- 25th Percentile: 24
- Median: 54
- 75th Percentile: 87
- Outliers: none (considering outliers all the RPNs more than three standard deviations away from the median).

Fig. 4.7 shows the boxplot of the RPN dataset for the WT under test, highlighting with different colors the area of interest. The green zone (below the median) stands for the negligible failures, the yellow region represents the ALARP zone and the red region (above the 75th Percentile) indicate the critical failure modes.

In particular, the proposed method suggests 25 failure modes inside the critical group (RPN higher than 87), 27 failure modes inside the ALARP region (RPN within the interval from 54 and 87) and 48 negligible modes (RPN lower than 54).

TABLE IV.III compares the results obtained with the proposed Boxplot-based approach and the other methods available in literature (note that 100 failure modes were identified in the subsystems under test and the range of possible RPN varies between 1 and 300).
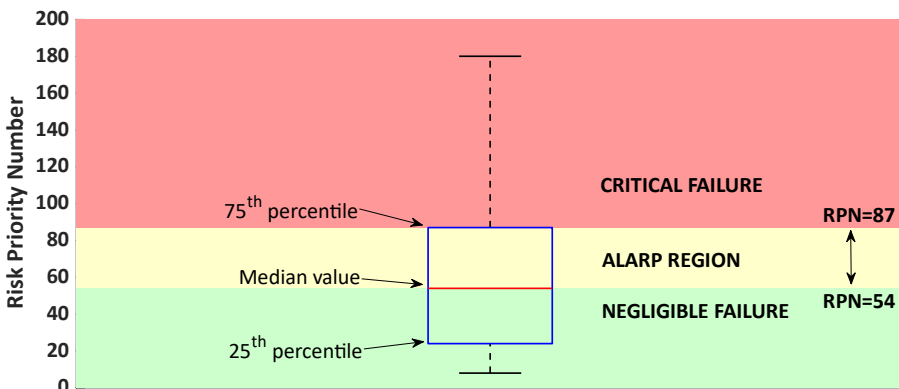
Fig. 4.7. Proposed approach for the Risk Priority Number threshold based on boxplot.

TABLE IV.III

COMPARISON BETWEEN PROPOSED METHOD AND LITERATURE.

METHOD	THRESHOLD	CRITICAL MODES	ALARP
Boxplot	87	25	Between 54 and 87 27 modes
Bluvband	100	11	Not Allowed
Zhao	140	4	Not Allowed
Pareto	48	55	Not Allowed

The RPN threshold identified by means of the proposed approach falls between the threshold estimated using Bluvband and Pareto methods. Quite the same consideration could be drawn also for the number of critical modes. Considering only the red zone of Fig. 4.7 (critical modes), the Boxplot method is a more conservative approach respect to the method proposed by Bluvband. Designers must always choose the best solution in terms of cost and risk level. It is generally more advisable to select the worst-case scenario, that is, the procedure providing the lowest RPN threshold, considering a larger number of failure modes in the critical area. In this application, the worst-case scenario is the 80:20 rule applied in the Pareto chart, but it provides not reasonable results in terms of the cost of the corrective actions. Indeed, it is not possible to apply countermeasures on the 55% of the failure. Therefore, the optimal trade-off between cost and threshold level is provided by the proposed method. Moreover, the new technique allows to introduce also an ALARP zone where each mode could be considered critical or negligible, depending on the scenario.

4.6.   Final Remarks

This section focuses on the problem of RPN threshold estimation in order to identify critical failure modes as the outcome of a Failure Mode, Effects, and Criticality Analysis. The problem of RPN threshold estimation is a fundamental aspect which is barely considered by both FMECA standards and scientific literature. However, it is a fundamental topic that requires particular attention since it allows to identify the most critical failure modes reducing the overall risk of the entire system, optimizing the cost of the countermeasures and the operation and maintenance costs.

To separate the failure modes into critical and negligible failures, most companies simply set an arbitrary threshold based only on expert's judgment.

Alternatively, some companies apply corrective actions in a hierarchical order starting from the most critical components. Then, countermeasures are applied until the budget allows it. This work compares the only three RPN threshold estimation available in literature applying the procedures to the E/E/PE components of a 2 MW Wind Turbine. The analyzed methods are the 80:20 rule applied in the Pareto chart and two graphical procedures proposed respectively by Bluvband and Zhao. The Bluvband method provides plausible results includes 11 failure modes inside the group of the most critical failure modes. However, the procedure is vague and extremely subjective. The Zhao method is too optimistic because it provides only two critical modes. The Pareto chart is just the opposite; it is too conservative and considers more than 50% of failure modes as critical. This is mainly linked to the way the Pareto method is defined and evaluated. By a theoretical point of view, the 80:20 rule suggests that 80% of the criticality should arise from 20% of the causes, therefore considering the 80% as threshold value the 20% of the modes should be critical. Actually, the case study presented in this paper highlights that this is not true. With this kind of dataset, the 80:20 relationship is not verified, and the number of critical modes is much higher than the 20%, leading to inaccurate and too conservative results.

Therefore, this work introduced a new approach based on a statistical analysis and a boxplot to separate negligible and critical modes. The proposed methodology represents the optimal trade-off between cost of the countermeasures and threshold level (by a risk reduction point of view). The major advantages of the proposed Boxplot procedure are the following:

- It is an easy, practical and repeatable methodology.
- Unlike other methods it takes into account the ALARP region.
- It is based on statistical analysis.
- It suffers no subjectivity in threshold definition.

CHAPTER 5

RELIABILITY ALLOCATION: THEORY AND IMPROVEMENTS

This chapter provides an overview of Reliability Allocation procedures focusing on some of the most known and widely used techniques. All the approaches available in literature are based on two assumptions: functional series architecture and exponential failure distribution. This chapter presents an innovative iterative approach that allows to overcome both assumptions and thus to apply reliability allocation as a central part of the proposed Reliability Life Cycle to any complex system. The validation of the proposed approach has been carried out implementing the method on three different applications: a numerical example, a sensors unit of an HVAC system for high-speed trains and a lube oil console for Oil&Gas applications. [1]

---

[1] The innovative reliability allocation approach presented in this chapter has been published as " M. Catelani, L. Ciani, G. Patrizi, and M. Venzi, "Reliability Allocation Procedures in Complex Redundant Systems," IEEE Syst. J., vol. 12, no. 2, pp. 1182–1192, Jun. 2018. ".

5.1. Why Reliability Allocation?

Let's consider the design of an industrial product (or system, or plant) with a certain degree of complexity. Obviously, this product will have several functional elements that need to work together to make it works properly. For instance, there will be a power supply, a microprocessor, some sensor, etc. Each functional element can be provided by a single component, a subsystem, a module or an assembly. For simplicity, this work will refer to these collectively as 'components.'

Each component is different. Based on different technologies. Created by different design teams. Perhaps supplied by different suppliers. The design team leader is almost forced to treat the design of each component as its own 'little design project.' However, this is not always possible. In fact, among the functional and design requirements, the design team could have a reliability goal for the overall product

Let's say the product consists of nine components working together to achieve a specific task. The overall system reliability goal is that the product needs to be 95% reliable after three years. (see Fig. 5.1).

Obviously, it is absolutely not enough to simply say to all the design teams and suppliers of the nine components that their reliability goals are also 95%.

As a matter of fact, nine components that each have 95% reliability will result in a product with 63% reliability according to the model of a series configuration.
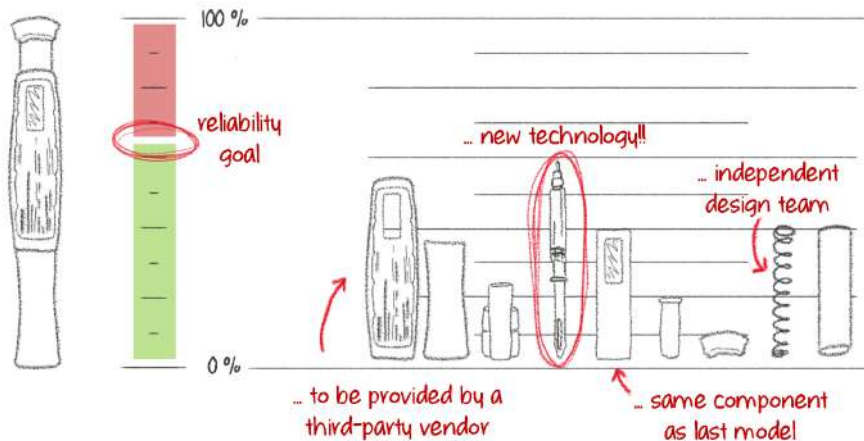
Fig. 5.1. Example of reliability goal for a product made up by extremely different components.

Therefore, it is necessary to assign a numerical reliability goals to subsystems and components in support of system level reliability performance characteristics. This is commonly done by means of Reliability Allocation (RA).

5.2. Basic concepts of Reliability Allocation

The choice of components in terms of reliability requirements represents a key issue to reduce failures occurrence and guarantee an adequate availability and safety of the whole system. In order to satisfy these requirements since the earliest design phases, the first step is to translate the overall system reliability goal into reliability requirements for each of the components making up the system; this process is known as Reliability Allocation (RA). Reliability allocation is a top-down technique that allows to apportion the reliability goal of the system between its components which is a very sensitive issue in industrial and commercial environments [151]. Therefore, RA plays a fundamental role in the development of a new industrial system. An accurate and efficient RA methodology allows designers to achieve the optimal target in compliance with the state of the art, the costs of the components, the operating conditions and the environmental factors [152]–[154].

When reliability allocation is implemented since the first design phases, it allows to achieve several benefits. First of all, RA evaluates the reliability parameters of each subsystem/unit/item that make up the system, allowing an in-depth knowledge of the system itself. Furthermore, RA optimizes the component reliability minimizing the life cycle cost and the unexpected and unpredicted failures. Moreover, RA is a realistic approach which includes several factors, that influence the system reliability and it gives the possibility to repeat the procedure at the various hierarchical levels.

The RA problem could be essentially divided into six consecutive steps:

1. Identify customer requirements in terms of system reliability or system failure rate, if any.
2. Establish system reliability goal, working out how the product or system needs to perform to achieve the design requirements.
3. Determine reliability design margin in order to take into account also the uncertainties on reliability data and the random processes of failures.
4. Establish a preliminary functional series design which model the top hierarchical level of the product/system.

5. Allocate the component reliability according to one of the several methods available in literature.

6. Do somethings, which means that if the goal could not be achieved with the current design, some improvements and modifications are required before putting into practice the RA procedure again.

Fig. 5.2 shows a generic design flow including the six steps of the RA procedure to effectively and efficiently achieve the design requirements in terms of reliability.

Fig. 5.2. Generic design flow of a complex system including the six steps of Reliability Allocation.

Basically, the first four steps of the procedure provide a system reliability goal $R_{SYS}^*(t)$ and a preliminary system architecture. Supposing to know the system architecture in terms of Reliability Bock Diagram (RBD), thus the system reliability is a function $f\{\cdot\}$ of the reliability of each component R_i. Then the reliability allocation procedure could be summarized in determining a possible solution for the following inequality [4], [155]:

$$R_{SYS}^*(t) \leq f\{R_1^*(t), R_2^*(t), \ldots, R_n^*(t)\} \qquad (5.1)$$

Where the generic term $R_i^*(t)$ stands for the reliability allocated to the component i-th after the allocation process, and n is the number of components making up the system. Unfortunately, without some restrictions, the inequality

in equation (5.1) has an infinite number of solutions. As a consequence, the RA problem consists in establishing a procedure that creates a unique or limited number of solutions with which reasonable reliability can be assigned to the various components.

For example, the allocated reliability for a simple subsystem of demonstrated high reliability should be greater than for a complex subsystem whose observed reliability has always been low. The allocation process is approximate, and the reliability parameters apportioned to the subsystems are used as guidelines to determine design feasibility. If the allocated reliability for a specific subsystem cannot be achieved at the current state of technology, then the system design must be modified, and the allocations reassigned. This procedure is repeated until an allocation is achieved that satisfies the system level requirement, within all constraints, and results in subsystems that can be designed within the state of the art.

5.3.   Reliability Allocation: general procedure

RA is a top-down technique much useful in industrial and commercial environments because it optimizes risk, development time, and the overall development costs. As the system design develops and more information about components and the operating environment becomes available, different allocation methods and reliability improvement techniques may also be considered.

Thus, many procedures have been developed to assess reliability allocation in the last few years. However, all of them follow the same modus operandi in which the failure rate to be allocated to a generic subsystem is directly proportional to the failure rate of the whole system. This is a very limited approach and requires a huge level of simplification. This section presets the general procedure used to carry out the allocation of the reliability requirements in almost all the papers available in literature.

5.3.1.   Required hypothesis

Similarly to every mathematical procedure, Reliability allocation requires some initial hypotheses to ensure the proper working of the RA model.

To the author knowledge, after a systematic and extensive literature review, it stands out that every allocation procedure proposed in literature is based on two assumptions:

Assumption i.   Functional series architecture of the system under test, which means that no redundancies could be implemented.

Assumption ii.   Exponential failure rate distribution, which means that the failure rate of the component has to be constant. Therefore, only the middle section of the failure rate bathtub curve could be considered, while early failure mechanisms and wear out processes must be neglected.

Assumption i. and Assumption ii. are quite popular in many RAMS methodology. For instance, series architecture and exponential failure distribution are the central core of the widely known reliability prediction.

Handbooks such as the MIL-HDB 217 F Notice 2 (published by the U.S. Department of Defense in 1995) [156], the HDBK-217Plus (published by Quanterion Solutions Incorporated in 2015) [146], the SR-332 Issue 4 (published by Telcordia network Infrastructure solutions in 2016) [147], the SN 29500 revision 07 (published by Siemens in 2013) [149] and the IEC 61709 (published by the International Electrotechnical Commission in 2017) [150] all relies on such initial hypothesis.

However, to limit the application scenario only to systems described by a series architecture of components characterized by an exponential failure distribution is too simplistic. In fact, redundancy plays a fundamental role in many different fields of application where it is absolutely required to ensure continuity of service in case of failure of a critical component. Furthermore, mechanical, electromechanical and hydraulic components are usually described by the Weibull probability density function to take into account wear-out and early-failure processes. Therefore, these simplifying hypotheses are not suitable for many industrial systems characterized by the presence of complex components, several redundancies and fault tolerant architectures.

As a consequence, the aim of this work is to introduce an innovative methodology able to overcomes both Assumption i. and Assumption ii. and consequently to extend the range of applicability of the allocation methods already available in literature.

5.3.2.   Influence factors

One of the strongest points of the reliability allocation is that it takes into account a set of influence factors that affect the RAMS performances of system under analysis.

A summary of the most used influence factors is illustrated in Fig. 5.3.
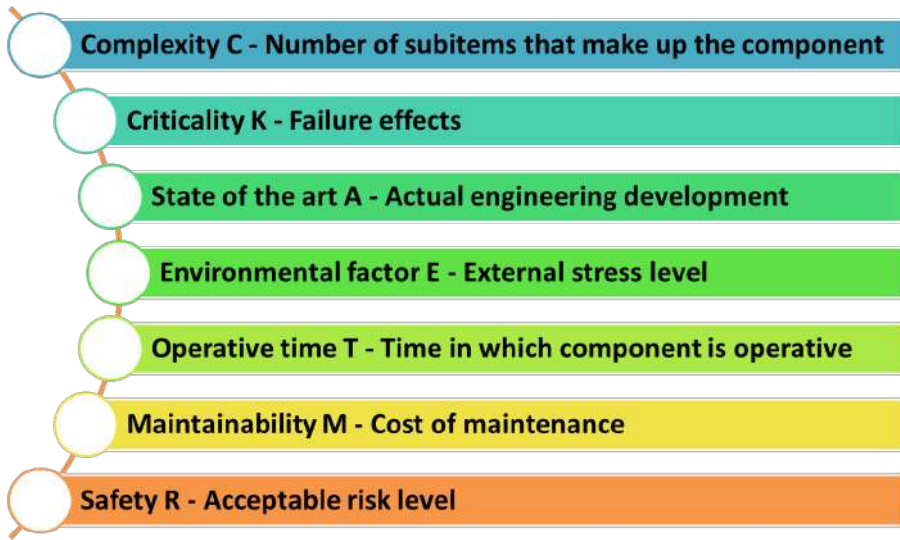
Fig. 5.3. Summary of influence factors for RA procedures.

The complexity **C** usually represents the degree of complexity of the considered item, including number of components, number and type of eventual redundancies, etc. The higher the value **C**, the greater the complexity of the considered item is.

Moving to the next influence factor, the State of the Art **A** measures the actual engineering development in the considered field. New technologies are considered likely to fail because the mechanisms of the component are not completely established, and failure data are not yet available. Thus, a higher state of the art value **A** is assessed to ensure a lower reliability. Quite the contrary, state of the art components that are present in the market since many years are considered more reliable, a thus a lower value of the state of the art parameter **A** is assessed.

The environmental factor **E** measures the level of external stress sources on the considered component. Temperature, humidity, vibrations, mechanical shocks, weather conditions, electromagnetic noise are some of the factors that are weighted during the assessment of the environmental factor **E**. Similarly to the complexity, the higher the stress of the external environment, the higher the value of the **E** parameter is.

The operative time **T** is a factor used by some approaches to take into account component that works for longer period than others. The longer the worked period with respect to the tola operative time, the lower the value of the influence factor **T**.

The influence factor **M** (Maintainability) measure the impact of a corrective maintenance operation that must be performed in case of failure of the considered component. It takes into account the cost of the maintenance operations, the time required to perform the task, the easiness of the procedures, and accessibility of the component, etc. If it is easy, fast and cheap to perform the maintenance operations, then a high value of the maintainability index **M** is assessed.

The criticality factor **K** is a parameter that takes into account the effects of an eventual failure on the entire system in terms of functionalities, productivity and availability.

In this case, the greater the criticality of the unit, the worsen the failure effects and the lower the criticality value **K** is. This is due to the fact that lower influence factor values lead to higher reliability allocated to the unit. Thus, a remarkably critical unit should have a very low **K** value to ensure a higher allocated reliability.

According to its definition, the criticality factor **K** is strictly related to the Severity factor S of the FMECA procedure. The only difference is that S and **K** are defined in a reverse order. However, the reasons and guidelines that lead to the assessment of one parameter are the same of the other one, except for the ordering.

The last factor taken into account in Fig. 5.3 is the Safety index **R**. It measures the impact of a possible failure by a safety point of view, considering the effects of failure on the system, environment, personnel and users. In this case, if the failure of a component will lead to catastrophic events and severe consequence by a safety point of view, then an extremely low value of the Safety parameter **R** is assessed. Also in this case, there is a strict correlation between the safety index **R** and the severity index S of the FMECA procedure. In fact, most of the time severity S takes into account the effect of failure also measuring the impact on the system safety. Similarly to the previous case, the only difference between S and **R** is that the RA influence factor **R** is defined in a reverse order with respect to the FMECA index S.

As a consequence, when RA and FMECA are implemented as part of an overall design for reliability as the one presented in this work, then the assessment of the criticality **K** and Safety **R** should be guided following the guidelines already studied during the FMECA for the assessment of Severity S.

This concept is clearly explained in TABLE V.I where the relationship between the FMECA index S (severity) and the RA indexes **K** (criticality) and **R** (safety) are studied.

TABLE V.I
SIMILARITIES BETWEEN RA INDEXES K (CRITICALITY) AND R (SAFETY) WITH FMECA
INDEX S (SEVERITY)

TECHNIQUE	PARAMETER	DESCRIPTION	RULES FOR THE ASSESSMENT
FMECA	Severity S	Magnitude of the failure effects at local and global level by economic, performance, availability and safety point of view.	**Maximum S** (usually 10) assigned to the most critical failures.
			Minimum S (usually 1) assigned to negligible failures.
RA	Criticality **K**	Consequences of a failure on the system by a productivity and availability point of view.	**Maximum K** (usually 10) assigned to non-critical components.
			Minimum K (usually 1) assigned to the most critical components.
	Safety **R**	Impact of the failure on system, environment, personnel and users by a safety point of view.	**Maximum R** (usually 10) assigned if the failure has no impact on safety.
			Minimum R (usually 1) assigned if the failure will lead to catastrophic events.

5.3.3. Overall procedure

As explained above, all the reliability allocation procedures available in literature follow a common structure. The central point of each procedure is the assessment of a proportionality constant ω called weight factor. Each RA technique differs from the other according to a dedicated procedure to assess its own weight factors.

A schematization of the generic structure of RA is illustrated in Fig. 5.4. The procedure starts with the specification of design requirement in terms of functional configuration, actual operating conditions, failure analysis, etc. At system level, all the techniques require a system reliability goal expressed in terms of either reliability $R_{SYS}{}^*(t)$ or failure rate $\lambda_{SYS}{}^*(t)$. Then a weight factor is introduced as proportionality constant to evaluate the component reliability based on a combination of some influence factor as in equation (5.3). Finally, the component reliability could be assessed according to the weight factor.
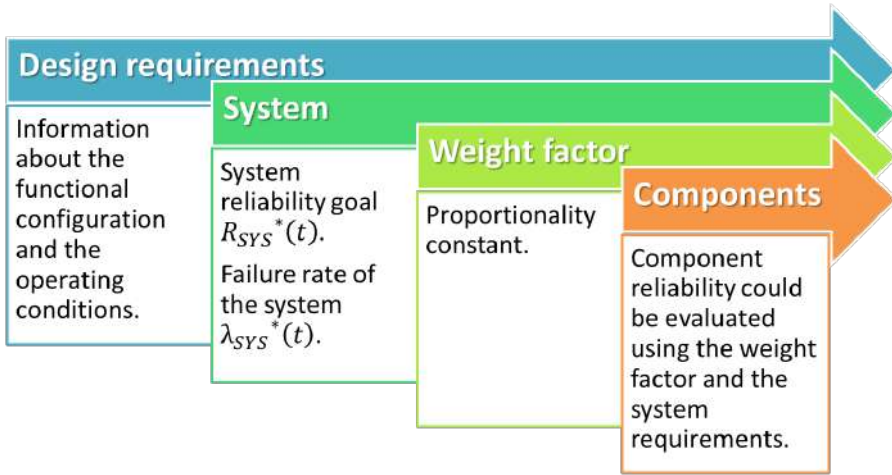
Fig. 5.4. Schematization of the RA procedure at different levels.

It is important to note that thanks to Assumption i. and Assumption ii. it is possible to convert the system reliability goal into a system failure rate goal and vice versa using the following relationship:

$$R_{SYS}{}^*(t_a) = exp\left(-t_a \cdot \lambda_{SYS}{}^*\right) \quad \Leftrightarrow \quad \lambda_{SYS}{}^* = -\frac{ln\left(R_{SYS}{}^*(t_a)\right)}{t_a} \qquad (5.2)$$

Where t_a is the allocation time and it is set prior the allocation, when the system goal is defined.

The overall reliability allocation procedure is illustrated in Fig. 5.5 highlighting four consecutive steps.
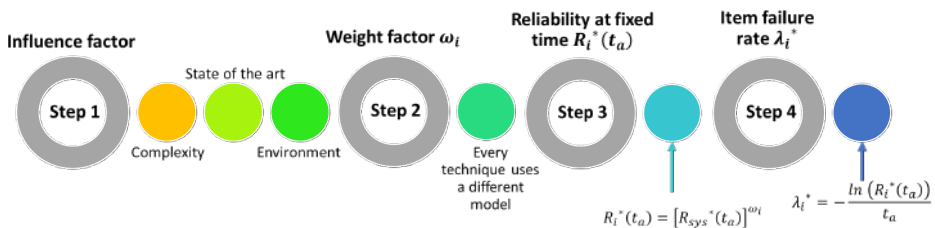
Fig. 5.5. General procedure applicable to several Reliability Allocation methods proposed in literature.

Firstly, the level of each considered influence factor must be evaluated for each item composing the system (STEP 1). Similarly to the FMECA, most of the techniques use a 10-point scale to assess the influence factor, as:

$$X_i \in [1, 10] \tag{5.3}$$

Where X_i represents a generic influence factor of the component i-th. Fig. 5.5 takes complexity, state of the art and Environmental factor as an example, however all the influence factors describe in the previous section could be considered, depending on the technique that is implemented.

Then, the second step consists in the evaluation of the weight factor ω_i for each one of the components under analysis. Every RA method in literature differs from the others only on the model used to calculate the weight factor. Generally speaking, the weight factor ω_i is a function g of some of the influence factors mentioned above, as follow:

$$\omega_i = g(C_i, A_i, E_i, O_i) \tag{5.4}$$

More information about how some of the widely known RA techniques assess the weight factor ω_i are provided in the following section.

The third step is the core of the procedure since it allows to calculate the reliability target R_i^* (t) allocated to each component. More in detail, considering the subscript i as notation for the component i-th, then R_i^* (t) is given by:

$$R_i^*(t_a) = [R_{SYS}^*(t_a)]^{\omega_i} \tag{5.5}$$

Finally, the Step 4 allows to evaluate the failure rate of the component i-th based on the allocated reliability R_i^* (t_a) under the assumption of exponential distribution as follow:

$$\lambda_i^* = -\frac{ln\,[R_i^*\,(t_a)]}{t_a} \tag{5.6}$$

5.3.4. Some notes about the weight factor

The weight factor ω_i is the mathematical object that allows to apportion the system reliability goal among the components that make up the system according to their characteristics. Thus, it is a powerful tool that must satisfy some constraints.

According to the definition of a series configuration, the system reliability goal could be expressed as the product of the reliability allocated to each component, as follow:

$$R_{SYS}{}^*(t_a) = \prod_{i=1}^{N} R_i{}^*(t_a) \qquad (5.7)$$

Where N represents the number of components making up the system.
Equation (5.5) clearly states that the reliability allocated to the i-th component is given by the system reliability goal to the power of the weight factor ω_i. Introducing equation (5.5) within equation (5.7):

$$R_{SYS}{}^*(t_a) = \prod_{i=1}^{N} [R_{SYS}{}^*(t_a)]^{\omega_i} \qquad (5.8)$$

Considering that $R_{SYS}{}^*(t)$ is a constant value and taking into account the properties of a product of sequence, equation (5.8) could be rewritten as:

$$R_{SYS}{}^*(t_a) = [R_{SYS}{}^*(t_a)]^{\sum_{i=1}^{N} \omega_i} \qquad (5.9)$$

Thus, the weight factor must satisfy the following relationship:

$$\sum_{i=1}^{N} \omega_i = 1 \qquad (5.10)$$

There is another important point that should be discussed when talking about the weight factor ω_i. Thanks to Assumption ii. it is possible to translate the reliability model in equation (5.5) into a failure rate model. In this way, instead of allocating a reliability to each component based on the system reliability goal $R_{SYS}{}^*(t_a)$ and the weight factor ω_i, it will be possible to allocate a component failure rate λ_i^* based on the system failure rate goal $\lambda_{SYS}{}^*$ and the same weight factor ω_i.

Under Assumption ii. the reliability R of a generic item can be written as function of the failure rate λ as follow:

$$R(t) = e^{-\lambda \cdot t} \qquad (5.11)$$

Thus, equation (5.5) can be rewritten as:

$$e^{-\lambda_i^* \cdot t_a} = \left[e^{-\lambda_{SYS}{}^* \cdot t_a}\right]^{\omega_i} \qquad (5.12)$$

$$e^{-\lambda_i^* \cdot t_a} = e^{-\lambda_{SYS}{}^* \cdot t_a \cdot \omega_i} \qquad (5.13)$$

$$\lambda_i^* \cdot t_a = \lambda_{SYS}^* \cdot t_a \cdot \omega_i \tag{5.14}$$

$$\lambda_i^* = \omega_i \cdot \lambda_{SYS}^* \tag{5.15}$$

Equation (5.15) shows how the failure rate allocated to the i-th component could be estimated as a simple fraction of the system failure rate goal. Equation (5.15) also proves why the weight factor is considered a proportionality constant. Using the failure rate model, ω_i actually represent a proportionality constant between the component failure rate and the system failure rate.

Once again, it is easy to prove that the sum of the weight factors must be equal to 1 as in equation (5.10) introducing the definition of series configuration according to Assumption i. as follow:

$$\lambda_{SYS}^* = \sum_{i=1}^{n} \lambda_i^* \tag{5.16}$$

Thus, using equation (5.15) to substitute the allocated failure rate λ_i^* within equation (5.16) it is possible to achieve the following relationship:

$$\lambda_{SYS}^* = \sum_{i=1}^{n} \omega_i \cdot \lambda_{SYS}^* = \lambda_{SYS}^* \cdot \sum_{i=1}^{n} \omega_i \tag{5.17}$$

And thus, the sum of the weight factor must satisfy the following constraint:

$$\sum_{i=1}^{N} \omega_i = 1 \tag{5.18}$$

5.4. Related works: classical approaches

This section presents a systematic review of the most common RA methods available in literature.

5.4.1. Equal method

The simplest and easiest allocation method is the "Equal Reliability Allocation". As it can be easily guessed from the name, this method allocates the same failure rate and the same reliability to all the components making up the

system. This means that the weight factor ω_i assessed using the Equal method is the same for all components i. As a consequence, the Equal method could be applied only to provide a first rough estimation of the reliability values to be allocated, but it cannot be considered a valuable solution.

The mathematical model of the equal allocation method is the following:

$$R_i^*(t) = \sqrt[N]{R_{SYS}^*(t)} = [R_{SYS}^*(t)]^{\frac{1}{N}} \tag{5.19}$$

$$\omega_i = \frac{1}{N} \tag{5.20}$$

5.4.2.   ARINC method

The ARINC apportionment method was designed in 1964 by ARINC Research Corporation, a subsidiary of Aeronautical Radio, Inc [157].

This method is based on the assumption that the reliability of components can be assessed using previous calculations on similar components.

The mathematical expression of weight factors is the following:

$$\omega_i = \frac{\lambda_i}{\lambda_{SYS}} = \frac{\lambda_i}{\sum_{j=1}^N \lambda_j} \tag{5.21}$$

Where λ_i is the estimated failure rate of the component i-th obtained through a similar system and λ_{SYS} is the estimated failure rate of the whole architecture [157].

The peculiarity of the ARINC technique is that it is one of the few methods that considers historical failure data to assess the weight factors rather than quantitative influence factors like most of other techniques. As a matter of fact, ARINC requires the knowledge of past allocations on similar systems to allocate reliability to the various levels of the current system.

The main advantage of this method is essentially its simplicity of calculations which allows to rapidly implement the allocation. However, ARINC suffers many flaws, such as:

- It is not possible to apply ARINC method to innovative systems since no past data related to a similar system are available.
- All failure rates must be extracted from the same source (single database), as they must be comparable to each other in order to have an optimal allocation.

5.4.3. AGREE method

AGREE (Advisory Group on Reliability of Electronic Equipment) technique considers three influence factors to calculate the weighting factors of each subsystem [158]. Complexity C_i is assessed as the number of elements of the generic subsystem n_i compared to the total number of components N_{sys} of overall configuration.

$$C_i = \frac{n_i}{N_{SYS}}$$

(5.22)

This technique also considers the importance I_i of each subsystem i, where importance is defined as the probability that the system fails when the subsystem fails, thus $I_i \in [0; 1]$ where $I = 1$ stands for the most critical items, while $I = 0$ means that the failure has no critical effects.

The third factor takes into account the effective time of use t_i' of the subsystems, as follow:

$$t_i' = \frac{t}{t_i}$$

(5.23)

where t_i is the time of use of item I, while t is the time of use of the whole system.

According to the AGREE method [158], the reliability of a series architecture composed by N subsystems is defined as follow:

$$R_{SYS}{}^*(t) = \prod_{i=1}^{N}\{1 - I_i[1 - R_i{}^*(t_i)]\} = \prod_{i=1}^{N}\{1 - I_i[1 - e^{-\lambda_i{}^* t_i}]\}$$

(5.24)

Using the Taylor approximation of the exponential function $e^{-x} \approx 1 - x$ when $x \to 0$, then:

$$R_{SYS}{}^*(t) \approx \prod_{i=1}^{N}\{1 - I_i[1 - (1 - \lambda_i{}^* t_i)]\} = \prod_{i=1}^{N}\{1 - I_i\lambda_i{}^* t_i\}$$

(5.25)

Introducing the Taylor approximation once again and rewriting the system reliability as exponential function:

$$R_{SYS}{}^*(t) \approx \prod_{i=1}^{N}\{e^{-I_i\lambda_i{}^* t_i}\} = e^{-\sum_{i=1}^{N_{SYS}}(I_i\lambda_i{}^* t_i)}$$

(5.26)

To solve equation (5.26) it is necessary to rewrite the left term using the exponential function.

Thus, considering the properties of exponential and logarithmic functions, equation (5.26) can be rewritten as follow:

$$e^{ln[R_{SYS}{}^*(t)]} = e^{-\Sigma_{i=1}^{N}(I_i\lambda_i{}^*t_i)} \tag{5.27}$$

$$ln[R_{SYS}{}^*(t)] = -\sum_{i=1}^{N} I_i\lambda_i{}^*t_i \tag{5.28}$$

Multiplying and dividing the first term of equation (5.28) by the same quantity N_{SYS}:

$$\frac{N_{SYS}}{N_{SYS}} ln[R_{SYS}{}^*(t)] = -\sum_{i=1}^{N} I_i\lambda_i{}^*t_i \tag{5.29}$$

However, N_{SYS} is the total number of components that make up the entire system. Thus, considering the definition of Complexity introduced by the AGREE method in equation (5.22), N_{SYS} can be rewritten as follow:

$$N_{SYS} = \sum_{i=1}^{N} n_i \tag{5.30}$$

Introducing equation (5.30) within equation (5.29):

$$\sum_{i=1}^{N} I_i\lambda_i{}^*t_i = -\frac{ln[R_{SYS}{}^*(t)] \cdot \Sigma_{i=1}^{N} n_i}{N_{SYS}} \tag{5.31}$$

Then, using the properties of the summation:

$$\sum_{i=1}^{N} I_i\lambda_i{}^*t_i = -\sum_{i=1}^{N}\left[n_i \cdot \frac{ln[R_{SYS}{}^*(t)]}{N_{SYS}}\right] \tag{5.32}$$

$$I_i\lambda_i{}^*t_i = -n_i \cdot \frac{ln[R_{SYS}{}^*(t)]}{N_{SYS}} \tag{5.33}$$

Introducing the definition of Complexity C_i as in equation (5.22) and the definition of effective time as in equation (5.23) the latter became:

$$\lambda_i^* = -\frac{C_i \cdot t_i' \cdot ln[R_{SYS}^*(t)]}{I_i t} \tag{5.34}$$

Now it is possible to define the weight factor of the AGREE method as a function of complexity, importance and effective time:

$$\omega_i = \frac{C_i \cdot t_i'}{I_i} \tag{5.35}$$

Introducing equation (5.35) and equation (5.2) within equation (5.34) the allocated failure rate according to the AGREE method could be expressed as:

$$\lambda_i^* = -\frac{\omega_i \cdot ln[R_{SYS}^*(t)]}{t} = \omega_i \cdot \lambda_{SYS}^* \tag{5.36}$$

The AGREE technique is a milestone in RA approaches. However, it suffers major drawbacks, such as:

- The importance factor, as it is defined, does not take into account the consequences that a subsystem failure induced on the system.
- It requires Taylor approximation, thus obtaining approximate result.
- The assessment of the weight factor takes into account only three influence factors.

5.4.4. FOO method

The FOO (Feasibility-Of-Objectives) technique was first introduced in 1976 by Anderson [159] and then included into the MIL-HDBK-338B Electronic Reliability Design Handbook from Department of Defense of USA in 1988 [148] as a method to develop and implement reliability programs for generic military products. Following the FOO method, the subsystem allocation factors are computed as a function of four influence factors, namely complexity **C**, environmental factor **E**, state of the art **A** and operative time **O**. Each rank is estimated using both design engineering and expert judgments and it is based on a scale from 1 to 10 as detailed described in TABLE V.II.

TABLE V.II

RULES FOR THE ASSESSMENT OF INFLUENCE FACTORS ACCORDING TO FOO METHOD.

INFLUENCE FACTORS	RATING
COMPLEXITY - **C**	1 2 3 4 5 6 7 8 9 **10** **LOW** **MAX**
ENVIRONMENT CONDITION - **E**	1 2 3 4 5 6 7 8 9 **10** **LOW** **MAX**
STATE OF THE ART - **A**	1 2 3 4 5 6 7 8 9 **10** **MAX** **LOW**
OPERATING TIME - **T**	1 2 3 4 5 6 7 8 9 **10** **MAX** **LOW**

The rating values are then multiplied to achieve a partial weight factor β_i.

$$\beta_i = C_i \cdot E_i \cdot A_i \cdot O_i \tag{5.37}$$

The final product has values ranging from 1 to 10000 and the subsystem ratings are normalized so that their sum is equal to 1.

Thus, the weighting factors are given by:

$$\omega_i = \frac{C_i \cdot E_i \cdot A_i \cdot O_i}{\sum_{j=1}^{N}\left(C_j \cdot E_j \cdot A_j \cdot O_j\right)} = \frac{\beta_i}{\sum_{j=1}^{N}\beta_i} \tag{5.38}$$

The FOO method is a simple technique easily implementable using software tools. However, it is characterized by some major flaws (quite similar to the RPN drawbacks described in Section 3.2):

- The partial weight factor β_i is not unique. In fact, different combinations of the influence factors could provide the same β_i.
- Although the partial weight factor β_i could assume values between 1 and 10000, there are many gaps in the range and only a very limited part of these 10000 possible values is obtained from a unique combination of factors.
- All the different combinations of influence factors that lead to the same partial weight factor will also lead to the same allocated reliability. This may not be correct as the nature of the influence factors producing the same β_i can be remarkably different.

- All the four influence factors have the same importance within the equation.
- High subjectivity of the definition, which is deeply influenced by the expert's judgments.

5.4.5. Bracha method

Bracha method uses the same factors of FOO technique (see TABLE V.II) but it privileges the state of the art factor **A** in the formula to calculate the partial weight factors β_i [160]:

$$\beta_i = A_i \cdot (C_i + O_i + E_i) \tag{5.39}$$

According to the Bracha method, the values of the influence factors are not determined by an expert like the FOO approach. Instead, the influence factor ratings are calculated through a set of complex mathematical models using several base factors, some of them are listed below:

- the number of components of each subsystem;
- the number of components of the most complex subsystem;
- the number of redundancies;
- the time of use of each subunit;
- the operating time of each subsystem;
- the applied stress;
- the age of the database;
- the time required to design the system.

These models result in a set of four influence factors mathematically estimated varying in the range from 0 to 1. The subsystem ratings are then normalized, therefore the weighting factors are given by [160]:

$$\omega_i = \frac{A_i \cdot (C_i + O_i + E_i)}{\sum_{j=1}^{N} [A_i \cdot (C_i + O_i + E_i)]} = \frac{\beta_i}{\sum_{j=1}^{N} \beta_i} \tag{5.40}$$

The Bracha method is able to solve two out of five drawbacks of the FOO method, namely the high subjectivity of the factor definition and the same importance assigned to all the factor in the equation to calculate ω_i. However, it is not able to solve the other three major drawbacks of the FOO method, and it is also characterized by a high computational complexity due to the

models required to assess the complexity **C**, the environmental factor **E**, the state of the art **A** and the operative time **O**.

5.4.6. Karmiol method

The Karmiol method is based on the assessment of four influence factors, namely complexity **C**, state of the art **A**, operative time **O** and Criticality **K**. Each rank is estimated using both design engineering and expert judgments and it is based on a scale from 1 to 10 [161].

The procedure used to calculate the partial weight factor β_i and the weight factor ω_i is quite similar to the FOO model. The only difference is that the Karmiol method allows two different approaches. In the first one the partial weight factor β_i is based on the product of the indexes similarly to the FOO, as follow:

$$\beta_i = C_i \cdot A_i \cdot O_i \cdot K_i \tag{5.41}$$

Then, the weight factor is achieved after a normalization process to ensure that equation (5.10) is satisfied. Thus:

$$\omega_i = \frac{C_i \cdot A_i \cdot O_i \cdot K_i}{\sum_{j=1}^{N}(C_i \cdot A_i \cdot O_i \cdot K_i)} = \frac{\beta_i}{\sum_{j=1}^{N}\beta_i} \tag{5.42}$$

Alternatively, it is possible to calculate the partial weight factor as sum of the indexes and then evaluate the weight factor after the normalization process, as follow:

$$\beta_i = C_i + A_i + O_i + K_i \tag{5.43}$$

$$\omega_i = \frac{C_i + A_i + O_i + K_i}{\sum_{j=1}^{N}(C_i + A_i + O_i + K_i)} = \frac{\beta_i}{\sum_{j=1}^{N}\beta_i} \tag{5.44}$$

5.4.7. AWM method

In 1999 Kuo [162] introduced an Averaging Weighted Method (AWM) as a guide for reliability allocation design.

The method uses a questionnaire investigation to select the most influential system reliability factors such as complexity, state-of-the-art, system criticality, environment, safety, and maintenance in order to determine the subsystem reliability allocation ratings. All the influence factors included in Fig. 5.3 are

allowed, depending on the results of the questionnaire. Each rank is estimated on a scale from 1 to 10 using design engineering and expert judgments to obtain the subsystem reliability rate [162]. TABLE V.III shows the admissible influence factors and their rating rules according to the guidelines described in section 5.3.2.

TABLE V.III
INFLUENCE FACTORS ADMISSIBLE BY AWM ALLOCATION METHOD

INFLUENCE FACTORS	DESCRIPTION	RATING
COMPLEXITY - **C**	Number of components; system architecture.	**1** 2 3 4 5 6 7 8 9 **10** **LOW** **MAX**
ENVIRONMENT CONDITION - **E**	External stress factors (humidity, temperature, vibration, etc.).	**1** 2 3 4 5 6 7 8 9 **10** **LOW** **MAX**
STATE OF THE ART - **A**	Scientific development in the system specific engineering context.	**1** 2 3 4 5 6 7 8 9 **10** **MAX** **LOW**
CRITICALITY - **K**	Subsystem importance; consequences of a potential fault on the entire system.	**1** 2 3 4 5 6 7 8 9 **10** **MAX** **LOW**
MAINTAINABILITY - **M**	Average repair cost; average repair time.	**1** 2 3 4 5 6 7 8 9 **10** **LOW** **MAX**
SAFETY - **R**	Impact of failure on system safety	**1** 2 3 4 5 6 7 8 9 **10** **MAX** **LOW**

Considering a system composed by N subsystem, m is the number of influence factors and p the number of experts. Let Y_{ij} denotes the j-th rating for subsystem i. $X_{K_{ij}}$ is the j-th rating for subsystem i set by L-th expert and each factor is defined as follows:

$$Y_{ij} = \frac{1}{p}\sum_{k=1}^{p} X_{K_{ij}} \ \forall i = 1,\dots,m \, \forall j = 1,\dots,N \qquad (5.45)$$

Then, similarly to the Karmiol method, also in this case two different models can be used to allocate weighting factors ω_i.

The geometric model is based on the product of the influence factors, and thus the weight factor is given by:

$$\omega_i = \frac{\prod_{j=1}^{N} Y_{ij}}{\sum_{f=1}^{m} \prod_{j=1}^{N} Y_{ij}} = \frac{\beta_f}{\sum_{f=1}^{m} \beta_f} \tag{5.46}$$

While the arithmetic model is based on the sum of the influence factors:

$$\omega_i = \frac{\sum_{j=1}^{N} Y_{ij}}{\sum_{f=1}^{m} \sum_{j=1}^{N} Y_{ij}} = \frac{\beta_f}{\sum_{f=1}^{m} \beta_f} \tag{5.47}$$

The AWM has many advantages, such as:
- The higher the experts number, the lower the impact of a possible evaluation error.
- Minimum subjectivity issue due to factors assessment performed after a questionnaire-based investigation.
- Possibility to choose which influence factors represent the best alternative to fit the specific system judging on system features. Thus, only the factors that actually influence the system performances are taken into consideration.
- Low complexity.

The main drawback of the AWM method is the equal weight that the influence factors have in the final equations (5.46) and (5.47).

5.5. Related works: other innovative approaches

This section reports some of the innovative RA approaches available in literature as an alternative to the classical methods presented in the previous section. Currently, many works in literature about Reliability Allocation are focusing on giving high priority to certain influence factors and on minimizing the subjectivity of the expert judgments.

To solve the above-mentioned problems Fullér R. and Majlender P. [163] introduced the MVOWA (Minimal Variance Ordered Weighting Averaging) operator to minimize the risk of giving too much importance to a single parameter. This is done by proposing an innovative method to estimate the auxiliary vector of the OWA operators minimizing the variance of the system).

As an alternative, Chang et al. in 2009 [162] introduced the MEOWA (Maximum Entropy Oredered Weighting Averaging) method which is able to assign different importance to the information available in a situation of uncertainty. More information about MEOWA method will be discussed in the following section.

In order to take advantages of both MV-OWA and MEOWA methods Chen et al. [164] developed the MEMVOWA (Maximum Entropy Minimal Variance Ordered Weighting Averaging) method. Another approach that uses the MEOWA method as starting point of the RA procedure is presented in [165] integrating MEOWA and DEMATEL.

To reduce the subjectivity during expert definition of the influence factors De Felice et al. [166] proposed the IFM (Integrated Factors Method) in which objectively established parameters are used. A method based on fuzzy logic has been developed in [167] to take into account unclear information in the allocation in case the experts' conclusions are inaccurate or confused.

The ordered weighted geometric averaging (OWGA) operators have been used as central part of the allocation procedure in [168]. Then, the approach has been extended in [169] combining OWGA and fuzzy sets to ensure the benefits of both approaches.

Other techniques available in literature are based on a preliminary risk analysis. For instance, Di Bona et al. [170] introduces the CFM (Critical Flow Method) which estimates the influence parameters starting from a PHA (Preliminary Hazard Analysis). In [171] a new distribution of the Criticality parameter **K** is presented to accurately allocate the reliability to the most dangerous subsystems for the operation of the system, for the user or for the environment. Similar approach has been presented also by Yadav et al. [172] assigning a greater weight to the Criticality parameter **K**.

Some papers take into account the problem of uncertainty. For instance, in [173] an innovative RA method to allocate system reliability together with confidence level is presented, while Guangyan et al. [174] proposed a software that obtains the best allocation with an iterative procedures. An improved differential evolution algorithm is proposed in [175] to reallocate subsystem reliability for minimum cost and minimum uncertainty.

The idea of allocate the component reliability by means of a comparitve analysis with similar systems was firstly introduced by ARINC method [157]. However, most of the allocation methods are generally applied to electronic systems, while in case of mechanical or hydraulic systems is difficult to allocate component reliability by similarity approach. To solve this problem, Wang et al. [176] presents a comprehensive failure rate allocation method, while in [177] an RA

method based on Meta-Action has been presented combining the FOO method with the FMA (Function-Movement-Action) decomposition technique.

Other methods proposed some improvements to the classical allocation methods. For example, the AGREE allocation method has been extended in [178], while the Boyd method introduced in [179] combines the Equal and ARINC approaches.

Some interesting literature review about Reliability Allocation have been recently published by Forcina et al. [152] and Silvestri et al. [153].

5.6.   Related works: MEOWA method

In this section one of the most interesting and widely used innovative RA approach is presented and detailed discussed.

In 1988 Yager [180] introduced the concept of OWA operators, which are important aggregation operators within the class of weighted aggregation methods. OWA operators have the ability to derive optimal weights of the attributes based on the rating of the weighting vectors after an aggregation process [180].

An OWA operator of dimension n is a function F from $I^n \rightarrow I$, where $I = [0, 1]$. An auxiliary vector $W = [w_1, w_2, ..., w_n]^T$ is associated to the OWA operators and it could be defined as follows:

$$\sum_{i=1}^{n} w_i = 1 \quad \forall w_i \in [0,1], \quad i = 1,2, ... n \tag{5.48}$$

$$f(a_1, a_2, ..., a_n) = \sum_{i=1}^{n} w_i b_i \tag{5.49}$$

Where b_i is the i-th largest element in the collection $a_1, a_2, ..., a_n$ and the following ordering is ensured $b_1 \geq b_2 \geq \cdots \geq b_n$ [180].

Later, Yager also introduced two important characterizing measurements with respect to the auxilliary vector W of the OWA operator. One of these two measures is "Orness of the aggregation", which is definedas follows. Assume F is an OWA aggregation operator with an auxiliary vector $W = [w_1, w_2, ..., w_n]^T$, the degree of Oorness associated with this operator is defined as:

$$Orness(W) = \alpha = \frac{1}{n-1} \sum_{i=1}^{n} (n-i) w_i \tag{5.50}$$

Where Orness(W) = α is called situation parameter and it can vary within the interval [0; 1].

The second characterizing measurement introduced by Yager is the "Dispersion of the aggregation" that is defined as:

$$Dispersion(W) = -\sum_{i=1}^{n} w_i ln\,(w_i) \tag{5.51}$$

O'Hagan in 1988 combined the principle of maximum entropy and OWA operators to propose a particular OWA weight that has maximum entropy with a given level of Orness [181]. This approach is based on the process of maximization of Dispersion(W):

$$\frac{1}{n-1}\sum_{i=1}^{n} (n-i)\,w_i = \alpha \tag{5.52}$$

Where:

$$0 \leq \alpha \leq 1; \qquad \sum_{i=1}^{n} w_i = 1; \qquad 0 \leq w_i \leq 1 \tag{5.53}$$

Fuller and Majlender in 2001 [181] used the method of Lagrange multipliers on Yager's OWA equation to derive a polynomial equation, which can determine the optimal auxiliary vector under the maximal entropy. According to this method, the associated auxiliary vector is easily obtained solving the following system of equations:

$$\begin{cases} w_j = \sqrt[n-1]{w_1{}^{n-j}\,w_n{}^{j-1}} \\ w_n = \dfrac{[(n-1)\alpha - n]w_1 + 1}{(n-1)\alpha + 1 - nw_1} \\ w_1[(n-1)\alpha + 1 - nw_1]^n = [(n-1)\alpha]^{n-1}\{[(n-1)\alpha - n]w_1 + 1\} \end{cases} \tag{5.54}$$

With situation parameter $\alpha \in \left[\frac{1}{2}\,;1\right]$ and $\sum_{i=1}^{n} w_i = 1$.

The Maximal Entropy Ordered Weighted Averaging (MEOWA) method presented by Chang in 2009 [182] uses the OWA operators and the optimal auxiliary vector under maximal entropy as in [181] to develop an innovative RA method which is able to assign the optimal weight to each influence factor. The Maximal Entropy Ordered Weighted Averaging Method (MEOWA) [182] gives the opportunity to select the number and type of factors to the expert

that carry out the allocation. In this work, two scenarios have been investigated in order to compare the MEOWA method with the other approaches such as FOO and AWM. The 4-parameter MEOWA has been customized in this work to implement the same factor as FOO, while the 6-parameter MEOWA starts from the six influence factors used in the AWM method. According to MEOWA method, the auxiliary vector W can be estimated using the procedure presented in equation (5.54). Thus, the auxiliary vector W depends only on the number of selected influence factors and on the situation parameter α. The evaluation of the auxiliary vector W in case of 4 influence factors (4-parameter MEOWA) is shown in TABLE V. IV while

TABLE V.*V* reports the case of 6 influence factors (6-parameter MEOWA).

TABLE V. IV

COMPONENTS OF THE AUXILIARY VECTOR W IN COMPLIANCE WITH 4-PARAMETER MEOWA

α	w_1	w_2	w_3	w_4
0.5	0.250000	0.250000	0.250000	0.250000
0.6	0.347440	0.272208	0.213266	0.167086
0.7	0.461371	0.275618	0.164651	0.098361
0.8	0.596482	0.252032	0.106491	0.044996
0.9	0.764108	0.182133	0.043413	0.010348
1	1	0	0	0

TABLE V.V

COMPONENTS OF THE AUXILIARY VECTOR W IN COMPLIANCE WITH 6-PARAMETER MEOWA

α	w_1	w_2	w_3	w_4	w_5	w_6
0.5	0.166666	0.166666	0.166666	0.166666	0.166666	0.166666
0.6	0.246782	0.207240	0.174034	0.146148	0.122731	0.103066
0.7	0.347494	0.239774	0.165447	0.114160	0.078772	0.054353
0.8	0.478120	0.254752	0.135737	0.072323	0.038535	0.020532
0.9	0.663738	0.223831	0.075482	0.025455	0.008584	0.002895
1	1	0	0	0	0	0

Then, the overall factor Z_k can be achieved and then allocated to each subsystem [181]. This index takes into account all n influence factors, each of them multiplied by the optimal weight.

$$Z_k = \sum_{i=1}^{n} w_i b_{i,k} \qquad (5.55)$$

where $b_{1,k} > b_{2,k} > \cdots > b_{n,k}$ are the values assigned to the influence factors of the k-th subsystem in descending order.

Finally, the weight factors ω_k are given by:

$$\omega_k = \frac{Z_k}{M_\alpha} \qquad where \qquad M_\alpha = \sum_{i=1}^{n} \left(w_i \sum_{j=1}^{N} b_{i,j} \right) \qquad (5.56)$$

MEOWA technique provides a situation parameter $\alpha \in [0.5\,;1]$ that is necessary to achieve the reliability allocation values: $\alpha = 1$ is used in case of high confidence of the decision-maker, while $\alpha = 0.5$ is used when the decision-maker faces a moderate uncertainty. Consequently, when this parameter assumes high values, the RA procedure associates a lower reliability to the items characterized by influence factors with high ranks. This characteristic is crucial and it is not valid for all the other allocation methods where the weight factors are calculated simply as sum or product of the influence factors.

When $\alpha = 0,5$ the MEOWA method assigns the same weight to all influence factors, as the other RA techniques.

The benefits of using the conditional parameter are highest in case of RA assessment during early design phase when information and data are imprecise, incomplete or uncertain.

The MEOWA allocation technique is one of the best techniques available in literature. The benefits of MEOWA are listed below:

- It has no bounds on number and type of influence factors, allowing to customize each application based on the actual condition that affect the system under analysis.
- The engineers performing the RA process can also decide to define new influence factors that can be particularly characterizing for the system.
- The optimal weights are assigned to each factor thanks to the OWA operator, the Lagrange multipliers and the maximal entropy principle.
- No subjectivity problem thanks to the auxiliary vector.
- It is possible to express the desired level of confidence for the specific allocation based on the value of the situation parameter α.
- Setting $\alpha = 0.5$ the same weight is attributed to each value of each factor. Instead $\alpha = 1$ provides greater weight to the largest value among all those assigned to the subsystem factors. Thus, MEOWA is the only method that allows to assign greater importance to the pejorative factor (the highest) of each subsystem

The only drawback of MEOWA is related to the high computational complexity of the software to solve the equations that provide the auxiliary vector.

5.7.   The critical role of redundancies

By a reliability point of view, it is possible to identify several different configurations that are commonly implemented in complex systems. Such functional configurations can be classified into three categories according to the type of redundancy realized. Each one of them includes one or more base configurations, as follow:

- No redundancy. In this scenario there are no redundant components that can provide continuity of service in case of failure.
  - Series configuration: the system works if and only if all the components making up the configuration work properly. This is the case required by Assumption i. and all the RA methods available in literature require this configuration to be applied [154], [183]. Considering a system composed by N components, each one of them characterized by the reliability function $R_i(t)$, then the reliability of a series architecture $R_{series}(t)$ is given by:

$$R_{series}(t) = \prod_{i=1}^{N} R_i(t) \qquad (5.57)$$

- Static redundancy. In this scenario the system includes two or more components working simultaneously to ensure the achievements of the same functionality/goal. Thus, redundancy is continuously used by the service of interest, regardless of whether faults are present or not. Faults are tolerated implementing the fault masking technique without proper fault detection (i.e. Fault masking is the systematic application of error compensation, even in absence of errors) [154], [183].
  - Parallel configuration: in this case the system fails if and only if all the components of the configuration are failed. This means that, considering a parallel configuration composed by N items, the system works if at least 1 item out of N (1ooN) is functioning. The reliability of the parallel configuration $R_{par}(t)$ is given by:

$$R_{par}(t) = 1 - \prod_{i=1}^{N} [1 - R_i(t)] \qquad (5.58)$$

o k-out-of-N (kooN): in this configuration, considering a system composed by N items, the proper functionalities are ensured if at least k items out of N works properly. To analyze this architecture, some hypotheses are required. Usually, the binomial distribution under the assumption of identical items (same product, same manufacturer, same supplier, same external stresses, same installation point, etc) is required. Thus, the reliability of a kooN configuration $R_{kooN}(t)$ is given by:

$$R_{kooN}(t) = \sum_{i=k}^{N} \binom{N}{i} R_i(t)^i \, [1 - R_i(t)]^{N-i} \qquad (5.59)$$

- Dynamic redundancy. Redundancy is activated on demand by a service of interest in presence of faults typically after reconfiguration. So, dynamic redundancy consists of fault detection and system reconfiguration with a standby unit. In case of the main component (active unit) fail, then the standby unit is activated to complete the mission [184]–[187]).

  o Cold standby: in this case only the main unit is operative; the standby unit is inactive and completely disconnected from the power source. Therefore, quiescent components during the inactive period do not age and cannot fail. In this configuration a diagnostic unit is necessary to detect main unit failure and switch the load to the standby equipment on demand. Switching devices can't be considered failure free by definition because a fault in such unit nullifies redundancy advantages. The response time necessary to activate and initialize the standby unit and the addition of the switch failure rate are the main drawbacks of cold standby architecture compared to static redundant architecture. Considering R_1 the reliability of the main component, p the failure probability of the switching device, f_1 the probability density function of the main component, $R_{2,a}$ the reliability of the standby item when it operates in active mode, and x the time to failure of the main component. Then, the reliability function for a cold standby configuration $R_{cold}(t)$ is expressed as:

$$R_{cold}(t) = R_1(t) + (1 - p) \cdot \int_0^t f_1(x) \cdot R_{2,a}(t - x) \, dx \qquad (5.60)$$

      o   Warm standby: In this case both units are connected to the power source, but only the main item is used. The standby is half operative and ready to work in case of failure of the main item. An important advantage of this configuration is the reduction of the response-time. Thus, it is not necessary to wait for standby unit start-up because the equipment is ready to use. Standby units age during the quiescent period and can fail before switching the load; for this reason, it is necessary to introduce a specific failure rate for the quiescent status. Standby equipment is always described by two different failure rates: λ_0 when the main unit is working properly so standby unit is half-operative; λ when the standby unit is fully operative after main equipment fail. Considering $R_{2,sb}$ the reliability of the standby item in the quiescent mode evaluated using failure rate λ_0 The reliability function for a warm standby configuration $R_{warm}(t)$ is given by:

$$R_{warm}(t) = R_1(t) + (1-p) \cdot \int_0^t f_1(x) \cdot R_{2,sb}(x) \cdot R_{2,a}(t-x)\, dx \qquad (5.61)$$

Considering all the redundant configuration just described, it is clear how Assumption i. of considering only the series architecture is too simplistic and absolutely not reasonable.

5.8. Proposed iterative RA approach for complex systems

The aim of this work is to extend the range of applicability of the RA techniques available in literature overcoming both the initial hypothesis described in section 5.3.1. (Assumption i. and Assumption ii.).

Thus, this section introduces an innovative iterative approach to overcome both Assumption i. and Assumption ii. and extend the range of applicability to any kind of complex system (including static redundancies, dynamic redundancies and component characterized by non-constant failure rate) [188].

The innovative procedure proposed in this work is illustrated in Fig. 5.6. The required inputs are the system reliability goal $R_{SYS}{}^*(t_a)$ at the allocation time t_a and the system Reliability Block Diagram (RBD).
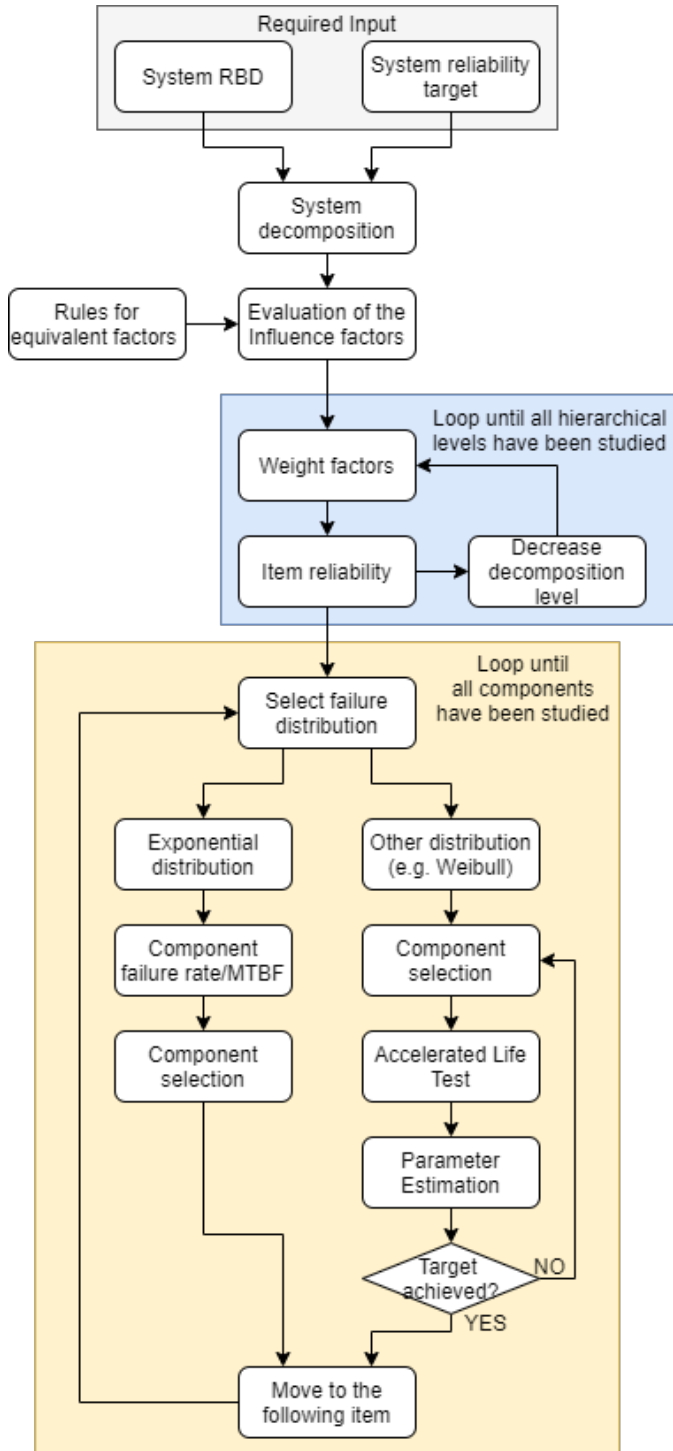
Fig. 5.6. Proposed allocation procedures for complex systems.

5.8.1. System decomposition

The first step of the procedure consists in the decomposition of the system RBD according to the different hierarchical levels. Each level must be assembled by a unique reliability architecture, such as series, parallel, standby or k-out-of-n. Usually, but not always, the top level corresponds with the equivalent series architecture of the system under test, which means that each redundant block is grouped in a single equivalent series item. Then, the redundancies grouped in the top level are decomposed in the subsequent levels.

The system decomposition is performed until all the single components included in the RBD are treated separately.

An example of system decomposition performed on a generic complex system is illustrated in Fig. 5.7. The green blocks stand for the base component identified by the symbols from R_1 to R_{11}. The red boxes represent the equivalent subunit required for the system decomposition at the different levels. For instance, the entire central block of the RBD become a single item R_{EQ1} at the top hierarchical level, while it is then decomposed as a parallel architecture between R_{EQ2} and R_{EQ3} at the 2nd level. The 3rd level is composed by two separated architectures. The first one is the top branch of the parallel configuration R_{EQ1} and it represents the series decomposition of the block R_{EQ2}.
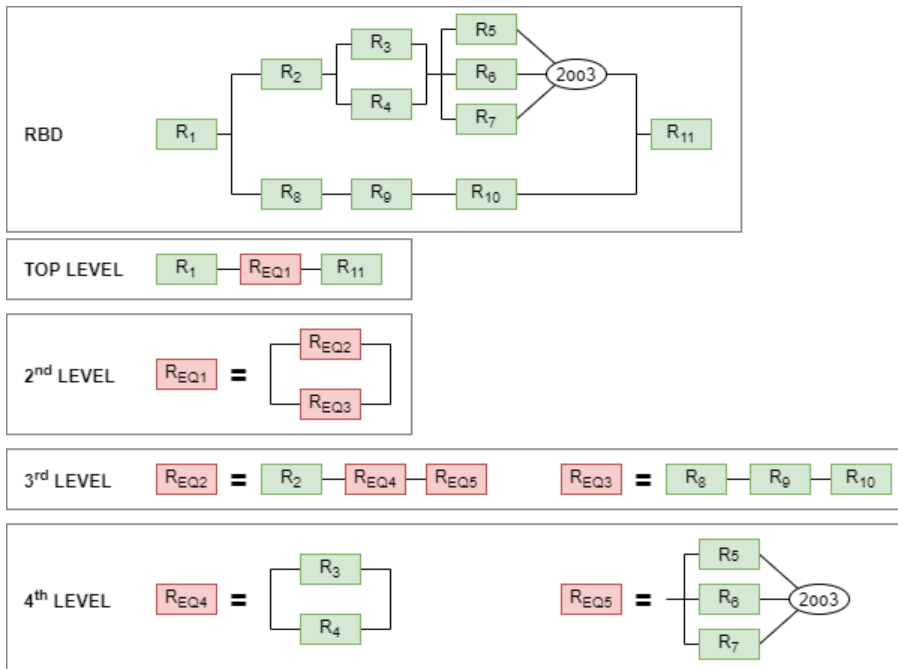
Fig. 5.7. Example of complex system decomposition into four hierarchical levels.

Furthermore, the 3rd level also includes the decomposition of the equivalent block R$_{EQ3}$ which is the actual series of R$_8$, R$_9$ and R$_{10}$ blocks. Similarly, the 4th level includes the decomposition of the parallel architecture between R$_3$ and R$_4$ blocks and the decomposition of the 2oo3 configuration.

5.8.2.   Influence factors

The following step is the evaluation of the influence factors based on expert's judgments. Depending on the techniques implemented, different influence factors can be considered.

The experts that perform the assessment assign the influence factors to the single items making up the system. In other words, taking once again the system decomposition in Fig. 5.7. as an example, the experts have to assign the influence factors of all the component identified by green boxes (i.e. all the single items).

Subsequently, it is necessary to estimate the equivalent influence factors of the subsystems identified in the different hierarchical levels. This means that a set of rules to derive the influence factors of the equivalent items (red boxes) from the factors of the single items (green boxes) is required.

Considering a worst-case scenario, the following list of rules has been proposed to effectively estimate the influence factors of the equivalent subsystems.

- Complexity **C** → the total complexity factor of an equivalent unit is given by the maximum complexity value between the elements belonging to the unit. In this way, the principal of worst-case scenario is ensured. Consider a system composed by M equivalent units, where each unit is composed by a number N$_i$ of base items. Then, the complexity of the equivalent unit i is given by:

$$\boldsymbol{C}_{EQ_i} = \max_{j=1,\dots,N_i} \boldsymbol{C}_j \quad \forall i = 1, 2, \dots, M \tag{5.62}$$

- Criticality **K** → the total criticality factor of an equivalent unit is given by the minimum value among all the criticality factors of the item making up the unit. Since the criticality is defined in reverse order, in this way the principal of worst-case scenario is ensured. Consider the same system of the previous case, the criticality of the equivalent unit i is given by:

$$\boldsymbol{K}_{EQ_i} = \min_{j=1,\dots,N_i} \boldsymbol{K}_j \quad \forall i = 1, 2, \dots, M \tag{5.63}$$

- State of the Art **A** → the total state of the art factor rating of a unit is the mean between the states of the art of the elements belonging to

the unit. In this case, it is more reasonable to provide a metric that describe the entire equivalent unit as the average value between the engineering advancement of all the components included in the unit. Consider the same system of the previous case, the state of the art of the equivalent unit i is given by:

$$A_{EQ_i} = \frac{1}{N_i} \sum_{j=1}^{N_i} A_j \quad \forall i = 1, 2, \dots, M \tag{5.64}$$

- Environmental factor **E** $\rightarrow$ the total environmental factor of the entire unit is equal to the maximum value among all the environmental factors of the considered items. Thus, the principal of worst-case scenario is ensured. Consider the same system of the previous case, the environmental factor of the equivalent unit i is given by:
$$E_{EQ_i} = \max_{j=1,\dots,N_i} E_j \quad \forall i = 1, 2, \dots, M \tag{5.65}$$

- Operating Time **T** $\rightarrow$ the overall operating time of the entire unit is equal to the operating time of the most used item. Thus, the principal of worst-case scenario is ensured. Consider the same system of the previous case, the operating time of the equivalent unit i is given by:
$$T_{EQ_i} = \max_{j=1,\dots,N_i} T_j \quad \forall i = 1, 2, \dots, M \tag{5.66}$$

- Maintainability **M** $\rightarrow$ similarly to the state of the art, also the maintainability factor rating is assigned as the mean value between the maintainability of the elements belonging to the unit. In this way, the maintainability of the entire equivalent unit is the average value between the maintenance cost, the task duration and the accessibility of all the items. Consider the same system of the previous case, the maintainability of the equivalent unit i is given by:

$$M_{EQ_i} = \frac{1}{N_i} \sum_{j=1}^{N_i} M_j \quad \forall i = 1, 2, \dots, M \tag{5.67}$$

- Safety **R** $\rightarrow$ the total safety factor of an equivalent unit is given by the minimum value among all the safety factors of the item making up the unit. This is due to the fact Safety **S** represents the impact of the failure on system, environment, personnel and users by a safety point of view and it is assessed in reverse order. Thus, the worst-case scenario is ensured only selecting the minimum value between all the component

making up the unit. Consider the same system of the previous case, the criticality of the equivalent unit i is given by:

$$\boldsymbol{R}_{EQ_i} = \min_{j=1,\dots,N_i} \boldsymbol{R}_j \quad \forall i = 1, 2, \dots, M \tag{5.68}$$

5.8.3. Allocation of reliability requirements: the extension to redundant architectures

The following steps involve the implementation of the allocation loop highlighted by the blue box in Fig. 5.6.

Starting from the top hierarchical level and using the system reliability goal as input of the procedure, this phase requires to estimate the weight factors of the units and then allocate the unit reliability according to the corresponding weight. Then, the procedure must be repeated in the following hierarchical level in a TOP-DOWN manner using the results of the previous level as input of the current level. This iterative approach should be repeated until all the different hierarchical levels have been studied and the corresponding reliability allocated. Moving back once again to the system decomposition taken as example in Fig. 5.7. it is necessary to repeat this iterative procedure four times. The results achieved for R_{EQ1} during the first cycle become the input to allocate the reliability at the 2nd level. Then similar considerations lead to the reliability allocation of the 3rd and 4th levels. At the end of the fourth repetition, the reliability of all the ten components (green boxes) identified by the symbols from R_1 to R_{10} will be allocated.

All the allocation techniques previously mentioned could be implemented in this phase to calculate the optimal weight factor and then allocate the component reliability. It is important to note that to overcome Assumption i. and extend the range of applicability of such methods to redundant architecture it is necessary to deal with each configuration separately. The following subsections illustrates how the reliability is allocated to each component based on the system architecture.

5.8.3.1. Series configuration: classical approach

As a reminder, under Assumption i. the classical approach to allocate the reliability follows a simple structure. Firstly, one or more influence factors are allocated, usually using a 1-to-10 scale.

$$X_i \in [1, 10] \tag{5.69}$$

Where X_i represents a generic influence factor of the component i-th. Then the weight factor ω_i is estimated as a function g of the influence factors:

$$\omega_i = g(C_i, A_i, E_i, O_i) \tag{5.70}$$

Then the reliability allocated to the i-th component R_i^* (t) is given by:

$$R_i^*(t_a) = [R_{SYS}^*(t_a)]^{\omega_i} \tag{5.71}$$

5.8.3.2. A proposal for parallel configuration

In order to enlarge the range of applicability of the allocation methods, the following hypotheses have been proposed in this work in case of parallel configuration [188]:

- Replacement of the reliability function R(t) with unreliability function F(t) within the equations.
- Inversion of the influence factor rating. This step is necessary to keep the right relationship between the definition of the influence factors and the rating. For example, in traditional methods for series system the complexity factor **C** is based on a scale from 1 to 10, where the least complex system is rated 1 and the most complex system has a rank equal to 10. In this way a growth in the complexity increases the weighting factor and consequently decreases the reliability allocated. Such relationship must be ensured also in present of parallel configuration.

More in detail, if the system is described by a parallel architecture, the weight factor $\widetilde{\omega_\iota}$ is evaluated using the same function g of the inverted influence factors, as follow:

$$\widetilde{\omega_\iota} = g(\widetilde{C_\iota}, \widetilde{A_\iota}, \widetilde{E_\iota}, \widetilde{O_\iota}) \tag{5.72}$$

Where the generic inverted factor $\widetilde{X_\iota}$ in case of a 10-point scale will be expressed as follow:

$$\widetilde{X_\iota} = 11 - X_i \tag{5.73}$$

Then, the reliability allocated to each unit is given by:

$$F_i^* (t_a) = \left[F_{sys}^*(t_a)\right]^{\omega_i} \tag{5.74}$$

$$R_i^* (t_a) = 1 - F_i^* (t_a) = 1 - \left[F_{sys}^*(t_a)\right]^{\omega_i} \tag{5.75}$$

$$R_i^* (t_a) = 1 - [1 - R_{SYS}^*(t_a)]^{\omega_i} \tag{5.76}$$

In case the method selected to allocate reliability includes other parameters, it is necessary to also invert such value. For instance, considering then MEOWA method, the assumption of the inversion of the situation parameter α rating is required in case of assessing the allocation procedure for parallel configurations. The relation performing this inversion is shown below:

$$\tilde{\alpha} = 1.5 - \alpha \tag{5.77}$$

Equation (5.77) assigns to the new situation parameter $\tilde{\alpha}$ image values in the range from 0.5 to 1. When $\alpha = 0.5$ the corresponding value is $\tilde{\alpha} = 1$. Instead for $\alpha = 1$ the corresponding value is $\tilde{\alpha} = 0.5$.

According to the proposed approach, several Reliability Allocation techniques can be successfully extended and applied to parallel configuration. More in detail, taking the approaches described in the previous sections, the proposed method works properly with Equal, FOO, Bracha, Karmiol, AWM and MEOWA. More generally, the proposed extension to parallel configuration can be applied to any method which is based on weight factors defined as follow:

$$\omega_i = \frac{f(Y_{ij})}{\sum_{i=1}^{N} f(Y_{ij})} \tag{5.78}$$

Where Y_{ij} denote the j-th rating for subsystem i, and f is a function of Y_{ij}. Hence, two RA milestones such AGREE and ARINC cannot be extended to parallel configuration.

5.8.3.3. A proposal for k-out-of-N configuration

As explain in section 5.7.1. the k-out-of-N configurations is generally made up by three modules with the same reliability properties. Thus, the allocation methods shown in Section 5.4. and Section 5.5. cannot be implemented in this architecture. In fact, all these techniques do not allow to allocate the reliability goal evenly to the items. The only alternative is the Equal Allocation Method

that can apportion the reliability target evenly between the redundant items [188]. Taking the 2oo3 (2 items out of 3 need to be properly working) as an example the following steps illustrate how the reliability $R_i^*(t_a)$ can be allocated equally among the components of a kooN configuration. The reliability of a 2oo3 configuration $R_{2oo3}{}^*(t)$ is given by:

$$R_{2oo3}{}^*(t_a) = 3 \cdot [R_i^*(t_a)]^2 - 2 \cdot R_i^*(t_a)^3 \qquad (5.79)$$

For the sake of simplicity, let assume:

$$R_i^*(t_a) = p \qquad (5.80)$$

Then, substituting equation (5.80) into equation (5.79) and solving the equation:

$$R_{2oo3}{}^*(t_a) = 3p^2 - 2p^3 \qquad (5.81)$$

$$2p^3 - 3p^2 + R_{2oo3}{}^*(t_a) = 0 \qquad (5.82)$$

$$p^3 - \frac{3}{2}p^2 + \frac{1}{2}R_{2oo3}{}^*(t_a) = 0 \qquad (5.83)$$

After few mathematical steps the solution of the third-grade polynomial equation (5.83) can be expressed as follow:

$$R_i^*(t_a) = \frac{1}{2}\left(z + \frac{1}{z} + 1\right) \qquad (5.84)$$

$$z = \sqrt[3]{2\sqrt{[R_{2oo3}{}^*(t_a)]^2 - R_{2oo3}{}^*(t_a)} - 2 \cdot R_{2oo3}{}^*(t_a) + 1} \qquad (5.85)$$

5.8.3.4. A proposal for standby redundancy

As explained in section 5.7.1. component reliability of a standby architecture is given by an integral equation not always easy to solve. As a consequence, it is not possible to precisely apply such equation within the already complex model of RA techniques.

Nevertheless, a different proposal to apply reliability allocation techniques to standaby redundancies (either cold standby or warm standby) is presented in this secton.

More in detail, in this paper standby redundancy are processed as parallel configuration. Therefore, the innovative method introduced in 5.7.1.2 based on

inversion of the influence factors and unreliability estimation is taken into account also in present of standby redundancies. However, it is necessary to introduce some adjustment to the influence factor of the standby unit to take into account the time in which it is inoperative. For example, the operative time **O** and the criticality **K** could be easily updated in order to optimally describe the differences between an active component or a standby unit.

5.8.4. Final loop: the extension to non-constant failure rate

Regardless the configurations, the previous step provides a reliability value R_i^* estimated at time t_a for each one of the items included in the system RBD. Then, it is necessary to find the components in the market with specific characteristics that allows to achieve the estimated reliability. Only if all the components included in the system achieve their own reliability goal then it is possible to ensure that the system reliability goal $R_{SYS}^*(t)$ is fulfilled.

Under Assumption ii. the exponential failure rate is considered. In this case, the hypothesis of constant failure rate remarkably simplifies the procedure. In fact, under such assumption, the reliability allocated to a generic component i could be expressed as a function of the constant failure rate λ_i^* as follow:

$$R_i^*(t_a) = exp\left(-t_a \cdot \lambda_i^*\right) \tag{5.86}$$

Thus, knowing the allocation time t_a the failure rate allocated to the considered component could be easily estimated as:

$$\lambda_i^* = -\frac{ln\left[R_i^*(t_a)\right]}{t_a} \tag{5.87}$$

Or alternatively, the allocated Mean Time Between Failures $MTBF_i^*$ could be achieved as the reciprocal of the allocated failure rate, as follow:

$$MTBF_i^* = \frac{1}{\lambda_i^*} = -\frac{t_a}{ln\left[R_i^*(t_a)\right]} \tag{5.88}$$

Once the component failure rate or the component MTBF are estimated using equations (5.87) and (5.88) it is possible to select a component on the market that allows to fulfill the obtained requirements.

In the last years, manufacturer started providing information about the component failure rate or the component MTBF under the assumption of

exponential failure distribution. Alternatively, in case for example of component to be used in safety-related systems, the certification committee provides a safety certificate that includes the failure rate of the item.

As a general comment, in case of exponential distribution, it is quite easy to identify a component in the market that fulfill the requirements in terms of either allocated failure rate λ_i^* or allocated $MTBF_i^*$.

Quite the contrary, in case of failure distribution different from the exponential, such operation become quite difficult.

Let's take the Weibull distribution as an example. Under the assumption of Weibull failure distribution, the reliability allocated to component i could be expressed as a function of two parameters: the shape parameter β and the scale parameter η, as follow:

$$R_i^*(t_a) = exp\left[-\left(\frac{t_a}{\eta}\right)^{\beta}\right] \tag{5.89}$$

While the component failure rate under Weibull assumption could be expressed as a function of the same two parameters, as:

$$\lambda_i^*(t_a) = \frac{\beta}{\eta}\left(\frac{t_a}{\eta}\right)^{\beta-1} \tag{5.90}$$

As a consequence, the component failure rate cannot be precisely estimated since equation (5.90) depends on two different parameters. Thus, without the introduction of some improvements of the methodology, the RA procedure can assign only a fixed reliability value R_i^* allocated at a certain time t_a.

The same problem arises also in present of any other failure distribution that does not consider a constant failure rate. For instance, the reliability and the failure rate under lognormal failure distributions are function of the location parameter μ and the scale parameter σ, just the same as the normal distribution.

Trying to solve this problem, this work introduces a new methodology based on accelerated life test to estimate the parameters of the selected failure distribution and choose the proper component on the market. This solution represents the right branch of the second loop (yellow box) in Fig. 5.6. and it is implemented only in case the constant failure rate assumption is not applicable. The complete flowchart of the procedure supposing a Weibull failure distribution is illustrated in Fig. 5.8.

According to the proposed method illustrated in Fig. 5.8. the RA procedure continues regularly until the component reliability $R_i^*(t_a)$ has been assessed.

Then, the reliability function is written as function of the distribution parameters. The following step is the selection of the most suitable component available in the market. However, manufacturers usually do not provide information about the shape and scale parameters of the failure distribution. Thus, an Accelerated Life Test (ALT) procedure is carried out to evaluate the reliability performances of the selected components. ALT allows to achieve information about the component reliability based on the results of tests performed subjecting a product to conditions above the nominal service operations [123], [124], [189]. A set of devices (usually the test bed must comprise a set of 10 - 30 identical components) are subjected to external stress sources such as temperature, humidity, vibration, voltage and current bias, etc. After the test it is possible to estimate the item reliability by means of probabilistic assessment and life data analysis [129]–[131], [190].
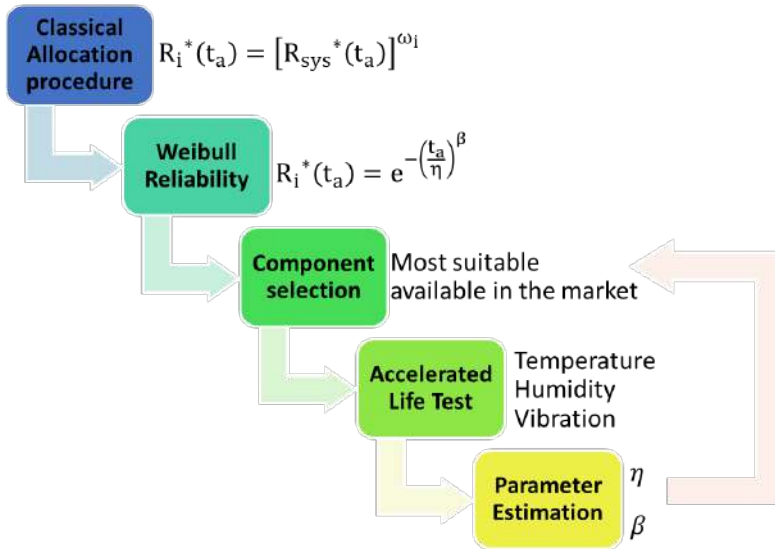
Fig. 5.8. Proposed alternative to allocate component reliability also in case of non-constant failure rate.

Life data analysis (LDA) is the study of a representative sample of units that allows analyst to estimate a life distribution for all the products of the same population (e.g. reliability function, probability of failure at a fixed time, failure rate, etc.). LDA consists of four major steps, as follow:

1. Perform an accelerated test plan to collect a dataset of Times To Failure (complete or censored dataset are admissible).
2. Identify the distribution that best fit the available failure data. This best-fitting distribution provides information about the entire population.

115

3. Estimate the parameters of the selected distribution.
4. Generate plots and results to estimate product life characteristics.

There are several distributions available in literature that could be used to describe the life of a population [131]. The behaviour of each distribution is described and influenced by characteristics and parameters that vary from distribution to distribution.

The exponential failure distribution is used in many handbooks to describe electronic components. The Probability Density Function (PDF) $f_{exp}(t)$ depends only on a single parameter λ, as follow [154]:

$$f_{exp}(t) = \lambda e^{-\lambda t} \tag{5.91}$$

The 2-parameter Weibull distribution is the most common probability distribution in LDA. The PDF $f_{2w}(t)$ depends on the shape parameters β and the scale parameter η [154]:

$$f_{2w}(t) = \frac{\beta}{\eta}\left(\frac{t}{\eta}\right)^{\beta-1} e^{-\left(\frac{t}{\eta}\right)^{\beta}} \tag{5.92}$$

A valid alternative to the 2-parameter Weibull distribution is the 3-parameter Weibull distribution which introduce a location parameter γ, as follow [154]:

$$f_{3w}(t) = \begin{cases} \frac{\beta}{\eta}\left(\frac{t-\gamma}{\eta}\right)^{\beta-1} \cdot e^{-\left(\frac{t-\gamma}{\eta}\right)^{\beta}} & t \geq \gamma \\ 0 & t < \gamma \end{cases} \tag{5.93}$$

The lognormal distribution is used to describe the infant mortality of a population. The PDF $f_{log}(t)$ depends on a location parameters μ and the scale parameter σ [154]:

$$f_{log}(t) = \frac{1}{\sqrt{2\pi}\sigma t} e^{-\frac{(lnt-\mu)^2}{2\sigma^2}} \tag{5.94}$$

Strictly related to the lognormal distribution, also the PDF of the normal distribution $f_{nor}(t)$ depends on the same location parameters μ and the scale parameter σ [154]:

$$f_{nor}(t) = \frac{1}{\sqrt{2\pi}\sigma} e^{-\frac{(t-\mu)^2}{2\sigma^2}} \tag{5.95}$$

Another useful life distribution is the Gamma distribution. The PDF $f_g(t)$ depends on a shape parameters k and the scale parameter μ [154]:

$$f_g(t) = \frac{\mu}{\Gamma(k)} \cdot (\mu \cdot t)^{\alpha-1} \cdot e^{-\mu \cdot t} \tag{5.96}$$

Where $\Gamma(\cdot)$ is the gamma function.

Regardless the life distribution, the reliability of the population at a time t could be achieved integrating the PDF from t to infinitive, while the failure rate is the ratio between the PDF and the reliability, as follow:

$$R(t) = \int_t^\infty f(u) \, du \tag{5.97}$$

$$\lambda(t) = \frac{f(t)}{\int_t^\infty f(u) \, du} = \frac{f(t)}{R(t)} \tag{5.98}$$

In order to fit a statistical model to a life data set, the analyst should estimate the parameters of the life distribution that will make the function fitting the data in the best way. Several methods have been developed to estimate the parameters that will fit a lifetime distribution to a particular dataset, the most common are the Rank Regression (RR) and Maximum Likelihood Estimation (MLE). The RR (also called Least Square method) requires that a straight line is fitted to a set of data points in order to minimize the sum of the squares of the distance of the points to the fitted line. The MLE method is considered one of the most robust parameter estimation techniques. The basic idea is to obtain, for a given distribution, the most likely values of the parameters that will best describe the data. Both approaches require to estimate the cumulative distribution starting from the Time to Failure data. The most widely used method of determining the coordinates of the point is the median rank for each failure. The median rank is the value that the true probability of failure should have at the i-th failure out of a sample of N units at the 50% confidence level. The rank can be identified by solving the cumulative binomial equation for Z.

$$0.5 = \sum_{k=j}^{N} \binom{N}{k} Z^k (1-Z)^{N-k} \tag{5.99}$$

Alternatively, the Kaplan-Meier (K-M) method could be implemented. In case of complete data, the cumulative distribution $F(t_i)$ is given by:

$$F(t_i) = \frac{i - 0.5}{N} \qquad (5.100)$$

In case of right-censored data, the cumulative distribution $F(t_i)$ is given by:

$$F(t_i) = 1 - \frac{(1 - p_i) + (1 - p_{i-1})}{2} \qquad (5.101)$$

$$p_i = 1 - \prod_i \left(\frac{N - i}{N - 1 + 1} \right)^{\delta_i} \qquad (5.102)$$

An automated measurement system that continuously monitor the devices during the test should be implemented in order to acquire the exact Accelerated Time To Failure (ATTF) of each device. To convert the ATTF into the corresponding Time To Failure (TTF) in normal operating conditions the acceleration model described in section 3.6.1 could be implemented.

After that, the obtained data can be used to estimate the parameters of the failure distribution for the considered device. This is the final step of the procedure illustrated in Fig. 5.8. Then, as explained also in Fig. 5.6, if the reliability target come out from the RA process has been achieved it is possible to move to the following components. Otherwise, if the estimated parameters do not allow to fulfill the allocated reliability it is necessary to select another component available on the market and repeat the test. This is done until all the components included in the system have been analyzed.

Obviously, performing ALT leads to a significant increase of the design phase duration and increase the cost of the product. Thus, the use of non-constant failure rate could be sustained only in presence of extremely critical components in case of safety-related systems. Otherwise, the overall procedure could not maintain an adequate cost-benefits ratio.

5.9.   Case study A: a numerical example

This section presents a first application of the proposed procedure on a numerical example. The RBD of the system under analysis is illustrated in Fig. 5.9. The system is not a real RBD, it simply represents a numerical example of a generic complex system composed by 5 parallel branches (M = 5). Each branch is composed by a number N_i of components as follow: $N_1 = 3$, $N_2 = 4$, $N_3 = 2$, $N_4 = 1$, $N_5 = 5$.
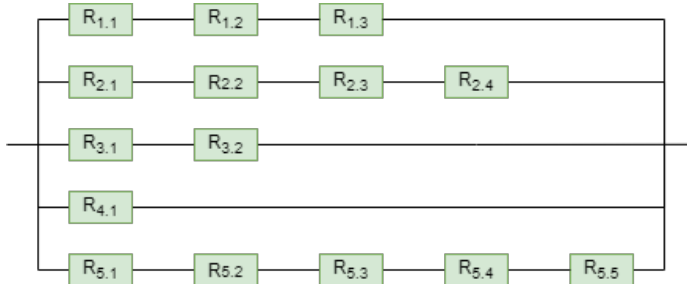
Fig. 5.9. Reliability Block Diagram of Case Study A

The system reliability goal to achieve through the Reliability Allocation procedure is:

$$R_{SYS}^*(t_a)|_{t_a=8760\,h} = 0.99 \qquad (5.103)$$

According to the proposed procedure, the first step required to allocate the component reliability to the system described by case study A is the system decomposition into hierarchical levels, as illustrated in Fig. 5.10.
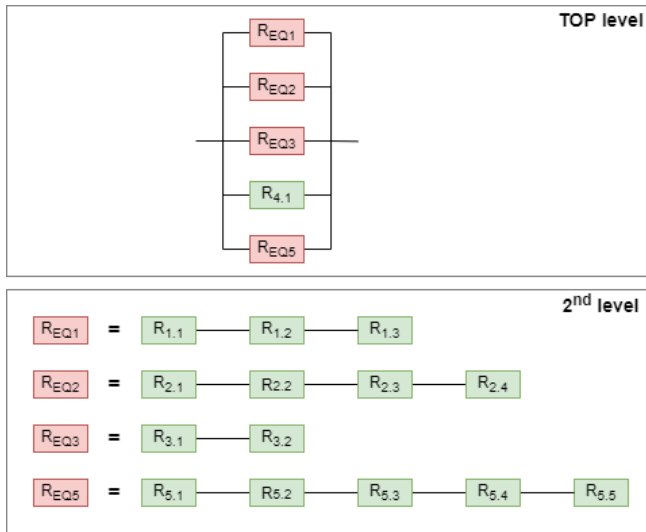
Fig. 5.10. Case study A: System decomposition into two hierarchical levels.

Then, it is necessary to estimate the influence factors and the weight factors of the items composing the system. After a great number of tests and simulations, the MEOWA method has proven to be the best solution among all the methods presented in this work. The auxiliary vector W solves the problem arisen with the other methods to assign an appropriate weight to influence factors with very high/low values. This is possible precisely tuning the situation parameter

α to allocate the proper reliability to the items characterized by extremely high influence factors. Thus, this section applies the proposed method presented in section 5.8. using the influence factors and the weight factor of the 6-parameter MEOWA approach described in section 5.6. TABLE V. VI shows the influence factors of the 6-parameter MEOWA (namely Complexity **C**, Environmental factor **E**, State of the art **A**, Criticality **K**, maintainability **M** and safety **R**) and their assessed values in order to implement the proposed method.

TABLE V. VI

INFLUENCE FACTORS ACCORDING TO 6-PARAMETER MEOWA USED TO IMPLEMENT THE PROPOSED METHOD ON CASE STUDY A.

BRANCH	ITEM	INFLUENCE FACTORS					
		C	E	A	K	M	R
1	1.1	1	4	7	7	7	6
	1.2	1	5	4	8	8	10
	1.3	1	2	10	6	9	3
2	2.1	3	5	9	9	8	8
	2.2	2	7	6	9	8	4
	2.3	4	6	7	10	6	7
	2.4	3	2	6	9	10	9
3	3.1	2	5	10	8	10	3
	3.2	2	6	6	7	6	8
4	4.1	7	3	2	6	10	6
5	5.1	2	4	9	8	6	8
	5.2	2	3	9	10	6	4
	5.3	2	5	9	5	4	3
	5.4	1	2	9	5	8	4
	5.5	1	2	9	8	6	7

After the assessment of the influence factors for the 15 components included in the system (as in the RBD illustrated in Fig. 5.9.) it is necessary to evaluate the influence factors of the equivalent units (i.e. the red blocks in Fig. 5.10.) according to the rules described in section 5.8.2.

The results for the four equivalent units are illustrated in TABLE V. VII (N.B. the fourth branch of the RBD is composed by one single component, thus it is not necessary to identify an equivalent unit of the branch.)

TABLE V. VII

ESTIMATION OF THE INFLUENCE FACTORS FOR THE EQUIVALENT SUBUNITS.

BRANCH	ITEM	INFLUENCE FACTORS					
		C	E	A	K	M	R
1	EQ1	1	5	7	6	8	3
2	EQ2	4	7	7	9	8	4
3	EQ3	2	6	8	7	8	3
5	EQ5	2	5	9	5	6	3

Since the top level is composed by a parallel configuration the proposed procedure for redundant architecture as in section 5.8.3.2. must be used. Thus, the inversion of the influence factor as in equation (5.72) and equation (5.73) has been implemented and reported in TABLE V. VIII.

TABLE V. VIII

INVERTED INFLUENCE FACTORS ACCORDING TO THE PROPOSED PROCEDURE.

BRANCH	ITEM	INFLUENCE FACTORS					
		$\tilde{C}$	$\tilde{E}$	$\tilde{A}$	$\tilde{K}$	$\tilde{M}$	$\tilde{R}$
1	EQ1	10	6	4	5	3	8
2	EQ2	7	4	4	2	3	7
3	EQ3	9	5	3	4	3	8
4	4.1	4	8	9	5	1	5
5	EQ5	9	6	2	6	5	8

The next step is the allocation of the reliability requirements to the top hierarchical level (i.e. the equivalent parallel composed by five branches as in the top side of Fig. 5.10.). Thus, according to the MEOWA method, the influence factor of the equivalent unit must be sorted in descending order, as in TABLE V. IX.

After that, the auxiliary influence factor con be evaluated multiplying the ordered influence factors b_i as in TABLE V. IX. by the 6-parameter auxiliary array w_i as in TABLE V.V. The value of the situation parameter α has been set equal to 0.8 to emphasize the items characterized by high influence factors close to 10. Thus, according to equation (5.77), the inverted situation parameter $\tilde{\alpha}$ for parallel architecture will be set to 0.7. The products $w_i \cdot b_i$, the overall factors Z_k as in equation (5.55) and the normalization factor M_α as in equation (5.56) are reported in TABLE V. X.

TABLE V. IX

ORDERED INFLUENCE FACTORS FOR THE EQUIVALENT SUBUNITS REQUIRED TO EVALUATE
THE WEIGHT FACTOR BY MEANS OF 6-PARAMETER MEOWA.

BRANCH	ITEM	INFLUENCE FACTORS					
		b_1	b_2	b_3	b_4	b_5	b_6
1	EQ1	10	8	6	5	4	3
2	EQ2	7	7	4	4	3	2
3	EQ3	9	8	5	4	3	3
4	4.1	9	8	5	5	4	1
5	EQ59	9	8	6	6	5	2

TABLE V. X

AUXILIARY INFLUENCE FACTORS AND OVERALL FACTOR.

BRANCH	ITEM	$w_1 \cdot b_1$	$w_2 \cdot b_2$	$w_3 \cdot b_3$	$w_4 \cdot b_4$	$w_5 \cdot b_5$	$w_6 \cdot b_6$	Z_k
1	EQ1	3.4749	1.9182	0.9927	0.5708	0.3151	0.16310	**7.4348**
2	EQ2	2.4325	1.6784	0.6618	0.4566	0.2363	0.10870	**5.5743**
3	EQ3	3.1274	1.9182	0.8272	0.4566	0.2363	0.1631	**6.7289**
4	4.1	3.1274	1.9182	0.8272	0.5708	0.3151	0.0544	**6.8131**
5	EQ5	3.1274	1.9182	0.9927	0.6850	0.3939	0.1087	**7.2258**
								$M_\alpha =$ **33.7769**

After that, the values in TABLE V. X. can be used to evaluate the weight factor
according to equation (5.56) (MEOWA method) and then the allocated
reliability of the five branches using equations (5.74)-(5.77) specifically
proposed for parallel architectures. The results are included in TABLE V. XI.

TABLE V. XI

WEIGHT FACTORS AND ALLOCATED RELIABILITY TO THE FIVE PARALLEL BRANCHES.

BRANCH	ITEM	WEIGHT FACTOR ω_i	ALLOCATED RELIABILITY $R_i^*(t_a)$
1	EQ1	0.220114	0.637112
2	EQ2	0.165034	0.532337
3	EQ3	0.199215	0.600452
4	4.1	0.201709	0.605014
5	EQ5	0.213928	0.626627

This phase concludes the first iteration of the proposed method. Considering the branch number 4, the result included in TABLE V. XI. is directly the reliability to be allocated to component $R_{4.1}$.

Then, it is necessary to repeat the procedure to the 2nd hierarchical level in order to assign the reliability of the equivalent units among the components that make up each branch.

Thus, firstly the reliability of the branch number #1 $R_{EQ1}^* = 0.637112$ become the target reliability of a second iteration in which the reliability values are assigned to component $R_{1.1}$ $R_{1.2}$ and $R_{1.3}$ considering a series configuration.

Then, quite similar operation will lead to the assessment of the reliability requirements to each branch. For the sake of brevity, the complete assessment at 2nd hierarchical level is not fully reported.

As an example, the different steps of the application to branch #3 are reported in TABLE V. XII where the reliability is calculated considering the reliability of the equivalent unit $R_{EQ3}^* = 0.600452$.

TABLE V. XII

PROPOSED ITERATIVE PROCEDURE: APPLICATION TO BRANCH #3 OF CASE STUDY A.

ITEM	C	E	A	K	M	R
3.1	2	5	10	8	10	3
3.2	2	6	6	7	6	8

ITEM	b_1	b_2	b_3	b_4	b_5	b_6
3.1	10	10	8	5	3	2
3.2	8	7	6	6	6	2

ITEM	$w_1 \cdot b_1$	$w_2 \cdot b_2$	$w_3 \cdot b_3$	$w_4 \cdot b_4$	$w_5 \cdot b_5$	$w_6 \cdot b_6$
3.1	4.7812	2.5475	1.0859	0.3616	0.1156	0.0411
3.2	3.8250	1.7833	0.8144	0.4339	0.2312	0.0411

ITEM	Z_k	M_α	WEIGHT FACTOR ω_i	RELIABILITY $R_i^*(t_a)$
3.1	8.9329	16.0618	0.556160	0.753006
3.2	7.1289	16.0618	0.443840	0.797406

Finally, TABLE V. XIII shows the reliability allocation results using the developed iterative approach. As a result, lower reliability is allocated to components with high influence factors.

TABLE V. XIII
OUTPUT OF THE PROPOSED APPROACH FOR CASE STUDY A (WEIGHT FACTORS IN COMPLIANCE WITH 6-PARAMETER MEOWA).

BRANCH	ALLOCATED RELIABILITY				
1	0.878770	0.849513	0.853435		
2	0.852271	0.861832	0.856324	0.846346	
3	0.753006	0.797406			
4	0.605013				
5	0.906414	0.903343	0.921514	0.913622	0.908997

This case study highlights the huge benefits that are achievable using the conditional parameter, in particular when RA procedures are assessed during design phase with imprecise, incomplete or uncertain pieces of information.

The tool calculates also the failure rate to be apportioned to each item, assuming that all the blocks of the system are single elements and not subsystems in turn. Fig. 5 shows an example of the tool outcomes containing the simulation results for MEOWA technique.

5.10. Case study B: sensors unit of an HVAC

In this section the proposed RA iterative approach for complex system has been applied to a sensor unit of an HVAC system for high-speed trains (for more detail see section 2.2.). The RBD of the system under analysis is illustrated in Fig. 5.11.
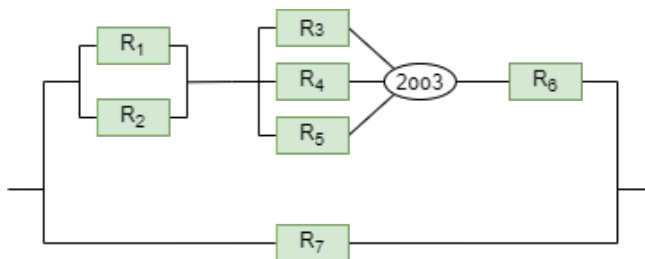
Fig. 5.11. Reliability Block Diagram of Case Study B: safety system of an HVAC unit.

The system is basically composed by two redundant branches. The top branch includes two temperature sensors in parallel configuration (identified by reliability R_1 and R_2) and three pressure transmitters in 2oo3 configuration (identified by reliability R_3 R_4 and R_5). This branch also includes a series element called voter unit used to elaborate the output of the pressure sensors in 2oo3 architecture. The voter (identified by reliability R_6) must diagnose any anomalies in the sensors output and guarantee the proper output in case of failure of one sensor. An example of application of voter system is illustrated in Fig. 5.12 considering three sensors S1, S2 and S3. In such case, the output of the 2oo3 architecture is equal to the intermediate value among the output of the three sensors. In case of failure of one single sensor (fail-to-low condition), the voter detect the failure and reconfigure the output which continue to be reasonable despite the failure of one sensor.
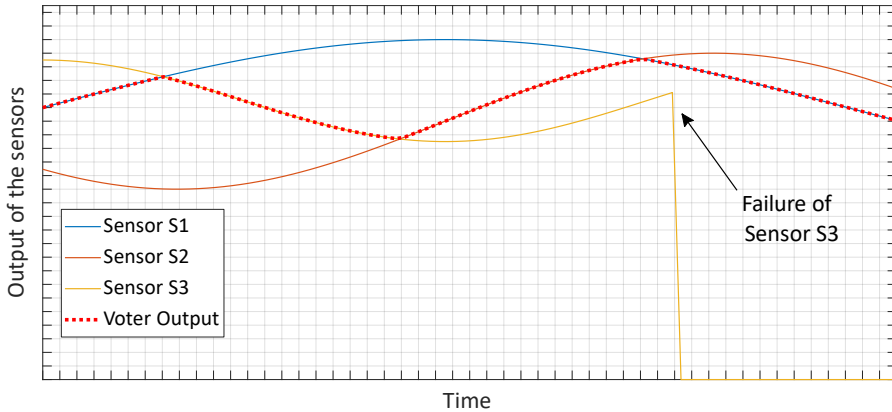
Fig. 5.12. Example of application of voting system in 2oo3 architecture.

Moving back to the RBD in Fig. 5.11., the second branch is composed by a single unit used for redundant and safety issues. Component R_7 is a safety device able to measure temperature and pressure of the refrigerant gas and communicate the measurement data to the central unit. In case of failure of the main sensors included in the top branch, the safety device R_7 provides redundant information to ensure continuity of service.

The system reliability goal to achieve through the Reliability Allocation procedure has been set as 95% reliability at the end of the HVAC life cycle, which is estimated after 20 years.

$$R_{SYS}{}^*(t_a)|_{t_a=20 \ years} = 0.95 \qquad (5.104)$$

125

The first step required to allocate the component reliability to the sensor unit of the HVAC under analysis is the system decomposition into hierarchical levels, as illustrated in Fig. 5.13. In this case, three different levels have been identified.

The top level is a simple parallel configuration between the first branch (equivalent item EQ1 which stands for the temperature and pressure sensors) and the safety device R_7.

Then, the second level includes the series configuration between the equivalent item EQ2, the equivalent item EQ3 and the voter unit R_6.

Finally, the third level is used to model the two parallel temperature sensors and the 2oo3 configuration composed by three pressure transmitters.
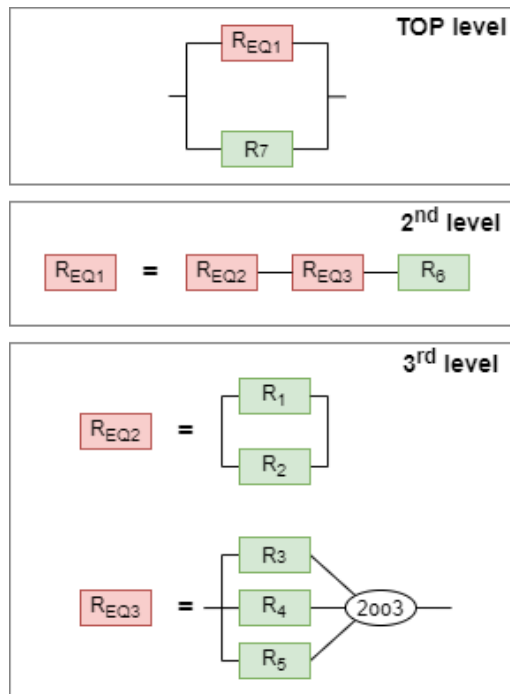
Fig. 5.13. System decomposition of case study B into three hierarchical levels.

Also in this case, the influence factors of the 6-parameter MEOWA method have been used to evaluate the weight factors of the components. The complete assessment of the influence factors is reported in TABLE V. XIV.

Note that the same factors have been assigned to items R_3, R_4, and R5 because they are considered in 2oo3 configuration.

TABLE V. XIV

INFLUENCE FACTORS ACCORDING TO 6-PARAMETER MEOWA USED TO IMPLEMENT THE PROPOSED METHOD ON CASE STUDY B.

ITEM	INFLUENCE FACTORS					
	C	E	A	K	M	R
R_1	6	5	10	4	10	4
R_2	8	5	6	5	6	5
R_3 - R_4 - R_5	5	5	7	4	6	6
R_6	3	2	3	2	4	2
R_7	7	4	2	1	2	1

The estimation of the influence factors for the equivalent subunits according to the proposed model as in equations (5.62)-(5.68) is reported in TABLE V. XV.

TABLE V. XV

ESTIMATION OF THE INFLUENCE FACTORS FOR THE EQUIVALENT SUBUNITS.

LEVEL	ITEM	ITEM USED TO ASSESS THE FACTORS	INFLUENCE FACTORS					
			C	E	A	K	M	R
2nd level	EQ2	R_1 - R_2	8	5	8	4	8	4
	EQ3	R_3 - R_4 - R_5	5	5	7	4	6	6
Top level	EQ1	R_{EQ2} - R_{EQ3} - R_6	8	5	6	2	7	2

Following the procedure illustrated in the previous case study (section 5.9), the item reliability has been allocated at the top hierarchical level (i.e. parallel configuration between equivalent unit EQ1 and component R7) using the proposed approach for parallel configuration as in section 5.8.3.2. The results varying the situation parameter α are illustrated in Fig. 5.14 where the reliability allocated to the safety unit R_7 and to the top branch EQ1 are compared with system reliability goal (red dashed line).

As it is possible to see in Fig. 5.14, the extremely low influence factors of the safety unit R_7 led to higher reliability with respect to the reliability of the equivalent unit EQ1 regardless the value of the situation parameter α.

The following step is the allocation of reliability requirements to the 2nd hierarchical level using the results of the equivalent unit EQ1 as input target. In this case, model for series configuration has been implemented as in section 5.8.3.1. The results achieved varying the situation parameter α are illustrated in Fig. 5.15.
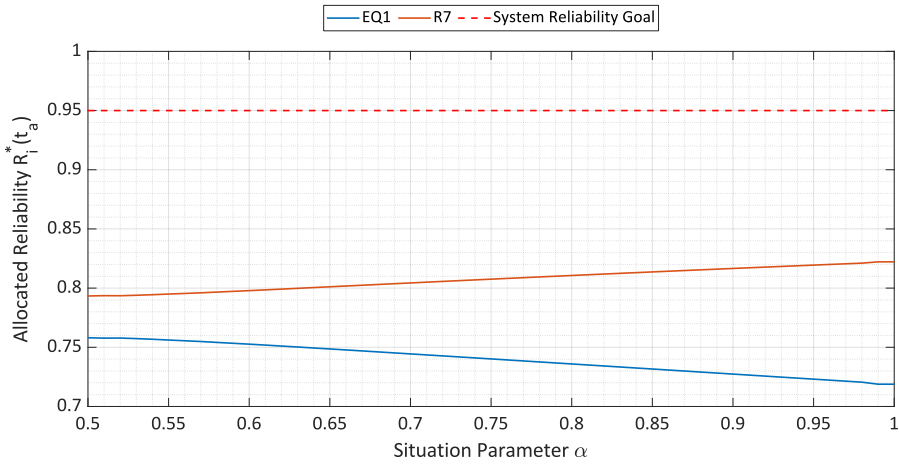
Fig. 5.14. Reliability allocated at the top hierarchical level of case study B varying the situation parameter α.
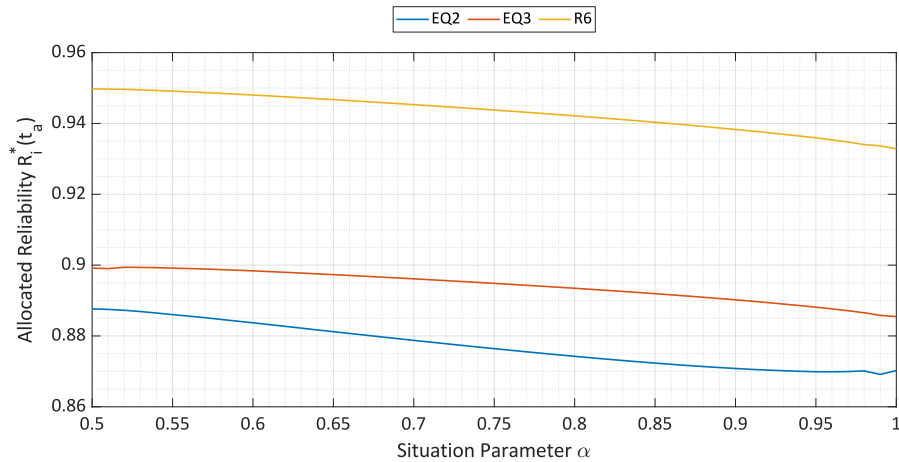
Fig. 5.15. Reliability allocated at the second hierarchical level of case study B varying the situation parameter α.

Finally, the procedure is repeated at the 3rd hierarchical level considering the two different architectures left.

Firstly, the proposed model for parallel configuration as in section 5.8.3.2. has been used to allocate reliability requirements to components R_1 and R_2 (parallel temperature sensors) starting from the reliability results achieved for the equivalent unit EQ2.

Then, the proposed model for k-ot-of-N configuration as in section 5.8.3.3. has been used to allocate reliability requirements to the 2oo3 architecture composed by the pressure transmitters R_3, R_4 and R_5 starting from the results of the equivalent unit EQ3.

The overall results achieved for the seven considered items varying the situation parameter α are illustrated in Fig. 5.16. Note that the reliability of the three pressure transmitters has been illustrated using a single line (yellow trend). This is due to the fact that the proposed RA procedure assigns the same reliability to all the items making up a 2oo3 configuration as required by the initial hypotheses of the k-out-of-N architectures.

What stands out from Fig. 5.16 is the extremely high reliability values assigned to both the voter unit (R_6) and the safety instrumentation unit (R_7). This is due to the very low influence factors assigned to both components.
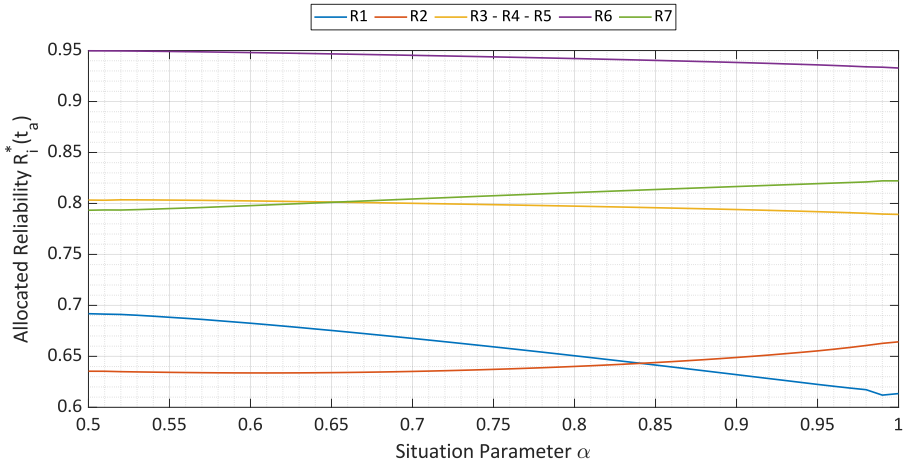
Fig. 5.16. Results of the reliability allocation procedure to Case study B considering the proposed models.

The reliability results varying the situation parameter as in Fig. 5.16 are extremely helpful to designer during the allocation process. However, at the end of the procedure is necessary to provide a reliability at a certain time. In this case, according to equation (5.104) the allocation time has been set equal to $t_a = 20 years = 175200\,h$.

Considering a situation parameter $\alpha = 0.85$ the reliability allocated to each component $R_i^*(t_a)$ is included in TABLE V. XVI.

TABLE V. XVI

RESULTS OF THE ALLOCATION PROCESS FOR CASE STUDY B: RELIABILITY VALUES.

ITEM	ALLOCATED RELIABILITY AT $t_a =$ 20years
R_1	0.6414731
R_2	0.6439310
R_3 - R_4 - R_5	0.7957998
R_6	0.9403383
R_7	0.8136760

Then, according to the final step of the proposed procedure (as in section 5.8.4) it is necessary to estimate the failure rate of the components making up the system. The temperature sensors (R_1 and R_2) and the pressure transmitter (R_3, R_4 and R_5) are electronic components that can be easily described by an exponential failure distribution. Similarly, also the voter unit can be approximated to a constant failure rate item. Thus, the failure rate of such items can be estimated using equation (5.87). The results achieved for these components are reported in TABLE V. XVII. The unit of measurement of the failure rate is FPMH (Failure Per Million Hours).

TABLE V. XVII

ALLOCATED FAILURE RATE TO COMPONENTS OF CASE STUDY B THAT FOLLOW THE EXPONENTIAL FAILURE DISTRIBUTION.

ITEM	ALLOCATED FAILURE RATE
R_1	2.5341783 FPMH
R_2	2.5123499 FPMH
R_3 - R_4 - R_5	1.3036969 FPMH
R_6	0.3511166 FPMH

After that, it is necessary to find a component on the market that allows to achieve the requirements as in TABLE V. XVII. Taking the temperature and pressure sensors as an example, the certification of the component failure rate under exponential failure distribution of many distributors are available on the Safety Automation Equipment List (SAEL) of the Exida certification company. Quite the opposite, the safety unit used as redundant source of information about both temperature and pressure data is a complex equipment that could

130

be better described by a Weibull failure distribution. Thus, according to the proposed procedure as in section 5.8.4 an accelerated life test plan is required to ensure that the allocated reliability of the unit R_7 as in TABLE V. XVI will be satisfied.

5.11. Case study C: lube oil console for Oil&Gas systems

In this section the proposed iterative approach has been applied to a lube oil console for Oil&Gas systems (for more information about the case study, see section 2.5.). In this case, the impacts of minor components (such as piping, wires, connectors and alike) on system reliability have been neglected due to their relatively low probability of failure with respect to the other items.

The reliability block diagram of the system under test has been illustrated in Fig. 2.9 and it is not reported here for the sake of brevity. The system is composed by 24 different components, as follow:

- Four differential pressure transmitters, three located in the oil tank making up a 2oo3 configuration (PDIT) and one located in filter section (PDIT_F).
- One level sensor (LIT).
- Three temperature sensors, one located in the oil tank (TIT) and other two located in the temperature regulation unit (TIT_1 and TIT_2).
- One heater.
- Two pumps (MAIN PUMP and AUX PUMP).
- Four motors (MAIN MOTOR, AUX MOTOR, STD-BY MOTOR and STD-BY MOTOR_2).
- Two pressure safety valves (MAIN PSV and AUX PSV).
- One absolute pressure sensor (PIT).
- Two pressure control valves (PCV_1 and PCV_2).
- One temperature control valve (TCV).
- Two filters in cold standby architecture (MAIN FILTER and STD-BY FILTER).
- One Fan.

The system reliability goal to achieve through the Reliability Allocation procedure has been set as 90% reliability after 5 years of use.

$$R_{SYS}{}^{*}(t_a)|_{t_a=5\ years} = 0.9 \qquad (5.105)$$

In compliance with the proposed iterative approach, the first step of the procedure consists in the decomposition of the system RBD into different hierarchical levels. Each level must be assembled by a unique reliability architecture, such as series, parallel, standby or k-out-of-n. The decomposition of the lube oil under test is illustrated in Fig. 5.17, highlighting four levels.
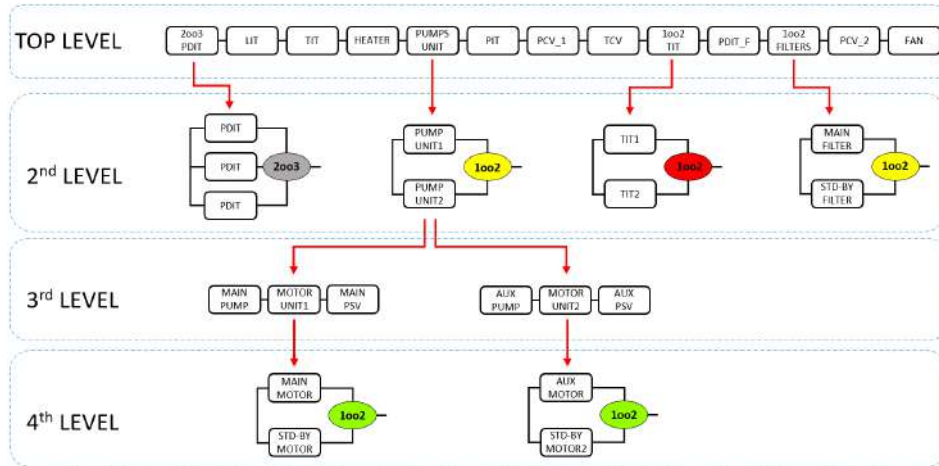
Fig. 5.17. System decomposition of case study C into four different hierarchical levels.

The top level corresponds with the equivalent series architecture of the system under test, which means that each redundant block is grouped in a single equivalent series item. Then, the redundancies grouped in the top level are decomposed in the 2nd level. For instance, the 2oo3 PDIT item in the top level become the actual 2-out-of-3 architecture in the 2nd level. Quite the same the 1oo2 TIT and the 1oo2 FILTERS items. Instead, the pump unit is a more complex architecture that requires four decomposition levels. The 2nd level is composed by a cold standby architecture including the Pump Unit 1 (main unit) and the Pump Unit 2 (standby unit). Then, each unit is divided into a series configuration of three components: motor, pump and PSV. In particular, the Pump Unit 1 is composed by the main pump, the main PSV and the motor unit 1, while the Pump Unit 2 is composed by the auxiliary pump, the auxiliary PSV and the motor unit 2. Finally, the 4th level includes the decomposition of the motor units into a warm standby configuration each one including an active and a standby motor.

Seven influence factors (namely Complexity **C**, Environmental factor **E**, State of the Art **A**, Operative Time **T**, maintainability **M**, criticality **K** and safety

R) have been evaluated for each one of the components included in the RBD of the system under test based on expert's judgments. Using these factors, it is possible to allocate the component reliability using many existing techniques, such as FOO, arithmetic AWM, 4-parameter MEOWA and 6-parameter MEOWA. The complete assessment report is included in TABLE V. XVIII.

TABLE V. XVIII

INFLUENCE FACTORS USED TO ASSESS THE WEIGHT FACTORS OF EACH COMPONENT INCLUDED IN THE CASE STUDY C.

ITEM	C	E	A	T	M	K	R
PDIT	5	10	5	10	6	4	9
LIT	4	10	5	10	6	2	8
TIT	5	10	5	10	6	2	8
Heater	1	10	5	6	6	4	7
Main Pump	9	6	5	8	10	4	2
Main Motor	7	2	5	7	8	5	3
Std-by Motor	6	2	5	3	8	4	3
Main PSV	5	8	5	8	4	4	4
Aux Pump	9	4	5	2	10	1	1
Aux Motor	7	2	5	2	8	4	2
Std-by Motor 2	6	2	5	1	8	1	2
Aux PSV	5	4	5	2	4	1	4
PIT	5	8	5	10	3	2	8
PCV_1	3	8	5	10	4	1	8
TCV	3	8	5	10	3	2	6
TIT_1	5	8	5	10	3	5	9
TIT_2	5	8	5	10	3	5	9
PDIT_F	5	8	5	10	3	2	8
Main Filter	2	6	5	8	2	9	5
Std-by Filter	2	6	5	2	2	7	5
PCV_2	3	8	5	10	4	1	8
FAN	3	2	5	7	3	4	7

Analyzing the main motor and the standby motor it is easy to understand how the allocation is weighted in case of standby redundancy. The main motor is a more complex item working for longer period; therefore it is characterized by a higher complexity **C** and a higher Operating time **O** with respect to the standby motor. Moreover, it has also a higher criticality **K** which means it is a less critical component due to the presence of the standby unit. Such considerations have been drawn in order to extend the applicability of the RA process to standby redundancies according to the proposed method as in section 5.8.3.4.

The influence factors of the equivalent units can be estimated considering the principle of the "worst-case scenario" as detailed illustrated in section 5.8.2. The results of the assessment are included in TABLE V. XIX.

TABLE V. XIX
INFLUENCE FACTORS OF THE EQUIVALENT UNITS: CASE STUDY C.

LEVEL	UNIT	ITEM USED TO ASSESS THE FACTORS	C	E	A	T	M	K	R
3rd	Motor Unit 1	Main Motor - Std-by Motor	7	2	5	7	8	4	3
3rd	Motor Unit 2	Aux Motor - Std-by Motor2	7	2	5	2	8	1	2
2nd	Pump Unit 1	Main Pump - Motor Unit1 - Main PSV	9	8	5	8	7	4	2
2nd	Pump Unit 2	Aux Pump - Motor Unit2 - Aux PSV	9	4	5	2	7	1	1
TOP	2oo3 PDIT	PDIT - PDIT - PDIT	5	10	5	10	6	4	9
TOP	Pumps Unit	Pump Unit 1 - Pump Unit 2	9	8	5	8	7	1	1
TOP	1oo2 TIT	TIT_1 - TIT_2	5	8	5	10	3	5	9
TOP	1oo2 Filters	Main Filter - Std-by Filter	2	6	5	8	2	7	5

The following steps require to calculate the weight factors and the allocated reliability to the component included in the top hierarchical level. The procedure has been repeated considering the weight factors of four different approaches:

- FOO method based on Complexty **C**, Environmental factor **E**, state of the art **A** and operative time **O**.
- 4-parameter MEOWA based on the same influence factor as FOO method.
- Arithmetic AWM based on Complexty **C**, Environmental factor **E**, state of the art **A,** Maintainability **M**, Criticality **K** and Safety **R.**
- 6-parameter MEOWA based on the same influence factor as arithmetic AWM.

The weight factors estimated for each hierarchical level in case of Arithmetic AWM and FOO methods are included in TABLE V. XX.

TABLE V. XX

WEIGHT FACTORS OF ARITHMETIC AWM AND FOO ASSESSED FOR DIFFERENT LEVELS.

Top level			2nd level				3rd level				4th level			
Item	AWM ω_i	FOO ω_i	Higher-level	Item	AWM ω_i	FOO ω_i	Higher-level	Item	AWM ω_i	FOO ω_i	Higher-level	Item	AWM ω_i	FOO ω_i
2oo3 PDIT	0.316901	0.122130	2oo3 PDIT	PDIT	0.333333	0.333333								
LIT	0.112676	0.097704												
TIT	0.140845	0.122130												
Heater	0.049296	0.014656												
Pumps Unit	0.016901	0.140694	Pumps Unit	Pump Unit 1	0.212598	0.125000	Pump Unit 1	Main Pump	0.525292	0.508236				
PIT	0.056338	0.097704		Pump Unit 2	0.787402	0.875000		Motor Unit 1	0.163124	0.115294	Motor Unit 1	Main Motor	0.406780	0.285714
PCV_1	0.022535	0.058622						Main PSV	0.311284	0.376471		Std-by Motor 2	0.593220	0.714286
1oo2 TIT	0.158451	0.097704	1oo2 TIT	TIT1	0.500000	0.500000								
TCV	0.025352	0.058622		TIT2	0.500000	0.500000	Pump Unit 2	Aux Pump	0.398230	0.514286				
PDIT	0.056338	0.097704						Motor Unit 2	0.247788	0.200000	Motor Unit 2	Aux Motor	0.358974	0.418605
1oo2 Filters	0.007042	0.023449	1oo2 Filters	Main Filter	0.333333	0.250000		Aux PSV	0.353982	0.285714		Std-by Motor 2	0.641026	0.581395
PCV_2	0.022535	0.058622		Std-by Filter	0.666666	0.750000								
FAN	0.014789	0.010259												

Obviously, it is important to take into account that in case of series configuration the weight factor could be estimated directly using the equations proposed in each method, while in case of parallel configuration equations (5.69) - (5.70) must be used. Moreover, the 2oo3 configuration has been dealt with the method proposed in section 5.8.3.3. while the standby redundancies have been dealt with during the influence factors assessment as required by the method proposed in section 5.8.3.4.

Using the reliability target in equation (5.105) it is possible to calculate the reliability of the items composing the top hierarchical level simply applying the weight factors in TABLE V. XX to equation (5.71) since the top level is a series configuration. Then, in case of redundancies, the results achieved at the previous steps are used as reliability target for the evaluation of the component reliability at the 2nd level. In this case, it is important to evaluate the allocated reliability using the correct formula, such as Equation (5.71) in case of series architecture, equations (5.74) - (5.76) in case of parallel configuration or standby redundancies, and equations (5.84) - (5.85) in case of k-out-of-n configuration. Then, the same approach is repeated consecutively to the subsequent hierarchical levels, every time considering the results of the next higher level as input reliability target.

Fig. 5.18 shows the results of the procedure applied using the reliability models based on four influence factors, i.e. FOO and 4-parameter MEOWA. Quite the same, Fig. 5.19 shows the results of the procedure applied using the reliability models based on six influence factors, i.e. Arithmetic AWM and 6-parameter MEOWA.
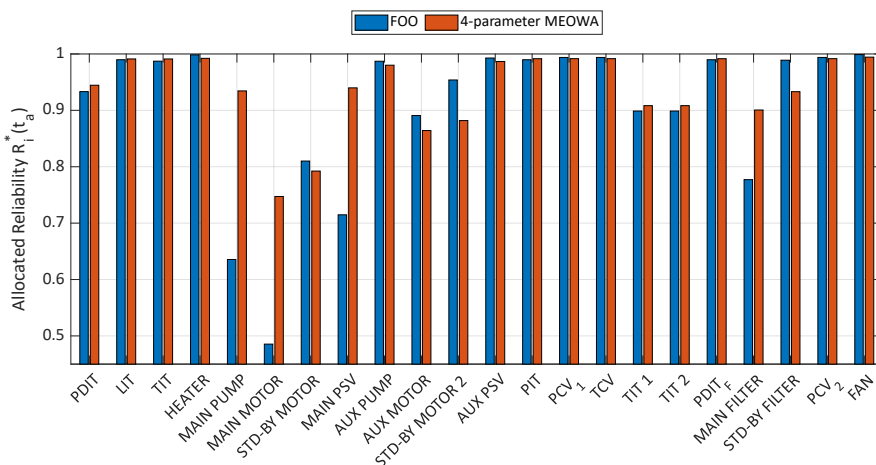
Fig. 5.18. Reliability allocated using the proposed method to the components that make up the lube oil console by means of FOO and 4-parameter MEOWA.
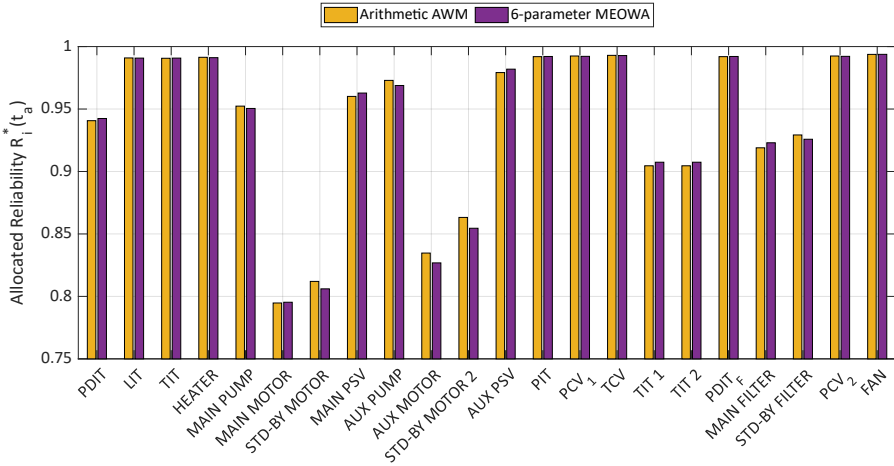
Fig. 5.19. Reliability allocated using the proposed method to the components that make up the lube oil console by means of Arithmetic AWM and 6-parameter MEOWA.

The FOO model cannot allocate the correct reliability to some critical components, such as the main motor, the main pump and the main PSV. In fact, using this model the impact of a great standby redundancy unit lead to untrustworthy reliability results for the main unit. Quite the opposite, MEOWA and AWM methods provides comparable results.

Finally, it is important to consider that there is a large uncertainty associated with known values of reliability parameters in commercially available devices. The accelerated test (using for example temperature, vibration or humidity stress factors) proposed as final loop of the procedure presented in this work could provide more accurate reliability data about commercial components available on the market.

5.12. Final remarks

The first part of this section contains a complete survey of Reliability Allocation techniques available in literature. The classical RA approaches such as Equal, ARINC, AGREE, FOO, Bracha, Karmiol and AWM have been discussed thoroughly in separate subsections. Then, some of the innovative approaches recently published in literature have been studied and analyzed, with an in-depth analysis of the MEOWA method.

The main criticalities of all the RA procedures available in literature is the presence of two initial assumptions not always reasonable: the series configuration of the system RBD and the exponential failure distribution of all the components.

Trying to fill this gap, the second part of this section presents an innovative iterative procedure which is able to overcome both initial hypothesis and thus it can be applied to any kind of complex system. The proposed method is a general procedure that use the weight factor of the other methods available in literature. It simply provides a set of guidelines to extend the applicability of the other techniques to any kind of complex system.

The first test bench of the proposed method was the standard parallel architecture, and it shows some interesting results. The ARINC and AGREE techniques turn out not to be suitable for this kind of application (due to some mathematical restrictions in the weight factors definition) so their application continue to be limited to series configurations. On the other hand, all the other approaches such as FOO, Bracha, AWM, Karmiol and MEOWA techniques could be easily applied to parallel architectures introducing the approach presented in section 5.8.3.2. Quite similarly, the application of such techniques could be extended also to standby redundancies following the guidelines proposed in section 5.8.3.4. Finally, the proposed procedure allows to extend the applicability of the RA approach also to k-out-of-N configuration as described in section 5.8.3.3. The final loop of the procedure presented in this chapter allow to extend the applicability of all the techniques available in literature to component characterized by a non-constant failure rate by means of accelerated life tests performed on the selected components.

After the comparison between the weight factors of the allocation methods available in literature, the MEOWA technique turned out to be the best solution since it solves the problems of the weight factor assessment arisen in the other techniques.

In conclusion, the optimal Reliability Allocation procedure can be summarized as follows:

1. System decomposition into hierarchical levels as in section 5.8.1.
2. Assessment of the influence factors of the components making up the system.
3. Estimation of the influence factor for the equivalent units included in the different hierarchical levels following the principle of the worst-case scenario as in section 5.8.2.
4. Assessment of the weight factors according to MEOWA technique as a function of the situational parameter α as in section 5.6.

5. Evaluation of the component reliability at the top hierarchical level starting from the system reliability goal. The proper equations should be used according to the system configuration as in section 5.8.3.

6. Repeat the previous step to evaluate the component reliability at the lower hierarchical levels starting from the reliability results achieved at the level above. The proper equations should be used according to the system configuration as in section 5.8.3.

7. Selection of the most suitable component available in the market and evaluation of the component failure rate by means of proper equations (in case of exponential distribution) or by means of accelerated life test (in case of non-constant failure rate). If the reliability target is not achieved, another component in the market should be used.

The final part of the chapter presents the implementation of the proposed procedure to three different applications:

- Case study A - it is a numerical example composed by 5 parallel branches, each one including a different number of series items.
- Case study B - it is a sensors unit used to monitor temperature and pressure of the gas used in an HVAC system for high-speed train. The analyzed system includes several redundancies: two parallel temperature sensors, three pressure transmitters mounted in 2oo3 configuration by means of a voting unit and a safety unit that directly provides redundant information about temperature and pressure.
- Case study C - it is a lube oil console for gas turbine. The system is basically a series chain of different subunits, each one including different redundant architectures, such parallel, k-out-of-N, Cold standby and Warm standby.

The analysis of the three case study proves the effectiveness of the proposed procedure highlighting the advantages of the method and emphasizing how it is possible to overcome the initial hypotheses required by every other allocation method.

CHAPTER 6

ENVIRONMENTAL STRESS SCREENING

The first part of this chapter presents the development of a customized test plan and test bed for characterization of Inertial Measurement Units under Environmental Stress Screening. The reliability and metrological performances of the IMUs have been characterized introducing adequate figures of merits to study the behavior of the devices in time and frequency domains. The second part of this chapter presents a test plan for characterization of DC-DC converters under harsh environment. Also in this case, the reliability and the electrical performances of the device have been investigated using different parameters. The results of both case studies prove how it is possible to integrate an ESS test plan within a Life Cycle Reliability procedure to efficiently and effectively improve the performances of the system through its entire life cycle. [1, 2]

---

[1] The test plan for characterization of the IMUs has been published as:

- "D. Capriglione et al., "Experimental Analysis of Filtering Algorithms for IMU-Based Applications Under Vibrations," IEEE Trans. Instrum. Meas., vol. 70, Article No. 3507410, 2021".

- "D. Capriglione et al., "Development of a test plan and a testbed for performance analysis of MEMS-based IMUs under vibration conditions," Measurement, vol. 158, Article No. 107734, 2020".

- "D. Capriglione et al., "Performance Analysis of MEMS-based Inertial Measurement Units in terrestrial vehicles", Measurement, Vol. 186, Article No. 1102337, 2021".

[2] The characterization of the DC-DC converters has been published as "G. Patrizi et al., "Electrical Characterization under Harsh Environment of DC-DC Converters used in Diagnostic Systems", IEEE Trans. Instrum. Vol. 71, Article No. 3504811, 2022."

6.1. Introduction: the importance of screening test in design for reliability

Accelerated Life Tests and aging tests are excellent methods of learning about the design of equipment over a relatively short span of time and affecting that design prior to committing the program to production. Once production begins, other types of test procedures can provide important intelligence on how well the product has been built and tested. This is the reason why screening tests are sometimes included as final part of design for reliability procedures. Screening is defined as the process carried out to detect and remove non-conforming items, or those susceptible to early life failure. When screening plans are included in the manufacturing process, then, they should be performed on all the equipment being produced in order to stress the product so that out-of-specification weaknesses will be exposed.

The stresses are chosen to address possible failure modes found in a manufacturing process—modes such as loose fasteners, improper solder joints or weldments, missing hardware, defective components, and improper solder joints. Typically for electronic and mechanical devices, temperature cycling and random vibration up to specification level are used to uncover possible manufacturing defects.

In other words, the producer performs the screening exposing all the produced components to certain level of environmental and/or electrical stress so that the customer doesn't need to do so in use.

But why screening tests are so important in the context of a design for reliability procedure?

The answer to such question is quite simple and straightforward. Any findings coming out from a screening process are generally expensive, but not as expensive as returns and unsatisfied customers. In fact, screening test not only keeps potential problems out of the customer's hands, but they also allow continuous improvements of product quality and system reliability.

Among the different screening procedures, environmental test plays a central role in design for reliability approaches. In fact, designers have to take into account that customers will use the product somewhere and somehow. That implies there will be a set of environmental and use conditions or stresses. Hence, the designed product should operate as expected by the customer where and how the customer expects the product to work.

There are a few ways to approach evaluating if the developed product will work within the expected customer environment and under the customer's use conditions. Environmental screening allows to select specific failure mechanisms

of interest and thus to identify stress conditions related to those specific failure mechanisms. Then, the product can be tested under the identified test conditions in order to simulate customer environments and evaluate if early failure will be exposed by the actual operating conditions in which the customer will install the developed equipment.

For these reasons, environmental screening procedures have been studied and discussed in this work as part of the proposed Reliability Life Cycle.

6.2. Environmental Stress Screening: an overview

The process for detecting flaws (i.e. imperfections that could result in failures) by applying environmental and/or operational stresses to precipitate them as detectable failures is usually called Environmental Stress Screening (ESS) [191] or Reliability Stress Screening (RSS) [192].

ESS is the tailored application of electrical and environmental stresses to electronic parts, module, units and systems to identify and eliminate defective, abnormal or marginal parts and manufacturing defects. ESS is composed by a process or a series of process in which environmental stimuli, such as rapid thermal cycling and random vibration, are applied to the device under test.

The processes of ESS or RSS are used to detect flaws in a population of items, usually components, leading to the subsequent removal of these flawed items from the population. The removal of such components facilitates rapid achievement of the reliability level expected for the population over the useful life.

ESS is a common and widely-conducted practice used to eliminating latent defects due to infant mortalities in electronic equipment (see Fig. 6.1) [148], [191], [193]–[196].

Fig. 6.1 illustrates the classical trend of a component failure rate (usually called the bathtub curve) which is divided into three sections [131], [183]:

- Early failure or infant mortality: in this phase failure are caused by intrinsic material defects, design or assembly mistakes and so on.
- Random failure: this section is also called useful life, and the failure rate trend is approximately constant.
- Wear-out failure: in this phase, the failure rate increases due to fatigue and material deterioration.
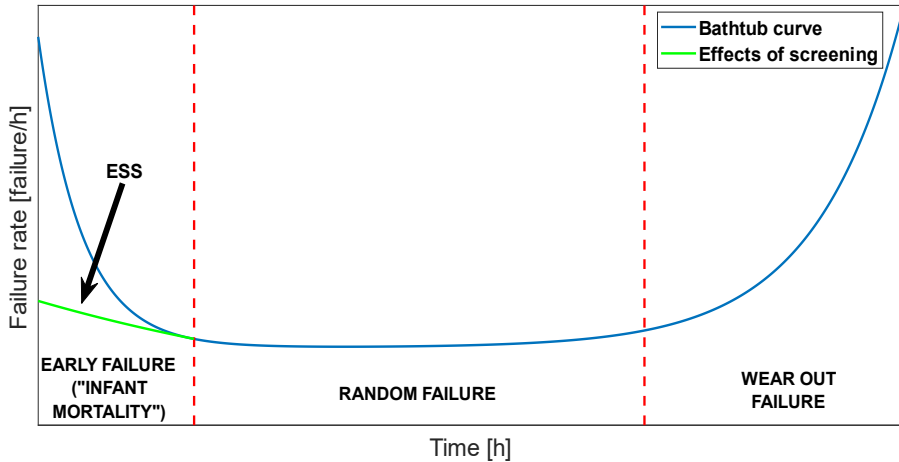
Fig. 6.1. Effects of environmental stress screening on the bathtub curve.

Electronic components are adequately described using a constant failure rate model (i.e., exponential failure distribution). This is due to the fact that such type of items is characterized by a long-time useful life, which is predominant respect to the other two sections. This is a basic assumption for many reliability approaches existing in literature, like reliability prediction (see for instance [146], [147], [156]), Reliability Block Diagram (RBD) [197], reliability allocation (as detailed described in section 5), reliability importance, and so on.

As a matter of fact, fatigue is not a real failure mode for electronic components because wear-out will occur when the item will be already obsolete, so the last zone of the bathtub curve could be easily neglected for this type of device.

Quite the opposite, the infant mortality section could not absolutely be neglected because intrinsic defects due to the manufacturing process are very common, especially in low-cost commercial components. Therefore, environmental stress screening must be used to evaluate design and materials problems and consequently decrease the failure rate in the first zone of the bathtub curve (see the green trend in Fig. 6.1).

ESS is typically conducted on 100% of manufactured products to accelerate early failures in the most cost-effective solution. It can identify failure modes that usually are not discovered through simple inspection or testing, such as:

- Parameter drifts;
- Shorts and open on the electronic board;
- Incorrect installation;
- Wrong part installation;
- Contaminated part;

- Hermetic seal failure;
- Foreign material contamination;
- Cold solder joints;
- Defective parts.

The screening level should not exceed the design limits, but they must be of sufficient strength to precipitate failures due to weak parts and manufacturing defects at the earliest time such that corrections are most cost-effective.

Considering the entire population of generic manufactured products just came out of the production process. The robustness of these population is usually distributed according to a bimodal normal probability density function. The highest peak stands for the strong population (i.e. subset of the total population of items made up of non-weak items), the items that belongs to this group generally fail because of random failures or wear out failures. The lowest peak represents the intrinsically weak population (i.e. subset of the total population of items made up of only weak items), that covers the first zone of the bathtub curve (early failures). Effective screening requires stresses of sufficient magnitude and time duration to precipitate failures from latent defects without accumulating significant damage to the remaining non-defective structural elements (see Fig. 6.2).
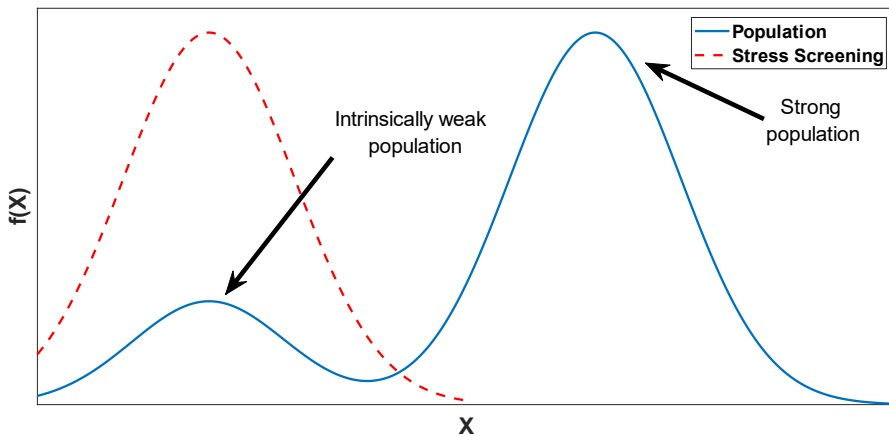
Fig. 6.2. Comparison between population robustness and ESS strength.

There are a number of common types of screening procedures which could be used with some degree of success. These common screening procedures (stresses) are shown in

TABLE VI.*I* in compliance with [192].

TABLE VI.I

COMMON SCREENING TYPES AND TYPICAL DEFECT TYPES PRECIPITATED BY ESS.

STRESS	DEFECT TYPES PRECIPITATED
Thermal cycling	Component parameter drift Hermetic seal failure Poor thermal coefficient matches Stress relaxation Loosening of connections or parts Cracks
Vibration	Particle contamination Defective oscillator crystals Poorly bonded internal parts Poorly secured high-mass parts Mechanical flaw Loosening of connections or parts Part mounting issues
Combined thermal cycling and vibration	All mechanisms under vibration and thermal cycling Interaction between mechanisms
High voltage	Shorted connections
Humidity	Sealing properties Hygroscopic contamination Circuit stability Corrosion
High temperature	Performance degradation Chemical reaction
Acceleration	Cracks Mechanical defects
Gas pressure test	Leaks and hermetic failure
Power cycling	In-rush current response Circuit transients

There are a number of types of ESS: constant stress screening, step stress screening, and Highly Accelerated Stress Screening (HASS).

More in detail, a constant stress screening is a screening procedure where a constant environmental and/or operational stress is used for the duration of the process.

A step stress screening is a screening procedure where environmental and/or operational stresses are changed at planned intervals, usually increasing in strength for the duration of the process. Step stress screening is often used to shorten process times, and to give some idea of likely failures rates at different stress levels.

Highly Accelerated Stress Screening (HASS), is intended to be an on-going process either performed on the whole production (100 % screening) or on a sample from the production or from a batch. The HASS process is typically set up as a rapid temperature change between the upper operating limit reduced by some amount and the lower temperature limit plus the same amount.

If no operating limits have been identified, a level as high as appropriate for the item's technology is chosen. Normally the screening strength of the HASS screening is adjusted by increasing or decreasing the number of temperature cycles. HASS normally stays within the items' operational limits to allow continuous monitoring of the function of the item, but operational limits can be exceeded where the items under HASS are not monitored during the screening. However, it is important that the stress levels remain below the destruction limit for good items. The items should then be tested for function after the HASS.

Generally, the purpose of all of these screening types is to cause relevant failures to occur in the item. Such relevant failures are those that would have prevented the item from achieving its reliability requirements in service.

6.3. Research questions and direction of this work

The interest in diagnostic, fault diagnosis and condition monitoring rapidly increase over the last years due to the fast development of Industry 4.0. Considering the great increase of automation and the high complexity of the industrial equipment, the diagnostics process has become fundamental in every manufacturing field representing an essential part of performance requirements [35], [198]–[201].

This is due to the fact that diagnostic and fault diagnosis allow to increase the reliability and maintainability of the system under test, and consequently also its availability. At the same time the need of corrective maintenance is minimized as well as the overall management costs. Essentially, diagnostic is based on monitoring some condition parameters of a system to acquire a large amount of data. Processing these data, it is possible to identify some particular conditions that are indicative of a possible incipient fault. There are many requirements to implement diagnostic on complex industrial system. Accurate sensors, multi-channel acquisition system, fast processing unit able to elaborate large amount of data, and high reliability are mandatory requirements.

In this point of view, this work presents an Environmental Stress Screening test plan for two electronic devices used in diagnostic units: a Inertial measurement unit (case study A) used to monitor acceleration and angular rate of industrial machinery and a DC-DC converter (case study B) used to supply WSN-based diagnostic unit.

In particular, the reliability of diagnostic systems is a key factor as well as their accuracy and all their metrological characteristics. This statement represents a critical aspect during the design phase because diagnostic elements are usually considered failure-free by definition. This assumption means that diagnostic must provide a continuous and reliable flow of information, without loss of calibration, erratic data or hardware failures in order to assure the expected behavior and the correct operation of the monitored system.

As a consequence, accuracy and reliability performances of diagnostic systems are becoming fundamental requirements in almost all applications to ensure the proper expected behavior of the monitored system and consequently mitigate its related risk. Nevertheless, in recent literature, the dynamic metrological performance and how the actual operating conditions can affect the metrological performances, the electrical performances and reliability of such systems is not adequately dealt with. This kind of analysis is called context-awareness assessment because it considers the real scenario in which the system is operating, characterized by the presence of significant temperature, humidity, vibrations, mechanical shocks and so on.

Trying to fill this gap, the main objective of this chapter is to introduce an ESS-based test plan to characterize the performances of the DUTs ensuring that the system will work in presence of significant external stress sources. The results of the tests are used to investigate both reliability and metrological performances of the DUTs at the same time.

6.4.   Case study A: Inertial Measurement Units

Inertial Measurement Units (IMUs) represent an essential part of monitoring, diagnostic, and/or controlling system in many different application fields, like navigation and transportation, automotive and self-driving vehicles, Unmanned Aerial Vehicles (UAVs) and aerospace devices, cellular phones, human motion, robotics, and many other contexts (see for instance but not only [24], [26], [202]–[206]).

Based on the complexity, costs, size and weight requirements of the specific application, Inertial Measurement Units could integrate all the following sensors, or only a subset of those [29], [207]:

- A triaxial accelerometer used to measure the linear acceleration toward the three axes.
- A triaxial gyroscope used to measure the angular rate toward the three axes.
- A triaxial magnetometer used to measure the static magnetic field toward the three axes.

Several technologies of IMU are available in the market. Micro-Electro-Mechanical Systems (MEMS) devices are a practical, low-cost, and low-power solution that allows to ensure high accuracy and stable performances within small easy-integrated chip. Consequently, nowadays, MEMS-based IMUs are dominating the inertial platform market in every field of application [23], [32], [208]–[210]. For more information about MEMS-based IMU see section 2.3.

6.4.1.   Research motivations

The expected performance of such systems is provided in the related datasheets by microelectronic manufacturers which, generally, consider simplified operating conditions that are not well representative of the actual way of such devices operating. Indeed, typical information that can be found in datasheets deals with selectable ranges for measuring linear acceleration, angle rate, and static magnetic field, as well as the related sensitivity (to each detected quantity) and the temperature operating range. Nevertheless, the influence of the actual operating conditions on the dynamical metrological performances and on the system reliability is not sufficiently dealt with.

Recent literature extensively focuses on MEMS-based IMUs design and calibration (see, for instance, but not only [24], [25], [31], [32], [202], [204]).

Quite the opposite, the characterization of IMUs under a real operating context well-representative of actual scenario is not adequately considered.

Despite this lack, a context-awareness reliability analysis and metrological performance analyses of MEMS-based IMU under the actual operating conditions are crucial for many application fields. Relevant temperature variation, high humidity level, significant vibration stresses, mechanical shocks are only a few lists of environmental factors that profoundly affect the performances of microelectronic devices [211]–[213].

As an example, in the automotive context, in navigation and industrial environments, IMUs mounted on terrestrial vehicles are continuously interested in mechanical stresses as random vibrations, so it is expected that the effects of such vibrations could generally affect both the metrological performance, the reliability and the time to failure [126], [214].

Another example of such criticalities arises when commercial IMUs are mounted in UAVs (and more generally in aeronautical applications). Varying for instance the altitude of the flight, the temperature and humidity of the external air could remarkably change, leading to drifts or even failure of the measurement units [30], [210].

Furthermore, a context-awareness analysis is the most suitable one to characterize the performances of either software or algorithms that are embedded in microcontrollers. In fact, the real operating conditions could activate some hardware failure mechanisms that in nominal conditions are generally neglected, as well as could lead to software malfunctions, parameters drift, increase of the convergence time, data misinterpretation, and many other issues [215]. As for the low-cost IMUs, which are widely employed in popular applications as low-cost UAV and automotive, they are generally characterized by low Output Data Rates (typically close to 100 Hz).

On the other hand, many international testing standards agreed that road vehicles experienced vibration up to hundreds of Hz. Consequently, it is fundamental to investigate the performances of such devices in a context-awareness scenario to identify possible unexpected behavior in the presence of a high-frequency stimulus. Despite this, testing the performance of positioning algorithms operating under vibration stimuli comparable to the real vibration (impressed for instance, by the wind or by motor propulsion) is another significant aspect not adequately described in recent literature.

Furthermore, there is another missing point in recent literature. Currently, there are not international standards specifically designed for the environmental test of IMUs, as well as customized standards for MEMS devices are not yet available.

6.4.2. Aim of the test procedures

Trying to fill all the above-mentioned gaps, this work proposes a customized test plan and a measurement setup in order to characterize the effects of the actual operating conditions (in terms of temperature and vibration) on a set of widely-used commercial low-cost MEMS-based IMUs for automotive and UAVs applications.

The operating performances of both automotive and low-cost commercial UAV applications were considered to develop a test that is well-representative in terms of both these contexts.

The proposed test plan allows to carry out different kinds of analysis at the same time focusing on many goals strictly related to each other:

- Screening of the weak population by a reliability point of view. The proposed test plan can be contextualized within the context of ESS-RSS test procedures. Thus, the investigation of early failure due to infant mortality can be performed. This will allow to significantly decrease the failure rate of the device in the first phase of its lifecycle, avoiding unexpected early failures.

- Characterization of the IMU's metrological performances under harsh environment. The analysis of the raw data outcoming for the IMUs during the test allows to estimate miscalibration issue, loss of accuracy and stability, cross-axis sensitivity, spurious response ratio, etc.

- Characterize the performances of different positioning algorithms under temperature and vibration conditions. Two different well-known filtering algorithms for positioning were tested basing on the data acquired by the IMUs during the tests. More in detail, the considered filtering algorithms are based on the Complementary filter and on the Attitude and Heading Reference Systems (AHRS) Kalman filter with the aims of analyzing and comparing two kinds of opposite approaches: the former based on suitable high/low pass filters, and the latter based on the capability of prediction given by the Kalman filter.

- Analysis of the IMU frequency response in presence of an additive high-frequency white gaussian noise, typical of the automotive and aerospace contexts.

- Verification of the MEMS-based IMU performances in order to ensure that the system will work properly when it is subjected to vibration and temperature stresses (well-representative of low-cost automotive or UAVs applications).

6.4.3. Failure analysis of MEMS-based IMU

The environmental conditions remarkably affect the metrological and electrical performances as well as the component reliability of microelectronic devices. For instance, MEMS-based IMUs developed to work on automotive and UAV applications are subject to temperature excursion and vibration conditions that could cause fatigue and fracture on the devices, as well as stiction of the mechanical parts, creep and plastic deformation, short and open circuit, etc. [216]–[219].

A preliminary functional failure analysis is required prior the draft of the test plan to understand every possible failure mechanism that could lead to faults and malfunctions of the whole inertial module. In this work, the failure analysis focuses on both mechanical and electrical physical domains in order to cover all the failure mechanisms typical of MEMS technology.

According to many works in recent literature (see for instance [218], [220]–[227]), the typical failure mechanisms of MEMS sensors are detailed included in TABLE VI.II.

The table also provides a list of one or more failure causes and one or more acceleration factors for each one of the failure mechanisms. The acceleration factors are extremely helpful parameters useful to understand which environmental condition influences most the component reliability and its performances [228], [229].

Vibrations, and more generally all mechanical shocks, influence almost all the possible failure mechanisms of the MEMS sensors, as highlighted using blue bold character in TABLE VI.II.

Quite similarly, also temperature is a critical influence factors able to trigger many failure mechanisms of MEMS devices, as emphasized using red bold character in TABLE VI.II. As a matter of fact, temperature stress could be useful to investigate the ability of soldering to endure high and low temperatures, as well as it is useful to highlight electrical and/or physical drifts in the parameters of the microelectronic device. These parameter drifts produce effects on both system performances and reliability.

As a conclusion, almost all the identified failure mechanisms can be quickly investigated using thermal and vibration tests. For this reason, this work proposes an ESS-based test plan based on two different accelerating factors: temperature and vibration. Different test procedures based on these two stress sources have been developed in order to fulfil all the test objectives presented in section 6.4.2.

TABLE VI.II

FAILURE ANALYSIS OF MEMS SENSORS INCLUDING FAILURE MECHANISMS, ROOT CAUSES AND ACCELERATION FACTORS.

FAILURE MECHANISM	ROOT CAUSES	PHYSICAL DOMAIN	ACCELERATION FACTORS
Creep and plastic deformation	Intrinsic stress Applied stress Thermal stress	Mechanical	**Temperature** Applied strain **Vibration**
Fracture due to mechanical shocks and vibrations	Overload Fatigue Shock Stress corrosion	Mechanical	Acceleration Frequency (at resonance) **Vibration**
Wear	Adhesive Abrasive Corrosion Surface fatigue	Mechanical	**Mechanical shock** Speed **Temperature** Environment
Contamination	Intrinsic Fabrication-Induced User Environments	Mechanical	Environment **Temperature**
Stiction	Capillary force Van der Walls force Electrical static force Residual stress Chemical bonding	Mechanical Electrical	Humidity Mechanical shocks **Vibrations** Voltage
Short/open circuit	Dielectric material degradation High electric field Electromigration Ohmic contact	Electrical	Electric field **Temperature** Humidity
Dielectric charging	Dielectric material degradation High electric field	Electrical	Electric field **Temperature** Radiation Humidity
Electrostatic discharge (ESD)	Static electricity Electrostatic induction	Electrical	Charged devices Charged Environment

6.5. Case study A: Test plan and Measurement setup

This section presents the proposed ESS-based test plan and the measurement setup used to characterize the performance of the MEMS-based IMU under test.

6.5.1. Structure of the test plan

The proposed test plan for characterization of MEMS-based IMU is basically composed by two major parts: a vibration-based test plan and a thermal-based test plan. Both of these test plans include several test profiles with different features, as detailed described in the following subsections.

As described in section 2.3., a proper data acquisition unit has been developed to store the outcomes of the DUTs during the test. For the sake of reliability analysis, each test included in the following test plans is based on a predetermined data acquisition procedure developed in three phases:

- "Before zone". It is the time slot prior to the application of the considered stress (either temperature or vibration). It lasts 3 minutes in order to acquire enough data to characterize the performance of the DUT before the stress application.
- "Test zone": It is the time slot in which the test profile is applied to the DUT. During this phase, the IMU acquire data and transfer them to a laptop utilizing the suitable acquisition chain described in section 2.3. The duration of this phase depends on the time duration of the considered test. The data analysis is performed offline after the conclusion of the test plan to characterize the metrological performances of the IMU under the actual operating conditions of the considered environment. The data could also be used to evaluate the performances of different positioning algorithms.
- "After zone": It is the reciprocal time slot of the before zone. The DUTs endure no stress (neither temperature nor vibration) during this time. It lasts 3 minutes. The data analysis performed on this time slot allows to investigate miss calibrations and other phenomena that the proposed test profile could have triggered. Ore in detail, Comparing the performances of the DUTs before and after the stress application it is possible to identify potential failure mechanisms or any possible damages exposed by the test. As a consequence, this phase provides

fundamental information for the reliability analysis and the early failure analysis of the DUTs.

Fig. 6.3 summarizes this concept illustrating with different colors two consecutive repetitions of the same service condition.
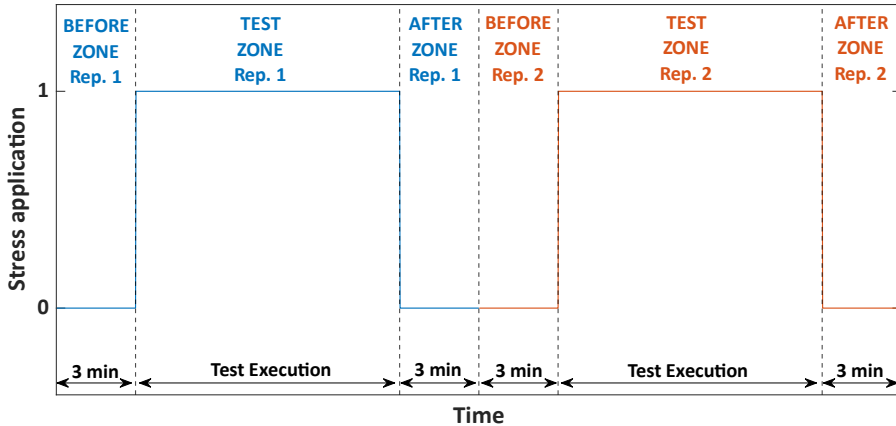
Fig. 6.3. The test procedure's schematic representation is divided into three zones: before zone, test zone, and after zone. The different colors stand for different repetitions of the test.

6.5.2. Proposed test plan: vibration stress profiles

This work proposes a non-standard procedure specifically tuned to reflect the operative condition of the MEMS inertial module, taking into account the real environmental stresses of the field of application. From a vibration point of view, the operating conditions of electronic devices installed on cars, motorcycles, or on low-cost commercial UAVs are comparable and could be reasonably approximate as equal.

The proposed vibration test plan is composed of four kinds of tests: a sinusoidal vibration profile, a random vibration test, a vibration step-test and a sine-on-random vibration profile.

6.5.2.1. Random vibration test

The random vibration profile provides the possibility to study the behavior of the device under test at different frequencies simultaneously, emulating the

operating conditions of these devices (in terms of vibration) when they are installed and used in real scenarios.

Since there are no specific standards available for the device and applications studied in this work, the test setup was settled comparing several test profiles included in many international standards:

- IEC 60068-2-64 [230] is the European standard published by International Electrotechnical Commission (IEC) in 2008. The general standard regulates the environmental testing, while section 2-64 is about random vibration.
- MIL-STD-810G [231] is a milestone for environmental testing developed by the U.S. Department of Defense in 2008. It is currently the guideline for the majority of the laboratory tests.
- JESD22-B103B.01 (2016) [232] is an international standard published by "Jedec solid state technology association" in 2016. It proposes testing procedures for microelectronics devices focusing on vibration at variable frequency.
- ETSI EN 300 019-2-5 [233] developed by the European Telecommunications Standards Institute (ETSI) in 2002. It deals with the environmental testing area for different kinds of telecommunications equipment installed in vehicles.
- ISO 16750-3 (2003) [234] provided by the International Organization for Standardizations in 2003. It covers the environmental testing of electrical and electronic components installed on road vehicles.
- ANSI C136.31 [235] is an American standard developed in 2010 that covers the vibration test methods for roadway and area luminaires.

During the random test, the IMU is vibrated using normally distributed random vibrations. The standards mentioned above use the Acceleration Spectral Density (ASD) to characterize a random vibration profile over a frequency domain. According to the international standard IEC 60068-2-64 [230] ASD is defined as "the mean-square value of that part of an acceleration signal passed by a narrow-band filter of a center frequency, per unit bandwidth, in the limit as the bandwidth approaches zero and the averaging time approaches infinity". The developed test profile is divided into two zones: a low-frequency span, including the range from 5 Hz to 20 Hz and a high-frequency span from 20 Hz up to 500 Hz. In the first frequencies span, the Acceleration Spectral Density is defined as follow:

$$ASD_{LF} = 2 \; {m^2}/{s^3} = 0.02 \; {g^2}/{Hz} \tag{6.1}$$

Instead, in the high-frequency span ASD_{HF} decreases as -3 dB/oct. Fig. 6.4 shows a graphical representation of the developed profile.
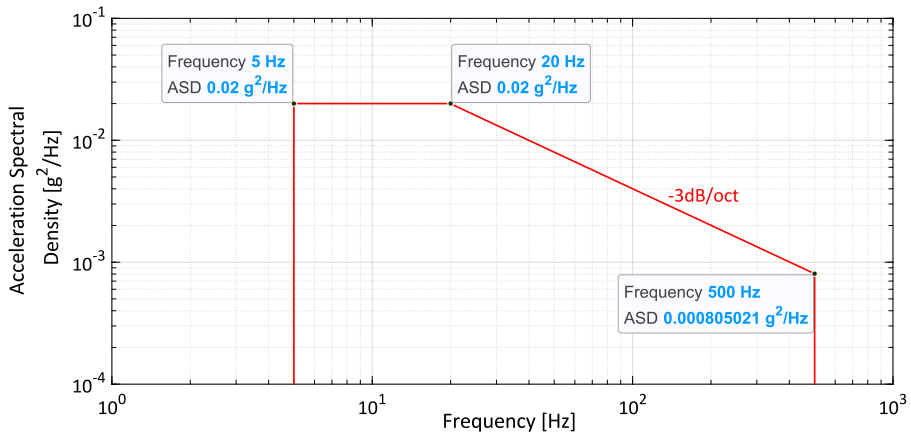
Fig. 6.4. Proposed random vibration test profile showing the trend of the Acceleration Spectral Density in the considered range of frequencies. The data tips are located in the most significant points of the profile.

In compliance with the standard mentioned above, both axes in the figure are illustrated on a logarithmic scale. Even if the trend illustrated in Fig. 6.4 is quite representative of the profile, other parameters must be defined in order to provide a complete and exhaustive description of the test. The Root Mean Square Acceleration a_{RMS} (expressed using the RMS value of the gravitational acceleration g) is a useful parameter that measures the amount of acceleration impressed to the DUT during the test. In fact, it can be monitored continuously during the test, and consequently, it can be used by the shaker controller to ensure that the demanded profile will be fulfilled. It is defined as the RMS value of the square root of the surface area below the Acceleration Spectral Density trend through the frequency domain. The random vibration profile defined above results in a Root Mean Square Acceleration of $a_{RMS} = 1.2864\ g$.

The ASD test level shall be applied within a tolerance of $\pm 3\ dB$ of the nominal value at any frequency, allowing for the instrument and random error, referred to the specified ASD. The RMS acceleration levels shall not deviate more than $\pm 10\%$ of the nominal value defined above.

The test profile is repeated along X, Y, and Z axes, with a time duration of 30 minutes on each axis and a peak displacement RMS $d_{RMS} = 1.85\ mm$. The controller samples the profile and provides 400 different spectral lines to the shaker that implement the test.

The random vibration test in this work has been developed to simulate the effects of the vibration induced by several factors in a motorcycle or a drone,

such as a gust of wind, wind buffeting, motor propulsion, a sudden brake, road bumps, linear acceleration or deceleration of the entire vehicle, path harshness, etc.

6.5.2.2. Sinusoidal vibration test

The sinusoidal vibration test is used to investigate any mechanical weakness and/or degradation in the device under test, to demonstrate the mechanical robustness of the specimen and/or to study its dynamic behavior. In order to achieve these objectives, the test is based on a continuous sweep of frequencies changed exponentially with time.

The sinusoidal test plan was developed based on the procedures included in the international standard IEC 60068-2-6 [236], which is a European standard published by the International Electrotechnical Commission (IEC) in 2009. This standard provides general guidelines for sinusoidal vibration testing of commercial devices; therefore, the AEC-Q100-rev.H [237] is used to customize the test on the field of application. In fact, the AEC-Q100 is an international standard that contains a set of qualification tests for integrated circuits used on automotive applications.

The test is based on a continuous frequency swept of sinusoidal stimuli, and it is divided into two-zone:

- A first zone from 20 Hz to the so-called "cross-over frequency" in which the severity of the test is expressed as constant displacement. In this phase the amplitude of the acceleration increases according to the frequency of the stimuli. In the proposed test plan, this zone is characterized by 1 mm peak-to-peak displacement.
- A second zone from the cross-over frequency up to 2 kHz in which the severity of the test is expressed as constant acceleration, while the displacement is uncontrolled. In the proposed test plan, the test has been performed with three different service conditions: 2 g - 4 g - 8 g peak acceleration.

The value of displacement amplitude is related to the value of acceleration amplitude in such a manner that the magnitude of vibration is the same at the cross-over frequency. In this way, the frequency range may be swept continuously, changing from constant displacement to constant acceleration and vice versa at the cross-over frequency.

For this reason, every sinusoidal vibration test is generally characterized by a different cross-over frequency so that the above-mentioned relationship is

fulfilled. In particular, the cross-over frequencies of the three service conditions are reported in TABLE VI.III along with the other parameters of the test severity.

TABLE VI.III

COMPLETE TEST SEVERITY OF SINUSOIDAL VIBRATION PROFILES.

SERVICE CONDITION	PEAK ACCELERATION	PEAK-PEAK DISPLACEMENT	CROSS-OVER FREQUENCY	FREQUENCY RANGE
S1	8 g	1 mm	63 Hz	[20 - 2000] Hz
S2	4 g	1 mm	45 Hz	[20 - 2000] Hz
S3	2 g	1 mm	32 Hz	[20 - 2000] Hz

The test is performed according to a constant sweep rate performed in a logarithmic manner at 1 decade/minute speed rate. The sweep is performed four times, from the minimum to maximum, and returns to the minimum frequency. Considering the above information, a complete sweep is performed in 4 minutes, leading to a complete test which lasts 16 minutes.

The complete test is repeated in each of the orientation axes X, Y, and Z. A tolerance level of +/- 10% on the test being performed, either displacement or acceleration, is allowed.

Fig. 6.5 illustrates the service condition S3 of the sinusoidal vibration test proposed in this work, highlighting the most significant points using data tips.
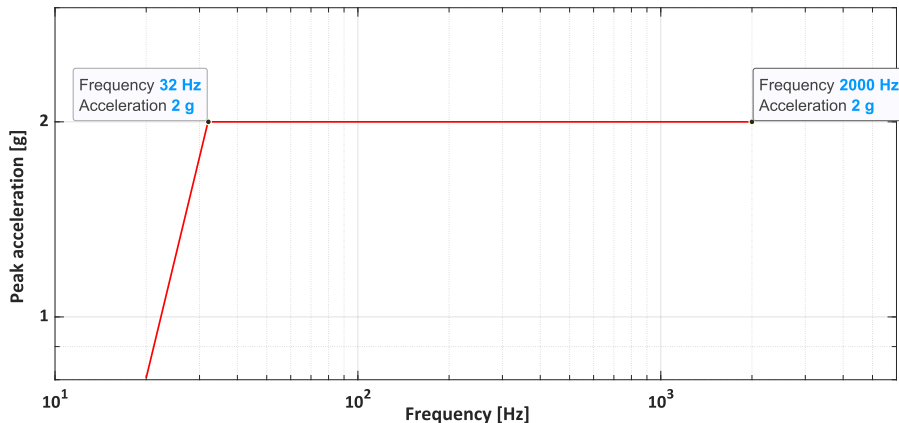
Fig. 6.5. Sinusoidal vibration test profile: service condition S3. The data tips are located in the most significant points of the profile.

The three service conditions S1, S2, and S3 are represented in Fig. 6.6, where the dotted lines stand for the cross-over frequencies f_{S1}, f_{S2} and f_{S3} related to the conditions S1, S2, and S3 respectively.

The first test to be performed is the service condition S3. If no failures are exposed after the test, then severity could be increased moving on the condition S2, and finally to condition S1.
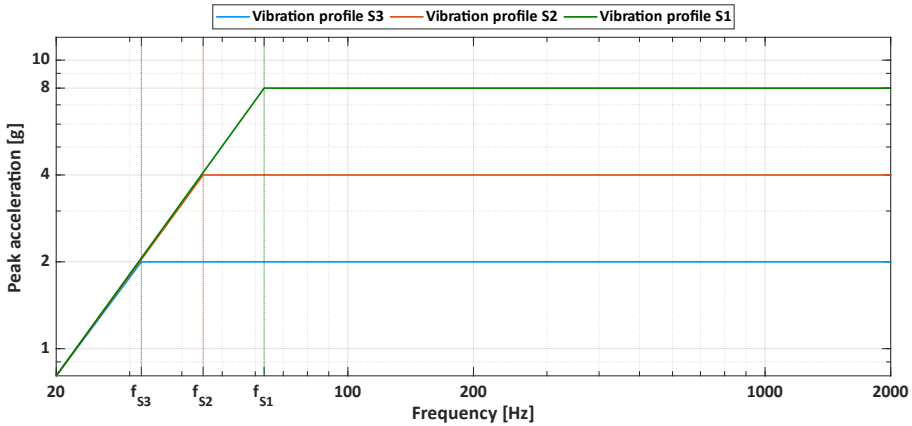
Fig. 6.6. Representation of the three sinusoidal vibration profiles S1, S2 and S3

6.5.2.3. Vibration step-test

The objective of this test profile is to characterize the frequency behavior of the MEMS-based IMUs subjected to a sinusoidal vibration at different frequencies, maintaining a constant peak acceleration. Starting from the widely known sinusoidal vibration profile (as described in section 6.5.1.1.), a customized test profile is presented in this section based on a frequency step-up of a sinusoidal stimulus over time to carefully investigate the frequency response of the inertial platforms. The developed test plan is a sort of vibration step-test, where the physical quantity that step up is not the peak acceleration but is the frequency of the stimulus. Using this test profile, it is possible to achieve information about the frequency response of the IMU under test and, at the same time, it is possible to investigate its ability to withstand a constant vibration stimulus over a large frequency span. The latter could also provide significant information on the reliability performances of the IMUs, which represents a critical requirement in many application fields. As mention above, the classical sinusoidal sweep vibration test is defined and illustrated in the international standards IEC 60068-2-6 (2009) [236]. Based on the test profile proposed in

section 6.5.1.1., the vibration step test adopted in this work consists of a single sweep from 40 Hz to 2000 Hz analyzing a single frequency for a fixed period of holding time. After such a period of time, the frequency will be increase of a fixed frequency step. An extract of the vibration profile proposed in this work is illustrated in Fig. 6.7, considering only the subrange 40 – 200 Hz.
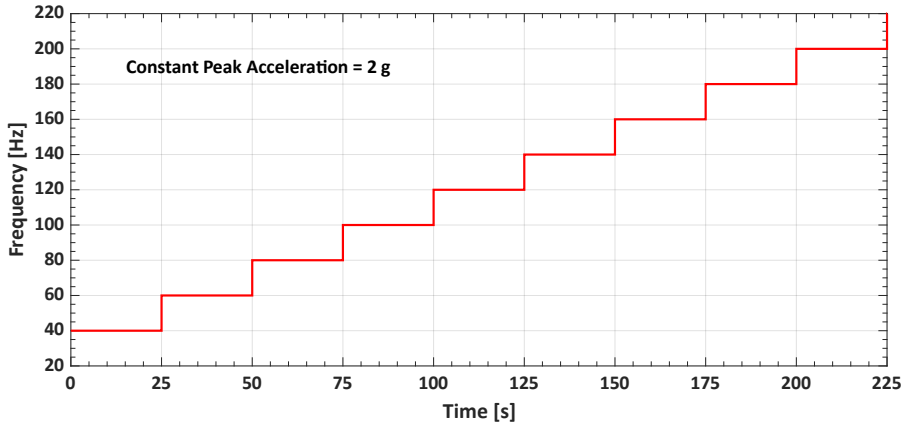
Fig. 6.7. Extract of the vibration step-test profile in the frequency range 40 - 200 Hz.

The severity of the complete test is the following:
- Minimum frequency: 40 Hz
- Maximum frequency: 2000 Hz
- Frequency step: 20 Hz
- Vibration peak: 2 g
- Type of vibration stimuli: Sinusoidal
- Holding time at each step: 25 s
- Number of cycles: 1
- Number of axes: 3

6.5.2.4. Sine-on-Random vibration test

Each one of the test profiles presented in the previous sections is based on a single type of vibration stress. However, according to the international standard ISO 16750-3:2003 [234] (Road vehicles- Environmental conditions and testing for electrical and electronic equipment – Part 3: Mechanical loads), the vibration endured by an electronic device mounted on a road vehicle can be divided into two types:
- Sinusoidal vibration: it could be one of the spectral components from the acceleration due to the vehicle's motion, or it could be caused by

161

> unbalanced mass forces, vibration induced by the pulsation of the intake air, etc....
> - Random noise from all the other vibration sources of an engine (e.g., closing of valves), the noise created by the gearwheels' friction, random vibration induced by rough-road-driving.

Hence, ISO 16750-3:2003 [234] suggests performing the test as a combined sine and random test in compliance with International Standard IEC 60068-2-80 [238]. The latter defines "swept frequency sinusoidal vibration on wideband random vibration" or simply Sine-On-Random as one or more sinusoids swept over a frequency range and superimposed on random vibration.

In other words, this kind of vibration test is based on the application of two different vibration stimuli at the same time: wideband random vibration stress and a sinusoidal vibration stimulus. This test requires the definition of a composite vibration severity, consisting of swept frequency sinusoidal components on a random background. In some instances, the sinusoidal stimulus could be maintained fixed instead of being swept over a frequency range.

Consequently, both sinusoidal and random vibration severities have been customized on the actual operating condition related to the application field (automotive and low-cost UAVs).

Regarding the sinusoidal vibration, this stimulus is a low-frequency sinusoid with a vibration peak of 1 g. Both frequency and amplitude are maintained constant over the testing time. This vibration stands for a hypothetical IMU input signal, which must be acquired without distortion since it represents the acceleration that the positioning algorithms must process. The truthfulness of this vibration has been proven in [239], [240] in which a suitable measurement system has been proposed to evaluate the driver's exposure to vibration during a ride on a motorcycle. The paper highlights that the vibration analysis band for a motorcycle varies from 0.25 Hz to 20 Hz.

As a consequence, four different service conditions (SC) have been developed to recreate different scenarios well representative of the automotive application's actual vibration.

For the sake of simplicity, the service conditions are based on a single sinusoid, which is not the real vibration experienced in the automotive field. Instead, it is only a single spectral component of the actual vibration.

Three SCs are based on a single sinusoid with constant frequency (i.e., 5 Hz – 10 Hz – 15 Hz), while the last one is based on a continuous frequency sweep from 5 Hz to 20 Hz.

The wideband random vibration is based on the excitation of all the frequencies in a defined spectrum at any given time. This test is extremely useful since vibrations found in everyday life scenarios are not repetitive or predictable like sinusoidal waveforms.

The severity of random vibration is described providing an ASD value over a frequency range. The proposed test plan is based on a constant density value $ASD = 0.01 \, g^2/Hz$ over the frequency range from 200 Hz to 2 kHz. This represents a wideband gaussian white noise that could distort the low-frequency signal related to the monitored item's actual motion. Because of the ODR of the DUTs, a 50 Hz antialiasing filter is introduced on the IMU (see section 2.3). Consequently, the random vibration should be completely cut-off by the antialiasing filter embedded in the considered devices (for more information see section 2.3).

Several standards agree that the vibration endured by an electronic device for automotive application is a wideband stimulus with a maximum frequency of up to 2 kHz. The frequency range is strictly related to the exact deployment of the DUT.

The most significant standards taken into account during the development of the proposed test plan are the following:

- ISO 16750-3 published by the International Organization of Standardization in 2003 [234].
- IEC 60068-2-64 published by the International Electrotechnical Commission in 2008 [230].
- ETSI EN 300 019-2-5 published by the European Telecommunications Standards Institute in 2002 [233].
- AEC-Q100-rev.H published by the Automotive Electronics Council in 2014 [237].

TABLE VI.*IV* summarizes the normative references used to identify the frequency range of the random vibration concerning installation type.

Most of the standards agree that devices mounted on-road vehicles are subjected to random vibration up to 2 kHz. This is why the proposed test plan includes a random vibration over the frequency range from 200 Hz to 2 kHz, although the ODR of the sensor is 119 Hz.

Additional information regarding the test are illustrated in the following:

- Test duration: 10 minutes.
- Axes involved: X, Y, and Z.

- Repetition: 5 consecutive tests for each SC of each axis.
- The same fixture must be used for all the test run along the same axes.
- For the sake of repeatability, several test repetitions must be carried out without dismounting and remounting the DUTs to the vibration table (so the position stays the same) to minimize the mounting uncertainties. This is fundamental to ensure that any mechanical load due to the fixture of the DUTs to the shaker remains the same in all the repeated tests.

TABLE VI.IV

NORMATIVE REFERENCE FOR RANDOM VIBRATION TESTING: EQUIPMENT INSTALLED ON A GROUND VEHICLES.

TYPE OF INSTALLATION	MAXIMUM FREQUENCY	REFERENCE STANDARD
Equipment mounted directly on the engine	up to 2 kHz	ISO 16750-3
Gearbox mounted equipment	up to 2 kHz	ISO 16750-3
Equipment mounted on sprung masses (vehicle body)	up to 1 kHz	ISO 16750-3
Equipment mounted on unsprung masses (wheel, wheel suspension)	up to 2 kHz	ISO 16750-3
Automotive application: Integrity test for semiconductor devised	up to 2 kHz	AEC-Q100
Automobile, chassis-mounted.	up to 1 kHz	IEC 60068-2-64
Automobile, engine compartment, attached to the body or the radiator.	up to 0.2 kHz	IEC 60068-2-64
Telecommunication equipment mounted on a ground vehicle	up to 0.5 kHz	ETSI EN 300 019-2-5
Equipment mounted directly on the engine	up to 2 kHz	ISO 16750-3

TABLE VI.V summarizes the severity of the proposed test plan highlighting the four different SCs. Note that the random vibration is kept unchanged for all service conditions.

TABLE VI.V

SUMMARY OF THE DEVELOPED TEST PLAN: FOUR SERVICE CONDITIONS WITH DIFFERENT SEVERITIES HAVE BEEN PROPOSED.

SERVICE CONDITION	SINUSOIDAL VIBRATION		RANDOM VIBRATION	
	Frequency	Peak vibration	Frequency range	ASD [g² / Hz]
SC 1	5 Hz	1 g	200 – 2000 Hz	0.01
SC 2	10 Hz	1 g	200 – 2000 Hz	0.01
SC 3	15 Hz	1 g	200 – 2000 Hz	0.01
SC 4	Sweep from 5 Hz to 20 Hz Sweep rate 1 oct/min	1 g	200 – 2000 Hz	0.01

To ensure repeatability of the results, every test repetitions of each SC of the same axes have been performed using the same fixture, without dismounting the setup between one acquisition and the following one.

According to the test plan and taking the Service Condition SC 2 as an example, Fig. 6.8 illustrates the acceleration spectral density generated by the shaker over the considered frequency range measured by a suitable accelerometer. It is visible the 10 Hz sinusoid and the wideband white noise over one order of magnitude lower than the sinusoids.
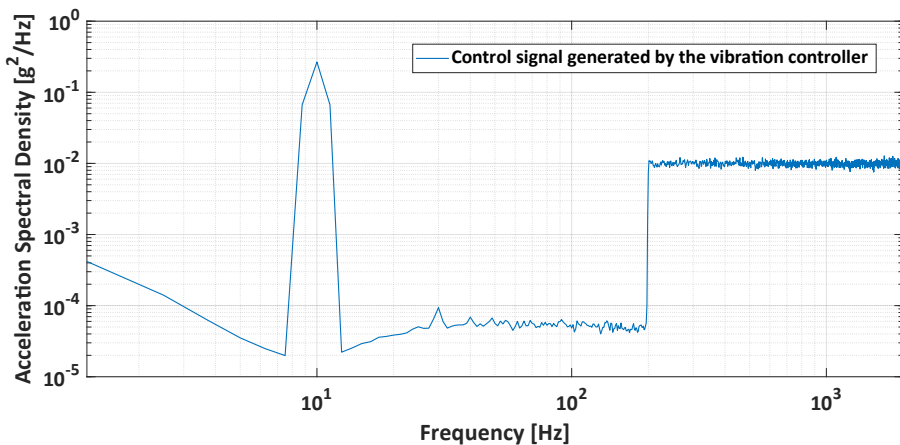
Fig. 6.8. Test Condition SC2: Vibration profile measured during the test.

Furthermore, since Fig. 6.8 illustrates the actual vibration endured during the test (i.e. it is not a theoretical trend), it is also present an additive noise over

the frequency domain not covered by the sinusoids and the random vibration included in the profile (i.e., for frequencies lower than 10 Hz and frequencies from 10 Hz to 2 kHz). Despite this, the latter noise is over two orders of magnitude lower than the gaussian white noise, and thus it could be neglected.

6.5.3. Proposed test plan: thermal stress profiles

This work proposes a non-standard procedure specifically tuned to reflect the operative condition of the MEMS inertial module, taking into account devices installed on cars, motorcycles, or on low-cost commercial UAVs. The proposed thermal test plan is composed of three kinds of tests: a thermal cycling test in a limited range with humidity exposure, a temperature cycling test in an extended range, and a temperature step test.

6.5.3.1. Thermal cycling test with humidity exposure

The aim of the test is the performance characterization of commercial IMU under temperature and humidity combined stresses. Both reliability and metrological performances can be investigated using an in-depth analysis of the raw data acquired during the test.

Different environmental testing standards with a generic field of application have been consulted in order to customize the proposed test plan for MEMS-based IMU, as follow:

- MIL-STD-810G [231] published by the U.S. Department of Defense in 2008 as generic guidelines for test procedures.
- IEC 60068-2-14 [241] published by the International Electrotechnical commission in 2011. The section 2-14 refers to the change of temperature during test.
- IEC 60068-2-38 [242] published by the International Electrotechnical commission in 2021. The section 2-38 refers to combined temperature and humidity cyclic test.
- JEDEC JESD22 A104E [243] published by "Jedec solid state technology association" in 2014. It proposes testing procedures for microelectronics devices focusing on thermal cycling test.

The proposed test plan is based on a cold/hot thermal cycling test repeated a few times, with humidity stress exposure at the maximum temperature. The severity of the proposed test profile is the following:

- Cold temperature: $T_C = -10\,°C$

- Hot temperature: $T_H = 50\ °C$
- Cold temperature exposition time: $t_{exp} = 30\ min\ @\ T_C$
- Hot temperature exposition time: $t_{exp} = 30\ min\ @\ T_H$
- Approximate temperature variation rate between T_C and T_H and vice versa: $\Delta_T \cong 2\ °C/min$
- Estimated cycle duration: $t_{cycle} = 2\ h$
- Number of consecutive cycle: $N = 2$
- Estimated test duration: $t_{test} = 4\ h$
- Maximum relative humidity: $RH_{max} = 95\ \%$
- Humidity control: Activated only during hot temperature exposition time to ensure the RH_{max} humidity level.

The detailed explanation of the proposed test plan is illustrated in Fig. 6.9, where the different phases of the test are highlighted.
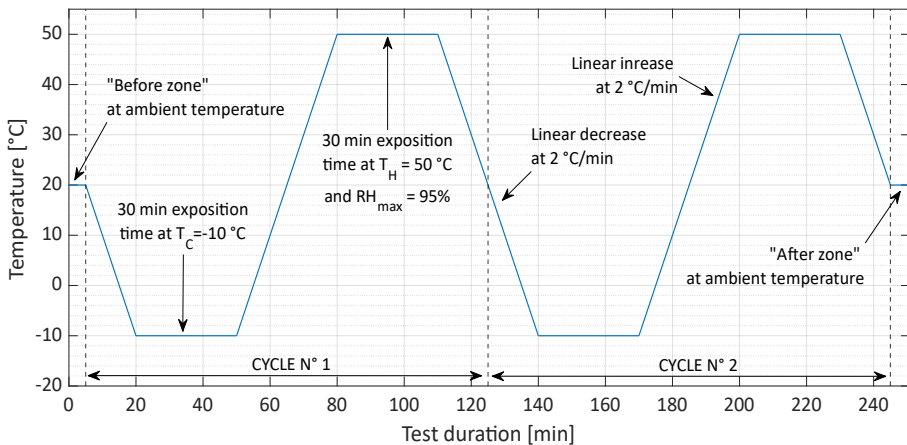
Fig. 6.9. Proposed combined temperature and humidity cycling test profile.

For the sake of reproducibility, different test repetitions should be run to acquire repeated data. The test profile implemented in each repetition is the same one illustrated in Fig. 6.9.

6.5.3.2. Temperature cycling test

This test set up was designed comparing different temperature test profiles from ISO 16750-4 [244], IEC 60068-2-14 [241], MIL-STD 810G [231], and JEDEC JESD22 A104E [243]. The severity of the test is the following:

- Cold temperature $T_A = -20℃$

- Hot temperature $T_B = 60°C$
- Exposition time $t_1 = 1h$
- Number of cycles: 4
- Raised time: 1h from T_A to T_B (approximately speed: 2°C/min);
- Lowered time: 2h from T_B to T_A (approximately speed: 1°C/min).

The developed test profile is illustrated in Fig. 6.10, and it is based on the repetition of four consecutive steps:

i.   Exposition at temperature T_A for t_1.
ii. Temperature increases from T_A to T_B at a specified rate.
iii. Exposition at temperature T_B for t_1.
iv. Temperature decreases from T_B to T_A at a specified rate.
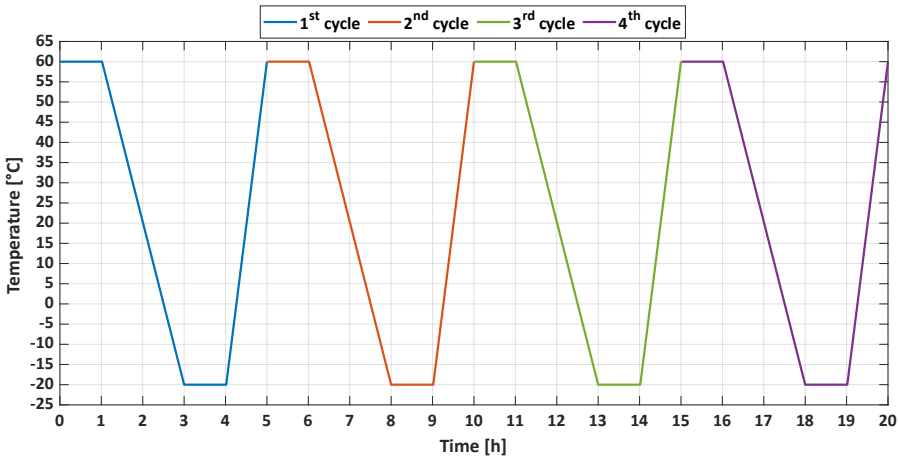
Fig. 6.10. Proposed temperature cycling test profile.

6.5.3.3. Temperature step-test

The proposed test plan is used to investigate the IMU's performance under test at different temperatures inside the guaranteed operability range. The test plan is based on the so-called temperature step stress test described in the international standards IEST-RP-PR-003.1 (2012) [245] regarding the Accelerated Life Test. The IMU under test has been developed as part of a fault diagnosis system to be implemented in a motorcycle. Therefore, the automotive field of the application must be considered during the design of the test profile. The following international standards have been used as guidelines to customize the proposed profile according to the automotive stress context: ISO 16750-4 (2010) [244] regarding the environmental testing for electrical and

electronic equipment integrated into road vehicles; AEC - Q100 - Rev-H (2014) [237] regarding the test qualification for an integrated circuit in the automotive field; ETSI EN 300 019-2-5 (2002) [233] about the environmental tests of telecommunication systems installed in ground vehicles.

The profile's main steps are summarized in TABLE VI.VI, highlighting the temperature task, the temperature interval, and each step's time duration. The proposed profile is a temperature step stress test, as the one illustrated in Fig. 6.11. It is characterized by a 5 °C step performed in 5 minutes followed by 15 minutes of exposition time at a constant temperature. In compliance with the components' datasheet and the automotive field's stress context, the proposed profile covers the range from -20 °C up to 60 °C.

TABLE VI.VI

TEMPERATURE STEPS OF THE PROPOSED TEST PLAN HIGHLIGHTING TASK, TEMPERATURE INTERVAL, AND TIME DURATION OF EACH STEP.

	Temperature Task	Temperature		Time
		From	To	
STEP 0	Lowered at maximum rate.	20 °C	-20 °C	-
STEP 1	Fixed exposition	-20 °C		15 minutes
STEP 2	Raised at the maximum rate.	-20 °C	-15 °C	5 minutes
STEP 3	Fixed exposition	-15 °C		15 minutes
STEP 4	Raised at the maximum rate.	-15 °C	-10 °C	5 minutes
STEP 5	Fixed exposition	-10 °C		15 minutes
STEP 6	Raised at the maximum rate.	-10 °C	-5 °C	5 minutes
...	...	...	...	...
STEP 31	Fixed exposition	55 °C		15 minutes
STEP 32	Raised at the maximum rate.	55 °C	60 °C	5 minutes
STEP 33	Fixed exposition	60 °C		15 minutes
STEP 34	Lowered at maximum rate.	60 °C	20 °C	-
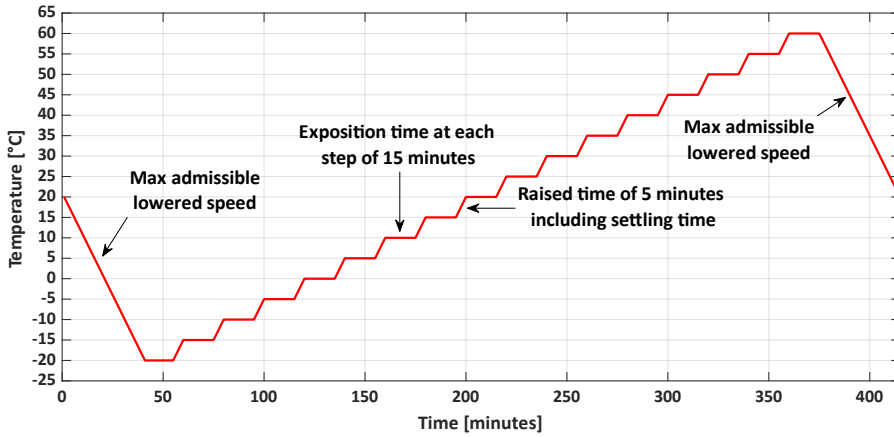
Fig. 6.11. Proposed temperature step stress test.

6.5.4.   Measurement setup for vibration test procedures

In order to implement the proposed vibration test plan, a suitable testbed has to be developed. It has to be designed for assuring three main goals:

1)   To host the DUTs and realize the vibration profiles previously defined.
2)   To allow testing the performances only of the DUT by avoiding the influence of any auxiliary devices adopted in the test set-up.
3)   To ensure that the DUTs are mounted in such a manner to simulate classical automotive or UAV applications or expected vibration during packaged shipment.

Moreover, during the vibration test the device has to be rigidly fastened on the vibration platform and the leads adequately secured to avoid excessive lead resonance.

The test method is based primarily on an electrodynamic or a servo-hydraulic vibration generator (also known as shaker) with an associated computer-based control system used as a vibration testing system. The experimental tests were fulfilled using two different shakers with different performances:

- Sentek M2232A used for X and Y axes (up to 22 kN force)
- LDS V730 DPA10K used for Z axis (up to 9.8 kN force)

TABLE VI.VII illustrates the main characteristics of the shakers. It is very important to note that the severities of the test proposed in the previous paragraphs are within the specification of both shakers.

TABLE VI.VII

MAIN FEATURES OF THE TWO ADOPTED SHAKERS.

Parameter	Sentek M2232A	LDS V730DPA10K
Force	22 kN	9.8 kN
Orientation	Horizontal	Vertical
Displacement Limit Peak	± 25.5 mm	± 25.4 mm
Max Velocity Peak	2 m/s	2 m/s
Max Acceleration Peak	99.93 g	75 g
Drive Frequency range	2 Hz to 2000 Hz	2 Hz to 2000 Hz

Both shakers are connected to the same controller Dactron laser LS2000, which is an 8-channels controller with the possibility to switch between the two different actuators.

The test set-up includes two identical 3056B2 General Purpose Piezoelectric Accelerometers by Dytran Instruments Inc. used as input channels for the vibration controller. TABLE VI.VIII summarizes the main performances of these sensors.

TABLE VI.VIII

MAIN FEATURES OF THE PIEZOELECTRIC ACCELEROMETERS.

Parameter	3056B2 Accelerometers by Dytran
Technology	Piezoelectric
Sensitivity, $\pm 5\%$	100mV/g
Frequency range	1Hz to 10kHz
Electrical noise	0.0004grms
Linearity	$\pm 1\%$ F.S.
Max vibration	± 400g

The controller requires at least two inputs, one called "Control Accelerometer" located on one of the DUTs and the other one called "Monitor Accelerometer", located on the table of the shaker. Using this configuration, it is possible to control the amplitude of the vibration produced by the shaker directly on the

DUTs allowing to apply on them the vibration profile with a high level of accuracy.

For the sake of repeatability, the "control accelerometer" is directly connected to the computer-based control system which uses a feedback to actuate the vibration shaker based on the response of the control accelerometer. Fig. 6.12 illustrates the complete testbed developed in this work, including both the vibration testing system and the acquisition system required to store the data monitored by the IMUs (as described in section 2.3.).
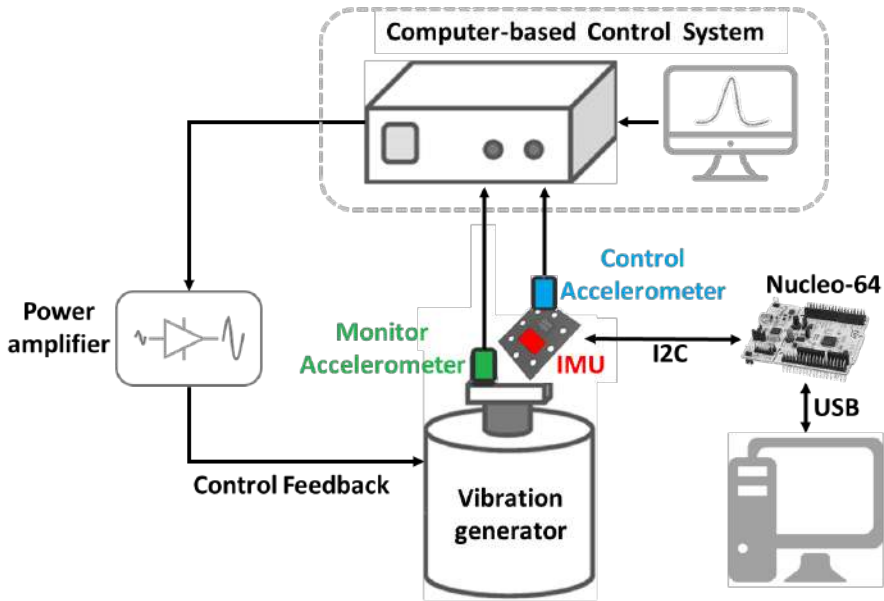
Fig. 6.12. Complete testbed developed for this project, including the vibration testing system, the device under test, and the acquisition system.

The fixing of the device to the shaker represents one of the most challenging steps of the vibration test, it must propagate the vibration equally to all the sections of the device under test without absorb it. Moreover, it must be safe, and it must have the resonance mode out of the profile frequency range.

An example of a fixture used for the Z-axis on the LDS V730 DPA10K shaker is illustrated in Fig. 6.13. while a picture of the complete measurement setup in case of Z-axis is illustrated in Fig. 6.14.

As for the X-axis and Y-axis, they were separately excited by suitably arranging the DUTs according to the shaker reference system (shaker Sentek M2232A is involved).
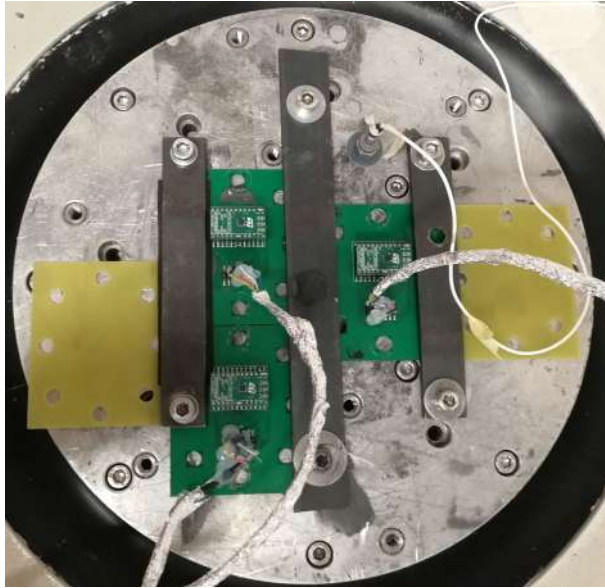
Fig. 6.13. Picture of the three DUTs mounted on the vibration generator during the test (Z-axis is involved).
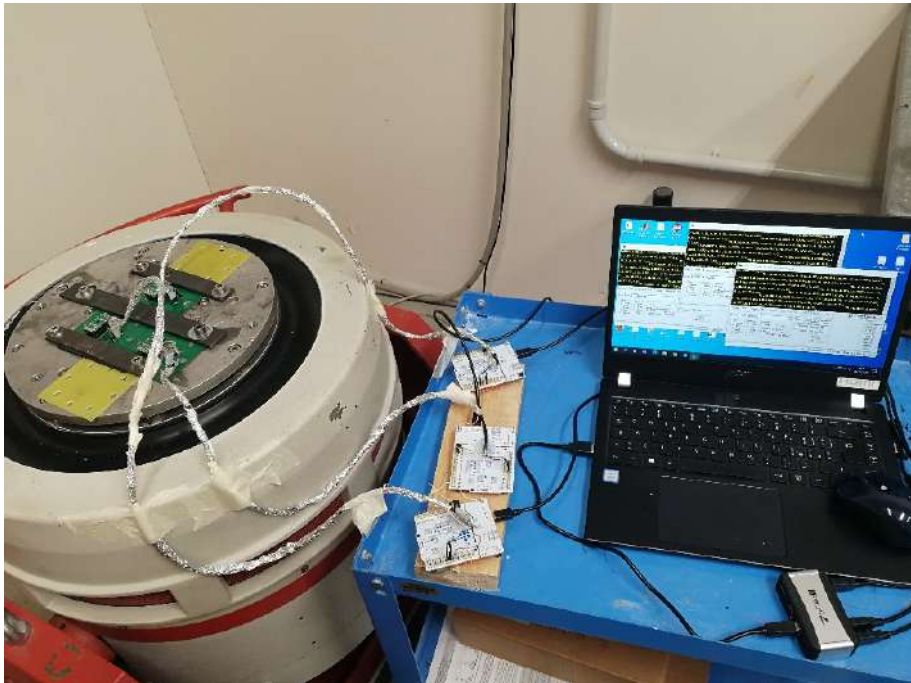
Fig. 6.14. Picture of the complete measurement setup in case of vibration test procedures (Z-axis is involved).

In particular, as for the X-axis, all the DUTs have been oriented parallel to the direction of the vibration stress provided by the shaker, whereas, as for the Y-axis, all the DUTs have been oriented perpendicular to the direction of the vibration stress provided by the shaker. In this way, the axis excited by the shaker is different with respect to the previous case even if the shaker works toward the same direction.

A picture of the complete measurement setup used for vibration test procedures in case of Y-axis is illustrated in Fig. 6.15 (shaker Sentek M2232A is involved). The red-box labels highlight the different equipment used in the proposed measurement setup.
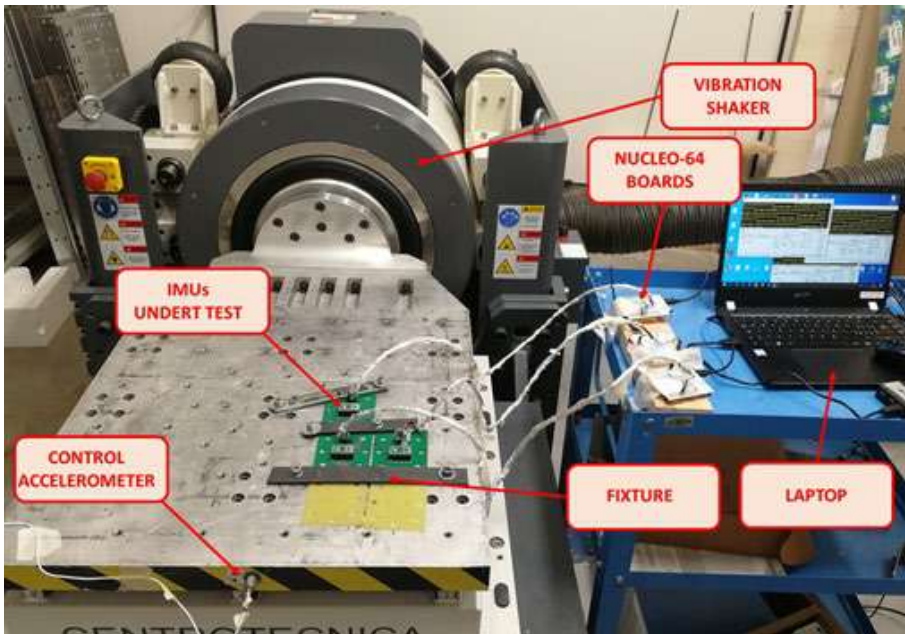
Fig. 6.15. Picture of the complete measurement setup in case of vibration test procedures (Y-axis is involved).

Looking at the previous figures, it is fundamental to note that only the IMUs are subjected to the vibration stress, while the Nucleo-64 boards are not tested in order to allow the characterization of the IMUs and the filtering algorithms avoiding the influence of external devices.

6.5.5. Preliminary characterization of the vibration testbed

Before the implementation of the proposed vibration profile, it is extremely important to run a preliminary test in order to investigate the presence or not of spurious effects such as self-resonance of the IMU board or of the fixture and anything else that may experience vibrations during the test. Moreover, it is fundamental to ensure the system withstands force and provides an adequate level of transmission and resonance, thus bringing to reliable results. To do that, it is important to ensure the stiffness of the fixture because the natural frequency of the systems depends upon the stiffness and mass present.

A useful parameter to investigate such effects is the testbed's transmissibility, which means the ratio of output acceleration to input acceleration. As previously described in section 6.5.4, the proposed measurement setup integrates a "monitor accelerometer" that measures the amount of vibration provided by the shaker (i.e., input acceleration) and a "control accelerometer" that measures the amount of vibration experienced by the DUTs (i.e., output accelerometer). Therefore, the transmissibility illustrated in Fig. 6.16 has been evaluated as the ratio between the two accelerometers' output during a sinusoidal test sweep from 20 Hz to 2000 Hz. The transmissibility is approximately 1 from 20 Hz to 1000 Hz proving that no spurious phenomena are present in this range. Quite the opposite, self-resonance of the fixture is experienced at a frequency higher than 1000 Hz. Consequently, it is important to limit the following analysis to the frequency range lower than 1000 Hz.
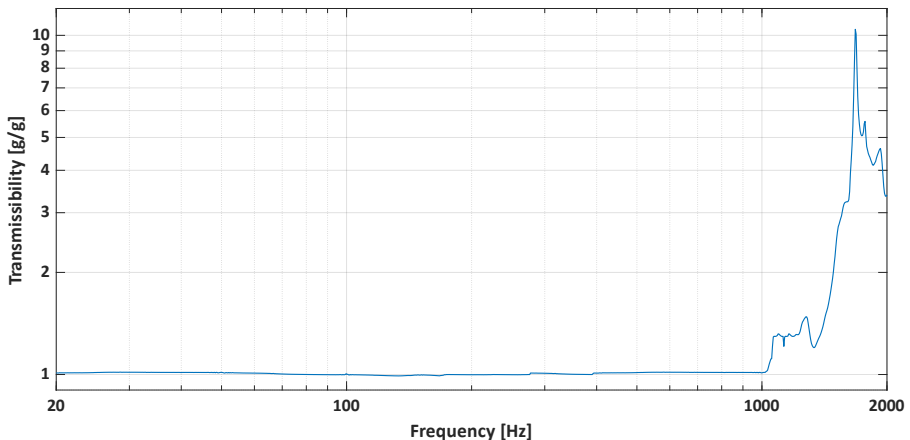
Fig. 6.16. Transmissibility of the proposed test setup evaluated as the ratio between control accelerometer output and monitor accelerometer output.

6.5.6. Measurement setup for thermal test procedures

The experimental setup used to characterize the IMUs under thermal stress is illustrated in Fig. 6.17. A climatic chamber able to regulate both temperature and humidity is used to carry out the proposed test plan.

The test was carried out using the climatic chamber UY1200C by "Angelantoni group" shown in Fig. 6.18.
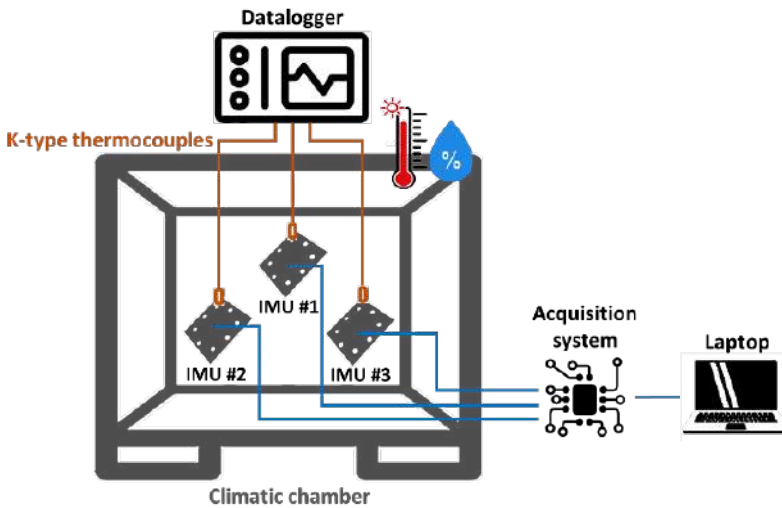
Fig. 6.17. Experimental setup proposed to evaluate the performances of IMUs under thermal stress.

Fig. 6.18. Climatic chamber used for thermal test procedures.

The main features of the chamber are the following:

- Control: Temperature and Humidity.
- Volume: $1.2\ m^3$
- Temperature range: $[-40 \div 180]\ °C$
- Relative humidity: up to 95%
- Maximum speed in optimal condition: $2\ °/min$

The temperature of the devices is monitored using a set of k-type thermocouples and PT100 resistance temperature detector (RTD) connected to a datalogger. The adopted datalogger is the LR8450 Memory HiLogger by HIOKI Corporate. The selected instrument is a 1 ms sampling portable datalogger expandable up to 120 channels. In the specific case, a U8551 universal input unit for voltage, temperature and humidity measurements has been used. A picture of the datalogger equipped with two input units is illustrated in Fig. 6.19.

Fig. 6.19. LR8450 datalogger used to monitor the temperature of the devices during thermal tests.

6.6. Case study A: Analysis of raw measurement data

This section reports the experimental results achieved during the implementation of both vibration and temperature test plans. A set of three

devices, namely DUT#1 - DUT#2 - DUT#3 have been subjected to all the test procedures described in section 6.5.2. and section 6.5.3.

For every test procedure, the discussion of the achieved results is designed to allow two kinds of analyses:

- Type 1 - Reliability Analysis: To compare the general operating of each sensor (accelerometer and gyroscope) of the DUTs before and after the application of the vibration profile, in order to verify the capability of the DUT sensors to keep the expected performance once the stimulus, due to applied operating conditions, stops.

- Type 2 - Metrological characterization: To evaluate the DUT sensors operating under the application of the considered stimulus in order to quantify some performance index.

6.6.1.   Random vibration test

This section reports the results achieved during the application of the random vibration test as in [207], [214].

In particular, Fig. 6.20 and Fig. 6.21 report the evolution of RMS values measured by the accelerometers and gyroscopes of DUT#1 on X-axis and Y-axis, when the shaker has actuated the vibration only along the Z-axis. Both figures clearly highlight the three different zones of operation as in Section 6.5.1. In particular: (i) S_1 corresponds to the "Before Test" zone in which no vibration is applied, (ii) S_2 corresponds to the "Test zone", and (iii) S_3 corresponds to the "After Test"phase achieved after the vibration has been stopped.
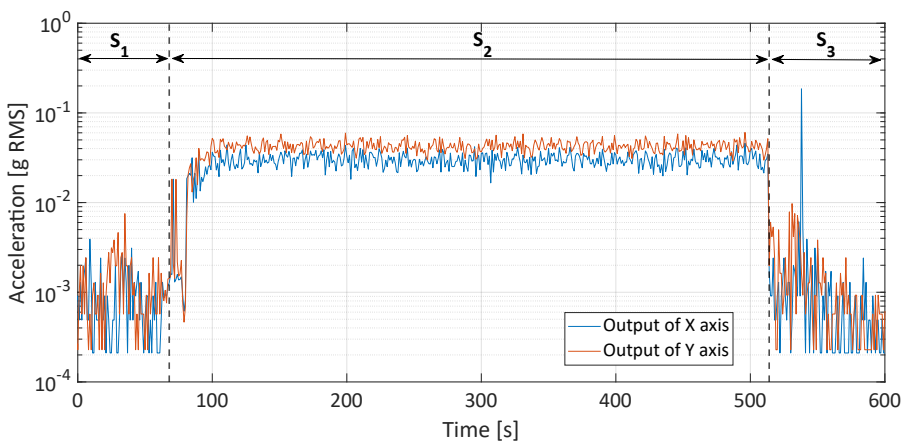
Fig. 6.20. Device #2: Accelerometer output during random vibration test (the vibration is applied on the Z-axis).
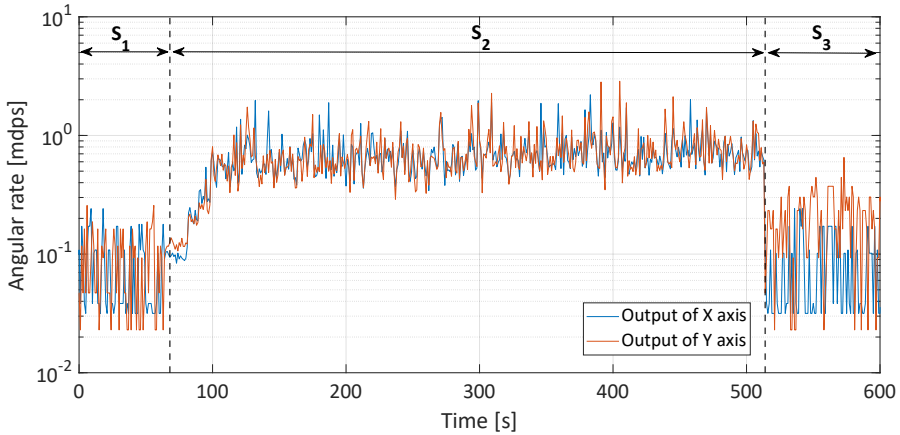
Fig. 6.21. Device #2: Gyroscope output during random vibration test (the vibration is applied on the Z-axis).

The most striking result to emerge from Fig. 6.20 and Fig. 6.21 is that both accelerometer and gyroscope show a sensitivity on the X-axis and Y-axis even if the vibration is actuated on the Z-axis. Indeed, in zone S_2, the RMS values measured by the sensors are significantly different from ones observed before and after the test. Similar trends have been observed for DUT #2 and DUT #3.

As for Type 1 analysis, TABLE VI.IX summarizes the results for all DUTs and for all the three axes by showing the mean value (μ) and standard deviation (σ) of RMS values observed in S_1 and S_3 in case of the accelerometer sensors.

From the values observed in TABLE VI.IX regarding the accelerometer sensors, the following main considerations can be drawn:

- Focusing the attention on the results achieved for the accelerometer sensor of DUT #1 (see the first row of TABLE VI.IX), they show, for each axis (x,y,z), the full compatibility (from a measurement point of view) of the results achieved in S_1 and S_3. This outcome means that the application of the considered vibration stimulus does not affect neither the accelerometer general operation nor the sensor calibration.

- As for DUT #2 and DUT #3, although the measured values of μ and σ are in some cases different from the case of DUT #1, the comparisons between the behaviors shown in S_1 and S_3 confirm the full compatibility of the related results for each axis.

Similarly to the previous case, the outputs of the gyroscope sensors are shown in TABLE VI.X in terms of mean value and standard deviation.

TABLE VI.IX

TYPE 1 ANALYSIS FOR THE THREE AXES OF THE ACCELEROMETER SENSORS DURING
RANDOM VIBRATION TEST.

DUT	X-Axis S_1 [g]		X-Axis S_3 [g]		Y-Axis S_1 [g]		Y-Axis S_3 [g]		Z-Axis S_1 [g]		Z-Axis S_3 [g]	
	μ	σ	μ	σ	μ	σ	μ	σ	μ	σ	μ	σ
#1	0.010	0.002	0.010	0.002	0.018	0.017	0.017	0.010	0.002	0.001	0.002	0.002
#2	0.003	0.001	0.003	0.001	0.003	0.019	0.003	0.008	-0.011	0.002	-0.011	0.002
#3	-0.018	0.002	-0.018	0.002	-0.019	0.019	-0.019	0.006	-0.023	0.002	-0.023	0.002

TABLE VI.X

TYPE 1 ANALYSIS FOR THE THREE AXES OF THE GYROSCOPE SENSORS DURING RANDOM
VIBRATION TEST.

DUT	X-Axis S_1 [°/s]		X-Axis S_3 [°/s]		Y-Axis S_1 [°/s]		Y-Axis S_3 [°/s]		Z-Axis S_1 [°/s]		Z-Axis S_3 [°/s]	
	μ	σ	μ	σ	μ	σ	μ	σ	μ	σ	μ	σ
#1	0.004	0.093	-0.006	0.088	0.002	0.100	0.011	0.100	-0.001	0.095	-0.028	0.099
#2	-0.021	0.126	-0.005	0.118	-0.021	0.120	-0.002	0.120	0.009	0.126	-0.077	0.131
#3	0.018	0.115	0.036	0.116	0.033	0.920	-0.062	1.300	-0.007	0.900	0.100	1.140

Focusing the attention on the results achieved for the gyroscope sensors, different values of μ were observed for S_1 and S_3 regardless the axis and the considered device. However, the observed values of σ cover these differences, which means that, once again, the application of the considered vibration stimulus does not affect neither the gyroscope general operation nor the calibration of the considered sensors.

As for the Type 2 analysis, during the application of the vibration profile the observed RMS values increase coherently with the input stimulus provided by the shaker as expected. However, even if the vibration is actuated only on one axis, a kind of sensitivity is observed also on the axis not excited during this test. In this work, the following parameters have been proposed to quantify such a generally unwanted sensitivity:

$$RR_{i,j} = \left| 20 \cdot log_{10} \frac{RMS_{i,S2}}{RMS_{j,S2}} \right| \tag{6.2}$$

$$SR_{i,j} = \left| 20 \cdot log_{10} \frac{RMS_{i,S2}}{RMS_{i,S1}} \right| \tag{6.3}$$

Where, i denotes the not excited (accelerometer or gyroscope) axis, j denotes the excited accelerometer axis, $RMS_{i,S2}$ and $RMS_{j,S2}$ the RMS values estimated in S_2 for the i and j axes, and $RMS_{i,S1}$ the RMS value estimated in S_1 for the i axis.

As a consequence, $RR_{i,j}$ describes the rejection ratio of the i axis when the excitation is applied on the j axis whereas, $SR_{i,j}$ provides the ratio between the spurious response of the DUT on the considered axis with respect to the expected value (i.e. the quite zone value). Of course, $RR_{i,j}$ should be as high as possible (∞ in the ideal case) whereas $SR_{i,j}$ should be as low as possible (0 in the ideal case).

TABLE VI.XI report the values of $RR_{i,j}$ for all the accelerometer sensors of the three DUTs.

TABLE VI.XI

REJECTION RATIOS FOR THE THREE AXES OF THE ACCELEROMETER SENSORS DURING RANDOM VIBRATION TEST.

DUT	EXCITED AXIS: X		EXCITED AXIS: Y		EXCITED AXIS: Z	
	$RR_{Y,X}$ [dB]	$RR_{Z,X}$ [dB]	$RR_{X,Y}$ [dB]	$RR_{Z,Y}$ [dB]	$RR_{X,Z}$ [dB]	$RR_{Y,Z}$ [dB]
#1	36.4	41.8	33.5	35.9	28.4	25.5
#2	33.2	35.7	40.5	40.2	29.7	25.5
#3	37.1	43.9	42.5	30.7	24.9	27.7

From the analysis of TABLE VI.XI, some considerations can be drawn:

- $RR_{i,j}$ falls in the range [25 dB ÷ 45 dB] regardless the considered DUT and the considered couple of axes (i and j);
- For each DUT, the worst performance (lowest values of rejection ratio) is observed for $RR_{x,z}$ and $RR_{y,z}$;
- DUT#1 and DUT#3 show the best rejection ratios in the case of $RR_{z,x}$, whereas DUT#2 shows the best performance in the case of $RR_{x,y}$.

The estimated spurious response ratios $SR_{i,j}$ are illustrated in TABLE VI.XII. From the analysis of the table the following considerations can be drawn:

- $SR_{i,j}$ falls in the range [8 dB ÷ 40 dB] regardless the considered DUT and the considered couple of axes (i and j). It means that the Spurious response ratios never approaches the zero value (ideal case).
- The worst cases are observed for the excitation on the z-axis (i.e. $SR_{x,z}$ and $SR_{y,z}$), coherently also with the results shown in TABLE VI.XI.

TABLE VI.XII

SPURIOUS RESPONSE RATIOS FOR THE THREE AXES OF THE ACCELEROMETER SENSORS
DURING RANDOM VIBRATION TEST.

DUT	EXCITED AXIS: X		EXCITED AXIS: Y		EXCITED AXIS: Z	
	$SR_{Y,x}$ [dB]	$SR_{Z,x}$ [dB]	$SR_{X,Y}$ [dB]	$SR_{Z,Y}$ [dB]	$SR_{X,z}$ [dB]	$SR_{Y,z}$ [dB]
#1	24.6	11.0	20.9	16.8	32.6	36.5
#2	19.9	15.7	23.3	11.8	23.5	31.5
#3	15.9	8.2	10.1	20.5	26.4	24.9

As for the gyroscope sensors, the meaning of $RR_{i,j}$ decays because the shaker does not apply any angular velocity. As a consequence, only the $SR_{i,j}$ parameter has been evaluated for the three gyroscopes under test. In this case, $SR_{i,j}$ allows comparing the working of the gyroscope between S_1 and S_2 regardless the excitation axis. TABLE VI.XIII reports the achieved results for each excited axis. From the analysis of such results, the following considerations can be drawn:

- $SR_{i,j}$ falls in the range [9 dB ÷ 37 dB] whatever be the DUT and the considered couple of axes (i and j). Therefore, also in this case the Spurious response ratios never approaches the zero value (ideal case).
- Once again, the worst cases are observed for the excitation on the z-axis (i.e. $SR_{x,z}$ and $SR_{y,z}$), coherently also with the results shown in TABLE VI.XI and TABLE VI.XII.

TABLE VI.XIII

SPURIOUS RESPONSE RATIOS FOR THE THREE AXES OF THE GYROSCOPE SENSORS DURING
RANDOM VIBRATION TEST.

DUT	EXCITED AXIS: X		EXCITED AXIS: Y		EXCITED AXIS: Z	
	$SR_{Y,x}$ [dB]	$SR_{Z,x}$ [dB]	$SR_{X,Y}$ [dB]	$SR_{Z,Y}$ [dB]	$SR_{X,z}$ [dB]	$SR_{Y,z}$ [dB]
#1	21.9	22.1	18.4	17.2	19.8	15.3
#2	11.8	11.2	9.9	17.0	16.9	15.9
#3	15.6	14.7	14.5	34.4	16.3	17.5

In summary, with reference to the Type 1 Analysis, the achieved results have shown that the proposed random vibration test does not affect the general operating and the calibration of both accelerometer and gyroscope sensors because, once the external stimuli have been stopped, the sensors recover its normal operating.

As for the Type 2 Analysis, some significant effects have been highlighted during the application of the external stimulus. In particular, thanks to the definition and the analysis of suitable rejection coefficients it has been highlighted how both the accelerometer and gyroscope sensors exhibit a significant sensitivity also on the not excited axes.

6.6.2.   Sinusoidal vibration test

As described in section 6.5.2.2. the sinusoidal vibration test requires to sweep the frequency from 20 Hz up to 2 kHz by continuously applying a sinusoidal stimulus for all the duration of the test. In addition, for each frequency sweep, three values of the actuated vibration magnitude, i.e. 2 g, 4 g and 8 g, respectively, were applied.

Also in this case, it is possible to identify three different zones of operations S_1, S_2, and S_3. Thus suggesting to consider the previously defined two kinds of analyses (i.e. Type 1 and Type 2) to investigate the effects of the tests on the considered Inertial Measurement Units as in [126], [214].

As for Type 1 analysis, TABLE VI.XIV and TABLE VI.XV summarize the achieved results for all DUTs and for all sensors axes by showing the means (μ) and standard deviations (σ) of RMS values observed in S_1 and S_3 in case of accelerometer and gyroscope respectively. From the values observed in both tables (8 g-stimulus magnitude is involved), similar considerations previously reported for the Random Vibration Test can be drawn. In particular, by comparing the values observed for μ and σ, in S_1 and S_3, the application of the Sinusoidal Vibration Test does not affect neither the general operation nor the calibration of both accelerometer and gyroscope sensors. This consideration is valid regardless the considered axis and the DUTs involved. Similar results have been obtained also during the 2 g-stimulus and 4 g-stimulus test.

TABLE VI.XIV

TYPE 1 ANALYSIS FOR THE THREE AXES OF THE ACCELEROMETER SENSORS DURING SINUSOIDAL VIBRATION TEST.

DUT	X-Axis S_1 [g]		X-Axis S_3 [g]		Y-Axis S_1 [g]		Y-Axis S_3 [g]		Z-Axis S_1 [g]		Z-Axis S_3 [g]	
	μ	σ	μ	σ	μ	σ	μ	σ	μ	σ	μ	σ
#1	0.010	0.002	0.010	0.002	-0.003	0.001	-0.003	0.001	-0.005	0.022	-0.006	0.011
#2	0.002	0.005	0.002	0.003	0.006	0.002	0.006	0.002	-0.022	0.026	-0.023	0.010
#3	-0.020	0.002	-0.020	0.002	0.033	0.002	0.034	0.002	0.014	0.031	0.012	0.007

TABLE VI.XV

TYPE 1 ANALYSIS FOR THE THREE AXES OF THE GYROSCOPE SENSORS DURING SINUSOIDAL
VIBRATION TEST.

DUT	X-Axis S_1 [°/s]		X-Axis S_3 [°/s]		Y-Axis S_1 [°/s]		Y-Axis S_3 [°/s]		Z-Axis S_1 [°/s]		Z-Axis S_3 [°/s]	
	μ	σ	μ	σ	μ	σ	μ	σ	μ	σ	μ	σ
#1	0.011	0.094	-0.021	0.094	-0.005	0.114	0.017	0.116	0.003	0.091	0.058	0.089
#2	0.017	0.106	-0.016	0.106	0.001	0.110	-0.010	0.106	-0.002	0.096	0.037	0.104
#3	-0.074	0.961	-0.159	0.675	-0.002	0.105	-0.298	0.100	0.000	0.107	-0.069	0.109

As for the Type 2 analysis, also in this case, during the application of the vibration profile the observed RMS values increases coherently with the input stimulus provided by the shaker. Indeed, as an example, Fig. 6.22 reports the evolution of the Root Mean Square values measured by the accelerometer of DUT #1 on y-axis, when the shaker has actuated a sinusoidal vibration with a stimulus-magnitude equal to 2 g along the y-axis. Note that the 2 g value provided by the shaker refers to a peak magnitude, while Fig. 6.22 (as well as the following figures) shows the RMS value acquired by the sensor.
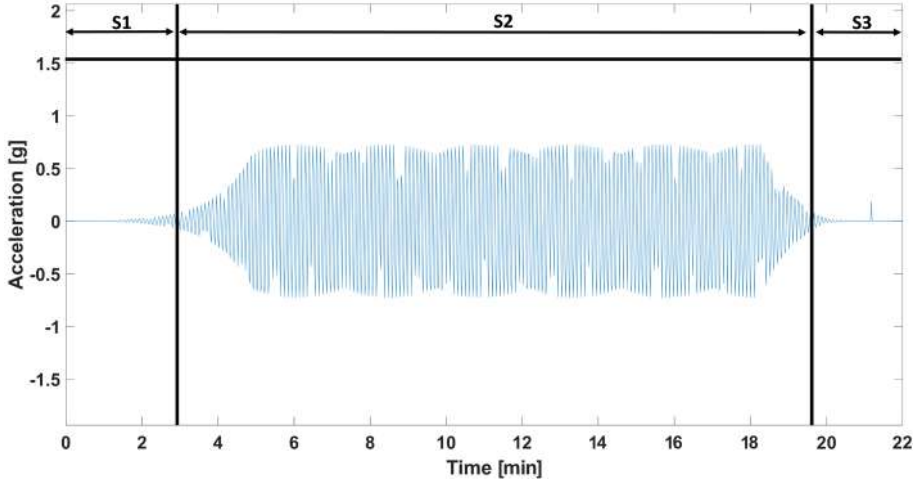
Fig. 6.22. DUT #1: output of the accelerometer sensor during sinusoidal vibration applied on the y-axis.

As it happened in the case of the random vibration test, also in the case of the sinusoidal vibration test, a kind of sensitivity has been observed on the axis not excited during the test and here not reported for a sake of brevity. Moreover, since the sinusoidal vibration test involves a frequency sweep, the observed

RMS values coming from the accelerometer and gyroscope sensors can be useful in order to analyze the frequency response of the systems. Fig. 6.23 reports the accelerometer sensor output of DUT #1, for the considered frequency sweeps actuated on the y-axis together with the corresponding applied profile stimulus. Note that the trends are reported as RMS values.
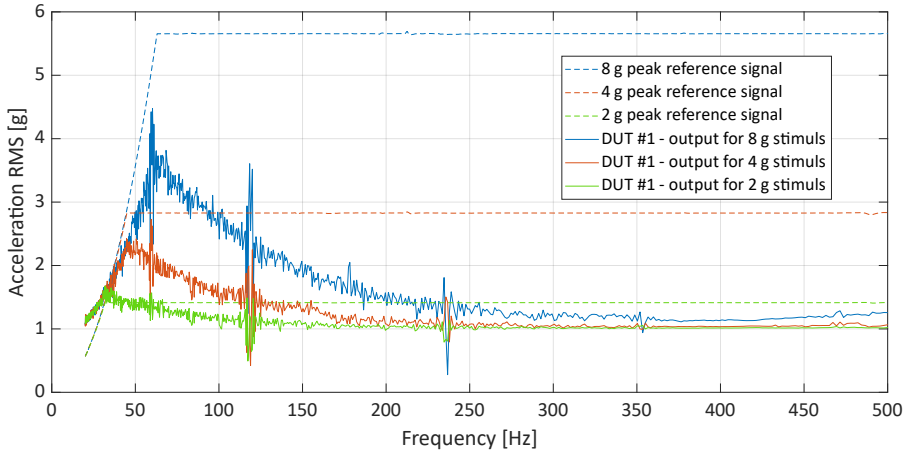
Fig. 6.23. DUT #1: accelerometer output versus frequency with a sinusoidal vibration applied on the y-axis.

Fig. 6.23 clearly shows that the accelerometer sensor has a low-pass filter behavior. This is due to the presence of the anti-aliasing filter, automatically inserted by the DUT once selected the sampling rate. In particular, since a sampling rate equal to 100 Hz has been selected, the 3 dB cut-off frequency of the anti-aliasing filter is nominally placed at 50 Hz and after such a frequency the accelerometer output generally decreases.

In more detail, focusing the attention on the case of the 4 g-stimulus magnitude (see Fig. 6.24), it is possible to verify the non-ideal response of the sensor. In fact, the sensor output is characterized by the presence of resonance zones highlighted by red circles in the figure in which very high variations of the gain are observable. The main criticality of such response is that it could make not forecastable the system frequency response.

Indeed, considering the transfer function shown in Fig. 6.25, we observed that even for frequencies greater than the cut-off (i.e. 50 Hz), the gain of the system reaches (or in some case overcomes) the one evaluated below the cut-off frequency, thus overcoming the expected gain (black dashed line) inside these zones. This behavior appears around a multiple of the frequency 60 Hz and could be imputable to unwanted mechanical resonance.
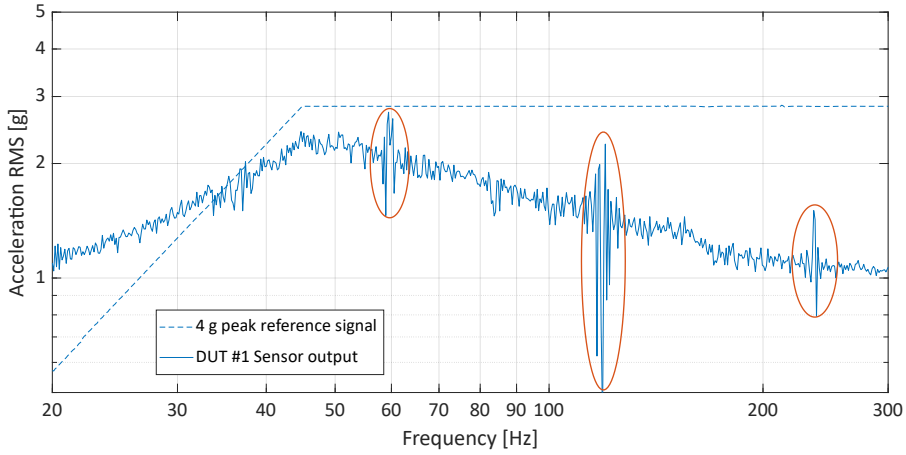
Fig. 6.24. Magnification of DUT #1 accelerometer output for the 4 g-stimulus magnitude applied on the y-axis.
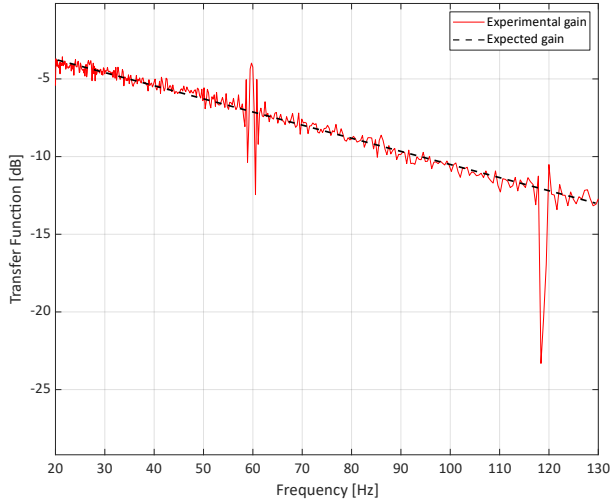
Fig. 6.25. Transfer function of the DUT #1 accelerometer output for the 4 g-stimulus magnitude applied on the y-axis.

To quantify the maximum deviation between the expected gain and the real one the Gain Deviation (GD_i) on the i-th axis has been defined and analysed:

$$GD_i = 20 \cdot log_{10} \frac{M_G}{E_G} \tag{6.4}$$

Where, E_G and M_G are the expected gain and the maximum measured gain, respectively, inside the first frequency resonance zone, on the i-th axis.

TABLE VI.XVI reports the GD_i values for all considered DUTs, excitation axes, stimulus magnitude, and accelerometer sensors. Analyzing the table, the following considerations can be highlighted:

- The values of GD_i fall in the range [2.0 dB, 4.0 dB];
- The stimulus magnitude does not significantly affect the value of GD whatever be the excited axis and the DUT.

TABLE VI.XVI

GD_i OF THE THREE AXES OF THE ACCELEROMETERS DURING SINUSOIDAL VIBRATION TEST.

DUT	GD_x [dB]	GD_y [dB]	GD_z [dB]
2g-stimulus magnitude			
#1	2.0	2.7	3.0
#2	2.9	2.7	2.5
#3	2.8	3.1	2.2
4g-stimulus magnitude			
#1	3.5	3.2	2.9
#2	3.4	2.8	2.8
#3	4.0	3.0	2.5
8g-stimulus magnitude			
#1	2.9	2.1	2.5
#2	2.5	2.6	3.0
#3	3.2	2.9	2.4

As for the gyroscope sensors, Fig. 6.26 reports the output acquired by DUT #1 on the three axes when the 4 g-magnitude sinusoidal test has been applied. As it is possible to see in the figure, there are unexpected angular rotations on all the three axes over the considered frequency sweep range, and once again, some resonance zones can be identified.

To evaluate such effect, the proposed figure of merit, namely Spurious Gain (hereinafter SG_i), is given by the ratio between the maximum RMS value evaluated over the whole frequency sweep range (i.e. S_2) and RMS value evaluated over the quite zone (i.e. S_1), for each axis, as defined in the following:

$$SG_i = 20 \cdot log_{10} \frac{\max_{f \in [f_{min}, f_{max}]} RMS_{S2}}{RMS_{S1}} \tag{6.5}$$
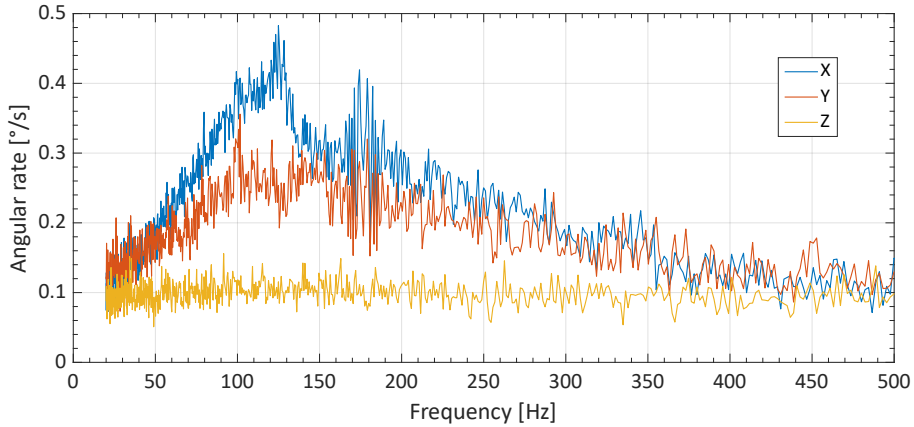
Fig. 6.26. DUT #1 gyroscope output (on all axes) versus frequency with a 4 g-magnitude sinusoidal vibration applied on the y-axis accelerometer sensor.

TABLE VI.XVII reports the value observed for SG_i for each DUT when the 4 g-stimulus magnitude sinusoidal vibration is applied. It proves how the gyroscope sensors are generally influenced by spurious gain on each sensor axis. In particular, the values of SG_i fall in the range [3.0, 20.0 dB] for each DUT, which means that a significant sensitivity to stimulus applied on the accelerometer axes is still observable as it happened in the case of Random Vibration test.

TABLE VI.XVII

SD_i OF THE THREE AXES OF THE GYROSCOPE SENSORS FOR THE 4 G-STIMULUS MAGNITUDE DURING SINUSOIDAL VIBRATION TEST.

DUT	EXCITED AXIS: X			EXCITED AXIS: Y			EXCITED AXIS: Z		
	SG_X [dB]	SG_Y [dB]	SG_Z [dB]	SG_X [dB]	SG_Y [dB]	SG_Z [dB]	SG_X [dB]	SG_Y [dB]	SG_Z [dB]
#1	17.6	9.9	19.3	13.8	8.8	4.3	8.7	4.7	4.3
#2	15.9	19.8	11.2	4.9	8.1	4.6	5.1	4.2	3.7
#3	5.2	4.3	4.3	18.0	4.9	3.4	14.4	7.6	4.4

6.6.3. Vibration step-test

This section reports the results of the vibration step-test carried out to estimate the frequency behavior of the three identical IMUs under test as in [29]. Similarly, to the previous test, Also in this case, it is possible to identify three different zones of operations S_1 (Before test), S_2 (Test zone) and S_3 (After test).

The first part of the experimental test is the reliability analysis aiming at evaluates the destructive or the miss calibration effect of the test on the devices under investigation. For this reason, it considers only the analyses of the S_1 and S_3 zones for each sensor of every IMUs (i.e. accelerometer and gyroscope).

TABLE VI.XVIII shows the mean values μ and the standard deviations σ acquired by accelerometers and gyroscopes toward X-axis before and after the test. The table is divided into three main sections, each one reports the results achieved when the vibration step-test is actuated toward a different axis. Similarly,

TABLE VI.XIX reports the results acquired by the sensors toward the Y-axis and TABLE VI.XX reports the data regarding the Z-axis of gyroscopes and accelerometers.

As can be seen from the tables, the measured values show for each sensor axis of both the accelerometer and gyroscope, full compatibility of the results achieved in the zones before and after the test. This is true for every step sine excitation applied on all the axes. This fact represents two fundamental results: i) the step sine test applied has not damaged both the accelerometers and the gyroscopes, ii) also in terms of sensor calibration (see the average values), the tests seem not to affect both of them.

TABLE VI.XVIII

TYPE 1 ANALYSIS: MEAN AND STANDARD DEVIATION OF X-AXIS SENSORS OUTPUTS.

DUT	ACCELEROMETER [g RMS]				GYROSCOPE [mdps RMS]			
	BEFORE TEST S_1		AFTER TEST S_3		BEFORE TEST S_1		AFTER TEST S_3	
	μ	σ	μ	σ	μ	σ	μ	σ
EXCITED AXIS: X								
#1	0.000	0.000	0.000	0.001	-0.014	0.133	0.032	0.129
#2	0.000	0.002	0.000	0.002	0.013	0.108	-0.153	0.126
#3	-0.001	0.002	0.000	0.002	0.018	0.105	0.023	0.112
EXCITED AXIS: Y								
#1	0.000	0.001	0.000	0.001	-0.032	0.105	-0.089	0.092
#2	0.000	0.002	0.000	0.002	0.009	0.113	-0.154	0.107
#3	0.000	0.001	0.000	0.001	0.003	0.074	0.060	0.094
EXCITED AXIS: Z								
#1	0.000	0.002	-0.001	0.002	0.000	0.127	-0.023	0.099
#2	0.000	0.002	-0.001	0.002	0.001	0.117	-0.026	0.110
#3	0.000	0.001	0.000	0.002	-0.015	0.094	-0.005	0.089

Table VI.XIX

Type 1 Analysis: Mean and standard deviation of Y-axis sensors outputs.

DUT	Accelerometer [g RMS]				Gyroscope [mdps RMS]			
	Before Test S_1		After Test S_3		Before Test S_1		After Test S_3	
	μ	σ	μ	σ	μ	σ	μ	σ
Excited axis: X								
#1	0.000	0.000	0.000	0.001	-0.014	0.133	0.032	0.129
#2	0.000	0.002	0.000	0.002	0.013	0.108	-0.153	0.126
#3	-0.001	0.002	0.000	0.002	0.018	0.105	0.023	0.112
Excited axis: Y								
#1	0.000	0.001	0.000	0.001	-0.032	0.105	-0.089	0.092
#2	0.000	0.002	0.000	0.002	0.009	0.113	-0.154	0.107
#3	0.000	0.001	0.000	0.001	0.003	0.074	0.060	0.094
Excited axis: Z								
#1	0.000	0.002	-0.001	0.002	0.000	0.127	-0.023	0.099
#2	0.000	0.002	-0.001	0.002	0.001	0.117	-0.026	0.110
#3	0.000	0.001	0.000	0.002	-0.015	0.094	-0.005	0.089

Table VI.XX

Type 1 Analysis: Mean and standard deviation of Z-axis sensors outputs.

DUT	Accelerometer [g RMS]				Gyroscope [mdps RMS]			
	Before Test S_1		After Test S_3		Before Test S_1		After Test S_3	
	μ	σ	μ	σ	μ	σ	μ	σ
Excited axis: X								
#1	0.000	0.000	0.000	0.001	-0.014	0.133	0.032	0.129
#2	0.000	0.002	0.000	0.002	0.013	0.108	-0.153	0.126
#3	-0.001	0.002	0.000	0.002	0.018	0.105	0.023	0.112
Excited axis: Y								
#1	0.000	0.001	0.000	0.001	-0.032	0.105	-0.089	0.092
#2	0.000	0.002	0.000	0.002	0.009	0.113	-0.154	0.107
#3	0.000	0.001	0.000	0.001	0.003	0.074	0.060	0.094
Excited axis: Z								
#1	0.000	0.002	-0.001	0.002	0.000	0.127	-0.023	0.099
#2	0.000	0.002	-0.001	0.002	0.001	0.117	-0.026	0.110
#3	0.000	0.001	0.000	0.002	-0.015	0.094	-0.005	0.089

The second part of the experimental investigation during the vibration step-test has the aim of investigating the operation of the IMUs at different frequency. For the sake of brevity, the analysis will regard only the accelerometer's outputs of the three identical DUTs.

Considering the test actuated along X-axis, the experimental results are reported in Fig. 6.27 where the RMS values, over each single step sine length window, are shown.
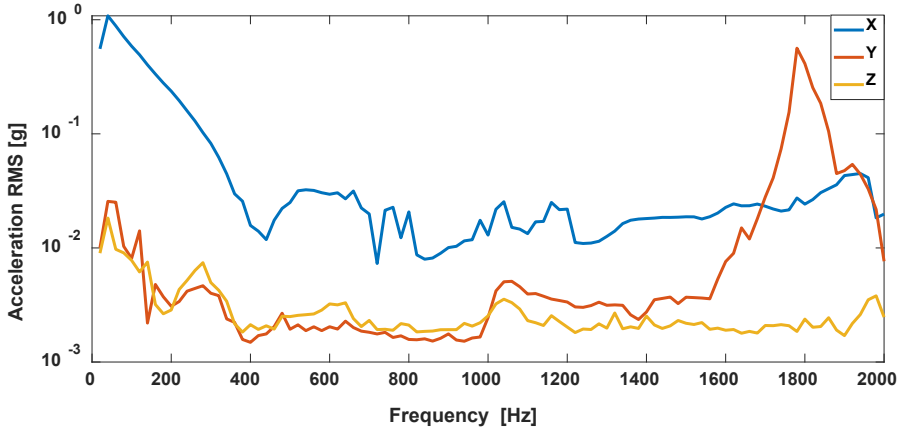
Fig. 6.27. RMS accelerometer's output with stimulus applied to the X-axis.

Similarly, Fig. 6.28 shows the results achieved when the vibration is actuated toward Y-axis while Fig. 6.29 refers to Z-axis.
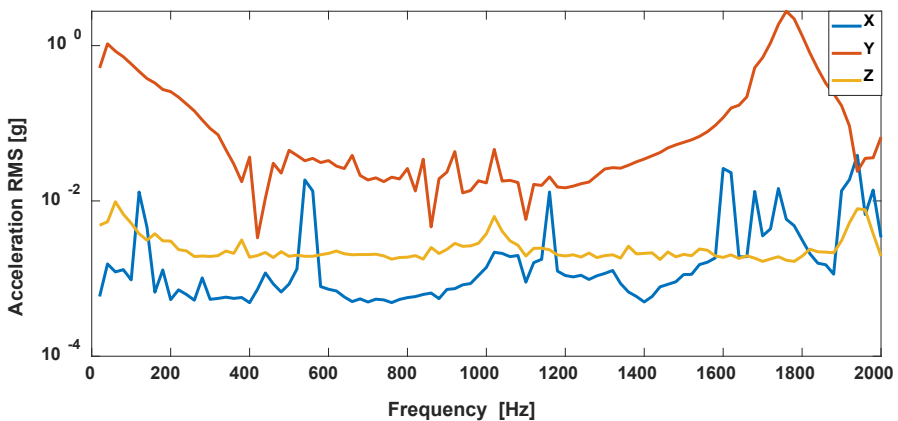
Fig. 6.28. RMS accelerometer's output with stimulus applied to the Y-axis.
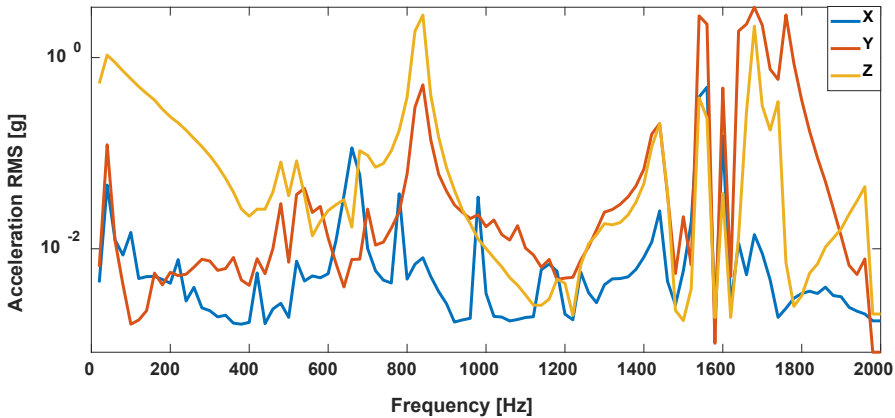
Fig. 6.29. RMS accelerometer's output with stimulus applied to the Z-axis.

First of all, it is interesting to look at the output of the sensors toward the axes not interested directly by the excitation. This means to look at Y-axis (red trend) and Z-axis (yellow trend) in Fig. 6.27, while X-axis (blue trend) and Z-axis (yellow trend) are the trend of interest in Fig. 6.28 and X-axis (blue trend) and Y-axis (red trend) are the trend of interest in Fig. 6.29. It can be seen that independently from the axis on which the stimulus is applied, all the accelerometer's show an unexpected behavior. More in detail, such outputs are significantly different from zero despite no vibration is actuated toward their reference. This fact means that the devices suffer of an undesired cross-axis sensitivity, a result that have been accurately and thoroughly discussed in section 6.6.1. (random vibration test) and 6.6.2 (sinusoidal vibration test).

The second significant result is retrieved, analyzing all the axes outputs: also if an output data rate has been set to 100Hz, which automatically introduce a low-pass filter on the outcoming data at ODR/2 (50 Hz), the outputs measured by the sensors follow the expectation only up to 400 Hz stimulus. After that, the outputs of all the axis start present suddenly gains and not linear behaviors. Furthermore, it is important to highlight the operation of all the axes with high frequencies stimulus. In such case, all the sensors measure high acceleration levels, which are not expected. The worst behavior seems to be exhibited by the application of stimulus on the Z-axes, the same results, previously mentioned, have been obtained for all the DUTs under test, confirming the presence of an important deviation of the operation from the expected one. Also, for the gyroscopes, similar considerations can be drawn from the analysis of RMS values achieved over the step sine tests.

6.6.4.   Sine-on-Random vibration test

In this section the experimental results obtained during the excitation of the three DUTs with the Sine-on-Random vibration profile (see section 6.5.2.4) are reported. The test aims to evaluate both the potential failure mechanisms or any possible damages on the DUTs and analyze their operation during the test's execution. For this reason, the experimental results section aims at two kind of analysis [246], [247]:

- Type 1 analysis: it reports the results of an analysis "Before-After" to investigate reliability, sensor miss-calibration, etc.
- Type 2 analysis: it reports the evaluation of few particular indexes devoted to the exploration of the DUT's behaviors under the excitations.

Even if the DUT is factory calibrated, to eliminate residual gain and offset errors due to the final installation and/or soldering procedure on development board, an initial 6-point tumble sensor calibration has been taken into account as in [246], [247].

Starting from the Type 1 analysis, this test aims to verify the impact of the proposed excitation on the DUTs. Generally, the test can report unwanted inducted miscalibration on the sensors after the test or permanent damages.

The outcome of these analyses is extremely important. Indeed, the evidence that no critical influences are exhibit after the tests reveal that the analysis during the test zones (reported in the following) has significance. At the same time, the Type 1 analysis can show how much DUTs are reliable in terms of any potential failure mechanisms or any possible damages during the entire experimental test.

For the sake of explanation, TABLE VI.XXI reports, for the three DUTs, the mean value μ and standard deviation σ of the acquisitions before (zone S_1) and after (zone S_3) the application of the test.

TABLE VI.XXI refers to the service condition SC 1 (for more detail see TABLE VI.V in section 6.5.2.4) and it illustrates all the five repetitions of test carried out consecutively for the sake of measurement reproducibility.

For the sake of brevity, the table illustrates only the mean and standard deviation acquired by the accelerometer sensors when the sine-on-random vibration test with severity SC 1 is applied on the X-axis. However, quite similar results have been obtained considering both the excitation on the Y-axis and Z-axis and considering all the other Service Conditions (SC2, SC3, and SC4).

TABLE VI.XXI

TYPE 1 ANALYSIS FOR THE THREE AXES OF THE ACCELEROMETER SENSORS WHEN THE
EXCITATION IS APPLIED ON THE X-AXIS.

REPETITION	X-axis [g]				Y-axis [g]				Z-axis [g]			
	BEFORE TEST S_1		AFTER TEST S_3		BEFORE TEST S_1		AFTER TEST S_3		BEFORE TEST S_1		AFTER TEST S_3	
	μ	σ	μ	σ	μ	σ	μ	σ	μ	σ	μ	σ
DUT #1												
#1	0.0013	0.0017	0.0013	0.0017	-0.0003	0.0019	-0.0003	0.0019	-0.0003	0.0019	-0.0003	0.0019
#2	-0.0002	0.0144	-0.0005	0.0139	0.0006	0.0017	0.0003	0.0017	0.0006	0.0017	0.0003	0.0017
#3	-0.0008	0.0016	-0.0006	0.0016	0.0007	0.0021	0.0008	0.0020	0.0007	0.0021	0.0008	0.0020
#4	0.0005	0.0017	0.0005	0.0017	-0.0007	0.0019	-0.0006	0.0018	-0.0007	0.0019	-0.0006	0.0018
#5	0.0008	0.0134	0.0006	0.0134	0.0018	0.0017	0.0015	0.0017	0.0018	0.0017	0.0015	0.0017
DUT #2												
#1	-0.0004	0.0016	-0.0001	0.0016	0.0001	0.0020	0.0002	0.0020	0.0001	0.0020	0.0002	0.0020
#2	-0.0012	0.0017	-0.0012	0.0017	0.0001	0.0019	0.0001	0.0019	0.0001	0.0019	0.0001	0.0019
#3	-0.0004	0.0139	-0.0006	0.0124	0.0011	0.0017	0.0008	0.0017	0.0011	0.0017	0.0008	0.0017
#4	-0.0003	0.0017	-0.0004	0.0017	-0.0006	0.0020	-0.0006	0.0021	-0.0006	0.0020	-0.0006	0.0021
#5	-0.0001	0.0017	-0.0001	0.0017	0.0011	0.0019	0.0011	0.0019	0.0011	0.0019	0.0011	0.0019
DUT #3												
#1	0.0010	0.0125	0.0006	0.0125	-0.0002	0.0017	-0.0002	0.0017	-0.0002	0.0017	-0.0002	0.0017
#2	-0.0005	0.0017	-0.0001	0.0017	0.0002	0.0021	0.0003	0.0073	0.0002	0.0021	0.0003	0.0073
#3	-0.0009	0.0017	-0.0009	0.0017	-0.0001	0.0019	-0.0002	0.0019	-0.0001	0.0019	-0.0002	0.0019
#4	0.0004	0.0126	0.0003	0.0120	-0.0002	0.0017	-0.0003	0.0017	-0.0002	0.0017	-0.0003	0.0017
#5	-0.0005	0.0017	-0.0006	0.0017	-0.0002	0.0072	-0.0003	0.0021	-0.0002	0.0072	-0.0003	0.0021

According to TABLE VI.XXI, (better represented in Fig. 6.30), full compatibility (from a measurement point of view) among all the "before S_1" and "after S_3" conditions has been discovered for all the repetitions and for all the considered sensors. Thus, the following considerations can be drawn:

  i) the tests have not influenced the devices correct operability;
  ii) non-miscalibration phenomenon (i.e., a changing of the mean value) has been observed during all the tests.

More in detail, Fig. 6.30 reports the error plots of the DUT#1 considering the X-axis of the accelerometer. The mean values (blue and red stars) and standard deviation (blue and red vertical lines) used to build Fig. 6.30 have been extracted from TABLE VI.XXI. In particular, the comparison of the measurements relative to the single repetition can be easily evaluated by analyzing the blue lines (relative to the zone S_1 before the test) and the red lines (relative to the zone S_3 after the test).
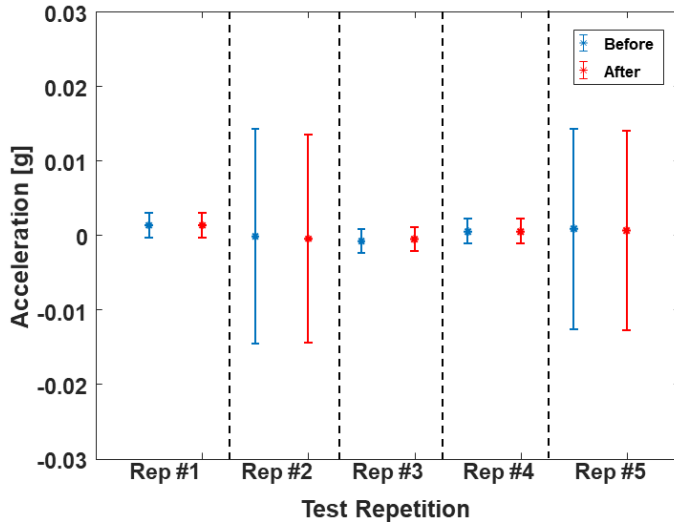
Fig. 6.30. Test Condition SC1: Error Bar for the Type 1 analysis of the accelerometer embedded in DUT#1 when the excitation is applied on the X-axis.

The same approach has been considered for the gyroscope sensors, obtaining the full compatibility of the output by a measurements point of view.

As for the Type 2 analysis, different indexes have been considered to evaluate unwanted sensitivity phenomena on axes different from the excited ones. In particular, the Rejection Ratios $RR_{i,j}$ defined in equation (6.2) and the Spurious response Ratios $SR_{i,j}$ defined in equation (6.3) have been evaluated for the three axes of the sensors.

Furthermore, due to the nature of the sine-on-random vibration test (i.e. a sine vibration at a single frequency belonging to a particular scenario related to the slow movement of suspended masses in vehicles, with the addition of a wideband random vibration noise), the Signal to Noise Ratio (SNR) has been evaluated with and without the random vibration introduced in each SC conditions.

Starting from the $RR_{i,j}$ index analysis, TABLE VI.XXII reports these values calculated for the severity SC1 during the test zone. In particular, to prove that tests results are consistent throughout the "Test Zone S2", five repetitions for all the DUTs considering the excitation on all the axes have been reported.

TABLE VI.XXII
REJECTION RATIOS FOR THE THREE AXES OF THE ACCELEROMETERS (SEVERITY SC 1).

Rep.	$RR_{Y.X}$ [dB]	$RR_{Z.X}$ [dB]	$RR_{X.Y}$ [dB]	$RR_{Z.Y}$ [dB]	$RR_{X.Z}$ [dB]	$RR_{Y.Z}$ [dB]
DUT #1						
#1	0.2	22.3	32.9	26.6	25.6	0.2
#2	0.0	22.4	32.9	26.6	25.6	0.2
#3	0.1	22.2	32.9	26.6	25.7	0.2
#4	0.1	22.3	33.0	26.7	25.8	0.5
#5	0.0	22.4	33.1	26.8	25.8	0.2
DUT #2						
#1	2.9	27.2	22.7	55.6	6.5	52.1
#2	3.0	27.3	22.3	46.1	8.7	22.4
#3	3.2	27.3	22.1	55.5	7.1	49.5
#4	3.0	27.3	22.0	57.5	5.2	49.3
#5	3.1	27.3	21.9	57.8	4.8	52.8
DUT #3						
#1	7.6	23.5	33.4	32.7	2.6	0.5
#2	7.3	23.5	33.8	32.8	2.7	0.5
#3	6.8	23.4	33.9	32.9	2.8	0.4
#4	6.9	23.5	33.5	32.9	2.9	0.3
#5	6.6	23.4	34.1	32.8	2.9	0.4

Ideally, the $RR_{i,j}$ should tend to infinite, representing the ideal case where the excitation provided on an axis does not influence the non-excited axis considered for the analysis. The analysis of TABLE VI.XXII can lead to several considerations:

- With except for one case (i.e., DUT#2, Rep. 2), the achieved results highlights good repeatability regardless the considered DUT and the considered $RR_{i,j}$.
- All DUTs generally show a non-ideal behavior in terms of cross-sensitivity for some couples of axes. This can be imputable to their

internal structure, which cannot perfectly avoid the partition of mechanical stress on a not excited axis.

- As for DUT#1, the worst performance is observed for $RR_{y,x}$ and for $RR_{y,z}$ which means that the Y-axis is the most sensitive to vibrations applied on the other axes (x and z, respectively).
- As for DUT#2, the worst performance is observed for $RR_{y,x}$, and for $RR_{x,z}$ which means that both the Y-axis and the X-axis are the most sensitive to vibrations applied on the other axes (x and z, respectively).
- As for DUT#3, the worst performance is observed for $RR_{x,z}$ and for $RR_{y,z}$ which means that the excitation on the Z-axis brings to the highest cross-sensitivity concerning the other axes.
- The different behaviors among the DUTs in terms of both $RR_{i,j}$ values (for a given couple of i,j they show different values of $RR_{i,j}$) and "worst couples of axes" can be due to the intrinsic features' dispersion of the considered low-cost DUTs.

The results reported in TABLE VI.XXII consider only severity SC 1 for the accelerometers. However, similar behaviors can be drawn also for SC 2, SC 3, and SC 4 profiles and for gyroscope sensors. Fig. 6.31 and Fig. 6.32 show the mean values and the standard deviations of the $RR_{i,j}$ calculated over the five repetitions for each SC of DUT#1 considering respectively accelerometer in Fig. 6.31 and gyroscope in Fig. 6.32.
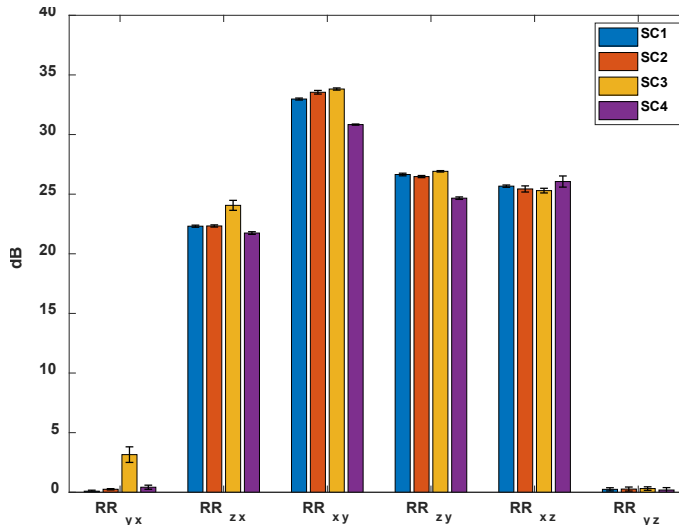
Fig. 6.31. Bar graph of the mean value of the $RR_{i,j}$ indexes over all the repetitions for the different SC conditions (accelerometer of DUT#1 is involved).
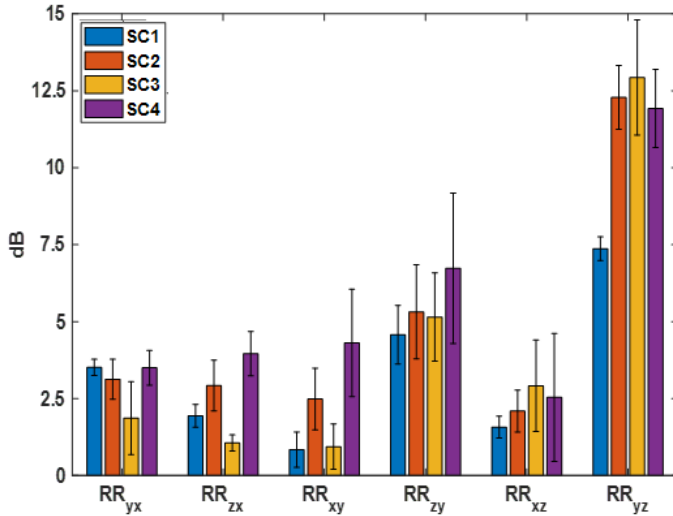
Fig. 6.32. Bar graph of the mean value of the $RR_{i,j}$ indexes over all the repetitions for the different SC conditions (gyroscope of DUT#1 is involved).

Comparing the behaviors obtained for different service conditions, it has been revealed a weak influence of the particular frequency of the sinusoidal of each SC on the $RR_{i,j}$ value. Similar results have been achieved also in the case of the other IMU under test (i.e. DUT #2 and DUT #3).

As for the analysis of the $SR_{i,j}$, note that such a figure of merit aims at the spurious rejection ratio among the measures regarding the quiet zone before each test S_1 and the actual test zone S_2 for each one of the non-excited axes. This index should be ideally zero, representing the scenario in which applying the excitation on a particular axis j, it does not influence the ratio among the measured RMS value of a non-excited axis i, evaluated before and during the stimulus's application.

TABLE VI.XXIII reports the $SR_{i,j}$ indexes (SC 1 condition is involved) for the three DUTs and five repetitions. Looking at the results reported in the table, some considerations can be drawn:

- The first and the last column of TABLE VI.XXIII, representing the evaluation of the spurious rejection analysis for the Y-axis when excitation is applied on the X-axis and the Z-axis, respectively, reveals to be the worst case. Therefore, once again, the lower rejection ability of the Y-axis seems to be confirmed.
- With except of few cases (i.e., DUT#2-Rep.2, DUT#3-Rep.1 and DUT#3-Rep.5), whatever be the DUT, the achieved results show good repeatability.

198

- Again, the differences among the DUTs in terms of $SR_{i,j}$ can be imputable to the intrinsic features' dispersion of the considered low-cost DUTs.

TABLE VI.XXIII
SPURIOUS REJECTION RATIOS FOR THE THREE AXES OF THE ACCELEROMETER (SEVERITY SC 1).

Rep.	$SR_{Y.X}$ [dB]	$SR_{Z.X}$ [dB]	$SR_{X.Y}$ [dB]	$SR_{Z.Y}$ [dB]	$SR_{X.Z}$ [dB]	$SR_{Y.Z}$ [dB]
DUT #1						
#1	52.8	30.7	23.4	29.8	27.7	53.1
#2	52.5	30.1	23.2	29.5	27.4	52.8
#3	52.2	30.1	23.0	29.3	26.6	52.1
#4	53.0	30.9	23.4	29.8	28.5	53.2
#5	51.2	28.9	22.8	29.0	25.9	51.4
DUT #2						
#1	50.0	25.7	35.7	37.5	42.7	43.2
#2	49.9	25.6	36.1	37.5	40.9	41.6
#3	48.6	24.4	36.1	37.2	34.1	45.4
#4	49.6	25.4	34.9	35.6	36.8	48.4
#5	49.7	25.5	36.8	37.3	36.8	48.5
DUT #3						
#1	45.4	29.4	23.5	24.1	37.9	40.0
#2	45.5	29.3	22.9	23.9	38.6	50.8
#3	45.8	29.2	23.0	24.0	38.8	51.1
#4	46.3	29.7	23.8	24.4	38.5	51.1
#5	46.5	29.7	22.9	24.2	39.7	42.3

Similar results have been obtained for the other SCs in the case of the accelerometer sensors, as showed in Fig. 6.33. In such case, the similar behaviors obtained among the different SCs reveal a low influence of the particular SC's sinusoidal frequency on $SR_{i,j}$.

As for the gyroscope sensors, Fig. 6.34 shows how the behavior is less regular respect to the accelerometer sensors. Indeed, in the case of $SR_{y,x}$ and $SR_{z,x}$, such values are weakly influenced by the considered SC (i.e., main frequency of the sinusoidal vibration), whereas in the other cases ($SR_{x,y}$, $SR_{z,y}$, $SR_{x,z}$ and $SR_{y,z}$) at least one condition between SC3 or SC4 show remarkably higher values.
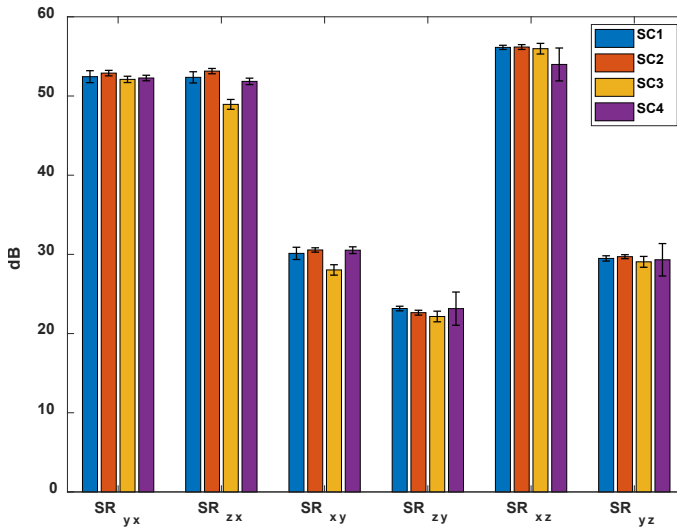
Fig. 6.33. Bar graph of the mean value of the $SR_{i,j}$ indexes over all the repetitions for the different SC conditions (accelerometer of DUT#1 is involved).
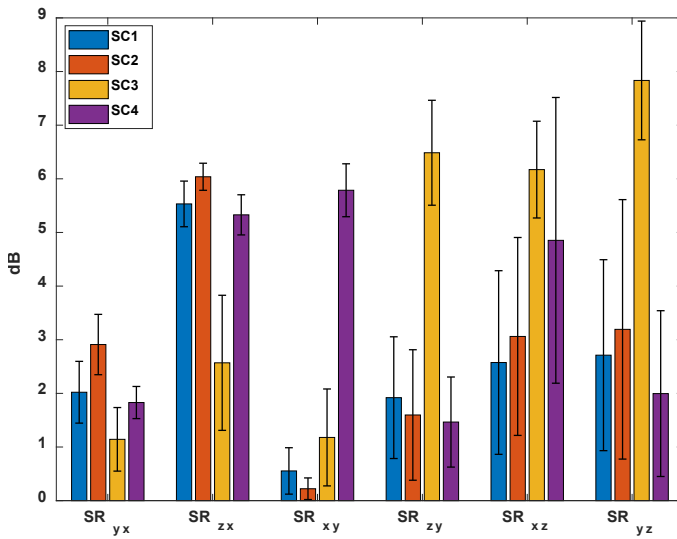
Fig. 6.34. Bar graph of the mean value of the $SR_{i,j}$ indexes over all the repetitions for the different SC conditions (gyroscope of DUT#1 is involved).

These results can be imputable to the gyroscope's intrinsic features: indeed, typically, they are devoted to measure only the rotational rate; however, in a real scenario, gyroscopes exhibit sensitivity to acceleration mostly due to the asymmetry of their micromachining inaccuracies and mechanical designs. These facts lead to significant sensitivity to linear acceleration and vibration

rectification, representing the largest error source. More importantly, low-cost gyroscopes are often not optimized for vibration rejection since they are generally designed using compact and straightforward mechanical systems. In addition gyroscopes are prone to drift, representing an additional error source. This phenomenon is mainly due to two causes: a slow-changing, named bias instability and a higher frequency noise variable reported in scientific literature as Angular Random Walk (ARW).

The final analysis performed after the sine-on-random vibration test aims to compare the Signal to Noise Ratio (SNR) indexes calculated during the tests and the one calculated considering only the single sine vibration (without the addition of the random noise vibration in the range 200 Hz – 2000 Hz).

According to the Nyquist criterium, the DUT under test, selecting an output data rate (ODR) of 119 Hz, applies a low pass filter with a cut-off frequency of 50 Hz for both the gyroscope and accelerometer. The introduction of the low pass filter with the reported specification is fundamental to avoid the aliasing phenomena. Consequently, this filter should eliminate the noise above the Nyquist frequency, mixed down into the baseband, improving the SNR.

To evaluate the SNR on each acquisition, a MATLAB built-in function (snr) available in the Signal Processing Toolbox has been employed. This function is able to calculate the signal's spectrum and automatically labels its main features as the fundamental component, the DC value, the harmonics, and the noise. The SNR analysis leads to evaluate its variation with and without random noise on a defined sine vibration (the main component of SC1, SC2, and SC3 condition, respectively 5 Hz, 10 Hz, and 15 Hz). These indications can qualify the sensors' ability to reject the vibration noise above the Nyquist frequency that, due to the nature of the DUTs (internal LPF with a cut-off frequency of 50 Hz in the proposed setup), should be irrelevant. To be valid, this analysis must be done on accelerometers' signal acquired on the same axes of the excitations.

TABLE VI.XXIV compares the reference SNR (achieved when no random vibration is applied) against the SNR achieved in the case of random vibration superimposed to the sinusoidal one in the case of SC 1 and all DUTs. Looking at results, the following considerations can be drawn:

- Since the SNRs values significantly decrease concerning the reference ones, it proves how the real behavior of the antialiasing LPF filter is sensitive to unexpected contributions at low-frequency even if the random vibrations have been generated in the frequency range from 200 Hz to 2000 Hz (which is higher than the filter cut-off frequency).

- The SNR calculation over all the DUTs considering the different repetitions and the excited axis, respectively, show good repeatability (over the 5 repetitions) regardless the DUT and the considered axis.
- According to the behaviors revealed with $RR_{i,j}$ and $SR_{i,j}$, also in this case, the SNR indexes calculated for the Y-axis during its excitation is smaller concerning the other ones, representing the lowest immunity (i.e., the higher sensitivity) to the random noise.

TABLE VI.XXIV

BAR GRAPH OF THE MEAN VALUE OF THE SNR OVER ALL THE REPETITIONS FOR THE DIFFERENT SC1, SC2, SC3 CONDITIONS AND REFERENCE (ACCELEROMETER OF DUT#1 IS INVOLVED).

REP.	SNR$_X$ [dB]	REFERENCE SNR$_X$ [dB]	SNR$_Y$ [dB]	REFERENCE SNR$_Y$ [dB]	SNR$_Z$ [dB]	REFERENCE SNR$_Z$ [dB]
DUT #1						
#1	13.3		7.1		12.0	
#2	13.6		7.3		12.3	
#3	13.4	27.8	7.1	30.1	11.7	28.5
#4	13.7		7.2		12.1	
#5	13.3		7.1		11.7	
DUT #2						
#1	10.8		2.3		11.8	
#2	10.8		2.4		12.3	
#3	11.0	27.3	2.6	28.5	12.2	26.2
#4	11.1		2.5		12.3	
#5	11.0		2.4		11.8	
DUT #3						
#1	9.2		5.2		9.4	
#2	9.9		5.1		9.8	
#3	9.9	26.2	5.1	25.7	9.8	27.3
#4	10.1		5.0		9.8	
#5	10.2		5.0		9.9	

Similar behaviors have been achieved in the case of SC2 and SC3, as shown in Fig. 6.35, where the mean values of the five repetitions of the SNR have been reported for all the SCs with respect to the reference SNR, in the case of

DUT#1. In particular, regardless the SC, an SNR decreasing (concerning the reference one) is clearly observable. Finally, similar behaviors have been achieved for DUT#2 and DUT#3.
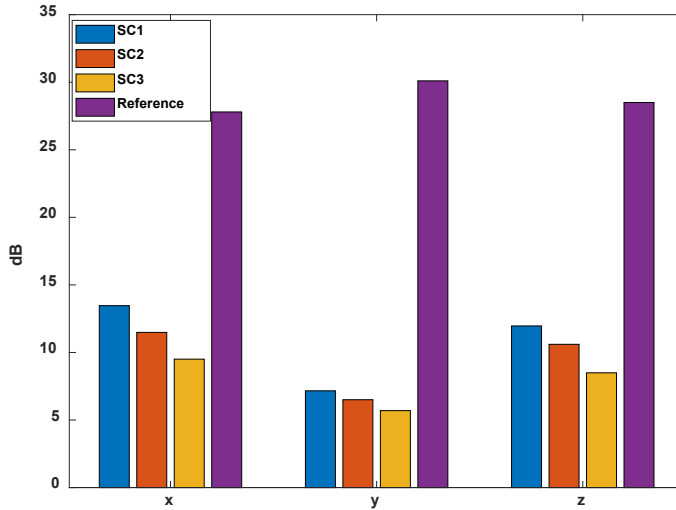
Fig. 6.35. Bar graph of the mean value of the SNR over all the repetitions for the different SC1, SC2, SC3 conditions compared with the reference (purple bars). Accelerometer of DUT#1 is involved.

Moreover, the Signal to Noise Ratio (SNR) analysis among the different working conditions revealed the non-ideality of the antialiasing LPF filters in such a low-cost device. Therefore, its non-ideality can mine the reliability of measurements made by these kinds of platforms.

The achieved results suggest taking into account such non-idealities for designing suitable data processing and digital filtering techniques to be applied in a real application to improve the measurement data's overall reliability that could generally feed further algorithms like positioning ones.

6.6.5. Thermal cycling test with humidity exposure

This section illustrates the behavior of the three devices when subjected to temperature and humidity exposure (test plan in section 6.5.3.1.). Also in this case, the experimental test has regarded two main aspects:

i.   The evaluation of miscalibration due to the test analyzing the output of the sensors before and after the test.

ii.   The influence of the temperature and humidity on the sensors' output considering a static operation.

Regarding the Type 1 analysis, TABLE VI.XXV reports the experimental results regarding the analysis of the accelerometer's output of three DUTs over three repetitions. More in detail, the table includes the mean value **μ** and standard deviation **σ** of the sensors' output over the 3-minute acquisition window before S_1 and after S_3 the test. Analyzing TABLE VI.XXV, the full compatibility from a measurement point of view regarding each sensor before and after the test zone can be seen. This fact leads to the absence of sensors' miscalibration caused by the thermal cycling test, and thus to the absence of failure mechanisms triggered during the test.

TABLE VI.XXV
TYPE 1 ANALYSIS FOR MISCALIBRATION CONSIDERING THREE DEVICES AND THREE REPETITIONS OF THE THERMAL TEST.

REPETITION	X-axis [g]				Y-axis [g]				Z-axis [g]			
	BEFORE TEST S_1		AFTER TEST S_3		BEFORE TEST S_1		AFTER TEST S_3		BEFORE TEST S_1		AFTER TEST S_3	
	μ	σ	μ	σ	μ	σ	μ	σ	μ	σ	μ	σ
DUT #1												
#1	-0.0071	0.0011	-0.0063	0.0010	-0.2044	0.0308	-0.2042	0.0308	0.0106	0.0016	0.0113	0.0017
#2	-0.0022	0.0004	0.0016	0.0003	-0.0025	0.0012	-0.0025	0.0013	0.0075	0.0012	0.0084	0.0013
#3	-0.0015	0.0003	0.0098	0.0015	0.0023	0.0004	0.0028	0.0005	0.0133	0.0020	0.0147	0.0022
DUT #2												
#1	-0.0006	0.0002	-0.0015	0.0016	0.0005	0.0002	0.0022	0.0004	0.0009	0.0003	-0.0010	0.0003
#2	-0.0004	0.0002	0.0001	0.0017	0.0061	0.0009	0.0100	0.0015	0.0107	0.0016	0.0057	0.0009
#3	0.0015	0.0003	0.0011	0.0124	-0.0010	0.0009	0.0030	0.0006	0.0017	0.0005	0.0021	0.0004
DUT #3												
#1	0.0089	0.0014	-0.0010	0.0002	-0.0093	0.0014	-0.0079	0.0012	-0.0161	0.0024	-0.0097	0.0015
#2	0.0000	0.0002	0.0010	0.0002	0.0001	0.0002	0.0008	0.0002	-0.0002	0.0006	-0.0093	0.0014
#3	0.0000	0.0002	-0.0002	0.0002	-0.0002	0.0002	0.0013	0.0003	0.0002	0.0004	0.0040	0.0006

Fig. 6.36 reports the evolution of the accelerometer sensors' output during the thermal test. Similarly, Fig. 6.37 shows the evolution of the gyroscope sensors' output during the test. As shown from the figures, both the sensors' output reports an evident correlation with the temperature.
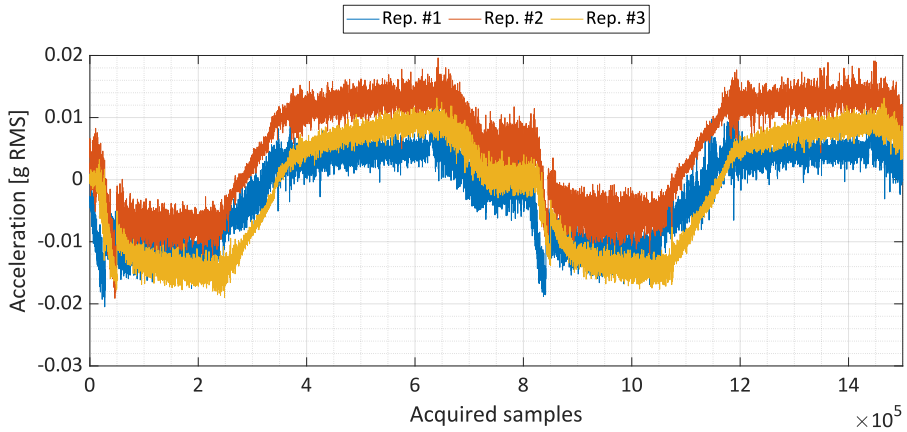
Fig. 6.36. Evolution of accelerometer outputs during the thermal test. (DUT#1, Y-axis is involved).
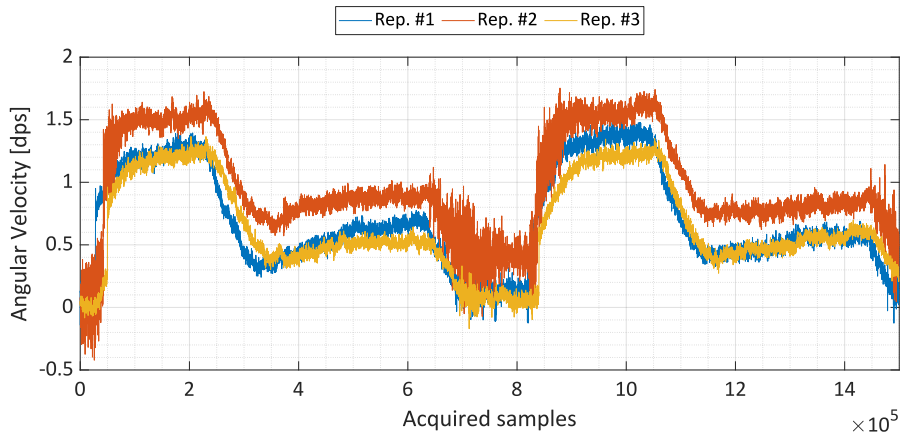
Fig. 6.37. Evolution of gyroscope outputs during the thermal test. (DUT#1, Y-axis is involved).

For the sake of brevity, Fig. 6.36 and Fig. 6.37 illustrates only the test regarding the DUT#1 and the Y-axis of both gyroscope and accelerometer. However, the same correlation has been observed for all sensors' axes considered in this work. To synthetically report the behaviors of all DUTs under test, TABLE VI.XXVI report the maximum and minimum sensors' output during the temperature test (three repetitions) and before the test for DUT#1. Similarly, TABLE VI.XXVII includes the same data about DUT#2 while TABLE VI.XXVIII reports the values regarding DUT#3.

Considering the minimum and maximum sensors' output during the zone before the test, a significant variation can be observed in all the sensors' axes during the execution of the thermal cycling test.

TABLE VI.XXVI

DUT #1 MAXIMUM AND MINIMUM SENSOR OUTPUTS VERSUS THERMAL CYCLES.

DUT#1 ACCELEROMETER [m/s²]								
	BEFORE ZONE		REPETITION 1		REPETITION 2		REPETITION 3	
AXIS	MIN	MAX	MIN	MAX	MIN	MAX	MIN	MAX
X	-0.003	0.000	-0.020	0.012	-0.013	0.014	-0.018	0.012
Y	-0.006	0.001	-0.020	0.014	-0.019	0.019	-0.019	0.013
Z	0.000	0.009	-0.011	0.029	-0.013	0.027	-0.026	0.023
DUT#1 GYROSCOPE [° /s]								
	BEFORE ZONE		REPETITION 1		REPETITION 2		REPETITION 3	
AXIS	MIN	MAX	MIN	MAX	MIN	MAX	MIN	MAX
X	-0.325	0.000	-0.712	3.418	-0.980	3.114	-0.582	3.623
Y	-0.096	0.101	-0.173	1.506	-0.421	1.753	-0.170	1.366
Z	-0.096	0.014	-0.256	1.042	-0.094	1.097	-0.452	1.080

TABLE VI.XXVII

DUT #2 MAXIMUM AND MINIMUM SENSOR OUTPUTS VERSUS THERMAL CYCLES.

DUT#2 ACCELEROMETER [m/s²]								
	BEFORE ZONE		REPETITION 1		REPETITION 2		REPETITION 3	
AXIS	MIN	MAX	MIN	MAX	MIN	MAX	MIN	MAX
X	-0.009	0.000	-0.016	0.000	-0.004	0.018	-0.003	0.028
Y	-0.001	0.000	-0.017	0.000	-0.017	0.014	-0.009	0.013
Z	0.000	0.012	0.000	0.030	-0.001	0.017	-0.003	0.000
DUT#2 GYROSCOPE [° /s]								
	BEFORE ZONE		REPETITION 1		REPETITION 2		REPETITION 3	
AXIS	MIN	MAX	MIN	MAX	MIN	MAX	MIN	MAX
X	0.000	0.122	-0.736	0.507	-1.072	0.390	-1.313	0.629
Y	0.000	0.457	-2.873	2.296	-2.969	2.791	-3.490	2.206
Z	0.000	0.113	-0.549	0.650	-0.499	0.731	-0.989	0.729

TABLE VI.XXVIII
DUT #3 MAXIMUM AND MINIMUM SENSOR OUTPUTS VERSUS THERMAL CYCLES.

DUT#3 ACCELEROMETER [m/s²]							
	BEFORE ZONE		REPETITION 1		REPETITION 2		REPETITION 3	
AXIS	MIN	MAX	MIN	MAX	MIN	MAX	MIN	MAX
X	-0.002	0.000	-0.023	0.026	-0.010	0.011	-0.013	0.015
Y	0.000	0.003	-0.035	0.031	-0.020	0.021	-0.025	0.018
Z	0.000	0.016	0.000	0.030	-0.009	0.011	-0.011	0.015
DUT#3 GYROSCOPE [˚ /s]							
	BEFORE ZONE		REPETITION 1		REPETITION 2		REPETITION 3	
AXIS	MIN	MAX	MIN	MAX	MIN	MAX	MIN	MAX
X	-0.581	0.000	-3.597	5.145	-4.123	4.842	-3.391	5.535
Y	-0.503	0.000	-3.834	7.369	-4.629	6.865	-3.779	7.859
Z	0.000	0.359	-2.677	2.797	-2.412	2.956	-3.081	2.502

In particular, once fixed the axis, intervals [MIN ÷ MAX] observed for the temperature test repetitions are very similar and generally overlapped concerning the single DUT for both the accelerometer and the gyroscope. However, for each gyroscope's axes and DUTs, a different excursion interval has been observed. More in details, the maximum excursion of DUT #1 gyroscope regards the X-axis and fall in the range [-0,712 ÷ 3,418] dps, while the maximum excursion of DUT #2 gyroscope regards the Y-axis and fall in the range [-3,490 ÷ 2,206] dps, and the maximum excursion of DUT #3 gyroscope regards the Z-axis and fall in the range [-3,779 ÷ 7,859] dps. These ranges can influence such devices' correct operation, mainly when employed in an environment characterized by significant temperature stress. This fact can probably be imputed to the slightly different mechanical construction processes, neglecting the possibility of using a unique function to correct the temperature influence. On the opposite, considering all the repetitions, axes, and DUTs, the accelerometers report an interval [MIN ÷ MAX] observed for the temperature stress very similar and overlapped.

6.6.6. Temperature cycling test

This section illustrates the behavior of the devices during the temperature cycling test defined in section 6.5.3.2.

During the test, the sensors exhibited abnormal drifts, as can be seen in Fig. 6.38 observing the X-axis response of the gyroscope, accelerometer and magnetometer output in case of DUT #1. The figure clearly highlights the effects of the temperature on all sensors. Indeed, although the DUT is kept steady during all the temperature cycles (so the ideal output of each sensor should be constant), significant dispersions of the sensor nominal outputs are observed as a function of the temperature excursion. In more detail, the magnetometer follows the trend of the temperature profile, whereas the gyroscope and the accelerometer show an opposite trend against the temperature profile. Very similar behaviors have been obtained for the other axes (y and z) of DUT #1 sensors, DUT #2 and DUT #3.
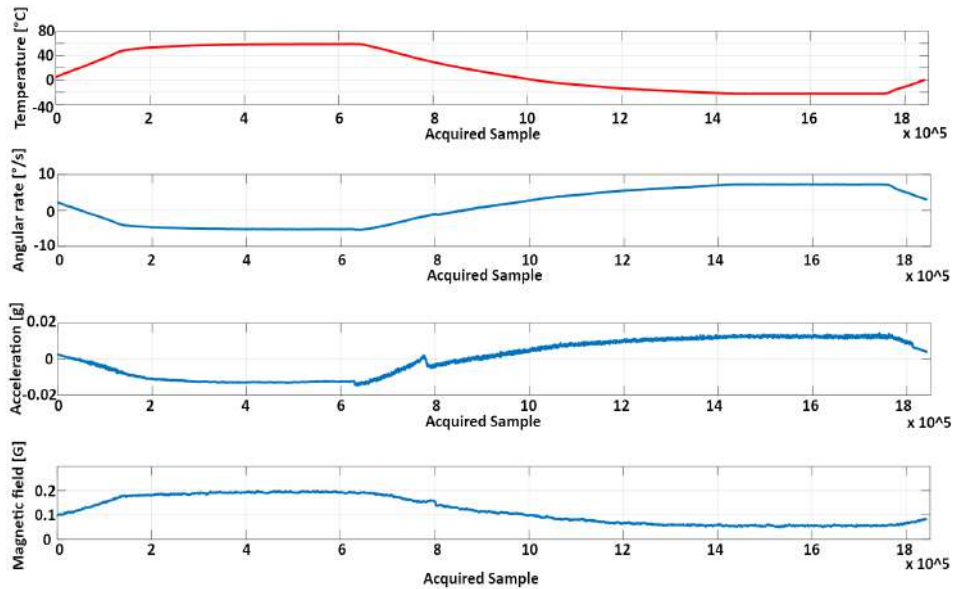
Fig. 6.38. Evolution of gyroscope, accelerometer, and magnetometer outputs during a single temperature cycle. (DUT#1 and x-axis is involved).

TABLE VI.XXIX summarize the results achieved for each DUT, sensor, and axis, in terms of μ and σ of the sensors output observed in S_1 and S_3 zone.
Focusing the attention on accelerometer sensors, the results reported in in the table prove the full compatibility of the sensor outputs achieved in S_1 and S_3 regardless the axis and the DUT considered. Moreover, the values observed for μ and σ in S_3 are very similar to ones achieved in S_1. As a consequence, the application of the temperature cycles between -20 °C and 60 °C does not affect the general operating and the calibration of the accelerometer sensors.

TABLE VI.XXIX

ANALYSIS OF THE THREE AXES OF THE ACCELEROMETER, GYROSCOPE AND MAGNETOMETER SENSORS
DURING TEMPERATURE CYCLING TEST.

DUT	ACCELEROMETER											
	X-Axis S_1 [g]		X-Axis S_3 [g]		Y-Axis S_1 [g]		Y-Axis S_3 [g]		Z-Axis S_1 [g]		Z-Axis S_3 [g]	
	μ	σ	μ	σ	μ	σ	μ	σ	μ	σ	μ	σ
#1	0.005	0.001	0.011	0.002	0.002	0.002	0.008	0.002	0.004	0.002	0.007	0.002
#2	0.001	0.001	0.015	0.014	0.008	0.006	0.015	0.014	0.003	0.002	0.024	0.019
DUT	GYROSCOPE											
	X-Axis S_1 [°/s]		X-Axis S_3 [°/s]		Y-Axis S_1 [°/s]		Y-Axis S_3 [°/s]		Z-Axis S_1 [°/s]		Z-Axis S_3 [°/s]	
	μ	σ	μ	σ	μ	σ	μ	σ	μ	σ	μ	σ
#1	0.145	0.114	0.166	0.106	0.115	0.108	0.289	0.106	0.146	0.098	2.807	0.094
#2	0.839	0.111	2.654	0.273	1.342	0.129	4.091	0.202	0.229	0.124	1.309	0.095
DUT	MAGNETOMETER											
	X-Axis S_1 [G]		X-Axis S_3 [G]		Y-Axis S_1 [G]		Y-Axis S_3 [G]		Z-Axis S_1 [G]		Z-Axis S_3 [G]	
	μ	σ	μ	σ	μ	σ	μ	σ	μ	σ	μ	σ
#1	0.566	0.005	0.468	0.004	0.144	0.017	0.298	0.012	0.454	0.008	0.518	0.007
#2	0.174	0.005	0.158	0.006	0.093	0.008	0.184	0.007	1.234	0.008	1.122	0.007

On the contrary, the results reported in TABLE VI.XXIX about the gyroscopes prove that the considered kind of temperature stress can alter significantly the sensor calibration. In more detail, for both the DUTs and for all the axes, the values of μ significantly increase in S_3 with respect to S_1. In some cases, such increase even reach about one order of magnitude. These results agree with the typical well-known drift effect of the gyroscope sensors concerning general temperature variations already highlighted during the thermal (temperature plus humidity stress) cycling test in section 6.6.5. As for the magnetometer sensors, TABLE VI.XXIX highlights how the effect of the thermal test is weakly visible, except in the case of the Y-axis where the values of μ doubles in S_3 with respect to the corresponding value observed in S_1, for both the DUTs.

Furthermore, a boundary analysis has been performed by evaluating the maximum and the minimum values observed for each sensor and each axis of DUT #1 during the four cycles. These results are summarized in TABLE VI.XXX, where the data have been achieved after a suitable pre-calibration phase and are compared against a reference values measured before the test.

Table VI.XXX
DUT #1 Maximum And Minimum Sensor Outputs Versus Temperature Cycles.

DUT#1 Accelerometer [g]										
	Reference		Cycle 1		Cycle 2		Cycle 3		Cycle 4	
AXIS	MIN	MAX	MIN	MAX	MIN	MAX	MIN	MAX	MIN	MAX
X	0.000	0.001	-0.016	0.014	-0.015	0.014	-0.024	0.014	-0.015	0.014
Y	0.000	0.001	-0.026	0.027	-0.023	0.013	-0.022	0.013	-0.024	0.013
Z	-0.001	0.002	-0.010	0.019	-0.008	0.018	-0.006	0.020	-0.003	0.022

DUT#1 Gyroscope [˚/s]										
	Reference		Cycle 1		Cycle 2		Cycle 3		Cycle 4	
AXIS	MIN	MAX	MIN	MAX	MIN	MAX	MIN	MAX	MIN	MAX
X	-0.08	0.02	-5.49	7.38	-5.38	7.32	-5.35	7.40	-5.37	7.29
Y	-0.01	0.02	-13.52	9.91	-13.63	9.79	-13.76	9.81	-13.63	9.84
Z	-0.01	0.01	-1.77	1.73	-1.89	-0.17	-1.97	-0.44	-1.95	-0.51

DUT#1 Magnetometer [G]										
	Reference		Cycle 1		Cycle 2		Cycle 3		Cycle 4	
AXIS	MIN	MAX	MIN	MAX	MIN	MAX	MIN	MAX	MIN	MAX
X	0.12	0.12	0.04	0.23	0.05	0.19	0.05	0.20	0.05	0.20
Y	-0.13	-0.13	-0.22	-0.04	-0.23	-0.04	-0.23	-0.05	-0.23	-0.06
Z	1.18	1.18	1.09	1.35	1.09	1.35	1.09	1.34	1.09	1.32

Focusing on Table VI.XXX, some considerations about DUT #1 can be drawn:

- As for the gyroscope sensor, once fixed the axis, the intervals [MIN ÷ MAX] observed for the four temperature cycles are very similar and generally overlapped. Compared with values achieved in reference conditions, for all axes, the temperature excursions have led to a significant increase in the range. The Y-axis shows the highest sensitivity with the widest range observed performing Cycle 3 (i.e. [13.76 dps ÷ 9.81 dps]). The order of magnitude of such values is very similar to the ones typically experienced in many real applications as aeronavigation, positioning control, and so on.
- As for the accelerometer sensor, once again, for a given axis, the intervals [MIN ÷ MAX] observed for the four temperature cycles are very similar and generally overlapped. Compared with values achieved in reference conditions, for all axes, the temperature excursions have led to a significant increase in the corresponding ranges. All the axes

exhibit ranges of the same order of magnitude. In this case, the widest range has been observed in the case of the Y-axis duing Cycle 1 (i.e. [26 mg ÷ 27 mg]). Once again, such values are very similar to ones typically experienced in many real applications as an inclinometer.

- As for the magnetometer sensor, once fixed the axis, the intervals [MIN ÷ MAX] observed for the four temperature cycles are almost identical. Compared with the reference conditions, a variation of the range is still observable even if less significant concerning the case of the gyroscope and the accelerometer sensors. The widest range has been observed in the case of the Z-axis during both Cycle 1 and Cycle 2 (i.e. [-1.09 G ÷ 1.35 G]). Such values are very similar to ones typically experienced in many real applications as the heading control of a vehicle.

Similarly to the previous case, the results achieved for DUT #2 are summarized in TABLE VI.XXXI.

TABLE VI.XXXI
DUT #2 Maximum And Minimum Sensor Outputs Versus Temperature Cycles.

DUT#2 Accelerometer [g]										
	REFERENCE		CYCLE 1		CYCLE 2		CYCLE 3		CYCLE 4	
AXIS	MIN	MAX	MIN	MAX	MIN	MAX	MIN	MAX	MIN	MAX
X	0.000	0.000	-0.018	0.018	-0.018	0.017	-0.018	0.017	-0.019	0.016
Y	0.000	0.000	-0.015	0.011	-0.015	0.011	-0.015	0.009	-0.016	0.009
Z	0.000	0.000	-0.011	0.008	-0.009	0.010	-0.008	0.011	-0.007	0.012
DUT#2 Gyroscope [˚ /s]										
	REFERENCE		CYCLE 1		CYCLE 2		CYCLE 3		CYCLE 4	
AXIS	MIN	MAX	MIN	MAX	MIN	MAX	MIN	MAX	MIN	MAX
X	-0.02	0.01	-0.71	0.36	-0.64	0.26	-0.69	0.35	-0.70	0.31
Y	-0.03	0.03	-0.34	1.75	-0.36	2.51	-0.30	1.89	-0.32	1.84
Z	-0.01	0.00	-0.15	3.20	0.71	3.33	0.66	3.44	0.67	3.47
DUT#2 Magnetometer [G]										
	REFERENCE		CYCLE 1		CYCLE 2		CYCLE 3		CYCLE 4	
AXIS	MIN	MAX	MIN	MAX	MIN	MAX	MIN	MAX	MIN	MAX
X	-0.54	-0.54	-0.83	-0.41	-0.84	-0.41	-0.85	-0.41	-0.84	-0.41
Y	-0.23	-0.23	-0.40	0.11	-0.39	0.11	-0.38	0.11	-0.38	0.12
Z	0.46	0.46	0.31	0.57	0.32	0.58	0.31	0.57	0.31	0.57

As for DUT #2, the following considerations can be drawn:

- As for the gyroscope sensor, once fixed the axis, the intervals [MIN ÷ MAX] observed for the four temperature cycles are similar and generally overlapped. Compared with values achieved in reference conditions, for all axes, the temperature excursions have led to a significant increase in the range. The Z-axis shows the highest sensitivity with the widest range observed in Cycle 1 (i.e. [-0.15 dps ÷ 3.20 dps]). Once again, the order of magnitude of such values is very similar to ones typically experienced in many real applications. Compared with the results achieved for DUT #1, the gyroscope sensor of DUT #2 seems to be less sensitive with respect to the gyroscope sensor of DUT #1 for each axis.

- As for the accelerometer sensor, for a given axis, the intervals [MIN ÷ MAX] observed for the four temperature cycles are very similar. Compared with values achieved in reference conditions, for all axes, the temperature excursions have led to a significant increase in the corresponding ranges. All axes show very similar ranges, and the widest range was observed for the X-axis in Cycle 1 (i.e. [-18 mg ÷ 18 mg]). Compared with the results achieved for DUT #1, the accelerometer sensor of DUT #2 shows a similar sensitivity with respect to the accelerometer sensor of DUT #1.

- As for the magnetometer sensor, once fixed the axis, the intervals [MIN ÷ MAX] observed for the four temperature cycles are almost identical, thus confirming the high repeatability also experienced in the case of DUT #1. Once again, compared with the reference conditions, a variation of the range is still observable. The widest range has been observed in the case of the X-axis (i.e. [-0.85 G ÷ -0.41 G]). Compared with results achieved in the case of DUT #1 the ranges experienced for DUT #2 are similar in terms of the order of magnitude.

6.6.7. Temperature step-test

This section reports the performances of the Inertial Measurement Units during temperature step-test. once again, the experimental test that has been carried out highlighted a significant correlation of the sensors' output with temperature. As an example, Fig. 6.39 illustrates DUT #1 gyroscope, accelerometer, and magnetometer time evolution for all the axes (Z-axis is perpendicular to the horizontal plane; thus, the accelerometer's z component has been reported without the DC value for better readability).
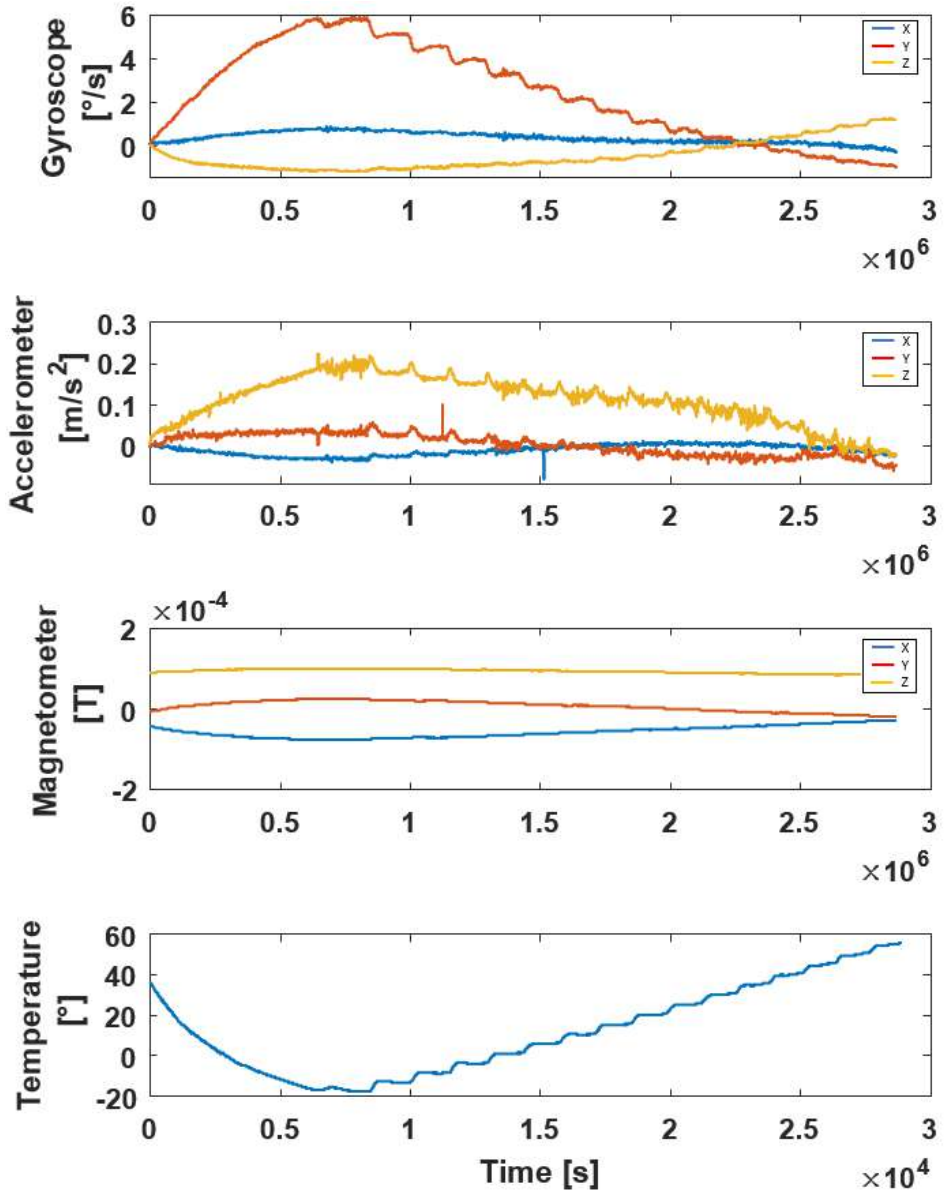
Fig. 6.39. Time evolution of the three axes of the gyroscope (a), accelerometer (b), and magnetometer (c) output during the stress test. The bottom figure (d) represents the trend of the temperature during the test.

For the sake of explanation, the maximum and minimum of the sensors' output signals are reported for DUT #1 and DUT #2 in TABLE VI.XXXII. The temperature has the same influence on gyroscopes and accelerometers sensors:

the span for each axis during the thermal cycle is up to two times the LSB values for both the sensors. As indicated by the manufacturer, the magnetometer exhibits a higher sensitivity to a temperature excursion. However, the internal temperature sensors embedded in the considered IMUs seem to be accurate enough for compensating the other sensors' output.

TABLE VI.XXXII
EXCURSION OF THE SENSORS OUTPUT DURING TEMPERATURE STEP TEST.

	T [°C]	GYROSCOPE [°/s]			ACCELEROMETER [m/s²]			MAGNETOMETER [T x 10⁻⁶]		
		X	Y	Z	X	Y	Z	X	Y	Z
DUT#1										
MAX	56.9	0.91	5.15	1.43	-0.13	0.09	10.14	1.06	30.00	36.30
MIN	-23.3	-0.29	-1.73	-1.06	-0.27	-0.07	9.90	-47.20	-13.30	-0.73
SPAN	80.2	1.20	6.88	2.49	0.40	0.16	0.24	48.26	43.30	37.03
DUT#2										
MAX	56.9	0.94	1.68	1.42	0.13	-0.21	10.03	0.45	26.80	18.70
MIN	-24.9	-0.02	-0.44	-0.95	-0.18	-0.44	9.87	-45.10	-18.60	-3.31
SPAN	81.8	0.96	2.12	2.37	0.31	0.21	0.16	45.55	45.40	22.01

By a reliability point of view, it has not been observed any internal MEMS failure during the temperature step test. A confirmation of the MEMS' reliability after the proposed screening test is highlighted by the reduced hysteresis in the sensors' output during the falling and the test's rising phases illustrated in TABLE VI.XXXIII. As an example, the maximum hysteresis exhibited by the Z-axis of the DUT #1 gyroscope is equal to 0.77°/s. Similar results have been achieved for the gyroscopes of the other devices.

TABLE VI.XXXIII
MAXIMUM HYSTERESIS ACHIEVED DURING TEMPERATURE STEP TEST.

DUT	GYROSCOPE [°/s]			ACCELEROMETER [m/s²]		
	X	Y	Z	X	Y	Z
#1	0.36	0.22	0.77	0.08	0.07	0.14
#2	0.52	0.69	0.52	0.10	0.06	0.10

A second confirmation that the screening test has not triggered any failure mechanisms has been obtained using the analysis "after-before" (Type 1 analysis) which shows the compatibility of the measurement results extracted

from the sensors' output data. As an example, TABLE VI.XXXIV reports the mean and standard deviation of the gyroscope Y-axis (characterized by the highest hysteresis) over 600 samples at 28°. Similar results have been achieved for the other gyroscope axes and the other sensors (accelerometers and magnetometers).

TABLE VI.XXXIV
TYPE 1 ANALYSIS FOR TEMPERATURE STEP TEST (GYROSCOPE Y-AXIS IS INVOLVED).

DUT	GYROSCOPE [°/s]			
	BEFORE TEST		AFTER TEST	
	μ	σ	μ	σ
#1	0.247	0.002	0.251	0.003
#2	0.122	0.003	0127	0.002

Furthermore, for all the sensors' output, the dependence on the temperature may be approximated with a piecewise linear regression, as can be seen in Fig. 6.40 that shows the scatter plot of the temperature with respect to the gyroscope's Y-axis for DU #1 and DUT #2 during the falling and the rising transient of the test cycle.
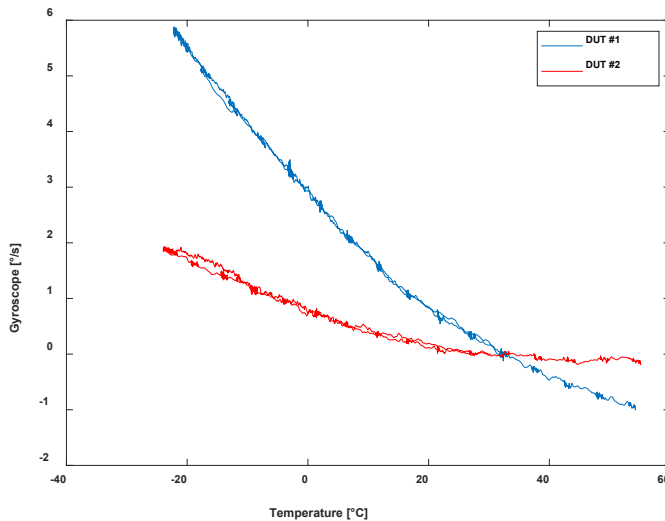
Fig. 6.40. Scatter plot among temperature and gyroscope's output for DUT#1 and DUT #2.

It is extremely important to point out that the estimated piecewise models' parameters of the sensor's output (gyroscope, accelerometer, and

215

magnetometer) vary for each DUT. This result prevents the choice of a unique calibration for all the sensors (indeed, the manufacturers do not provide the end-user of low-cost MEMS-based IMU with this type of information).

6.7. Case study A: Effects of the test on positioning algorithms

6.7.1. Some note on considered positioning algorithms

In literature exist various algorithms to compute orientation from inertial measurement units of an object. The algorithms employed in this work for the estimation orientation are based on a complementary filter and AHRS Kalman filter available in the Matlab R2020a Sensor Fusion Toolbox. Among various available algorithms, they have been chosen due to the widespread use in several practical applications. At the same time, they differ entirely in terms of internal structure, allowing the use of one or the other concerning the computation power available on the target platform and the estimation accuracy required. The complementary filter is a suitable orientation calculation tool for systems having memory constraints but presenting minimal tunable parameters. In the complementary filter, the accelerometer and the gyroscope play the central role in the orientation estimation while the magnetometer is used as a "corrective sensor". The name "complementary" well explains the algorithm's structure, where a low pass filter is used to eliminate small forces creating disturbances in the accelerometer's reading while a high pass filter is used to eliminate the drift usually accumulated due to the integration over a period of the gyroscope data [248]. On the contrary, the AHRS filter uses a nine-axis error-state Kalman filter structure, which is a standard estimation filter. More in detail, the Kalman filter aims to follow the errors in orientation, gyroscope offset, linear acceleration, and magnetic disturbance in order to calculate the final orientation and angular velocity. The Kalman filter estimates the state of the system based on the current and previous states, giving more accurate results with respect to the complementary filter. The orientations of the DUT used have been calculated in three dimensions coordinate system in agreement with the sensor plane [249]. The data acquired by the platforms has been scaled and converted to meet the algorithms' inputs requirements.

6.7.2. Preliminary information

In the following sections, the experimental results achieved during both random vibration test (described in section 6.5.2.1) and sinusoidal vibration test (described in section 6.5.2.2) are reported and commented.

For both the vibration profiles, the positioning algorithms performances under the application of the considered stimulus have been evaluated. Furthermore, to warrant that the results achieved do not depend on eventual damages or malfunctioning of the DUTs occurred during the application of the stimulus, the performance of positioning algorithms before and after the application of each vibration profile has been evaluated (and compared) as well. Then, each test sequence is constituted of three phases delimiting three zones:

i.   Quiet zone before the application of the stimulus (hereinafter S_1).
ii. Stimulus zone (hereinafter S_2).
iii. Quiet zone after the application of the stimulus (hereinafter S_3).

All the analyses have been carried out by considering the application of the vibrating stimulus on each of the axes (i.e. x, y, z) and the effects on the performance of the positioning algorithms have been evaluated by analyzing the deviations of the Eulero's angles (i.e. α, β, γ) due to the vibrations concerning their ideal values, which should be equal to zero degrees because the DUT is not moving (the DUT is mechanically bonded on the shaker plane). Moreover, to compare the deviations observed during the application of the stimulus against the intrinsic variability of the Eulero's angles due to the non-ideality of the measurement chain, the experimental standard deviation expressed as σ_d ($d \in \{ \alpha \mid \beta \mid \gamma \}$), calculated in S_1 has been considered as a baseline and reported in TABLE VI.XXXV. It is worth noting that the comparison between the Complementary filter and the AHRS Kalman filter is based on the same sensor raw data coming from each IMU and it is performed off-line by using the Matlab R2020a Sensor Fusion Toolbox.

TABLE VI.XXXV

EXPERIMENTAL STANDARD DEVIATION σ_d WITHIN S_1 FOR THE THREE DUTs AND FOR COMPLEMENTARY AND AHRS ALGORITHMS.

DUT	COMPLEMENTARY FILTER			AHRS KALMAN FILTER		
	α [°]	β [°]	γ [°]	α [°]	β [°]	γ [°]
#1	0.008	0.006	0.002	0.003	0.003	0.007
#2	0.005	0.006	0.005	0.004	0.008	0.007
#3	0.006	0.004	0.004	0.005	0.002	0.004

6.7.3. Random vibration test

Fig. 6.41 shows the time evolution of the Eulero's angles (α, β, γ) during random vibration test, in the case of the Complementary filtering. In this case, the raw data provided by DUT #1 have been used to evaluate the angles when the stimulus is applied on the X-axis. A similar scenario is illustrated in Fig. 6.42 where the AHRS Kalman filter algorithm has been used.
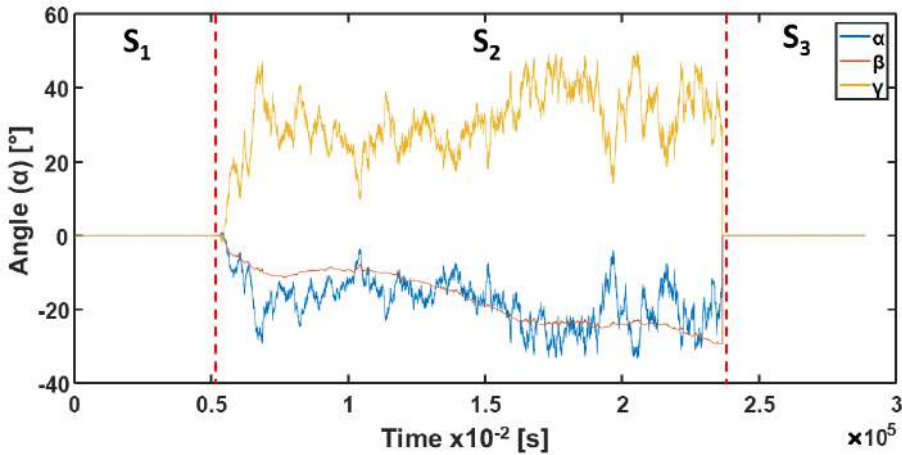
Fig. 6.41. Time evolution of Eulero's angles during random vibration test considering the Complementary algorithm (excitation on X-axis and DUT #1 are involved).
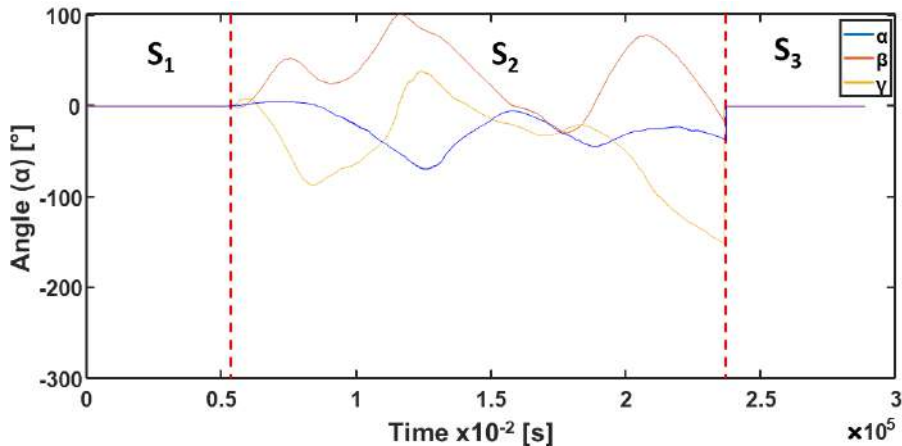
Fig. 6.42. Time evolution of Eulero's angles during random vibration test considering the AHRS algorithm (excitation on X-axis and DUT #1 are involved).

218

Observing the previous figures it is possible to see that, during the application of the random vibration test, all the angles are affected by the stimulus by showing a significant deviation concerning the ideal one (i.e., zero degrees). To quantify such a deviation, at first, the Root Mean Square (RMS) value of such angles have been evaluated in S_1, S_2, and S_3, respectively. Then, the following figures of merits (called absolute angle deviations) have been calculated as:

$$\Delta\alpha_a = \left|\alpha_{a,S2} - \alpha_{a,S1}\right| \tag{6.6}$$

$$\Delta\beta_a = \left|\beta_{a,S2} - \beta_{a,S1}\right| \tag{6.7}$$

$$\Delta\gamma_a = \left|\gamma_{a,S2} - \gamma_{a,S1}\right| \tag{6.8}$$

Where:
- a denotes the axis of excitation of the stimulus;
- $\alpha_{a,S2}$ denotes the RMS value of α within S_2;
- $\alpha_{a,S1}$ denotes the RMS value of α within S_1;
- $\beta_{a,S2}$ denotes the RMS value of β within S_2;
- $\beta_{a,S1}$ denotes the RMS value of β within S_1;
- $\gamma_{a,S2}$ denotes the RMS value of γ within S_2;
- $\gamma_{a,S1}$ denotes the RMS value of γ within S_1.

Based on the above-defined figures of merit, the results achieved for the Complementary and AHRS filtering are reported in TABLE VI.XXXVI. By analyzing such results, the following considerations can be drawn:
- The values of $\Delta\alpha_a$, $\Delta\beta_a$, and $\Delta\gamma_a$ are significantly bigger than the corresponding σ_d for every device and for every axis of excitation.
- For all DUTs, the lowest values of $\Delta\alpha_a$, $\Delta\beta_a$, and $\Delta\gamma_a$ have been achieved when stimulus is applied on the Y-axis in case of the Complementary algorithm, whereas the AHRS algorithm shows the lowest deviations in case of stimulus applied on the Z-axis.
- For both algorithms, once fixed the stimulus excitation axis, the three considered DUTs show different values of $\Delta\alpha_a$, $\Delta\beta_a$, and $\Delta\gamma_a$. This can be imputable to the combination of the following non-ideality:
  - The intrinsic features dispersion of the considered low-cost IMUs.
  - The poor repeatability of the measurement chain (i.e., embedded accelerometers, gyroscopes and magnetometers, antialiasing low-pass filters automatically set by the DUTs, quantization devices) when operating under vibration.

- ○ The residual differences of installation (mainly orientation and clamping) of the three DUTs on the shaker plane. As a consequence, for a given excitation axis (X, Y or Z) and a given angle (α, β or γ), the combined effects of the above-described non-ideality led to the results shown in TABLE VI.XXXVI, which can roughly give the order of magnitude and the range of variation of the $\Delta\alpha_a$, $\Delta\beta_a$, and $\Delta\gamma_a$ concerning both the considered kinds of DUT and stimulus. For the same reasons, a worst-case in terms of stimulus excitation axis cannot be univocally identified.

- Comparing the two algorithms, the values of $\Delta\alpha_a$, $\Delta\beta_a$, and $\Delta\gamma_a$ are generally lower for Complementary than AHRS. This behavior seems to be in opposition to the literature regarding those typologies of filters [250]. However, it is probably imputable to the different intrinsic operations of the filters: the unexpected vibrations for the two algorithms cause different responses, which in case of the Complementary, where there is not a weight of the actual angular estimations with the previous one, lowers the influence of the disturbs. On the opposite, the AHRS seems to be more affected by the disturbs due to an integral error depending on the filter's structure itself.

TABLE VI.XXXVI
ABSOLUTE ANGLE DEVIATIONS FOR COMPLEMENTARY AND AHRS ALGORITHMS.

COMPLEMENTARY FILTER								
DUT	EXCITED AXIS: X			EXCITED AXIS: Y			EXCITED AXIS: Z		
	$\Delta\alpha_x$ [°]	$\Delta\beta_x$ [°]	$\Delta\gamma_x$ [°]	$\Delta\alpha_y$ [°]	$\Delta\beta_y$ [°]	$\Delta\gamma_y$ [°]	$\Delta\alpha_z$ [°]	$\Delta\beta_z$ [°]	$\Delta\gamma_z$ [°]
#1	9.2	6.7	15.4	8.3	49.1	1.3	87.1	42.7	76.4
#2	67.6	46.3	86.6	0.6	15.4	3.6	36.4	22.9	42.3
#3	44.8	26.9	73.2	11.1	37.3	14.3	18.9	18.3	31.9
AHRS KALMAN FILTER								
DUT	EXCITED AXIS: X			EXCITED AXIS: Y			EXCITED AXIS: Z		
	$\Delta\alpha_x$ [°]	$\Delta\beta_x$ [°]	$\Delta\gamma_x$ [°]	$\Delta\alpha_y$ [°]	$\Delta\beta_y$ [°]	$\Delta\gamma_y$ [°]	$\Delta\alpha_z$ [°]	$\Delta\beta_z$ [°]	$\Delta\gamma_z$ [°]
#1	90.5	39.1	72.5	155.1	73.7	129.2	81.0	51.1	84.5
#2	53.3	24.3	116.3	87.5	41.5	127.4	11.5	69.6	20.4
#3	49.6	52.2	105.9	75.7	50.8	155.2	139.9	48.5	95.7

Finally, after the execution of all the random vibration tests, the experimental standard deviation, σ_d ($d \in \{ \alpha \mid \beta \mid \gamma \}$) has been again calculated and reported in TABLE VI.XXXVII. Comparing such values with ones shown in TABLE VI.XXXV, they are very similar. Consequently, they confirm how the results achieved during the random vibration tests are not due to damages or malfunctioning of the DUTs that could be occurred during the application of the stimulus.

TABLE VI.XXXVII

EXPERIMENTAL STANDARD DEVIATION σ_d WITHIN S_3 DURING RANDOM VIBRATION FOR THE THREE DUTS AND FOR COMPLEMENTARY AND AHRS ALGORITHMS.

DUT	COMPLEMENTARY FILTER			AHRS KALMAN FILTER		
	α [°]	β [°]	γ [°]	α [°]	β [°]	γ [°]
#1	0.006	0.004	0.003	0.006	0.004	0.003
#2	0.009	0.011	0.003	0.007	0.003	0.002
#3	0.010	0.012	0.016	0.010	0.011	0.017

6.7.4. Sinusoidal vibration test

As an example, Fig. 6.43 shows the RMS values of α versus the frequency during the application of the sinusoidal test in the case of Complementary filter algorithm, for DUT #1 and when the stimulus is applied on the X-axis. Fig. 6.44 shows the same scenario in case of AHRS Kalman filter.
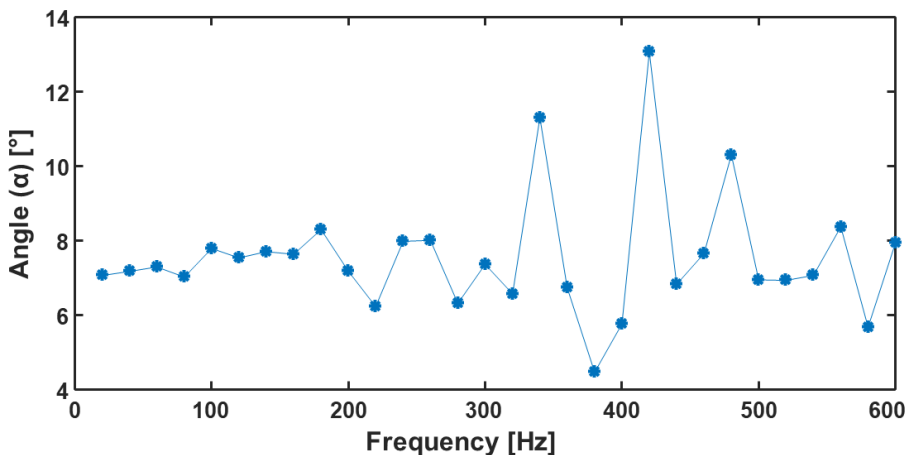
Fig. 6.43. Evolution of α versus frequency during sinusoidal vibration test in case of Complementary filter (excitation on X-axis and DUT #1 are involved).
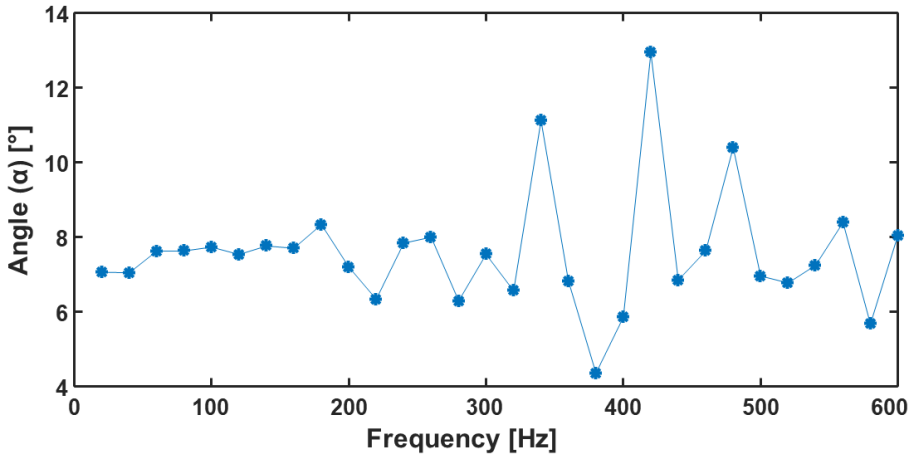
Fig. 6.44. Evolution of α versus frequency during sinusoidal vibration test in case of
AHRS Kalman filter (excitation on X-axis and DUT #1 are involved).

In particular, within S_2 a stimulus according to the vibration test profile described in section 6.5.2.2 has been applied by considering a maximum acceleration value equal to 2g. Then, the RMS values of Eulero's angles have been calculated over each frequency point belonging to the sweep range 20-600 Hz. This frequency range has been selected by taking into account the dynamics of typical applications.

Comparing Fig. 6.43 and Fig. 6.44 it is possible to see that the frequency response of both algorithms shows a not flat behavior highlighting a wide dispersion over the whole frequency range. As a matter of fact, this behavior can be imputable to mechanical resonances of the low-cost sensors (accelerometers, gyroscopes, magnetometers) employed in the DUTs, which in turn propagate through the filtering algorithms. Similar behaviors were achieved for β and γ.

To quantify such a dispersion and the deviation with respect to the quite zone before the test S_1, the mean value and standard deviation of the observed RMS values over the whole frequency range (hereinafter μ_f and σ_f, respectively), for each Eulero's angle, have been evaluated.

TABLE VI.XXXVIII compares the obtained results by showing such values for each stimulus excitation axis and for both the considered filtering algorithms. From the analyses of such results, some consideration can be drawn:

- Both Complementary and AHRS filters show a value of $\mu_f \neq 0$ for every DUT, for every excitation axis and for every considered Eulero's angle.
- For both Complementary and AHRS filters, the highest value of μ_f and

σ_f are observed in the case of the angle γ, meaning that, inside the considered frequency range (20-600 Hz), the evolution of γ is characterized by the greatest variability around the greatest mean value.

- Comparing the corresponding values in the table, they are very similar both in terms of μ_f and σ_f.
- As it happened in the case of random vibration tests, once fixed the stimulus excitation axis and the Eulero's angle, the three considered DUTs show different values of μ_f and σ_f which can be mainly imputable to the intrinsic features dispersion of the adopted low-cost DUTs, to poor repeatability of all the measurement chain (embedded sensors, filters, and quantization devices) when operating under vibration conditions, as well as to the residual differences of installation (mainly orientation and clamping) of the three DUTs on the shaker plane.

TABLE VI.XXXVIII

MEAN RMS AND STANDARD DEVIATION ANGLE IN THE RANGE 20-600 HZ FOR COMPLEMENTARY AND AHRS ALGORITHMS.

COMPLEMENTARY FILTER								
	EXCITED AXIS: X			EXCITED AXIS: Y			EXCITED AXIS: Z		
DUT	α [°]	β [°]	γ [°]	α [°]	β [°]	γ [°]	α [°]	β [°]	γ [°]
	μ_f	σ_f	μ_f	σ_f	μ_f	σ_f	μ_f	σ_f	μ_f
#1	7.5	1.6	29.5	5.0	46.8	14.8	5.8	42.7	61.1
#2	56.7	15.8	3.1	1.2	85.7	16.0	45.3	51.2	57.8
#3	15.6	4.8	10.4	9.4	57.5	12.9	71.3	46.2	70.8
AHRS KALMAN FILTER								
	EXCITED AXIS: X			EXCITED AXIS: Y			EXCITED AXIS: Z		
DUT	α [°]	β [°]	γ [°]	α [°]	β [°]	γ [°]	α [°]	β [°]	γ [°]
	μ_f	σ_f	μ_f	σ_f	μ_f	σ_f	μ_f	σ_f	μ_f
#1	7.6	1.6	29.9	5.1	46.0	14.9	11.9	43.9	61.5
#2	57.1	15.8	3.2	1.2	85.9	15.9	50.8	60.6	58.3
#3	11.5	8.0	17.7	10.9	57.7	12.9	28.3	16.8	71.3

Once again, the results shown in TABLE VI.XXXVIII can roughly give the order of magnitude and the range of variation of the $\Delta\alpha_a$, $\Delta\beta_a$, and $\Delta\gamma_a$ concerning

both the considered kinds of DUT and stimulus.

Finally, after the execution of all the sinusoidal vibration tests, the experimental standard deviation, σ_d ($d \in \{\alpha \mid \beta \mid \gamma\}$) has been again calculated and reported in TABLE VI.XXXIX. Comparing such values with ones shown in TABLE VI.XXXV, they are still very similar, and in any case, neglectable concerning μ_f and σ_f observed during the application of the stimulus. Consequently, they confirm how the results achieved during the sinusoidal vibration tests are not due to damages or malfunctioning of the DUTs that could be occurred during the application of the stimulus.

TABLE VI.XXXIX

EXPERIMENTAL STANDARD DEVIATION σ_d WITHIN S_3 DURING SINUSOIDAL VIBRATION FOR THE THREE DUTs AND FOR COMPLEMENTARY AND AHRS ALGORITHMS.

DUT	COMPLEMENTARY FILTER			AHRS KALMAN FILTER		
	α [°]	β [°]	γ [°]	α [°]	β [°]	γ [°]
#1	0.008	0.005	0.011	0.008	0.006	0.011
#2	0.005	0.014	0.007	0.004	0.005	0.009
#3	0.016	0.015	0.023	0.019	0.016	0.021

6.7.5. Temperature step-test

To analyze the effect of the temperature on the considered filtering algorithms, the orientations of the DUTs employed have been calculated in three dimensions coordinate system in agreement with the sensor plane. In addition, the IMUs sensors' output has been scaled and converted to meet the algorithms' inputs requirements.

Both the algorithms have been run on the data acquired from the IMUs during the temperature step-test.

These analyses have shown how even if the variation in terms of raw data outcoming from the sensors seems to be a constraint in a small range, its propagation reflects significantly on calculating the Eulerian angles in both Complementary filter algorithm and AHRS Kalman filter algorithm.

More in detail, considering Fig. 6.45, it can be seen that the application of the constant temperature step results in a significant deviation (in some cases approaching $\pm$ 200°) of the alpha angle for both the algorithms.

The estimation of the beta and gamma angles is less affected by the IMU Kalman filter's temperature test than the complementary filter. This fact is probably due to the IMU Kalman filter's capacity to take into account the

observation made in the last instants to correct the angle deviation in consequence of small perturbation.
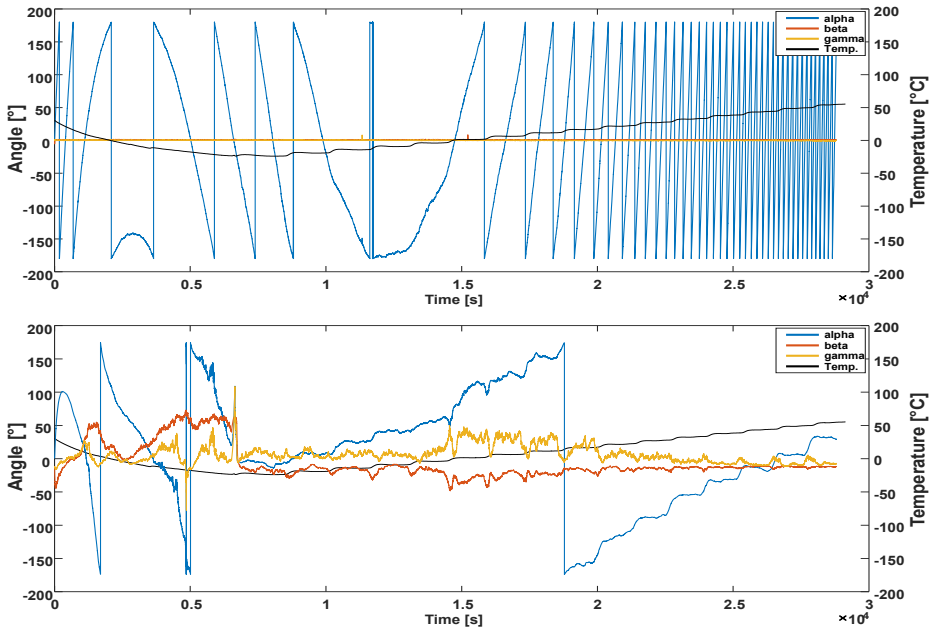
Fig. 6.45. Eulerians'angles calculated by the IMU Kalman filter in the upper subplot and by the Complementary filter in the bottom subplot.

6.8. Case study B: DC-DC converters for diagnostic units

Wireless Sensor Networks (WSNs) represent an optimal tradeoff to implement effective diagnostic in industrial plants [251], [252], allowing to monitor several condition parameters, assessing the system's remaining useful life of industrial plants [253], ensuring fault tolerance, saving costs and minimizing the plant downtimes. WSNs can be equipped with several different kinds of transducers, and each node of the network can be used to monitor different equipment using different sets of sensors. Moreover, a WSN can cover a large area of the plant and its architecture can be easily extended and updated with more nodes allowing a sparsely distributed monitoring of the system. For this reason, diagnostic and Condition Monitoring (CM) units play a critical role in the

operation and maintenance of industrial plants [15], [254]. In this scenario, it is fundamental to ensure that the diagnostic unit itself works properly during the complete system life cycle. However, diagnostic units installed in industrial plants or in offshore applications must endure several external stress sources that influence the performances of the devices. Both electrical/electronic performances and reliability are deeply affected by harsh environments, such as: hot temperature (e.g. units located nearby combustion chambers or motors, heaters, etc.), cold temperature (e.g. units located nearby cryogenic equipment or units located in offshore plants), rapid thermal excursion (e.g. units located on wind turbines, pipelines, etc.), mechanical shocks and random vibrations (i.e. produced by the wind, or by nearby rotor machines, system in motion, etc.) and high relative humidity [211], [215].

One of the most critical elements of a WSN-based diagnostic unit used in plant CM is the power supply. The main reasons for such criticality are threefold:

- The aim of the power supply is to convert energy from the primary source and to provide suitable supplies to the different parts of the diagnostic unit (e.g. microcontroller and elaboration units, transceiver, active transducers, etc). Therefore, a failure of the DC-DC converter inevitably lead to the unavailability of the entire node [255].

- WSNs are usually self-powered using a battery pack. Therefore, the conversion efficiency of the DC-DC converter used to supply the node is a fundamental aspect in order to guarantee a longer useful life of the unit [256]. Since each node collects and transmits data only in short intervals during the day, in the course of most of its life the node operates in energy saving mode. Therefore, the DC-DC converter will mainly operate under light load conditions. As known, the most used modulation technique for DC-DC converters is the Pulse Width Modulation (PWM). However, literature shows how PWM is affected by low conversion efficiencies with light loads. For this reason, in this work, a different control strategy called Pulse Skipping Modulation (PSM) has been used in order to increase the conversion efficiency and therefore the node autonomy. However, a comparison between PSM and PWM is presented to emphasize the benefits of PSM and to validate the results of the other analysis.

- Many electrical parameters of the DC-DC converter (e.g. efficiency, output ripple, input ripple, step response, etc.) are deeply affected by the harsh environment in which the converter could work in case of industrial onshore/offshore plants [257].

6.8.1. Related works

The characterization of the power supply under harsh stress conditions is a critical and fundamental aspect that surely must be taken into account during the design of a new customized DC-DC converter. However, in recent literature, most of the papers dealing with the design of innovative power supply characterize the performance of their device only in standard operating conditions (see for instance but not only [258]–[260]). There are no papers in recent literature dealing with the design and characterization of DC-DC converters under more than one external stress source. For example, [261], [262] presents the characterization of power converters under harsh environment dealing only with temperature stress. Van De Sande et al. [263] analyses the temperature dependence of electric variables in DC-DC converter. In [264] a PWM-based converter for high temperature is designed and tested using a thermal cycling test. The results of a highly accelerated thermal test are presented in [265] in order to highlight the MOSFET failure mechanisms without taking into account the effects that temperature induced on the converter performances. In [266], the characterization under temperature stress of a sensor node for wireless monitoring has been presented. Kosai et al. [267] presents the characterization of a boost converter under high temperature conditions, while a characterization under low temperature operation is presented in [268]. Quite the contrary, scenarios including high humidity or excessive random vibrations have never been dealt with in literature. Furthermore, the manufacturers of commercial equipment miss to consider such important characterization under considerable high stress levels. One of the main reasons for this lack is that there are no specific standards currently available to test the performances of power electronics for industrial applications.

6.8.2. Aim of the test procedures

Trying to fill the literature gaps described in the previous section, this work aims to achieve the following objectives:

1. Fill the above-mentioned gap characterizing the performances of a customized self-made DC-DC converter used in WSN-based diagnostic systems for industrial plants.
2. Test the electrical performances of the proposed converter under harsh environmental conditions typical of industrial and manufacturing

processes. Differently from all the other papers in literature, the proposed characterization is based on a sequence of five stress tests including high and low temperatures, high humidity and wideband vibration stress sources.

3. Investigate reliability and infant mortality of the converter using a customized Environmental Stress Screening (ESS) test plan to expose early failures.

4. Evaluate the advantages of the PSM over the PWM and characterized the behavior of each modulation for different operating temperatures. Since the DC-DC converter may operate in harsh environment, a comparison in terms of efficiency conversion between PWM and PSM for a DC-DC Buck converter under light load and high temperature conditions is presented. The advantages and disadvantages obtained from the proposed study are highlighted.

6.9.   Case study B: Test plan and Measurement setup

This section presents the proposed ESS-based test plan and the measurement setup used to characterize the performance of the customized DC-DC converters under test.

6.9.1.   Structure of the test plan

The proposed test plan for characterization of reliability and electrical parameters of DC-DC converters is basically composed by three major parts: a temperature-based test plan (composed by two consecutive tests integrating temperature and humidity stresses), a vibration-based test plan (composed by two consecutive tests) and a comparison between PWM-based converters (traditional solution) and PSM-based converters (innovative solution) under temperature stress.

The characterization of the developed DC-DC converter under harsh conditions has been carried out through a customized test plan which integrates different test guidelines:

- Environmental Stress Screening (ESS) according to MIL-HDBK-344 Rev. A Notice 2 (2012) [191] and in compliance with IEST-RP-PR001.2

(2016) [269].

- Reliability Stress Screening (RSS) according to IEC 61163-2 (2020) [192].

The base idea of RSS and ESS test plans is to expose a new electronic device to stress (or sequence of stresses) in order to expose latent defects manifesting transient or permanent failure mechanisms during the screening process. After the screening process, the surviving population can be assumed to have higher reliability than a similar unscreened population since the intrinsic failure due to manufacturing process have already been exposed. This reduces the failure rate of the components and consequently increase the device reliability [126]. Note that RSS and ESS procedures help manufacturers to detect product defects and production flaws exposing all the failures that would otherwise be encountered by the end user during the first hours of use. Quite the opposite, this kind of test does not aim at exposing random defects, which would appear after a long time of operation.

As a matter of fact, effective RSS or ESS procedures require stresses of sufficient magnitude and time duration to precipitate failures from latent defects without accumulating significant damage to the remaining non-defective items. Furthermore, RSS and ESS test plans are also extremely useful to characterize the performances of the device operating in harsh conditions.

Note that the effects of RSS and ESS test plans are to eliminate early failures and thus to decrease the failure rate only in the first region of the bathtub curve (for more information about the failure rate trend and the bathtub curve see [131]). For a complete analysis of the device failure rate during the useful life other methods have to be performed, such as a reliability prediction by means of handbooks (see for instance [185], [270], [271]) or an accelerated life test plan (see for instance [123], [129], [190]).

The proposed test plan is based on five consecutive tests. Similarly to the experimental characterization of case study A, also in this case before each test, a precondition phase is required to characterize the performances of the devices in standard conditions. After the test is completed, a stabilization phase at standard conditions is required to achieve useful information about the effects of the test on the devices.

A flowchart of the test plan including five different test procedures is depicted in Fig. 6.46. Each test includes 8 DC-DC converters. A set of 8 devices represents an optimal trade-off for RSS-based test plan in terms of cost, robustness and repeatability of the results, validation of the methods, investigation of early failures and characterization of the performances.
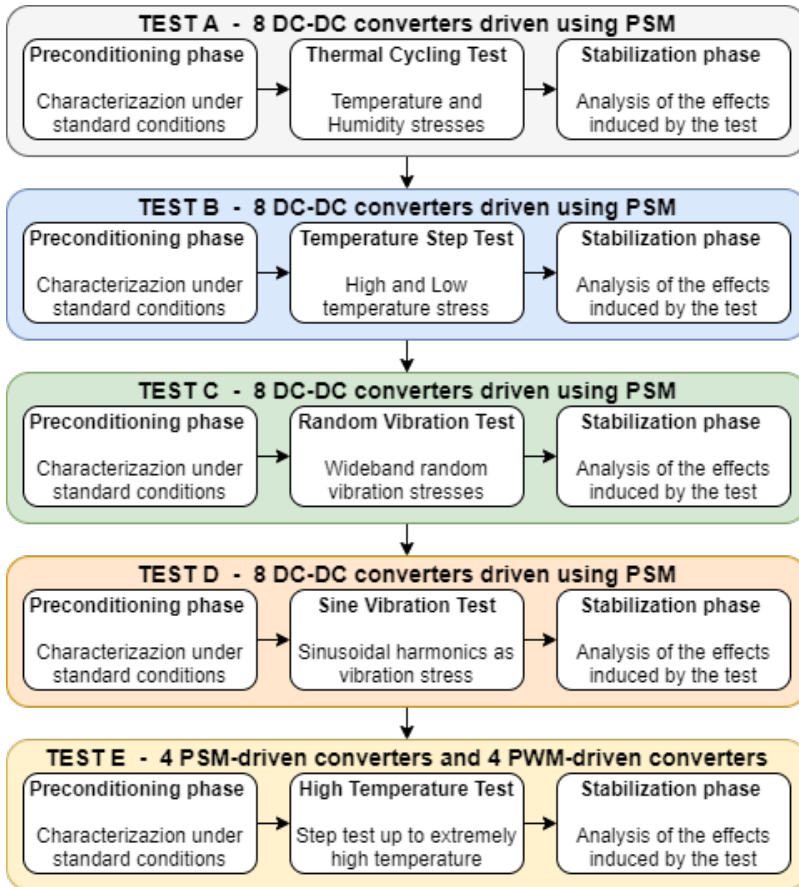
Fig. 6.46. Flowchart of the proposed test plan including five different test procedures.

6.9.2. Detailed description of the tests

The detailed description of the proposed tests is the following:

TEST A. Thermal cycling test. It consists of a cyclic repetition of low temperature T_{LOW} = -20 °C and high temperature T_{HIGH} = 80 °C maintained constant for an exposition time of 1 h. During the exposition at T_{HIGH} the relative humidity is set to RH = 95%. The transition between T_{LOW} and T_{HIGH} is performed at 3 °C/min. As illustrated in Fig. 6.47 two consecutive cycles have been carried out. The test has been developed following the guidelines of the international standards JEDEC JESD22-A100C (2007) [272], MIL-STD-883L (2019) [273] and IEC 60068-2-39 [274].
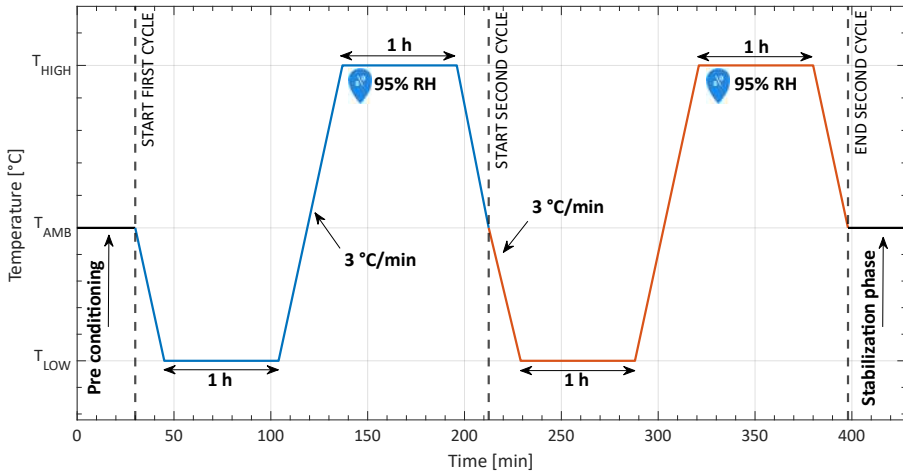
Fig. 6.47. Test plan definition for the characterization of DC-DC converters under harsh conditions. Test A: Thermal cycling test. Temperature and humidity stresses are involved.

TEST B. Temperature Step Test. It consists of a sequence of temperature steps $\Delta T = 5$ °C maintained constant for an exposition time of 10 minutes. The temperature interval is between $T_{LOW} = -20$ °C and $T_{HIGH} = 80$ °C. The transition between two consecutive steps is performed at 3 °C/min. The test is illustrated in Fig. 6.48 and it has been developed following the guidelines of the international standards ISO 16750-4 (2010) [244] and IEST-RP-PR003.1 (2012) [245].
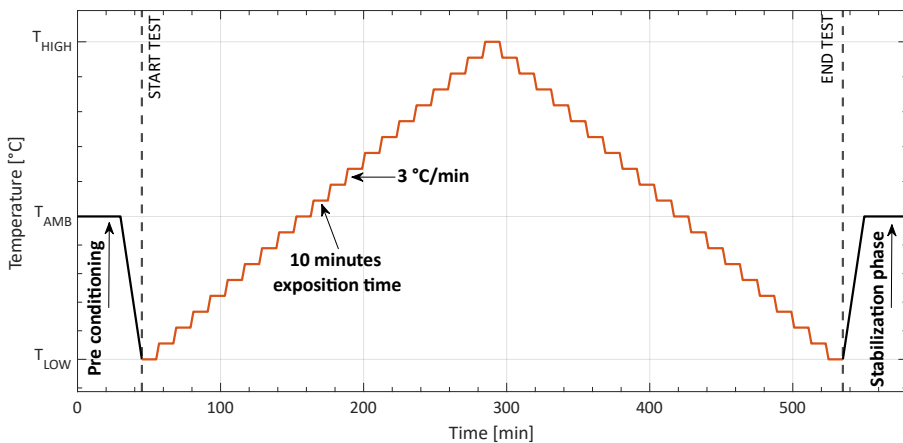
Fig. 6.48. Test plan definition for the characterization of DC-DC converters under harsh conditions. Test B: Temperature Step test.

TEST C. Random Vibration Test. It consists of a wideband random vibration profile described by an Acceleration Spectral Density (ASD) in compliance with the international standards IEC 60068-2-64 [230] and JEDEC JESD22-B103B.01 (2016) [232]. The vibration profile resembles the one presented for the characterization of the Inertial Measurement Units (Case study A) defined in section 6.5.2.1. The devices have to endure vibration between f_{min} = 5 Hz and f_{max} = 1 kHz with a maximum value which has been set equal to ASD = 0.02 g^2/Hz reached between f_A = 30 Hz and f_B = 200 Hz. The test is illustrated in Fig. 6.49 and it must be repeated three times along X, Y and Z axis for a duration of 30 minutes per axis.
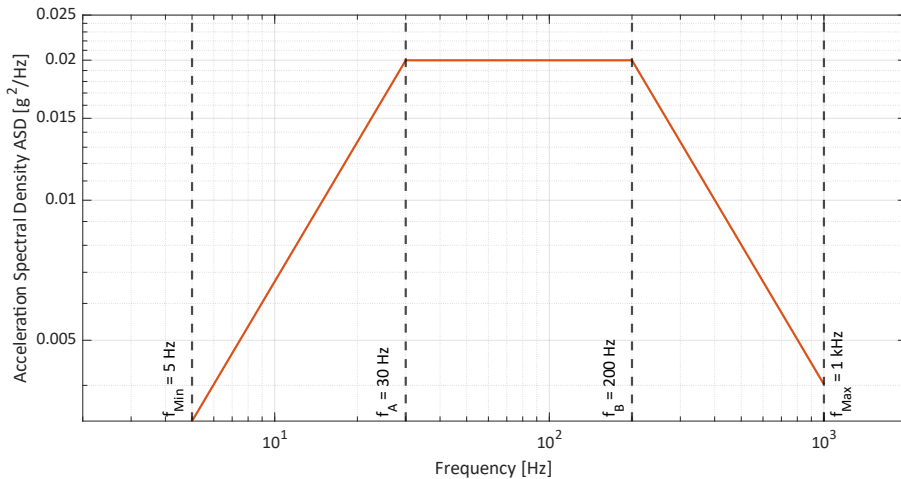
Fig. 6.49. Test plan definition for the characterization of DC-DC converters under harsh conditions. Test C: Random Vibration test.

TEST D. Sinusoidal Vibration Test. It consists of a single sweep of sinusoidal harmonics between f_{min} = 5 Hz and f_{max} = 1 kHz with maximum peak acceleration of A_p = 2g. The vibration profile resembles the one presented for the characterization of the Inertial Measurement Units (Case study A) defined in section 6.5.2.2. The test is illustrated in Fig. 6.50 and it must be repeated along X, Y and Z axis. It has been developed following the guidelines of the international standards IEC 60068-2-6 (2009) [236] and MIL-STD 810G [231].
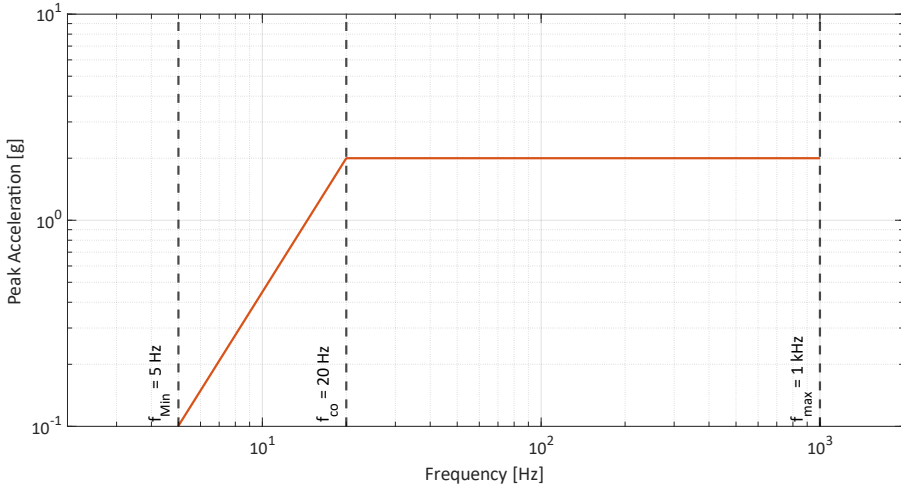
Fig. 6.50. Test plan definition for the characterization of DC-DC converters under harsh conditions. Test D: Sinusoidal Vibration test.

TEST E. High Temperature Test. It consists of a sequence of temperature steps $\Delta T_2 = 20$ °C maintained constant for an exposition time of 1 hour to ensure perfect temperature stability is reached within the chamber. It starts at ambient temperature $T_{AMB} = 20$°C up to extremely high temperature $T_{EX\_HIGH} = 120$ °C. Since this test has been specifically developed to investigate the advantages bring by the introduction of the innovative PSM against the PWM, the set of 8 DUTs has been divided into two groups: 4 PSM-based converters and 4 PWM-based converters. Furthermore, the test aims at extending the applicability of the results of the other tests, proving the ability of the PSM against PWM.

6.9.3 Measurement setup

The purpose of the proposed test plan is the electrical characterization under harsh conditions of 8 DC-DC converters specifically developed for this work as described in Section 2.6. The DUTs have been mounted on a metallic plate which has many purposes: it serves as heat sink facilitating the thermal dissipation, it is used as fixture for the DUTs during the vibration test and it facilitates the wiring. The base idea of the work is to measure different electrical parameters of the DUTs to achieve an overall characterization of the devices when they operate under different test conditions. Accordingly, the following

measurements have been performed during Test A, Test B, Test C, Test D and Test E:

- Measurement of the conversion efficiency η of the 8 DUTs by means of the power meters integrated into the prototype boards.
- Measurement of the conversion efficiency of one DUT by means of two Keithley 2110 5½-digit benchtop digital multimeters. The DMMs used in the setup are characterized by 1 mV resolution in the 100 V DC voltage range required to measure the input and output voltage of the DC-DC converter. The resolution in the 1 A DC current range required to measure input and output current is 10 µA.
- Measurement of the Input Ripple and Output Ripple of one DUT by means of a RIGOL DS1104Z, 100 MHz, 1 GSa/s 4-channel digital oscilloscope.
- Measurement of the step response in terms of Input Overshoot, Output Overshoot and Response delay using the digital oscilloscope described above.

Therefore, a suitable automated measurement setup is required to characterize the DUTs in case of standard operating conditions as illustrated in Fig. 6.51.
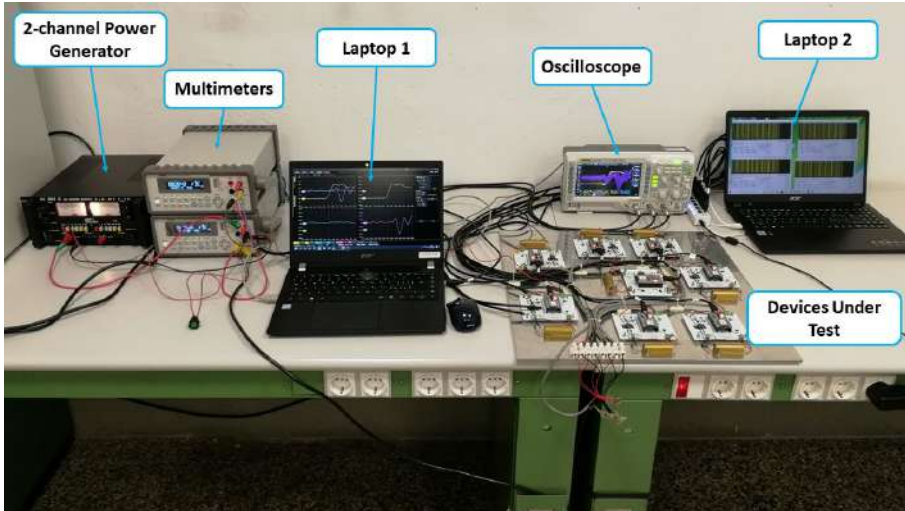
Fig. 6.51. Initial Measurement Setup used to characterize the DUTs in normal conditions without external sources of stress.

Along with the benchtop digital multimeters and the digital oscilloscope, the measurement also includes a 2-channel power generator and two laptops. The

first laptop has been used to store data acquired by the digital instruments (multimeters and oscilloscopes) while the second laptop has been used to store the data acquired by the power meters integrated with the DC-DC converters under test by means of USB serial communication interface.

The setup illustrated in Fig. 6.51 has been used not only for the characterization under standard operating conditions but also during the implementation of the test profiles used to simulate harsh conditions. Only minor adjustments are required, as follow:

- The DUTs must be inserted inside a climatic chamber to carry out the characterization under temperature and humidity stresses. The chamber must be able to regulate temperature and humidity at the same time and its operating limits must allow the implementation of Test A, Test B and Test E. Furthermore, a datalogger equipped with a set of k-type thermocouples and one humidity sensor has been used to monitor temperature and humidity inside the climatic chamber and to acquire data regarding the overheating of the DUTs.

- In order to carry out Test C and test D under vibration stress, an electrodynamic vibration generator (also known as shaker) with an associated computer-based control system is required. Two accelerometers (i.e. control and monitor) have been used to drive the shaker in compliance with the test profile. The setup used in Test C and Test D is shown in Fig. 6.52.
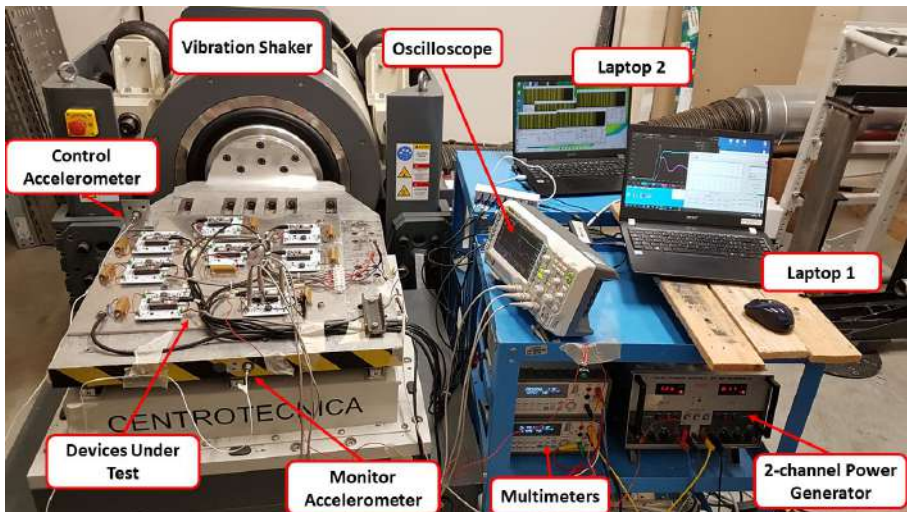
Fig. 6.52. Experimental setup for characterization of eight DC-DC converters under vibration stress (Test C and Test D).

6.10. Case study B: Results and Discussion

This section reports the results achieved on the 8 devices under test during the characterization under harsh conditions.

Fig. 6.53 shows the efficiency variation under temperature and humidity stresses during Test A (thermal cycling test). As an example, the efficiency of 4 out of 8 devices (from DUT 1 to DUT 4) are illustrated using blue trends in Fig. 6.53 while temperature inside the chamber during the test is illustrated using a red trend. The figure highlights a temperature dependence of the DUTs which increase their efficiency at low temperature, and then decrease the efficiency when temperature starts increasing. However, the efficiency variation during the test remains in a limited range for all the 8 DC-DC converters, with a maximum variation range of approximately 1%. This information is fundamental to ensure that the efficiency of the converters remain as expected when the devices operate at extremely low or extremely high temperature.
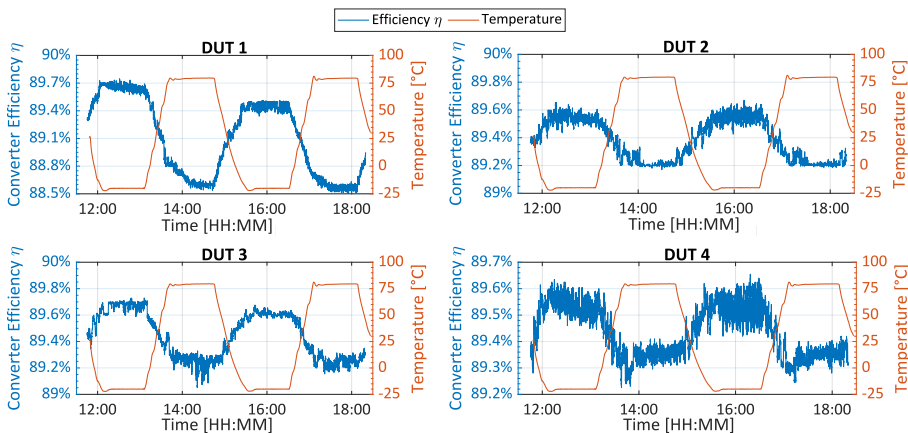
Fig. 6.53. Efficiency variation (left y axis - blue trend) during Test A (thermal cycling test) compared to the temperature of the climatic chamber (right y axis - red trend). DUT 1, DUT 2, DUT 3 and DUT 4 are involved.

Fig. 6.54 shows the input ripple of a DUT 1 during test A (blue dotted trend) compared to the temperature of the climatic chamber. When the device operates at 80 °C the input ripple slightly increases from approximately 80 mV up to about 85 mV. Quite the opposite, the output ripple of DUT 1 shown in Fig. 6.55 remains approximately constant, with slight variations between 5 mV and 6 mV thanks to the optimization of the output capacitor network. This proves the goodness of design of the proposed converter which is able to ensure a very limited output ripple at both -20 °C and 80 °C.
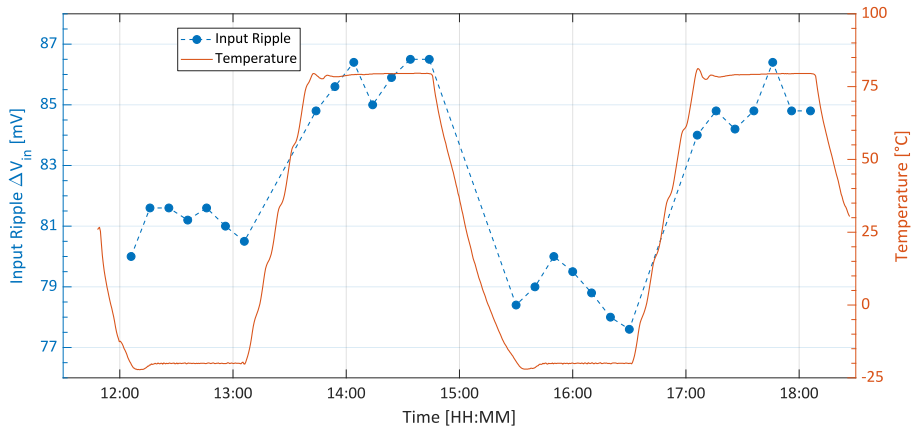
Fig. 6.54. Input ripple of DUT 1 during Test A (thermal cycling test) compared to the temperature of the climatic chamber (right y axis - red trend).
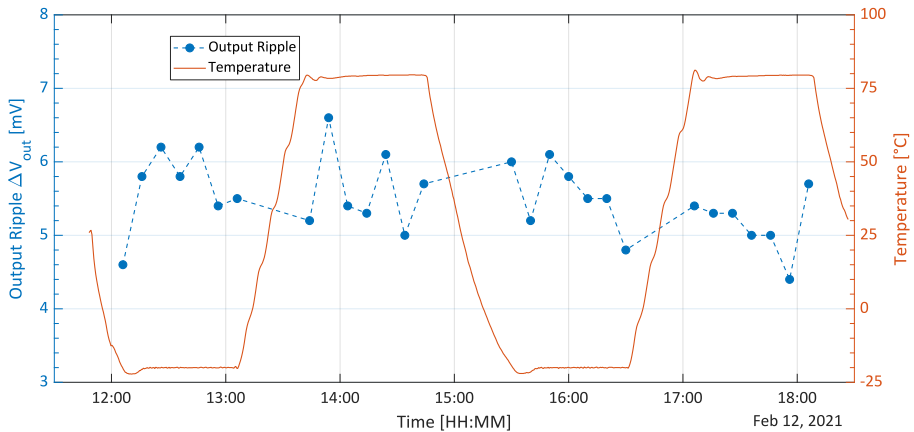
Fig. 6.55. Output ripple of DUT 1 during Test A (thermal cycling test) compared to the temperature of the climatic chamber (right y axis - red trend).

The final analysis of the converter's performances during Test A involves the estimation of the step response analyzing the average input overshoot at -20 °C and 80 °C, the average output overshoot at -20 °C and 80 °C and the average delay time at -20 °C and 80 °C. The results achieved for DUT 3 are summarized in TABLE VI. XL for each temperature and for each cycle. The average input overshoot has minor oscillations, but it does not show any particular dependence on temperature. Quite the same, the average output overshoot remains approximately constant during the complete Test A. However, the average delay time shows a significant increase from about 300 μs measured at -20 °C up to over 600 μs measured at 80 °C. As a consequence, the high

237

temperature does not influence both input and output overshoots of the converter, while it has some significant effects on the delay time.

TABLE VI. XL
STEP RESPONSE OF DUT 3 ESTIMATION DURING TEST A (THERMAL CYCLING TEST) INCLUDING INPUT OVERSHOOT, OUTPUT OVERSHOOT AND RESPONSE DELAY AT LOW AND HIGH TEMPERATURES.

TEMPERATURE	CYCLE	AVERAGE INPUT OVERSHOOT	AVERAGE OUTPUT OVERSHOOT	AVERAGE DELAY TIME
Standard conditions 25 °C	---	21.05 V	14.31 V	298 µs
-20 °C	1	20.96 V	14.44 V	301 µs
	2	21.49 V	14.66 V	289 µs
80 °C	1	21.84 V	14.24 V	961 µs
	2	21.32 V	14.38 V	638 µs

Fig. 6.56 illustrates the efficiency variation under Test B (temperature step test) of 4 out of 8 devices (from DUT 5 to DUT 8). The figure proves the temperature dependence of the convert's efficiency already highlighted by Test A (Fig. 6.53).
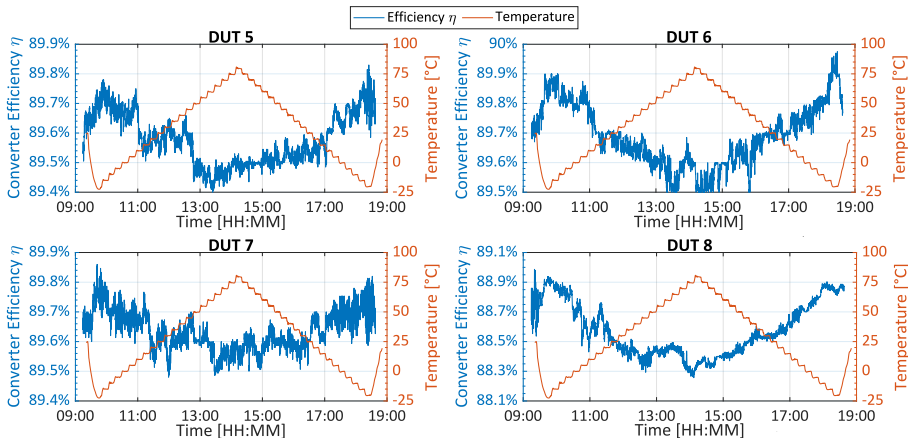
Fig. 6.56. Efficiency variation (left y axis - blue trend) during Test B (temperature step test) compared to the temperature of the climatic chamber (right y axis - red trend). DUT 5, DUT 6, DUT 7 and DUT 8 are involved.

During the 5 °C increasing steps of Test B the efficiency of all the 8 DC-DC converters slightly decreases reaching a minimum value when the device operates around 80 °C. Then, during the 5 °C decreasing steps, the efficiency slowly increases. However, as already happen during Test A, the efficiency variations remain in a limited range with a maximum variation of approximately 1 %. As in test A, the input ripple and the output ripple of the converters have been evaluated also during the temperature step test (Test B). The measurement results of DUT 4 are illustrated in Fig. 6.57 and Fig. 6.58 showing the input and output ripple respectively.
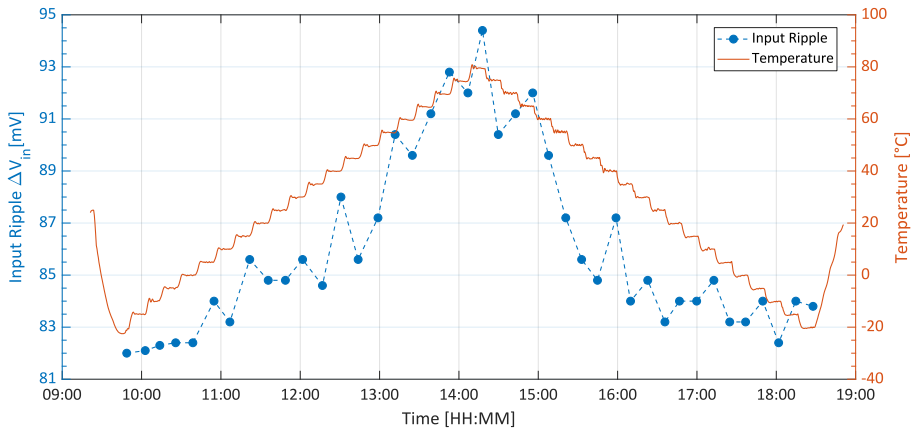
Fig. 6.57. Input ripple of DUT 4 during Test B (temperature step test) compared to the temperature of the climatic chamber (right y axis - red trend).
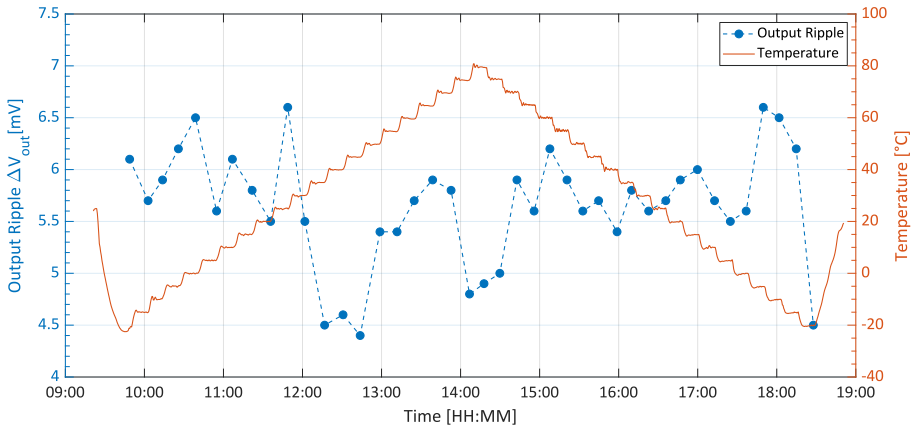
Fig. 6.58. Output ripple of DUT 4 during Test B (temperature step test) compared to the temperature of the climatic chamber (right y axis - red trend).

The input ripple follows the temperature trend slightly increasing when temperature increases, and decreasing when the temperature is lowered. Quite the contrary, the output capacitors allow to maintain the output ripple approximately constant nearby 5.5 mV during Test B.

The step response of DUT 5 evaluated during Test B is depicted in Fig. 6.59. The top subplot shows the input overshoot, while the bottom subplot shows the output overshoot. The input overshoot has some minor variation of approximately 0.8 V not related to the temperature profile. Instead, the output overshoot is more stable, but it shows a minor increase during the lowering phase of the test.
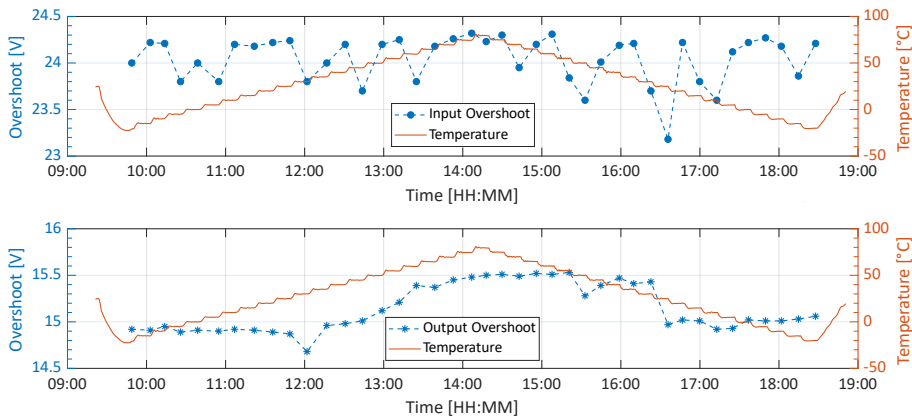
Fig. 6.59. Step response of DUT 5 estimation during Test B (temperature step test). The top subplot illustrates the input overshoot, while the bottom subplot shows the output overshoot.

Fig. 6.60 highlights the overheating of some critical components included in the developed DC-DC converters during Test B (i.e. the microcontroller, the resonant inductor, the 25 Ω load resistance, the power MOSFET and the driver circuit). The height of each bar in Fig. 6.60 represents the average overheating of the 8 DUTs during rising phase (blue bars) and during lowering phase (red bar) of the test. During the lowering phase, the average overheating is greater than the rising phase because of thermal inertia. The interesting aspect standing out from the figure is that the MOSFET and the driver suffer a significant overheating during the test, thus adequate countermeasures to dissipate the heath during normal conditions should be implemented. On the contrary, the overheating of the microcontroller is not excessive.
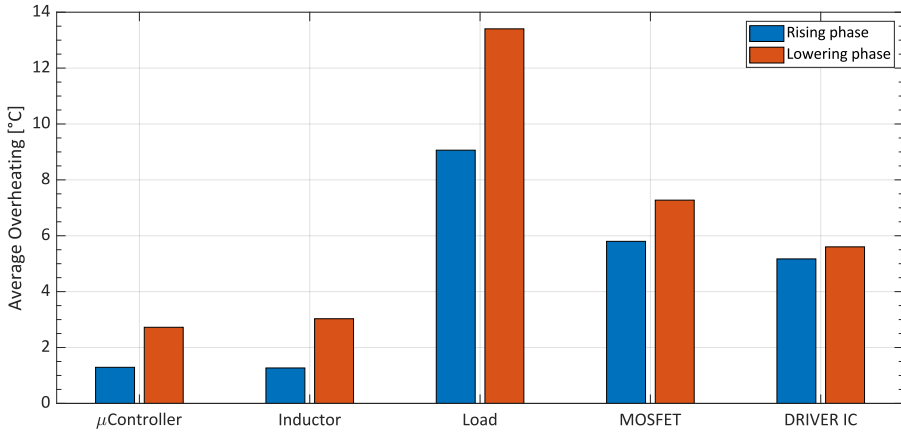
Fig. 6.60. Overheating of some critical components that make up the converters. The height of each bar stands for average overheating of the 8 converters during rising phase (blue bars) and lowering phase (red bars) of Test B.

To provide overall information of the efficiency variations $\Delta\eta$ during both Test A and Test B, Fig. 6.61 compares the results measured from all the 8 DUTs. The yellow bars represent Test A while the blue bars stand for Test B. Both tests have led to a minor variation of the conversion efficiency of all the 8 developed DC-DC converters. However, at the end of both tests, no failure mechanisms have been triggered and all the devices have kept working properly. This means that the temperature and humidity stresses of the proposed ESS test plan were not able to expose any hidden failure.
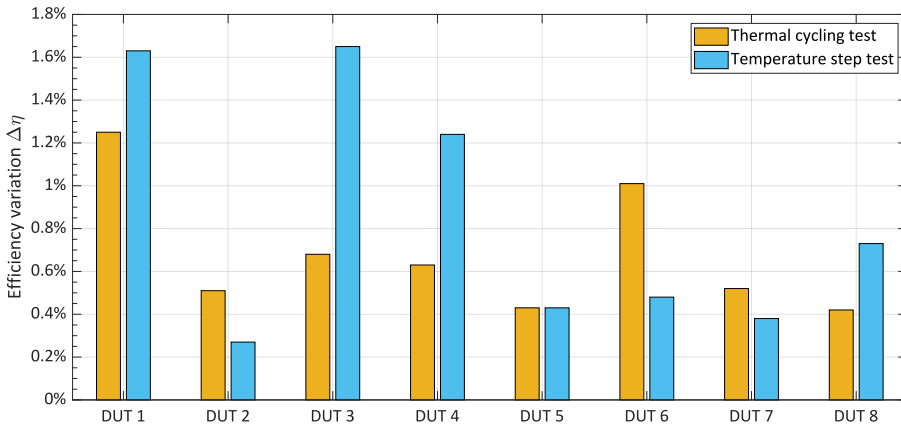
Fig. 6.61. Comparison of the efficiency variation $\Delta\eta$ during Test A (thermal cycling test - yellow bars) and Test B (temperature step test - blue bars).

After the conclusion of the thermal tests A and B, the test plane moves to the vibration stress carrying out random (Test C) and sinusoidal (Test D) vibration along X, Y and Z axis.

As an example, Fig. 6.62 compare the efficiency of DUT 6 before and after the execution of the random vibration test along Z axis.
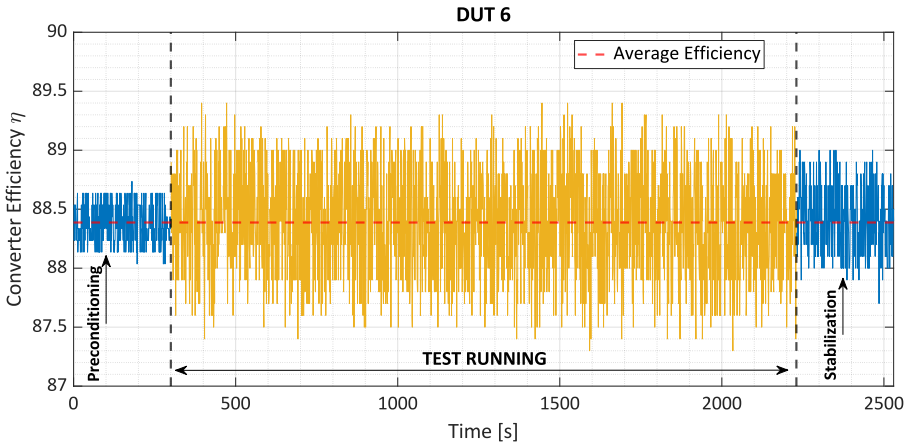
Fig. 6.62. Efficiency of DUT 6 before and after Test C (blue trends) compared to the efficiency measured during the test (yellow line). Z axis is involved.

During the test execution, the variability of the converter efficiency suddenly increases with respect to the standard conditions measured during the preconditioning phase. However, this unexpected behavior is not a major criticality for the system under test because of three reasons:

- The increment of the efficiency under vibration stress is not remarkable. In fact, it remains consistently within the 2% variability.
- The mean value of the converter efficiency before and after the test is approximately equal to the efficiency measured during the test running. This means that, overall, the vibration stress does not affect the efficiency of the device.
- After the test conclusion, the efficiency of the converter goes back to the values before the test, highlighting that no permanent failure mechanisms have been triggered during the test.

The same results have been obtained for every device and for each excitation axis. For the sake of brevity, the mean value and the standard deviation of the 8 DUT's efficiency is reported in TABLE VI.XLI.

TABLE VI.XLI

PERFORMANCE ANALYSIS OF THE EIGHT DUTs UNDER VIBRATION. BOTH TEST C AND
TEST D ARE INVOLVED. VIBRATION APPLIED ALONG X AXIS.

TEST ZONE	DUT 1	DUT 2	DUT 3	DUT 4	DUT 5	DUT 6	DUT 7	DUT 8
Pretest	Mean Value μ							
	89.145%	89.371%	89.532%	89.344%	89.382%	88.416%	88.911%	87.091%
	Standard Deviation σ							
	0.003%	0.003%	0.003%	0.005%	0.0021	0.081%	0.062%	0.004%
Test C Random Vibration	Mean Value μ							
	89.224%	89.314%	89.481%	89.334%	89.329%	88.388%	88.673%	86.973%
	Standard Deviation σ							
	0.026%	0.011%	0.004%	0.012%	0.0099	0.184%	0.091%	0.023%
Test D Sine Vibration	Mean Value μ							
	89.255%	89.304%	89.434%	89.334%	NaN	88.379%	88.742%	86.985%
	Standard Deviation σ							
	0.006%	0.004%	0.004%	0.012%	NaN	0.207%	0.057%	0.004%
After test	Mean Value μ							
	89.247%	89.304%	89.408%	89.312%	NaN	88.424%	88.923%	87.063%
	Standard Deviation σ							
	0.031%	0.002%	0.010%	0.004%	NaN	0.218%	0.098%	0.002%

In the table, the performance before the test is compared with the efficiency during Test C (random vibration), during Test D (sinusoidal vibration) and after the test execution. The table shows the measurement results when the vibration is performed along X axis. However, similar results have been achieved also during the actuation of the test toward Y and Z axis. It is important to note that Test C expose a hidden failure on DUT 5. At the end of the Random Vibration Test the DC-DC converter number 5 stopped working because of some problems during the manufacturing of the board. TABLE VI.XLI reports 'NaN' in the column of DUT 5 to highlights this issue.

Along with the characterization of the devices, the proposed test plan had the aim of precipitate any eventual hidden failure of the converters under test. In this case, the two temperature tests were not able to expose such failure, while the random vibration did. The failed solder joints of DUT 5 that lead to the converter failure are shown in Fig. 6.63.
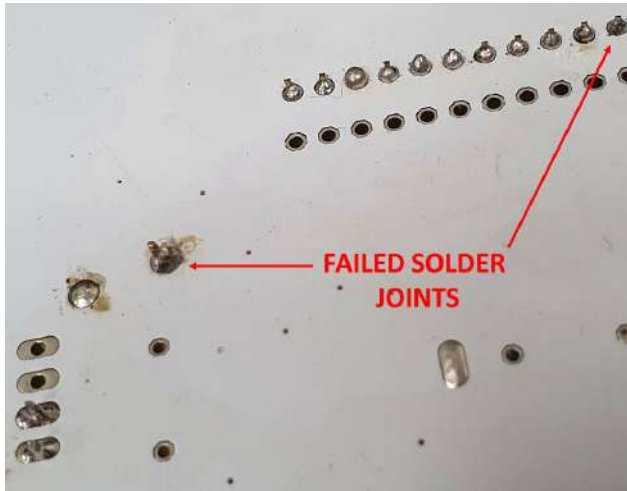
Fig. 6.63. Zoom of the bottom side of DUT 5 highlighting the failed solder joints as a consequence of Test C (Random Vibration test).

Another important analysis proposed in this work is the comparison between the PWM and PSM for different operating temperatures performed during Test E. The main aim of the test was to emphasize the benefits of PSM-based converters against PWM-based converters under light load conditions.

In Fig. 6.64(a), the DC-DC conversion efficiency for different loads is shown. For each modulation, the efficiency has been evaluated at two temperature, namely T = 20 °C and T = 120 °C. The variations of efficiency $\Delta\eta_T$ due to the temperature excursion are represented using double end arrows. The figure highlights how PSM allows to maintain remarkably high efficiency at both ambient temperature T_{AMB} and extremely high temperature T_{EX_HIGH} over a wide range of output power, from 0.5 W up to 20 W. For instance, the most striking result to emerge is that the higher efficiency decrease for the PSM-based converter is approximately $\eta T = 0.8$ % (increasing temperature from 20°C up to 120°C). On the other hand, the PWM-based converter decreases its efficiency by almost 7% moving from 20 °C up to 120 °C.

In Fig. 6.64(b), the gain of efficiency using the PSM respect to PWM for different output power and operating temperatures is highlighted. The observations that can be made are:

- The conversion efficiency can be remarkably improved in case of light load conditions using the PSM. The switching losses for light load are predominant and highly affect the conversion efficiency.
- The efficiency of the converter with PWM is highly affected by the temperature. On the other hand, the converter efficiency with PSM

244

remains almost unchanged with the temperature. Thus, the PSM modulation is suggested in every application field in which the operating temperature varies in a wide range.

As a consequence, PSM was selected as the best suited modulation for WSN application, where each node may operate in harsh environment.

(a)

(b)
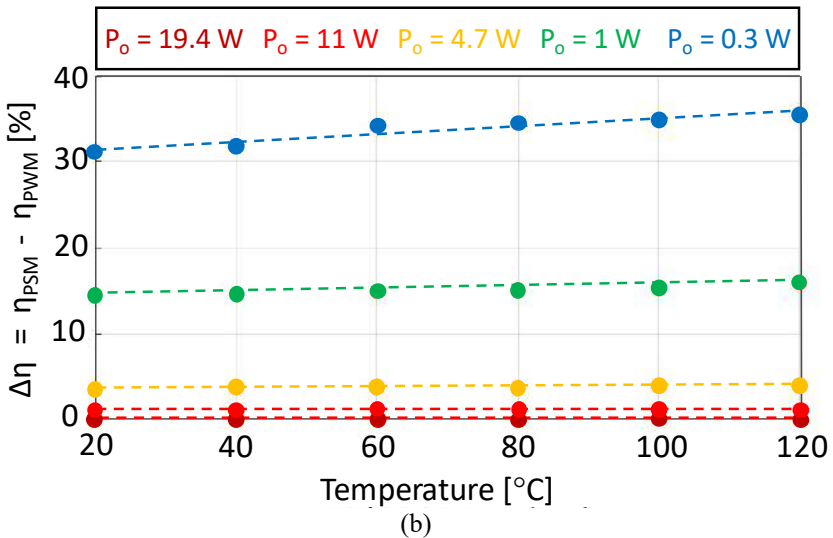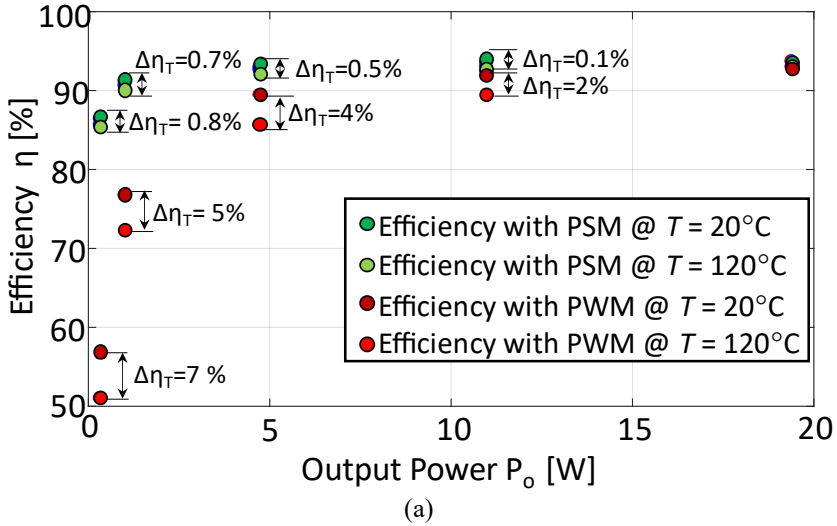
Fig. 6.64. Comparison between PWM and PSM efficiency for different operating temperatures. (a) Difference of efficiency for different power and temperature. (b) Comparison between PSM and PWM for different loads and temperatures.

CHAPTER 7

CONDITION MONITORING: FROM PLANNING TO IMPLEMENTATION

Condition monitoring (CM) plays a central role in maintenance-decision making of complex systems. Thus, it has been included in the proposed Reliability Life Cycle procedure. This chapter provides an overview of CM techniques taking a wind turbine as an example. An innovative diagnostic-oriented methodology to select the optimal maintenance policy is presented as an alternative to the classical RCM decision-making process. The chapter also presents a new data-driven CM system to efficiently monitor the health state and detect damages in the wind turbine by means of measurements of critical parameters. Finally, an innovative hybrid-tree Wireless Sensor Network is presented in order to effectively and efficiently implement condition monitoring on the whole wind farm. [1, 2]

---

[1] The innovative RCM approach and the application to the Yaw system included in this chapter have been published as "M. Catelani, L. Ciani, D. Galar, and G. Patrizi, "Optimizing Maintenance Policies for a Yaw System Using Reliability-Centered Maintenance and Data-Driven Condition Monitoring," IEEE Trans. Instrum. Meas., vol. 69, no. 9, pp. 6241–6249, Sep. 2020. ".

[2] The part of this chapter related to the condition monitoring of the whole wind farm has been published as "L. Ciani, A. Bartolini, G. Guidi, and G. Patrizi, "A hybrid tree sensor network for a condition monitoring system to optimise maintenance policy," ACTA IMEKO, vol. 9, no. 1, pp. 3–9, 2020.

7.1. Overview of maintenance planning

Since the last years, diagnostics process became fundamental in several different field of applications. Diagnostic is now an essential part of performance requirements in Industry 4.0, especially for industrial, energy and transportation system [34]–[36], [275]–[277]. Diagnostic is used to evaluate the current health state of the system under test predicting its remaining useful life based on features that capture the gradual degradation of its operational capabilities. As a matter of fact, diagnostic procedures allow to improve reliability, availability, maintainability and safety (RAMS) parameters of complex system, ensuring that the equipment works successfully and reducing down-time due to unexpected failures [278]–[282].

Condition monitoring (CM) is one of the most effective and powerful diagnostic procedure: CM is the process of monitoring one or more condition parameters in machinery to identify some changes that are indicative of an incipient fault or equipment health degradation [148]. In the past, condition monitoring was applied simply through routine manual diagnostic actions but, with the introduction of low-cost sensors and automated monitoring systems, online data-driven condition monitoring was adopted.

Condition monitoring is a type of condition-based maintenance (CBM) used to select and survey parameters from the sensors placed in the system in order to detect a change in the health machine condition [283], [284].

During the design phase of a product or plant the assessment of the optimal diagnostic and failure management policy is a critical phase that could be implemented using the Reliability centred maintenance (RCM) procedure. RCM allows to efficiently and effectively achieve the required safety, availability and economy of operation. Reliability Centred Maintenance provides a decision process to identify applicable and effective diagnostic and preventive maintenance requirements for equipment in accordance with the safety, operational and economic consequences of identifiable failures, and the degradation mechanisms responsible for those failures. RCM uses a FMEA analysis to lead the diagnostic and maintenance assessment toward the most cost-efficient and cost-effective solution. According to the international standard IEC 60300-3-11, the RCM procedure follows five steps providing a comprehensive program that addresses not only the analysis process but also the preliminary and follow-on activities necessary to ensure that the RCM effort achieves the desired results [285]–[288]:

1. Initial definition (Availability requirements, maintenance specification, environment and so on);
2. Failure modes and effects analysis;

3. Identification of the optimal maintenance task using the decision-making diagram;
4. Implementation of corrective actions;
5. Continuous improvements that give information to improve steps 2 and 3.

The above-mentioned five steps are summarized in Fig. 7.1.
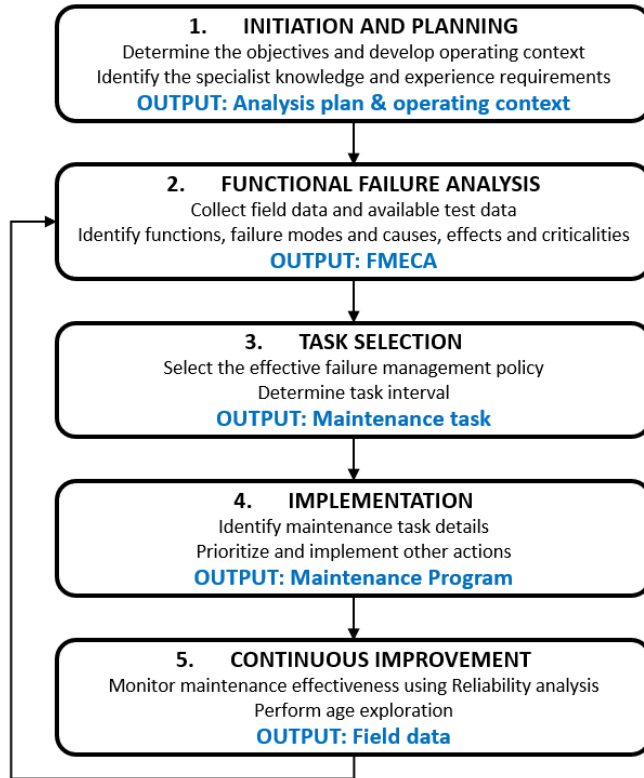
Fig. 7.1. Flow chart of the RCM process including five consecutive steps in order to select the optimal maintenance policy

Steps 2 and 3 are the core of Reliability Centred Maintenance. The "Identification of the optimal maintenance task" (step 3) is guided by the FMEA report that provides important information to select the most appropriate and effective failure management policy. In compliance with the international standard IEC 60300-3-11, the main maintenance task are [288]:

- Condition monitoring: it is a continuous or periodic task to evaluate the condition of an item in operation against pre-set parameters in

order to monitor its deterioration. It may consist of inspection tasks, which are an examination of an item against a specific standard.

- Scheduled restoration: it is the work necessary to return the item to a specific standard. Since restoration may vary from cleaning to the replacement of multiple parts, the scope of each assigned restoration task has to be specified.
- Scheduled replacement: it is the removal from service of an item at a specified life limit and replacement by an item meeting all the required performance standards.
- Failure-finding (FF): it is a task to determine whether or not an item is able to fulfil its intended function. It is solely intended to reveal hidden failures. A failure-finding task may vary from a visual check to a quantitative evaluation against a specific performance standard. Some applications restrict the ability to conduct a complete functional test: in such cases, a partial functional test may be applicable.
- No preventive maintenance: in some situations, no task is required, depending on the effect of failure. The result of this failure management policy is corrective maintenance or no maintenance at all. Sometimes, this approach is called "Run-To-Failure".

Condition monitoring and failure finding belong to the Condition Based Maintenance (CBM) procedures. CBM is the most effective policy because its goal is to monitor the health state of the system under test planning a maintenance task only in case it is necessary [289]–[292].

In compliance with international standard IEC60300-3-11 [288], Fig. 7.2 shows how to guide the maintenance task selection in order to identify the optimal maintenance solution for the system under test.

The maintenance decision-making diagram aims to simplify the assessment of the optimal maintenance tasks. However, the maintenance policy choice depends only on two conditions: if the failure is evident or not and if the failure will involve consequences on the safety level of the system under test. As a consequence, at least four possible task options are given in each orange box; this means the international standard gives the designer a high level of subjectivity. Overall, the diagram is very generic and doesn't lead to a unique task choice; the designer is free to choose one or another option, based only on his or her expertise.
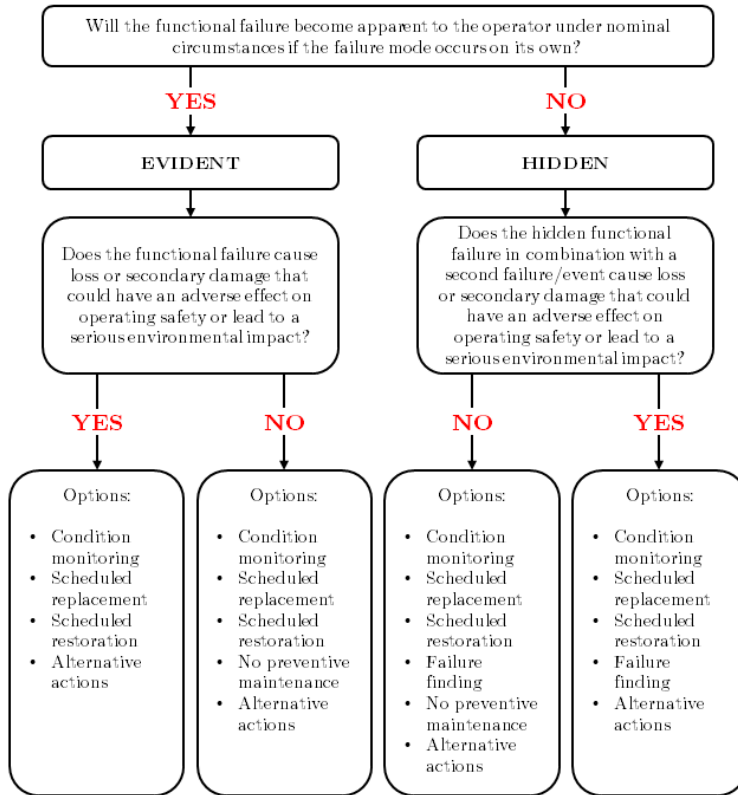
Fig. 7.2. Decision diagram for maintenance assessment according to the international standard IEC 60300-3-11.

7.2. State of the art of Reliability Centred Maintenance

The most important but challenging parts of the RCM process are failure mode effect and criticality analysis (FMECA) and task selection. FMECA is developed using the subjective knowledge of domain experts. Meanwhile, the decision diagram proposed by the international standard IEC 60300-3-11 [288] for task selection is very generic, and the task choice mostly relies on the experience of the analyst that performs the RCM [293]. Despite these disadvantages, RCM is a powerful solution, widely used in every industrial field in which service continuity represents a mandatory requirement, and maintenance must be optimized in terms of money and time [294].

Some researchers propose an effective RCM assessment using reliability software [295]. In [296] the RCM is applied to the whole system under test instead of focusing on individual components. Others papers use analytical models and a dynamic approach [297], [298], while some authors create their own framework for maintenance decision making [299], [300]. Zakikhani et al. [301] proposes an availability-based RCM, while in [302] a whole dependability study (RAMS) is introduced to optimize maintenance policy. In [303] the variation trends of the failure rates of components under imperfect maintenance are used to optimize the maintenance of metro trains based on the concept of RCM. Afzali et al. [304] proposes a weighted importance reliability index model to prioritize the components in a complete RCM report. In [305] a stochastic RCM is proposed, while other papers introduce genetic algorithms to solve the mathematical problem of RCM optimization [306], [307].

7.3. Proposed approach for maintenance decision-making of a wind farm

This work focuses on a Spanish wind farm located near Zaragoza, in the region of Aragon (Spain).

A wind farm, sometimes called wind park, is a group of wind turbines (WTs) in the same location used to produce electricity. A large wind farm may consist of several hundred individual wind turbines and cover an extended area of hundreds of square kilometers [13], [308]. This results in a very critical issue during the maintenance planning phase as well as during the design of condition monitoring and diagnostic systems. Furthermore, unexpected failure events and low availability are crucial challenges for wind-power operators, especially as the installed capacity of wind power has been growing exponentially in recent years [309]. Moreover, the decision-diagram presented in the RCM international standard (IEC 60300-3-11) is far to generic since it let to the user the possibility to choose between at least 4 different options without a detailed explanation of how to assess the optimal tasks between these options.

Trying to fill this gap, this work introduces a customized decision-making process able to solve the subjectivity of the procedure proposed in the standard and consequently to address the optimal maintenance policy to the wind farm. The proposed method uses a decision-logic diagram (Fig. 7.3) to suggest only one of the tasks illustrated in the previous section for each of the failure mode identified through the FMECA.
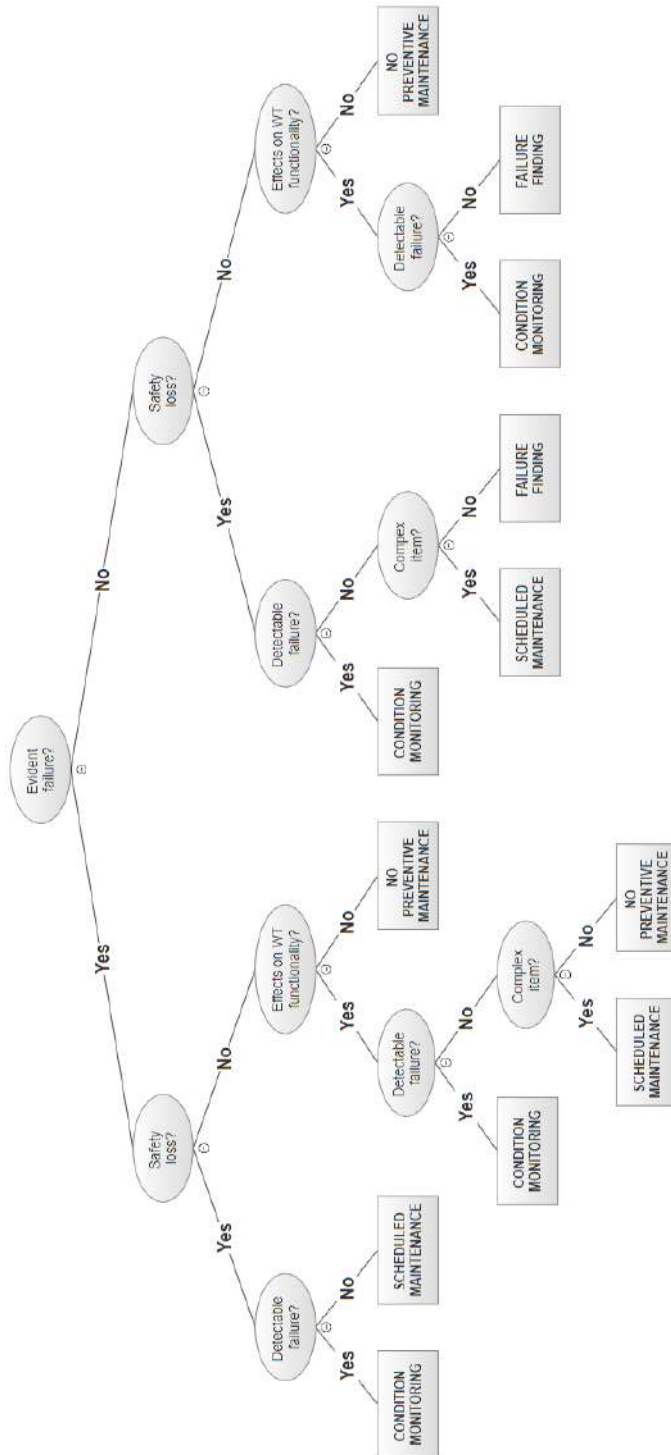
Fig. 7.3. Proposed procedure for maintenance decision diagram based on failure analysis

Firstly, the failure modes are classified as hidden or evident. Then the designer has to understand different characteristic of the failure mode depending on the path:

- Will the failure mode lead to a safety loss?
- Will the failure mode involve effects on the turbine functionality?
- Is it possible to detect the failure cause?
- Is the item under test characterized by high complexity?

The information included in the FMECA are mandatory in order to answer the previous questions and consequently address the optimal task to each failure mode. It is very important to note that several paths of the decision diagram led to the choice of CM. If it is possible to detect the cause that could lead to the failure, then the process guides the designer to assess the CM task despite the other information on the failure classification.

Overall, the approach could be considered as a diagnostic-oriented decision-making diagram which prefers the assessment of CBM tasks (either CM or FF) with respect to scheduled maintenance task. In case of extremely big systems under analysis as the considered wind farm, this will allow a remarkable decrease of Operation and Maintenance costs and a significant improvements of plant availability.

In case of failure finding or scheduled maintenance assessment the interval between two consecutive tasks must be evaluated. Taking the yaw system of a wind turbine as a case study, this work assesses the task interval by means of the occurrence of each failure mode. The occurrence O is a rate that the FMECA used to classify the probability that a failure mode will happen. Three scheduled maintenance intervals are planned: 3, 6, or 12 months.

Very short maintenance intervals are proposed because WTs are hybrid systems mainly composed of electric, mechanical and hydraulic sub-units. These kinds of components tend to degrade very quickly with time; therefore, the maintenance plan must be optimized to minimize the Life Cycle Cost (LCC) and ensure high availability. Hence the choice of a short interval between two consecutive tasks. The failure finding procedure is a cheaper and less complex practice than scheduled maintenance. Therefore, its task interval is shorter than the scheduled maintenance interval because failure finding doesn't involve all the turbine functionality. Moreover, FF could be run during the standard turbine operation. The task interval is not defined for condition monitoring or no preventive maintenance. CM is a continuous procedure that monitors some characteristic of the productive process during all the turbine run-time, so it is implemented continuously. Quite the opposite no preventive maintenance is

used only after failure (i.e., run-to-failure). TABLE VII.I summarizes the criteria proposed in this work to define the task interval for the wind turbines the compose the wind farm under analysis.

TABLE VII.I

CRITERIA FOR THE ASSESSMENT OF THE INTERVAL BETWEEN TWO CONSECUTIVE TASKS.

OCCURRENCE	SCHEDULED MAINTENANCE	FAILURE FINDING	CONDITION MONITORING	RUN TO FAILURE
From 1 to 4	12 months	6 months	Continuously	-
From 5 to 7	6 months	3 months	Continuously	-
From 8 to 10	3 months	1 month	Continuously	-

7.4.   Application: Yaw system of a wind turbine

In this section the proposed diagnostic-oriented maintenance decision-making has been applied to the yaw system of a 2 MW Wind Turbine as described in [15].

The analyzed yaw is mounted on the top of a 60-meter tubular tower with the function of moving the nacelle toward the wind direction. Fig. 7.4 depicts the low-level taxonomy of the yaw system according to the guidelines of the international standard ISO 14224 [310].
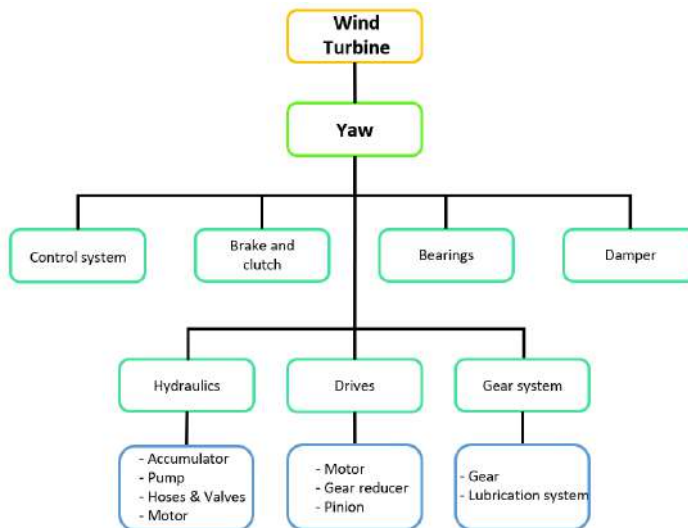
Fig. 7.4. Low-level taxonomy of the yaw system under study.

The RCM assessment starts with the "initiation and planning" step; the taxonomy depicted in Fig. 7.4 is mandatory to analyze the operating context and define the work plane. As highlighted by Fig. 7.1, after the taxonomy is identified, a functional failure analysis must be done to study all problems that might arise from malfunctions of the system. The investigation starts at the lowest taxonomic level and continues to the system level.

Using the decision-making diagram proposed in this work it is possible to assess the optimal maintenance task for each failure mode through the information provided by the FMECA. The choice guided by the diagnostic-oriented decision diagram in Fig. 7.3 results to be the optimal solution in terms of cost, plant productivity and unexpected downtimes.

TABLE VII.II summarizes an extract of the maintenance report for the yaw system under test. This table contains the answers to the questions asked in the proposed decision-making diagram.

Thus, for each failure mode identified during the preliminary functional failure analysis, the table includes:

- The occurrence rate O provided by five reliability experts in order to quantitatively consider the criticality of the components. The final value reported in the table is obtained through the average of the expert assessment.
- A description of the failure impact on the turbine functionalities (i.e. No impact, Reduced, Strongly Reduced, System does not work).
- The failure classification as hidden or evident according to the requirements of the standard IEC 60300-3-11.
- The impact that the failure produce on the overall system safety (expressed as simple binary option YES/NO).

FMECA results are crucial in the maintenance task assessment because they provide the expert with a mean to make the projects more cost-efficient and cost-effective. In fact, knowing the cause and the effect of a failure is important during the process of identification of the optimal maintenance policy. For instance, if it is possible to monitor the causes that could lead to a failure mode, then a condition monitoring system must be implemented in order to identify every possible event that indicate an incipient fault.

TABLE VII.II also includes the outcomes of the RCM procedure (task option, task interval, and task duration) following the guidelines proposed in the innovative approach described in the previous section.

TABLE VII.II

PROPOSED PROCEDURE FOR MAINTENANCE DECISION-MAKING: INPUT AND OUTPUT OF THE METHOD FOR THE YAW SYSTEM UNDER ANALYSIS

	INPUT						OUTPUT		
Upper level taxonomy	Item	Failure modes	O	Turbine functionality	Failure classification	Safety loss	Task option	Task duration	Task interval
-WT -Yaw	Brake and clutch assembly	Excessive Wear	6	Strongly reduced	Hidden	YES	Condition monitoring	-	Continuously
		Leaking	6	Strongly reduced	Evident	YES	Condition monitoring	-	Continuously
		Cracked housing	4	Barely Reduced	Hidden	NO	No preventive maintenance	-	-
-WT -Yaw	Damper	Fail to open/close	9	Reduced	Evident	YES	Scheduled restoration	8 h	3 months
		Leaking	6	Reduced	Evident	NO	Condition monitoring	-	Continuously
-WT -Yaw -Hydraulics	Hoses & valves	Leaking	6	Reduced	Evident	NO	Condition monitoring	-	Continuously
		Stuck Closed	4	Reduced	Hidden	NO	Failure finding	4h	6 months
		Stuck Open	4	Reduced	Hidden	NO	Failure finding	4h	6 months
-WT -Yaw -Hydraulics	Pump	Leaking	8	Reduced	Evident	NO	Condition monitoring	-	Continuously
		Improper Flow	7	Reduced	Hidden	NO	Condition monitoring	-	Continuously
		No Flow	6	Strongly reduced	Evident	NO	Condition monitoring	-	Continuously
-WT -Yaw -Drives	Motor	Winding Failure	4	Strongly reduced	Evident	NO	Scheduled restoration	16h	12 months
		Bearing Failure	4	Strongly reduced	Evident	NO	Scheduled restoration	16h	12 months
		Fails to Run, After Start	4	Strongly reduced	Evident	NO	Scheduled restoration	16h	12 months
		Fails to Start	3	Strongly reduced	Evident	NO	Scheduled restoration	16h	12 months
-WT -Yaw -Gear system	Lubrification system	Loss of oil	8	Reduced	Hidden	YES	Scheduled restoration	16h	3 months
		Oil overheating	8	Reduced	Evident	YES	Condition monitoring	-	Continuously
		Oil under temperature	8	Reduced	Evident	YES	Condition monitoring	-	Continuously

The results are summarized in Fig. 7.5, which is a pie chart containing the assigned percentages of each operational task within the maintenance plan. The percentages are obtained considering the value of the "task option" column in the complete maintenance report of the system under test, while TABLE VII.II includes only an extract of this assessment.

Fig. 7.5. Pie chart of the complete task selection for the yaw system under analysis

Fig. 7.5 highlights that only 5% of the assigned tasks are corrective maintenance (i.e. run to failure) in order to maximize the system availability. CBM (condition based maintenance, that comprises both condition monitoring and failure finding) is much larger because it maximizes availability and minimizes the life-cycle cost of the system by intervening before the occurrence of failure. Condition monitoring has the highest percentage (41%) of all tasks. These results come out from the previous consideration and they represent the proof of the importance of condition-based maintenance on real case. According to the plan, for the 67% of failure modes it is possible to implement maintenance only if some condition shows that the system is going to fail. In this way, it is possible to save money decreasing downtime due to unexpected failure because condition monitoring system informs the operating center that a possible failure is going to happen when the turbine is still working. At the same time, condition monitoring allows to decrease the maintenance cost avoiding scheduled maintenance at certain time in which the turbine doesn't need to be maintained. In fact, scheduled maintenance can sometimes lead to unnecessary maintenance routines and loss of production capacity.

The complexity and the cost of most of the components that make up the yaw is another reason why the allocation percentage of scheduled restoration is less

than the condition monitoring. In fact, the replacement of a component not yet broken is almost never acceptable for these kinds of items. In particular, not even one scheduled replacement is assessed, as a matter of fact the whole scheduled maintenance (28%) is scheduled restoration.

7.5. Implementation of Condition Monitoring for the Yaw system under analysis

This section proposes an effective data-driven CM system to monitor some of the most critical component of the Yaw under analysis according to the RCM report assessed using the guidelines of the proposed procedure (Fig. 7.3).

TABLE VII. III contains an extract of the proposed CM assessment for the yaw system of the studied WT.

TABLE VII. III

MEASUREMENT UNITS AND SENSORS USED BY THE CM UNIT TO MONITOR THE YAW

ITEM	FAILURE MODES	MEASUREMENT	SENSORS
Hydraulics system	- Leakage - Contamination - Improper flow - Stuck valve	Pressure	Piezoelectric pressure transmitter
		Flow	Ultrasonic meter
		Temperature	Thermocouple
		Level	Magnetic level meter
		Contamination	Contamination sensor
		Structural integrity	Ultrasound sensor
Gear	- Binding/Sticking - Excessive Wear - Fails to move - Mechanical damage	Vibration	MEMS accelerometer
		Temperature	Thermocouple
		Motion	Displacement transducer
		Applied force	Strain gauge
		Micro-deformation	Extensimeter
		Structural integrity	Ultrasound sensor
Control system	- Parameter drifts - No output - Short/Open circuit - Error in data elaboration	Temperature	Resistance temperature detector
		Humidity	Humidity sensor
		Vibration	MEMS accelerometer
		Power consumption	Integrated power meter

Considering some of the most critical components, TABLE VII. III illustrates the measurement units and the types of sensor proposed for monitoring the yaw of the WT under analysis by means of the CM system. The electrical failure causes are mainly influenced by environmental condition, therefore a Resistance Temperature Detector (RTD), a humidity sensor and a MEMS accelerometer are used to monitor the control system along with an integrated power meter to monitor current consumption and voltage at the same time. A Piezoelectric pressure transmitter, an ultrasonic flow meter, a thermocouple, a magnetic level meter and a contamination sensor are used to investigate the characteristics of the oil in the hydraulic system, while an ultrasound sensor is used to monitor the structural integrity of the hydraulic unit.

In compliance with [15], Fig. 7.6 and Fig. 7.7 propose two possible ways to implement data-driven condition monitoring in the hydraulic system: oil temperature and hydraulic pressure. For both, condition monitoring involves two crucial tasks:

- Data sampling and storage.
- Limit alarm monitoring by comparing the signals provided by the sensors against a pre-set limit.

Fig. 7.6 shows the variation of the oil temperature inside the pistons used to move the nacelle. The data were acquired by the CM tool using a 25 Hz sampling frequency by means of temperature sensors located in different points of the hydraulic subsystem. Fig. 7.6 proposes two different high limit levels for the oil temperature based on expert judgment and historical data acquired on different days.

The yellow line stands for the "first level alert". If the signal passes this limit, the CM system activates a relay output and sends a message to the operating center warning the operator of a possible incipient problem/failure. The red line represents the "hazardous alarm". If the signal passes this limit, the CM system commands a turbine emergency shutdown.

Fig. 7.7 shows a different approach, looking at the hydraulic pressure of the fluid. The sampled data must be compared with two low alarms ("low first level alert" and "low hazardous alarm") and two high alarms ("high first level alert" and "high hazardous alarm") at the same time.

The low alarms identify possible leakage or breakage in the hoses and valves. The high alarms warn about overpressure inside the pump or the valves that could lead to several mechanical failure mechanisms.
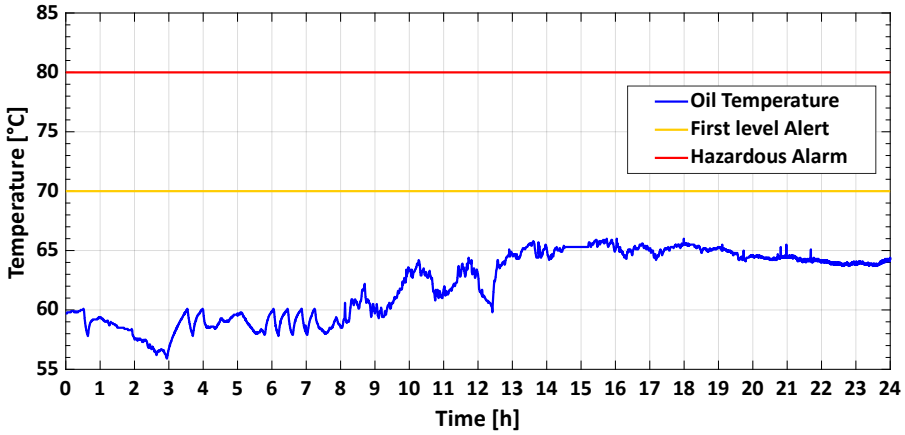
Fig. 7.6. CM for oil temperature: sampled data and limit alarm
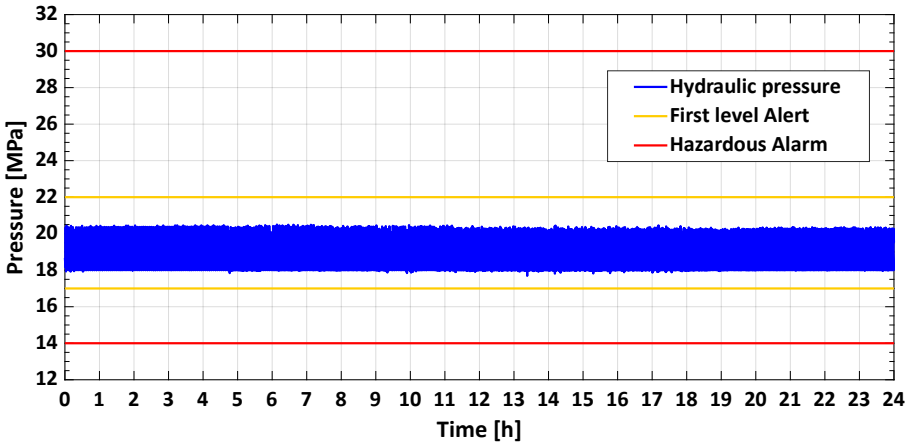
Fig. 7.7. CM for hydraulic pressure: sampled data and limit alarm.

Temperature is the perfect indicator of possible incipient failure for all kinds of items, especially electrical and electronical ones. Therefore, as reported in Table VII. III, a condition monitoring system based on the temperature inside the nacelle is the perfect solution for the control system.

Fig. 7.8 highlights the effects of temperature on control system reliability [311], [312]. The blue line is the reliability of the control system calculated using an RBD model where the failure rate of the components was evaluated using a reliability prediction with standard environmental conditions $\lambda_i^{(T_0)}$.
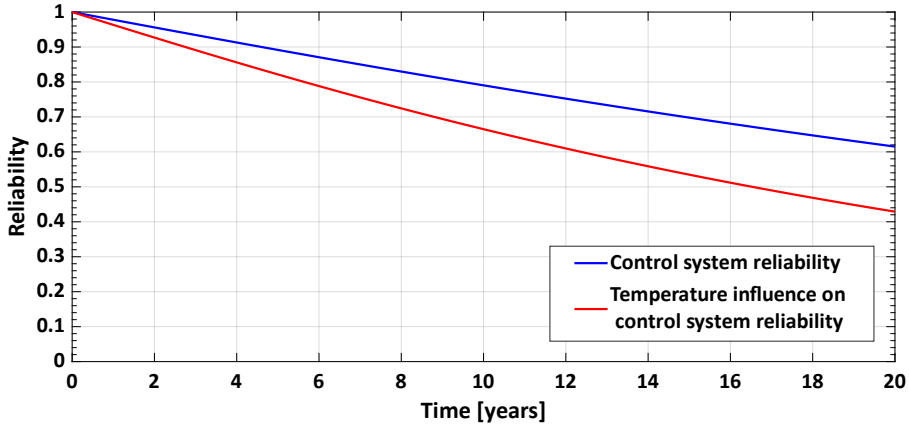
Fig. 7.8. Temperature effects on control system reliability.

According to Arrhenius's model illustrated in equations (7.1)-(7.2), the reliability of the electronic system is deeply influenced by temperature, and the probability of failure rapidly increases when the temperature increases [312], [313].

$$\lambda_i^{(T)} = AF_{Arr} \cdot \lambda_i^{(T_0)} \qquad (7.1)$$

$$AF_{Arr} = exp\left[\frac{E_a}{K_B}\left(\frac{1}{T_0} - \frac{1}{T}\right)\right] \qquad (7.2)$$

Where the activation energy E_a has been set according to handbooks and standards as $E_a = 0.6\,eV = 9.613 \cdot 10^{-20}\,J$ (see for instance [147], [150], [156], [312]) and the standard temperature is given by $T_0 = 25\,°C$.

The actual temperature $T = 35\,°C$ has been evaluated using the average of the acquired temperature during a week of operation.

The analysis carried out on the control system and illustrated on Fig. 7.8 highlights that the impact of temperature on electronic component increases over time and becomes particularly significant after approximately two years of the turbine life.

Fig. 7.9 proposes a condition monitoring implementation for the control system. The assessment is similar to the ones proposed for the oil temperature. The alarm level is quite low because even a little increase in the temperature could activate some failure mechanisms that are usually neglected at standard temperatures.
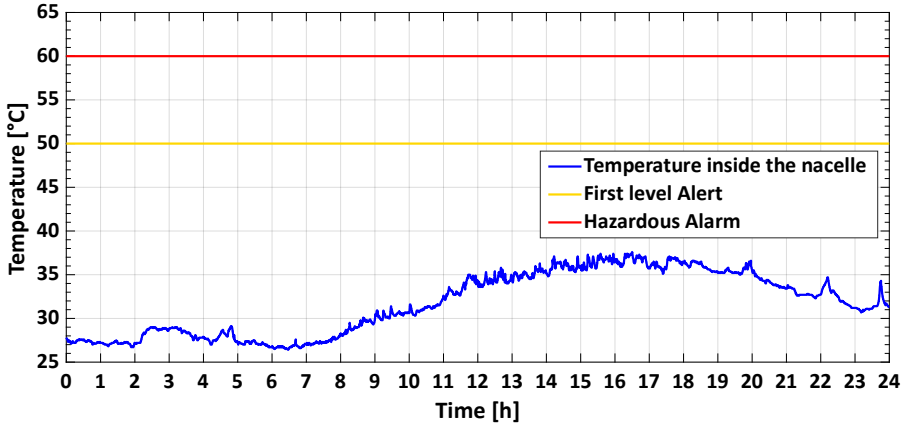
Fig. 7.9. Condition monitoring for electromechanical components: sampled temperature data and limit alarms.

7.6.　Integration of Failure Finding procedures within the Condition Monitoring tool

Together with condition monitoring, failure finding is key in attempts to improve the maintenance policies and avoid wasting money and time.

The effectiveness of failure finding is highlighted in TABLE VII.IV. This table compares the failure rate evaluation for a commercial solenoid valve with and without the implementation of the failure finding task (e.g. nondestructive test) to establish the valve's health status.

The failure rate is divided into four categories: λ_{SD}, λ_{SU}, λ_{DD} and λ_{DU}. As TABLE VII.IV indicates, the application of the failure finding task to this kind of valve can considerably reduce the number of undetected failures (both dangerous and safe failures are considered).

TABLE VII.IV

EFFECTS OF THE FAILURE FINDING TASK IMPLEMENTATION FOR SOLENOID VALVE.

CONFIGURATION	λ_{SD} [FIT]	λ_{SU} [FIT]	λ_{DD} [FIT]	λ_{DU} [FIT]
Solenoid valve without nondestructive test	0	129	0	145
Solenoid valve with nondestructive test	124	5	130	15

The undetected failure rate given by the sum of safe undetected failures and dangerous undetected failures for the two configurations is:

$$\lambda_U^{(No\ test)} = \lambda_{SU}^{(No\ test)} + \lambda_{DU}^{(No\ test)} = 274\ FIT \tag{7.3}$$

$$\lambda_U^{(with\ FF)} = \lambda_{SU}^{(with\ FF)} + \lambda_{DU}^{(with\ FF)} = 20\ FIT \tag{7.4}$$

A comparison between equations (7.3) and (7.4) indicates the undetected failure rate without test implementation is 13 times greater than the failure rate when failure finding is implemented. Considering all the valves in the yaw system, the reliability and availability improvement obtained by selecting the failure finding task for this type of component is remarkable.

Similarly to the previous analysis, TABLE VII.V shows the effects of FF procedure implemented on a ball valve of the yaw system under analysis. In this case, the selected FF procedure is the so-called PVST (Partial Valve Stroke Test). PVST is a technique used in safety valves to allow the user to test a percentage of the possible failure modes of a shutdown valve without the need to physically close the valve. In other words, PVST is used to assist in determining that the safety function will operate on demand without actually close the valve. PVST allows to expose hidden failures reducing the probability of failure on demand. It also allows to extend the time between consecutive maintenance tasks increasing the plant availability and optimizing the LCC.

TABLE VII.V compares the failure rate evaluation for a trunnion mounted ball valve with and without the implementation of the failure finding task (i.e. PVST) to establish the valve's health status. Once again, the failure rate is divided into four categories: λ_{SD}, λ_{SU}, λ_{DD} and λ_{DU}.

TABLE VII.V

EFFECTS OF THE FAILURE FINDING TASK IMPLEMENTATION FOR A BALL VALVE.

CONFIGURATION	λ_{SD} [FIT]	λ_{SU} [FIT]	λ_{DD} [FIT]	λ_{DU} [FIT]
Ball valve without PVST	0	114	0	382
Ball valve with PVST	113	1	201	181

The undetected failure rate for the two configurations is given by:

$$\lambda_U^{(No\ test)} = \lambda_{SU}^{(No\ test)} + \lambda_{DU}^{(No\ test)} = 496\ FIT \tag{7.5}$$

$$\lambda_U^{(with\ FF)} = \lambda_{SU}^{(with\ FF)} + \lambda_{DU}^{(with\ FF)} = 182\ FIT \tag{7.6}$$

A comparison between equations (7.5) and (7.6) indicates the undetected failure rate without test implementation is almost 3 times greater than the failure rate when PVST is implemented. The improvement obtained by selecting the failure finding task for this type of valve is lower than the improvements achieved for the solenoid valve. This is mainly due to the nature itself of the PVST that cannot close completely the valve and thus it cannot expose all the hidden failure mechanisms. However, it is still recommended to implement such procedure to improve the overall RAMS parameters of the plant.

7.7. Proposed Wireless Sensor Network to implement Condition Monitoring on a wind farm

Monitoring Systems plays a fundamental role in any wind farm because are crucial to guarantee the turbine functionality and to provide a quick advice in case of failure. Furthermore, the recent development of offshore wind farms makes the diagnostic implementation to control and manage the status of the turbines even more difficult. For example, the use of a wired monitoring system would entail higher additional costs compared to the wireless solution. Moreover, technological and structural changes are more difficult in a fixed (wired) installation.

Therefore, it is essential to use, low cost and plug and play system such as the Wireless Sensor Networks (WSNs). WSNs are networks characterized by a distributed architecture of small nodes. Each node can host multiple sensors and is equipped with computational and wireless communication unit [314], [315]. The monitoring system acquires several condition parameters to evaluate the health state of the turbine, as described in the previous sections.

The design of a monitoring system for a wind farm has four main issues:
- The large dimensions of the covered area.
- The great number of parameters that must be monitored.
- The condition parameters rapidly changing and consequently the required high sampling frequency.
- The possibility of increase the number of sensor node in case of new turbine installation inside the wind farm.

The previous problems require a proper trade-off in term of cover area and transmission protocol. In fact, the great number of parameter and the high sampling frequency require a high-frequency protocol with high bitrate that

usually is characterized by a limited coverage area. Wireless Mesh Networks (WMNs) are an optimal solution to provide broadband internet access to large geographical areas using a great number of nearby nodes and dynamic routing tables to guarantee high-frequency transmission and high bitrate despite the large geographical area [316]. Moreover, WMNs allow to increase the number of nodes inside the network in case of new turbine installation without requiring any changes in the already existing architecture, with a consequent decrease of management cost. The differences between a traditional WSN and Mesh network are the following [317]–[322]:

- A traditional WSN (Fig. 7.10) is a point-to-multipoint (star) network where a single central node, known as the access point (AP), is directly connected to all other nodes. Traditional infrastructure Wi-Fi networks have the disadvantage of limited coverage area because every station must be in a range directly connected with the access point. Furthermore, overloading is another relevant drawback of traditional wireless networks because the maximum number of stations permitted in the network is limited by the capacity of the AP.

- A WMN (Fig. 7.11) is a self-organized and self-configured sensors network. It is composed by several sensor nodes and a single root node that manages the entire network and allows data uploading to the cloud. Each node is able to communicate with all the neighboring nodes and consequently the network can cover very large areas. Another advantage of this network is that it is naturally a fault tolerant system. As a matter of fact, when a node stops working, the whole network does not fail, but the access point can be reached by different paths.
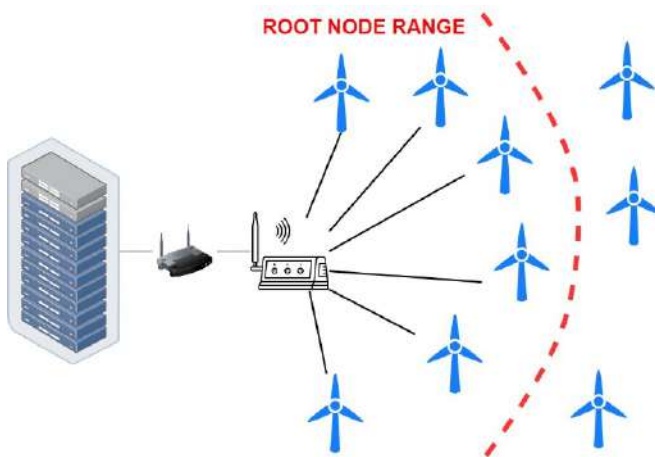
Fig. 7.10. Traditional Wireless Sensor Network used to monitor a wind farm.
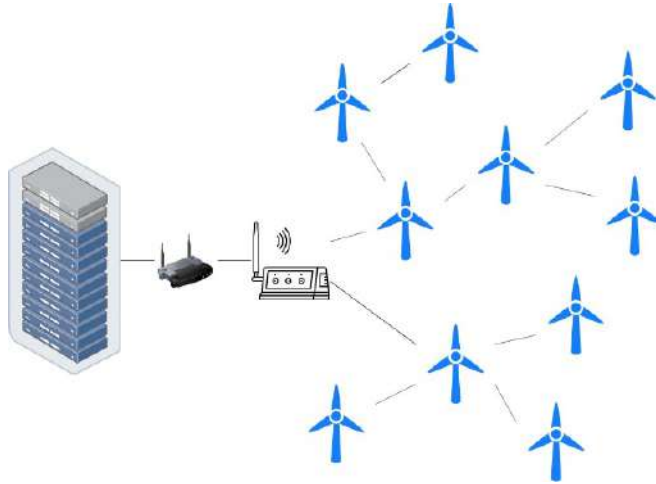
Fig. 7.11. Wireless Mesh Network topology to monitor a wind farm.

This work proposes the design of a wireless mesh network composed by low cost and low power sensor battery-based sensor nodes. Fig. 7.12 shows the block diagram of the developed sensor node which is composed by the following units:

- A power supply unit used to supply all the components of the sensor node. It is composed by a small photovoltaic panel, two lithium-ion batteries (INR18650-35e characterized by a capacity of 3500 mAh), a "Batteries Management System" (BMS) and a "Maximum Power Point Tracking" (MPPT). The photovoltaic panel and the batteries are necessary to guarantee a continuous power supply to the monitoring system. Using this architecture, the sensor node can provide a continuous flow of information regarding the state of the turbine. This kind of redundancy is mandatory to guarantee the self-sufficiency of the CM unit and consequently to allow a proper monitoring of the wind farm.

- A set of sensors according to the results of the RCM analysis carried out using the proposed approach.

- An external antenna.

- A radio and processing unit which is the real core of the sensor node. It is based on the ESP32 system-on-a-chip microcontroller by "Espressif". The ESP32 is configured to transmits data using IEEE 802.11 Wi-Fi protocol. The microcontroller is mounted on an evaluation board used for software programming by means of a USB-to-UART bridge controllers. The evaluation board also includes pin interface and power supply by means of an AMS1117 LDO. Two 8-channel 12-bit SAR ADCs and two 8-bit DACs are embedded in the ESP32. A customized interface

267

board is used to connect the power unit and the sensors unit to the ESP32 microcontroller. Furthermore, the interface board hosts some discrete components such as multiplexers, amplifiers, filters etc..
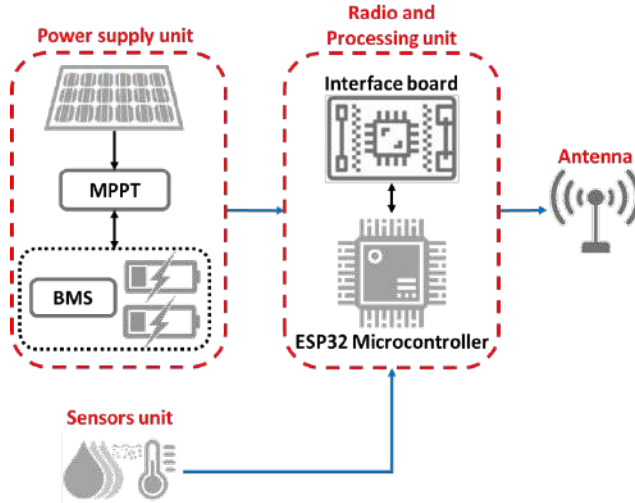
Fig. 7.12. Block diagram of the proposed sensor node for Condition Monitoring of Wind Turbines.

The proposed WSN provide continuous and near real-time data acquisition which can be used to [323]:

- Maintain process tolerances.
- Verify and protect machine, systems and process stability.
- Detect maintenance requirements.
- Minimize downtime.
- Prevent failures and consequently save cost and time.
- Plan a maintenance policy based on the prediction of failure.

Each turbine requires hundreds of different sensors to monitor the condition parameter that influence the wear-out process, therefore a hybrid tree-mesh network is proposed. Fig. 7.13 shows the network architecture divided into three layers:

- The first level is composed only by the root node (i.e. the access point).
- The second layer is the Wi-Fi mesh network where each node identifies a specific turbine.
- The third layer is a wired network directly connected only to the second layer node of the specific turbine.
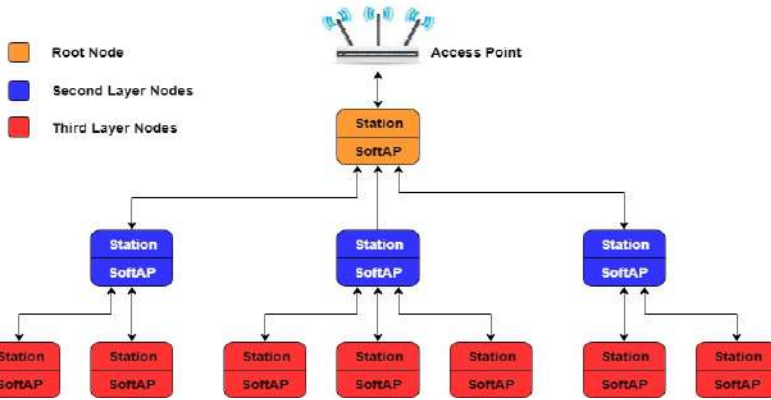
Fig. 7.13. Hybrid tree-mesh network architecture for Condition Monitoring of a wind farm.

The root node is the data collection point of the network, it also includes the router and the server, as shown in Fig. 7.14. Each one of the nodes in the second layer manages the data collection of a single wind turbine. It is also able to work as bridge node for the other second layer devices receiving data from a different node and retransmitting that to the root node in order to cover the entire wind farm area. Inside each turbine there are few third layers nodes with the aim to manage various sensors, as shown in Fig. 7.14 and Fig. 7.15. This level uses a shielded wired connection to carry information to the second layer node and to avoid interference caused by electronic and mechanical components of the turbine. Fig. 7.15 also shows an example of diagnostic implementation using the proposed network in the nacelle of the wind turbine under test. The red circle shows some possible locations of the processing unit of the nodes to manage the sensors of a specific turbine section.
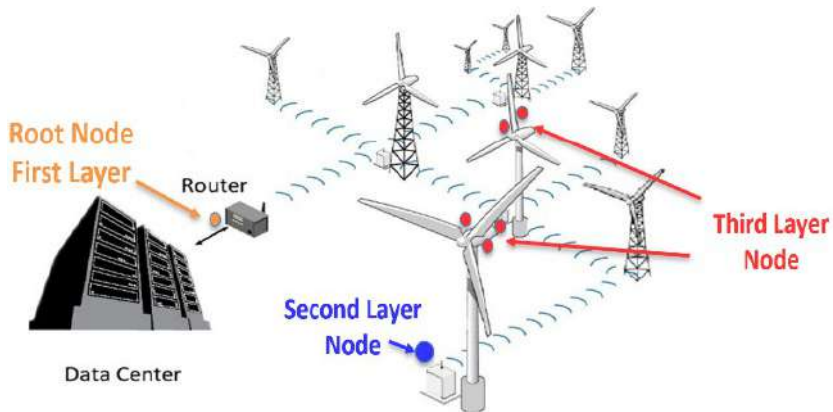
Fig. 7.14. Proposed architecture with first, second and third layer nodes location.
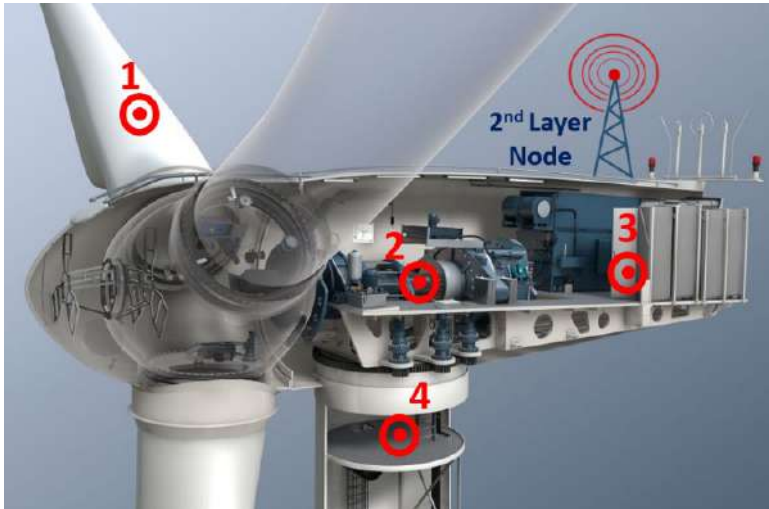
Fig. 7.15. Possible third level sensor (red circle) deployment inside the nacelle of a wind turbine.

Over the years, the power generation capability of the WT has increased, and consequently also the dimension of the blades and the overall WT extension have increased. Therefore, the distance between two neighbor turbines could be significant (over hundreds of meters) [11]. The ESP32 board is equipped with an integrated patch antenna which is absolutely not enough to cover such distances, so it is necessary the introduction of another antenna located above the nacelle used for the transmission of the acquired data (Fig. 7.15). It is not possible to use a directional antenna head towards a close node because the WMN is a self-organized and self-configured network in which every device must be able to communicate with many nodes located in different positions. Therefore, a power amplifier and a high-gain omnidirectional antenna are used as radio unit. Consequently, the second layer node is located outside the turbine, close to the antenna. It is very important to protect the electronic device by the weathering effects using a protective case to minimize the acceleration of the wear-out process due to temperature, humidity, rain, wind and solar radiation.

TABLE VII.VI reports an extract of the types of measurements and the sensors used by the proposed CM tool to monitor the wind farm under analysis. The table extends the information reported in TABLE VII. III which refers only to the yaw system whereas TABLE VII.VI provides an overall idea of the CM of the entire WT.

TABLE VII.VI

EXTRACT OF THE SENSORS USED TO MONITOR THE MOST CRITICAL ITEMS OF THE WT.

COMPONENT	MEASUREMENT	SENSORS
BLADES	Crack/Fatigue detection	Acoustic Emission
	Wind speed/direction	Anemometer
	Acceleration, pitch, roll and yaw	Inertial module
	Micro-deformation	Extensometer
GEARBOX	Vibration	MEMS accelerometer
	Temperature	Thermocouple
	Motion	Displacement transducer
	Stress	Strain gauge
HYDRAULIC SYSTEM	Pressure	Piezoelectric pressure transmitter
	Flow	Ultrasonic meter
	Level	Magnetic level meter
	Contamination	Contamination sensor
TOWER	Crack/Fatigue detection	Acoustic Emission
	Micro-deformation	Extensometer
UPS	Temperature	Resistance temperature detector
	Humidity	Humidity sensor
	Current	Hall effect integrated current sensor
POWER CONVERTER	Temperature	Resistance temperature detector
	Humidity	Humidity sensor
	Vibration	MEMS accelerometer
CONTROL SYSTEM	Temperature	Resistance temperature detector
	Humidity	Humidity sensor
	Vibration	MEMS accelerometer

7.8.   Final remarks

This chapter focuses on the maintenance policy optimization of a wind farm by means of a Condition Monitoring tool. The Reliability Centred Maintenance

approach is a widely known procedure described by the international standard IEC 60300-3-11 used to identify the optimal maintenance policy on a system/plant. However, the decision-making diagram included in the standard has a major subjectivity issue. As a matter of fact, for each identified scenario it let to the user the possibility to choose between many different options without explaining how to select the optimal maintenance policy. Thus, most of the choices are left to the experience of the operator that perform the assessment. To solve this problem, this work proposes a new decision-logic diagram based on failure information that could be included in the FMECA worksheet. The proposed method associates only one possible task to each scenario remarkably reducing the subjectivity problem since there is no longer need to rely only on expert's judgments. The proposed method is a diagnostic-oriented approach which favor the assessment of CBM task such as Condition Monitoring and Failure Findings. Considering the results of the assessment performed on the yaw system of a WT, only 5% of the assigned tasks are corrective maintenance; condition-based maintenance (CM and Failure Finding) constitutes the largest part of the assessed tasks, thus maximizing availability and minimizing the operational cost. The proposed assessment highlights the importance of a proper diagnostic management in complex systems. For this reason, the work also proposes some type of measurement and the respectively sensor technology that could be used to monitor some critical subsystems. Using the hydraulic system as first example, it proposes two condition monitoring systems, one based on the acquisition of oil temperature data and the other on hydraulic pressure data. When the sampled signal passes the first level alert, this warns the operator of an incipient problem/failure. If the signal passes the hazardous alarm level, the system commands a turbine emergency shutdown. The work also proposes a data-driven condition monitoring for the control system based on the temperature inside the turbine highlighting the effects of temperature on electronic components using the Arrhenius's law. The effectiveness of Failure Finding procedures carried out along with CM tools has been illustrated considering the effects of such procedures on two types of safety valves: a solenoid valve and a ball valve. The final part of this chapter focuses on the development of an hybrid tree wireless mesh network to effectively and efficiently implement CM on the entire wind farm. The work illustrates a possible deployment for the sensor nodes inside the wind farm highlighting the different node's level within the network and the interaction between nodes.

CHAPTER 8

PROGNOSTIC AND HEALTH MANAGEMENT

Prognostic and health management represent the final part of the proposed Reliability Life Cycle. In this chapter a hybrid approach based on both Condition Monitoring and physic model is presented to improve the accuracy and precision of prognostic for lithium-ion batteries. An artificial intelligence method is integrated with a state space estimation technique typical of filtering-based approaches. The state space estimation is used to generate a big dataset for the training of a neural network. Some additional deep layers are used to improve the prediction of nonlinear trends (typical of batteries) while the performance optimization of the network is ensured using a genetic algorithm. The proposed method has been applied to two battery degradation datasets from the data repository of NASA and from the Toyota Research Institute. Two different degradation models are compared, the widely known empirical double exponential model and an innovative single exponential model which allows to ensure optimal performance with fewer parameters required to be estimated. [1]

---

[1] This chapter has been published as "M. Catelani, L. Ciani, R. Fantacci, G. Patrizi, and B. Picano, "Remaining Useful Life Estimation for Prognostics of Lithium-Ion Batteries Based on Recurrent Neural Network," IEEE Trans. Instrum. Meas., vol. 70, Article No. 3524611, 2021".

8.1. Introduction

Prognostic and Health Management (PHM) techniques have emerged in recent years becoming more and more significant [324], [325]. PHM is starting to be recognized as a key feature in several industrial fields in order to maximize the safety level of the system and minimize the Life Cycle Cost (LCC). Prognostics is defined as the prediction of the future state of health of the system under test based on current and historical health conditions. PHM is usually divided into five consecutive steps, as follow [326], [327]:

1) Data acquisition;
2) Condition monitoring and anomaly detection;
3) Diagnostic;
4) Prognostic;
5) Maintenance decision.

Time-dependent data about materials degradation and environmental loads are collected during the first step. These data could be used during the subsequent phase to find unexpected behavior by comparing them with nominal conditions. This second phase can provide an early warning on the system's incorrect behavior, even though an anomaly does not necessarily identify a failure. The use of contextual parameters acquired using sensors to investigate performance anomaly is usually called Condition Monitoring (CM) [15], [201]. Then the diagnostic step allows to identify failure modes, mechanisms and damages from the previously found anomalies. In case diagnostic highlights no damages at the current moment, the future health state of the system is predicted in the Prognostic step. Prognostic allows to predict the Remaining Useful Life (RUL) of the system by estimating the progression of a fault based on given environmental conditions. Dedicated tools such as RUL estimation methods could provide essential information used to predict when the health state of the system will degrade reaching the failure threshold. Based on previous steps an effective Condition-based maintenance (CBM) could be carried out to avoid critical failures. Using this approach, the maintenance task will be carried out before the failure occurs, with a minimum effect on system availability.

Condition Based Prognostic Maintenance (CBPM) encloses the complete set of actions used to evaluate the current state of health of the system by monitoring the evolution of one or more parameter. Condition monitoring plays a fundamental role to acquire the data and to process theme before the

implementation of one or more prognostics methods. In this way operators can forecast the future state of health of the system providing as a result the time at which the system will no longer work. The general flowchart of a prognostic-based maintenance decision-making is illustrated in Fig. 8.1.
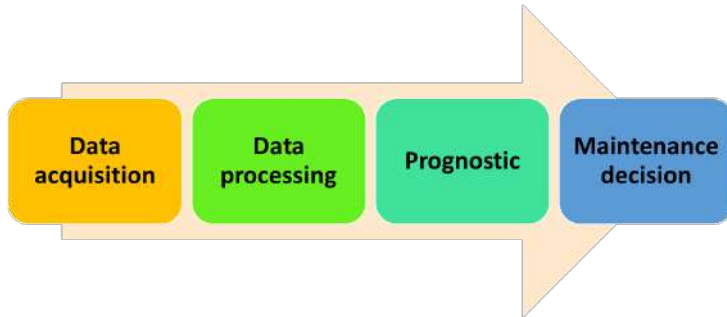
Fig. 8.1. The general flowchart of Prognostic-based maintenance decision plan.

Many applications require a proper and accurate prognostic methodology, such as wind turbine [328], gas turbine [329], railway systems [330], electronic components [331], induction motor [332], bearings [333] and batteries [334]. More in general, PHM and CBPM are fundamental techniques in every industrial and manufacturing field where fault diagnosis (as well as prevention and mitigation of failure consequences) allows to increase availability and safety of the whole system/plant with an essential decrease of the LCC.

Under these circumstances, it is clear how PHM plays an essential role in Lithium-Ion batteries State-Of-Charge (SOC) estimation. In fact, Lithium-Ion batteries are installed in a variety of systems, such as smartphones, laptops, and all consumer electronics, electric vehicles, aerospace systems, clean transportation systems, communication infrastructures, Wireless Sensor Networks and many others. Batteries are currently one of the most expensive components in several applications, therefore it is extremely important to monitor their health state and their SOC [335]. A long battery lifetime is required to ensure economic viability and minimize the LCC. However, ensure remarkable lifetime of Lithium-Ion batteries is a challenging task that is not always achievable due to the complex degradation mechanisms that affect the battery [336], [337]. For these reasons, the huge spreading of lithium-ion batteries in many technological fields has led to an increase interest in prognostics and RUL estimation.

The overall research objective of this chapter is to improve the accuracy and precision of RUL estimation for Lithium-Ion battery by means of state space

estimation and Recurrent neural network (RNN). More in detail, the RNN implemented is an Echo State Network (ESN). A hybrid approach based on both condition monitoring and physical degradation model is presented in this chapter to enhance and facilitate decision-making in operation and maintenance of Lithium-Ion batteries.

8.2.   Remaining Useful Life Estimation

Remaining Useful Life (RUL) is defined as the time remaining for a component to perform its functional capabilities before failure. In other words, RUL refers to the system lifetime left from the current time to the end-of-life (EOL), where the EOL represents the time in which the system health pass the failure threshold [154], [338], [339].

By taking RUL into account, engineers can schedule maintenance, optimize operating efficiency, and avoid unplanned downtime. For this reason, estimating RUL is a top priority in predictive maintenance programs [326].

The inputs of a RUL estimation model are condition indicators, i.e. features extracted from sensor data or log data whose behavior changes in a predictable way as the system degrades or operates in different modes. The method used to calculate RUL depends on the kind of data available:

i. Lifetime data indicating how long it took for similar machines to reach failure. In this case, proportional hazard models and probability distributions of component failure times are used to estimate RUL. A simple example is estimating the discharge time of a battery based on past discharge times and covariates, variables such as the environment in which the battery operated (such as temperature) and the load placed on it.

ii. Run-to-failure histories of machines similar to the one you want to diagnose. If a database of run-to-failure data from similar components (or different components showing similar behavior) is available, then RUL can be estimated using similarity methods. These methods capture degradation profiles and compare them with new data coming in from the machine to determine which profile the data matches most closely.

iii. A known threshold value of a condition indicator that detects failure. In many cases, run-to-failure data or lifetime data was not recorded. However, sometimes engineers have information on prescribed

threshold values. For example, the temperature of a liquid in a pump cannot exceed 71°C and the pressure must be under 155 bar. With this kind of information, it is possible to fit time series models to condition indicators extracted from sensor data such as temperature and pressure, which rise or fall over time. These degradation models estimate RUL by predicting when the condition indicator will cross the threshold. They can also be used with a fused condition indicator that incorporates information from more than one condition indicator using techniques such as principal component analysis. Depending on the type of component/system under analysis, the condition indicators can be fused to estimate the component State-of-Health (SOH). Then, the SOH is compared against the failure threshold to estimate the RUL. This approach is generally referred simply as data-driven.

The latter method (iii.) represents the most interesting solution in the point of view of an overall data-driven reliability life cycle as the one proposed in this work. As a consequence, this is the type of approach that will be discussed in this chapter.

Fig. 8.2 shows an example of data-driven RUL estimation comparing the SOH of a generic component with an acceptable health level known as failure threshold set as the 50% of the SOH (red dashed line). The other horizontal dashed black lines represent the health condition (from 100% to 85% of the SOH), a caution scenario (from 85% to 75%) and a need for repair (below 70%).
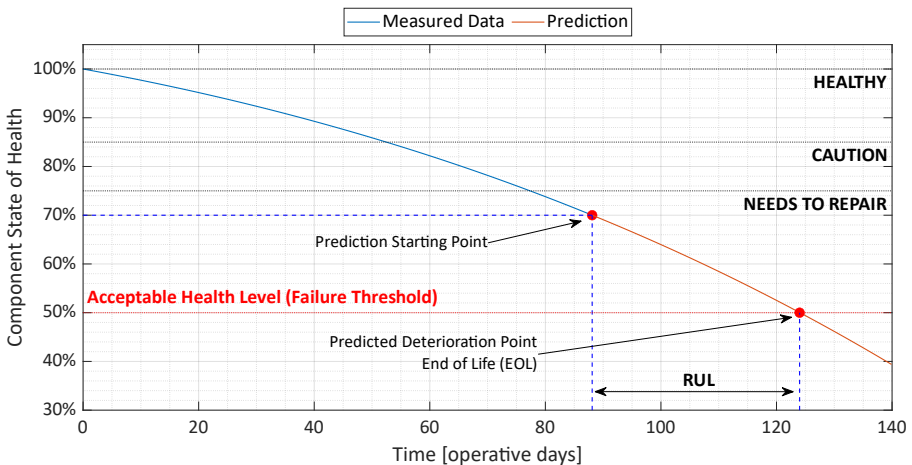
Fig. 8.2. Example of data-driven RUL estimation comparing the component SOH against an acceptable health level (failure threshold).

Using the measured data about the component SOH (blue line), a prediction of the future health is performed (red line). The time between the starting point of the prediction and the predicted deterioration point (i.e. the time in which the predicted SOH decrease below the failure threshold, called EOL) is the RUL of the component.

8.3. Related Works about PHM and RUL estimation of Batteries

Generally speaking, prognostic approaches could be classified as physics-based or data-driven models. Lithium-ion batteries (LIBs) are dynamic components characterized by nonlinear behavior and complex internal mechanisms. Furthermore, several causes influence battery degradation, including both physical and chemical failure mechanisms [336]. As a consequence, only few physics-based approaches are currently available for RUL estimation of batteries. Quite the opposite, many data-driven methods have been developed in the last few years. Data-driven RUL estimation method are basically divided into three categories [340]: stochastic process degradation, filtering methods and Artificial Intelligence (AI).

Stochastic degradation such as Gaussian and Weiner models are usually implemented to simplify the evaluation of RUL uncertainty. For example, Liu et al. [341] proposes a Gaussian Process Regression (GPR) to describe the uncertainty in State-Of-Health prediction, while in [342] GPR is combined with indirect Health Indicator (HI) to solve the capacity unmeasurable problem of operating batteries. A Wiener process model with random drift efficient is used to model the degradation process in [343]. Xu et al. [344] introduce the Weiner process combined with Maximum Likelihood Estimation (MLE) and a genetic algorithm (GA) to model batteries wear-out under time-varying temperature conditions.

A widely known approach for RUL estimation of batteries is based on filtering techniques such as Kalman Filter (KF) and Particle Filter (PF). The classical KF (used for example in [345]) is not suitable in case of strong nonlinear degradation process as the one of a lithium-ion battery. Therefore, some papers propose different optimization of Extended Kalman Filter (EKF) [346], [347] and Unscented Kalman Filter (UKF) [348], [349] to better estimate nonlinear battery degradation. Other approaches enhance and optimize the performance

of PF [350], [351] and Unscented Particle Filter (UPF) [352], [353] to solve these issues. Other papers combines different strategies such as [354] which integrates Wiener process and UPF to consider four different sources of degradation process variability at the same time. Similarly, [355] uses Gaussian process and PF for RUL estimation of Lithium-Ion batteries under uncertain conditions. In [356] PF is combined with sliding-window gray model, while in [357] long short-term memory technique is used to optime the performance of PF. Chen et al. [358] proposes an innovative fractional grey model combined with UPF. Nevertheless, most of these methods are based on several recurrent observations of battery degradation. Furthermore, these methods have limited modeling ability for complex nonlinear processes.

Some approaches based on artificial intelligence (AI) have been presented in the last few years to solve the problems of filter-based estimation methods. AutoRegressive (AR) models are used in [359] and in [360], while Support Vector Machine (SVM) have been used in [361] and [362]. Moreover, Relevance Vector Machine (RVM) has been implemented in several papers (see for instance [363] and [364]). RVM provides better performances in terms of accuracy and computational complexity respect to SVM. However, RVM-based methods are characterized by low stability issues. Neural Networks are the optimal mean to estimate RUL of Lithium-Ion batteries since the degradation process is strongly nonlinear. For instance, in [365] a deep neural network is integrated with autoencoder model to represent battery health degradation. However, Recurrent Neural Networks (RNN) are characterized by a larger feasibility for RUL prediction of Lithium-Ion batteries because of their superiority in time series prediction [366]. One of the best approaches in literature is presented in [367] where a monotonic echo state network (MONESN) algorithm is adopted to track the nonlinear patterns of battery degradation.

8.4. Proposed approach for RUL estimation of Lithium-Ion batteries

In this section a data-driven approach based on Artificial Intelligence for Remaining Useful Life estimation of batteries is presented.

The proposed method integrates different aspects of existing methodologies in

order to find the optimal RUL estimation with high accuracy and low computational complexity. An online hybrid method based on physics-based degradation model, state space estimation and ESN prediction is presented.

8.4.1. Overall procedure

The schematic representation of the online RUL estimation is presented in Fig. 8.3. A data-driven condition monitoring is used to acquire degradation data regarding the monitored system. After a pre-processing phase, the degradation data are compared to a safety threshold estimated using common knowledge and historical data. The aims of this real-time comparison are twofold:

- To provide an updated degradation model used to improve the safety threshold estimation.
- To estimate the Remaining Useful Life of the system under analysis and consequently to plan the optimal condition-based maintenance decision.
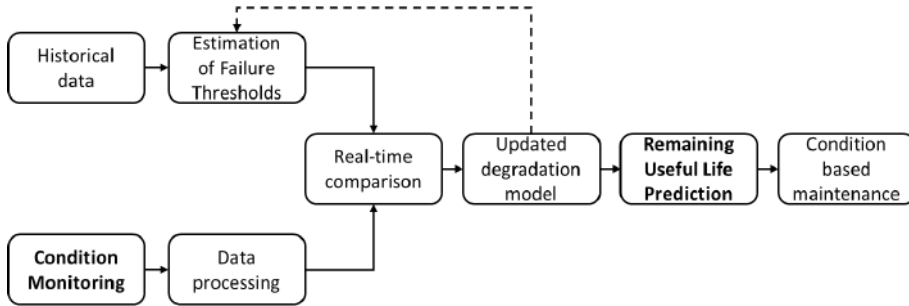
Fig. 8.3. Schematic representation of the proposed Online RUL estimation based on Condition Monitoring and Real-time comparison.

The most interesting phase of the online procedure presented in Fig. 8.3. is the data processing and elaboration phase required to estimate the RUL after the comparison with the safety threshold. In this chapter, an hybrid approach which use different features of physics-based model, filtering methods and AI methods is presented to estimate the future SOC of a Lithium-Ion battery. The complete flowchart of the proposed method is presented in Fig. 8.4.

The battery under test is continuously monitored by means of condition monitoring tools and appropriate measurements to obtain a capacity

degradation dataset C_k where $k = 1, 2, \ldots n$ represents the number of charge and discharge cycle and n is the number of samples in the considered dataset.

Then, similarly to many filtering-based methods (i.e. EKF, UKF, UPF, etc.) the state space of the battery under test is estimated.
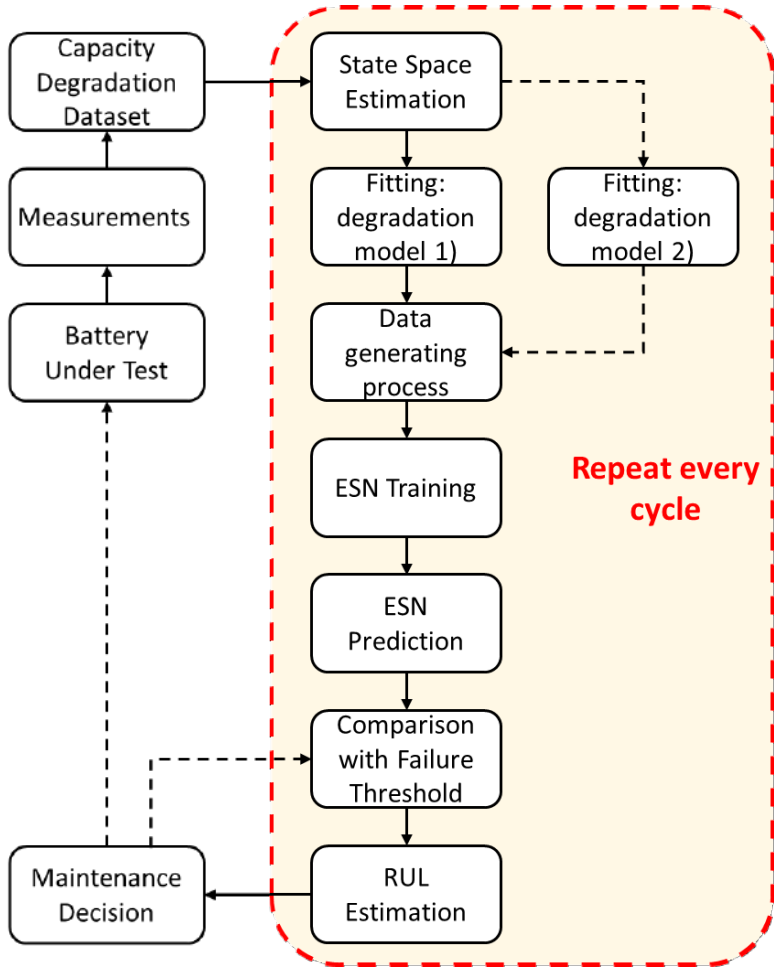
Fig. 8.4. Complete flowchart of the proposed approach used to estimate the Remaining Useful Life of Lithium-Ion batteries.

8.4.2. Double exponential degradation model

Many papers in literature use a double exponential degradation model to describe the physics-based degradation of Lithium-Ion batteries (see for instance [368]–[372]) which represents a good trade-off between modeling

accuracy and complexity. According to these papers, the capacity Q of the battery can be described as follow:

$$Q = a \cdot exp\,(b \cdot k) + c \cdot exp\,(d \cdot k) \tag{8.1}$$

Where a, b, c and d are the model parameters that need to be estimated while the independent variable k stands for the cycle number. Considering the degradation model in equation (8.1), parameters a and c characterize the initial capacity and are related to the internal impedance, while b and d represent the aging rate. Thus, the current state space estimated using the double exponential model can be written as follow:

$$\boldsymbol{X_z} = [a_z;\, b_z;\, c_z;\, d_z] \tag{8.2}$$
$$Q_z = a_z \cdot exp\,(b_z \cdot k) + c_z \cdot exp\,(d_z \cdot k) \tag{8.3}$$

Where the subscript z represents the z-th cycle (current estimation time) and $\boldsymbol{X_z}$ stands for state space estimated using the first model - double exponential in equation (8.3).

8.4.3. Proposed single exponential degradation model

In this work, a second degradation model has been introduced to better describe the battery degradation with a simpler state space. The proposed single exponential model is given by:

$$\widetilde{\boldsymbol{X_z}} = \left[\tilde{a}_z;\, \tilde{b}_z\right] \tag{8.4}$$

$$Q_z = C_0 + \tilde{a}_z \cdot exp\left(\tilde{b}_z\big/_k\right) \tag{8.5}$$

Where C_0 is the initial capacity of the battery and $\widetilde{\boldsymbol{X_z}}$ stands for state space estimated using the second model - single exponential in equation (8.5). The state space at the current cycle is estimated using the Matlab Curve Fitting Toolbox and the degradation model in equation (8.3) or equation (8.5). The notation for the current cycle is k_{pred} which is the number of the cycle in which the prediction is performed.

The following steps involve the use of the proposed RNN prediction.

8.4.4. Proposed Neural Network

The RNNs represent one of the most powerful tools to perform time series prediction, especially when there exist temporal dependencies among successive samples. The RNNs have gained momentum in time series forecasting when data are temporally related, since they are characterized by the presence of memory units which makes the network able to catch the existing temporal correlation among the samples of a time series. Due to the RNN outstanding ability in time series prediction [373], the application of the RNNs may represent a valuable approach to be integrated in the proposed predictive framework, as described in Fig. 8.4, aiming at forecasting the nonlinear behavior of the time series object of the analysis. Within the class of the RNNs, the ESN represents a fast and efficient type of RNN, due to its intrinsic simplicity in training and in its architecture [374]. A typical ESN consists of an input layer, a recurrent layer, called reservoir, and an output layer (as can be seen in Fig. 8.5). The connection weights of the input layer and the reservoir layer are fixed after initialization, and the output weights are trainable and obtained by solving a linear regression problem.

A typical ESN is characterized by [375]:

- an input layer;
- a recurrent layer, i.e., the reservoir;
- large number of sparsely connected neurons in the reservoir;
- an output layer;
- efficiency in time complexity and energy consumption.
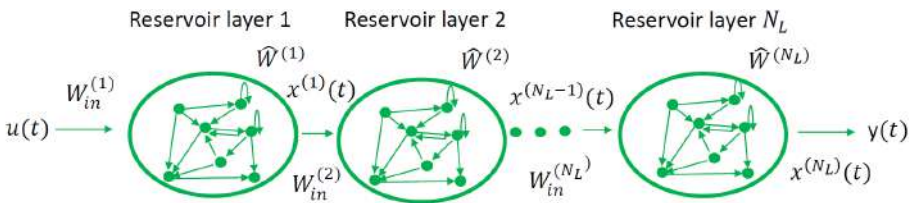
Fig. 8.5. Architecture of the proposed Deep Echo State Network.

Accordingly, we have applied an ESN with additional hidden reservoir layers, typically referred as deep ESN, which may improve the prediction performance in presence of complex time series. Therefore, as illustrated by Fig. 8.5, the proposed forecasting procedure consists of an input layer, multiple reservoir layers, and one output layer. In accordance to the ESN theory, the connections

of the reservoir layers are randomly initialized. Let **u** be the input vector of the s(i) values, i.e., given by:

$$\boldsymbol{u}(t) = [s(1),\ldots,s(n)]^T \tag{8.6}$$

whose state transition function for the layer λ is represented by [375]:

$$x^{(\lambda)}(t) = \left(1 - \alpha^{(\lambda)}\right)x^{(\lambda)}(t-1) + \alpha^{(\lambda)}\boldsymbol{Q}(t) \tag{8.7}$$

$$\boldsymbol{Q}(t) = tanh\left(\boldsymbol{W}_{in}^{(\lambda)}i^{(\lambda)}(t) + \boldsymbol{\theta}^{(\lambda)} + \widehat{\boldsymbol{W}}^{(\lambda)}x^{(\lambda)}(t-1)\right) \tag{8.8}$$

In which α is the smoothing constant, while $\boldsymbol{W}_{in}^{(\lambda)}$ represents the input weights matrix associated to the level λ. Furthermore, tanh represents the activation function, and $\boldsymbol{\theta}^{(\lambda)}$ is the array of the bias weight. Finally, the recurrent weights matrix for layer λ is denoted by $\widehat{\boldsymbol{W}}^{(\lambda)}$, and $i^{(\lambda)}$ is the input of the λ-th layer. More in detail, at the initial step, i.e., when λ=1, then $i^{(1)}(t) = u(t)$, whereas $i^{(\lambda)}(t) = x^{(\lambda-1)}(t)$ if λ≠1. Consequently, the output **y** is given by:

$$\boldsymbol{y}(t) = \boldsymbol{W}_{out}\left[x^{(1)},\ldots,x^{(N_L)}\right]^T + \boldsymbol{\theta}_{out} \tag{8.9}$$

In which N_L is the number of reservoir layers and $\mathbf{W}_{out}$ and $\boldsymbol{\theta}_{out}$ are the output weight matrix and vector, respectively. Then, using the state space $\mathbf{X_z}$ a big dataset is generated with the aim of training the proposed ESN to follow the double exponential model. Quite the same, a second dataset is generated using the state space $\widetilde{\mathbf{X}}_{\mathbf{z}}$ with the aim of training the network to follow the single exponential model. The network parameters optimization has been performed on the basis of the linear-weighted particle swarm optimization procedure adopted in [376]. Accordingly, a L_2 regularization has been applied, in order to avoid ill-posed configurations and to effectively monitor the ESN reservoir status.

The exploitation of the genetic algorithm (GA) [377] has been performed in order to optimize the global parameter of the ESN, i.e., the number of the nodes in the reservoir and the spectral radius. In this regard, it is important to point out that typically, in the ESNs, the search of these parameters is provided throughout an exhausting search or performing random experiments, which is time and computational consuming. As deeply certified by literature, the GA [378] is an iterative algorithm during which a range of solutions are produced passing through the selection and the reproduction processes. In fact, in order

to produce the next generation of solutions on the basis of the current population, the GA identifies the individuals with the best values of the fitness function, which represents the metric to perform selection criterion. The individuals exhibiting the best fitness values, named as elite, are directly admitted to the next generation, together with the children derived from the crossover and the mutation procedures [378], having valuable values of the fitness function.

Consequently, letting $\gamma = (N, \alpha)$ be the solution parameters we are interested in, in which N represents the amount of the nodes in the reservoir, and α is the spectral radius, respectively, the GA module behavior, accordingly with literature [377], [378], can be summarized as:

1) Generate a random initial population constituted by 100 individuals γ; try the ESN by setting the parameters accordingly with γ. Evaluate the corresponding fitness function, i.e., the percentage of MSE on the training data as in [377].

2) The algorithm uses the individuals belonging to the current population to produce the next one, as follow:
   - rank each individual on the basis of the fitness function evaluation;
   - select the best individuals as elite and pass them to the next population generation;
   - select parents by choosing individuals with high values of fitness function. Generate children by mutation, i.e., performing random changes from a single parent, or by combining the parameters of a pair of parents, i.e., by crossover. Replace the parent with the children in order to create the next generation.
   - terminate when the maximum number of mutation M is reached.

8.4.5. Battery SOC prediction and RUL estimation

After the training phase the ESN is able to predict the future SOC of the battery under test (in case of batteries, SOC correspond to SOH). The capacity dataset predicted by means of ESN is called $\widehat{C_k}$, where $k = k_{pred}, k_{pred} + 1, \dots n$ and it represents the first output of the proposed procedure.

The following step is the comparison of the estimated $\widehat{C_k}$ with a failure threshold which is indicative of a possible incipient failure. As a matter of fact, since the system under analysis is a battery, the failure threshold represents the end of life of the battery even if no failure is going to happen. In other words, the failure threshold is the point in time after which the battery's capacity is no

more sufficient to power the device. Usually, almost every work in literature set the failure threshold FTH equal to the 70% of the rated capacity value C_{nom}. Thus:

$$FTH = C_{rated} \cdot 0.7 \tag{8.10}$$

Considering $\widehat{\mathbf{K_r}}$ the set including all indexes k corresponding to estimated capacity values of the dataset $\widehat{C_z}$ lower than the threshold FTH.

$$\widehat{K_r} = \{\widehat{k_r} \mid \widehat{C_{\widehat{k_r}}} < FTH\} \quad \forall\, \widehat{k_r} \in [k_{pred}, m] \tag{8.11}$$

Thus, the predicted End of Life EOL_{pred} is determined identifying the cycle in which the capacity value of the predicted dataset decrease below the threshold. In other words:

$$EOL_{pred} = min\, \widehat{K_r} = min\{\widehat{k_r} \mid \widehat{C_{\widehat{k_r}}} < FTH\} \tag{8.12}$$

Thus, the predicted Remaining Useful Life RUL_{pred} can be determined as follow:

$$RUL_{pred} = EOL_{pred} - k_{pred} \tag{8.13}$$

RUL_{pred} is the second and most important output of the proposed method. It allows to evaluate the remaining life of the battery and consequently to plan the following maintenance activities accordingly. This results in an optimization of the operation and maintenance cost and an increase of the system availability since maintenance is performed only when it is needed.

As emphasized in Fig. 8.4 the proposed approach is a cyclical procedure that must be repeated continuously during the entire battery life cycle. Therefore, every subsequent estimation of the battery health will result in a lower RUL_{pred} level.

When the estimated EOL_{pred} starts rapidly approaching the FTH, then a maintenance task should be planned to replace the wore out battery before its capacity keeps degrade below a certain threshold. Moreover, the RUL estimation and the maintenance decision could be used to update the failure threshold.

As summary, the detailed steps of the proposed algorithm are presented in the following.

Algorithm 1 Hybrid algorithm for RUL estimation by means of RNN and state space estimation

---

Input: C_0= Initial battery capacity

k_1 = First prediction time

$C_{k_{pred}}$= dataset of battery capacity until k_{pred}

Start

1. Battery Condition Monitoring

2. **for** $i = k_1 : EOL$ **do**

3.   State space analysis using Matlab Curve Fitting Toolbox

4.   Estimation of single exponential model's parameters

5.   Generation of training dataset based on model's parameters

6.   ESN global parameters selection applying GA

7.   ESN prediction of future capacity with optimized parameters

8.   Comparison with failure threshold

9.   RUL evaluation

10.   Maintenance decision

11. **end for**

End

Output: RUL_{pred} = Predicted RUL of the battery

8.5.   Experimental Data

An extensive review of commercially and publicly available battery degradation datasets for prognostic and health management has been carried out in order to find the most suitable datasets to validate the proposed approach [379], [380]. More in detail, two different Lithium-Ion battery degradation datasets have been used in this work, as detailed described in the following subsections.

8.5.1.   NASA battery dataset

The LIB dataset "Dataset1_BatteryAgingARC-FY08Q4" from the data repository of Prognostics Center of Excellence at NASA Ames Research Center has been used as first testbench of the proposed method [381]. Among the six battery datasets included in this data repository, the Dataset1 considered in

this work is the only one that according to the guidelines provided by NASA is suitable for prognostic and RUL estimation. A battery testbed developed by NASA Ames Research Center for prognostic purposes has been used to acquire data regarding several commercially available Lithium-ion 18650 sized rechargeable batteries. According to [381] the measurement setup used for RUL estimation includes a power supply, a programmable load, a voltmeter, a thermocouple sensor and a climatic chamber used to regulate and stabilize the temperature during the test and a data acquisition system [381]. The dataset under analysis includes a set of four batteries (namely B0005, B0006, B0007 and B0018). Repeated charge and discharge cycles resulted in accelerated aging of the batteries, providing the optimal test solution for prediction of Remaining Useful life and more generally for prognostic purposes.

More in detail, charging was carried out in a constant current mode at 1.5 A. When the battery voltage reached 4.2 V, the charging continued in a constant voltage mode until the charge current dropped to 20 mA. Discharge was carried out at a constant current level of 2 A until the battery voltage fell to 2.7 V (in case of battery B0005), 2.5 V (in case of battery B0006), 2.2 V (in case of battery B0007) and 2.5 V (in case of battery B0018) [381].

The battery degradation dataset under analysis provides different data about battery aging, including the battery terminal voltage measured during charge and discharge phases, battery output current measured during charge and discharge phases, battery temperature and battery capacity. The Input of the proposed method is the battery capacity throughout different degradation cycles, as illustrated in Fig. 8.6. One of the main properties of ESN is the great ability to operate in presence of nonlinear and chaotic data including anomalies. Therefore, anomalies in the dataset have not been removed and all the available data have been processed equally. The rated capacity C_{rated} of the four batteries is 2 Ah, therefore according to equation (10) the failure threshold is given by:

$$FTH = C_{rated} \cdot 0.7 = 1.4 \, Ah \tag{8.14}$$

To test the performances of the proposed approach it is necessary to evaluate the real Remaining Useful Life of the measured dataset RUL_{meas} as follow. Considering the capacity degradation dataset C_k containing the measured capacity data. The set $\mathbf{K_r}$ including all the indexes k corresponding to measured data lower than the threshold is defined as:

$$\mathbf{K_r} = \{k_r \mid C_{k_r} < FTH\} \quad \forall \, k_r \in [k_{pred}, n] \tag{8.15}$$
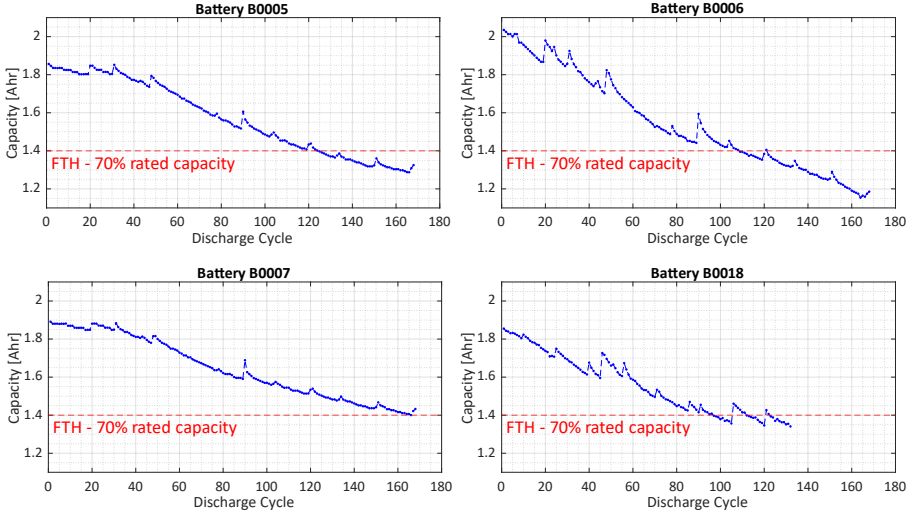
Fig. 8.6. Battery degradation dataset provided by NASA Ames Research Center regarding batteries B0005, B0006, B0007 and B0018. The failure threshold FTH has been set equal to the 70% of the rated capacity.

Then the End-of-Life of the measured data EOL_{meas} is determined identifying the cycle in which the capacity value of the measured data decrease below the threshold.

$$EOL_{meas} \ = \ min \ \boldsymbol{K_r} \ = \ min \left\{ k_r \mid C_{k_r} \ < \ FTH \right\} \qquad (8.16)$$

Consequently, the Remaining Useful Life RUL_{meas} of the measured dataset is given by:

$$RUL_{meas} = EOL_{meas} \ - \ k_{pred} \qquad (8.17)$$

Then, the estimation error EE between the predicted Remaining Useful Life RUL_{pred} and the real Remaining Useful Life of the measured dataset RUL_{meas} can be defined as:

$$EE \ = \ \left| RUL_{meas} \ - \ RUL_{pred} \right| \qquad (8.18)$$

Furthermore, the Mean Square Error MSE has been used to measure the average squared difference between the estimated capacity values $\widehat{C_k}$ and the measured data C_k as follow:

$$MSE \ = \ \frac{1}{m} \sum_{i=1}^{m} \left(C_k \ - \ \widehat{C_k} \right)^2 \qquad (8.19)$$

Where m is the dimension of the predicted dataset and the measured dataset. Furthermore, it is important to highlight here that the proposed strategy assumes as loss function the Mean Square Error (MSE) metric.

8.5.2. TRI battery dataset

The performances of the proposed procedure have been tested and validated using also another dataset [382] provided by the Toyota Research Institute in collaboration with MIT (Massachusetts Institute of Technology) and Stanford University (simply referred as TRI dataset in the following) [382].

The dataset refers to 124 commercial LIBs tested under fast-charging conditions. The batteries under test are lithium-ion phosphate (LFP)/graphite cells manufactured by A123 Systems. Each battery is characterized by a rated capacity of 1.1 Ah and a nominal voltage of 3.3 V.

All the LIBs (except for 2 cases) have been tested until the battery End-Of-Life EOL_{meas} is reached. The LIB's FTH is the 80% of the rated capacity (i.e. 0.88 Ah) and the measured EOL_{meas} varies from 150 cycles up to 2300 cycles. The LIBs under test have been cycled with different fast-charging profile and a common CC-discharge policy (4C). The one-step or two-step fast-charging profiles used in the experimental setup follow the notation "C1(Q1)-C2". In this charging policy, a constant-current step of C1 is performed until the state of charge Q1 is reached. After that, charging goes on as a constant-current step C2 until the SOC = 80%. After that, all batteries are charged at 1C CC-CV.

The data is split into three batches corresponding to three blocks of experiments carried out separately in different dates: "Batch 2017-05-12", "Batch 2017-06-30" and "Batch 2018-04-12". Focusing the attention on the most recent batch of batteries ("Batch 2018-04-12"), 46 different batteries have been analyzed. Within this batch, the LIBs are gathered according to 8 different fast-charging conditions. The complete dataset is illustrated in Fig. 8.7 where each subplot shows a group of batteries charged with a different fast-charging policy.

The major effect of the different conditions is the variation of the batteries EOL according to the specific charging policies.
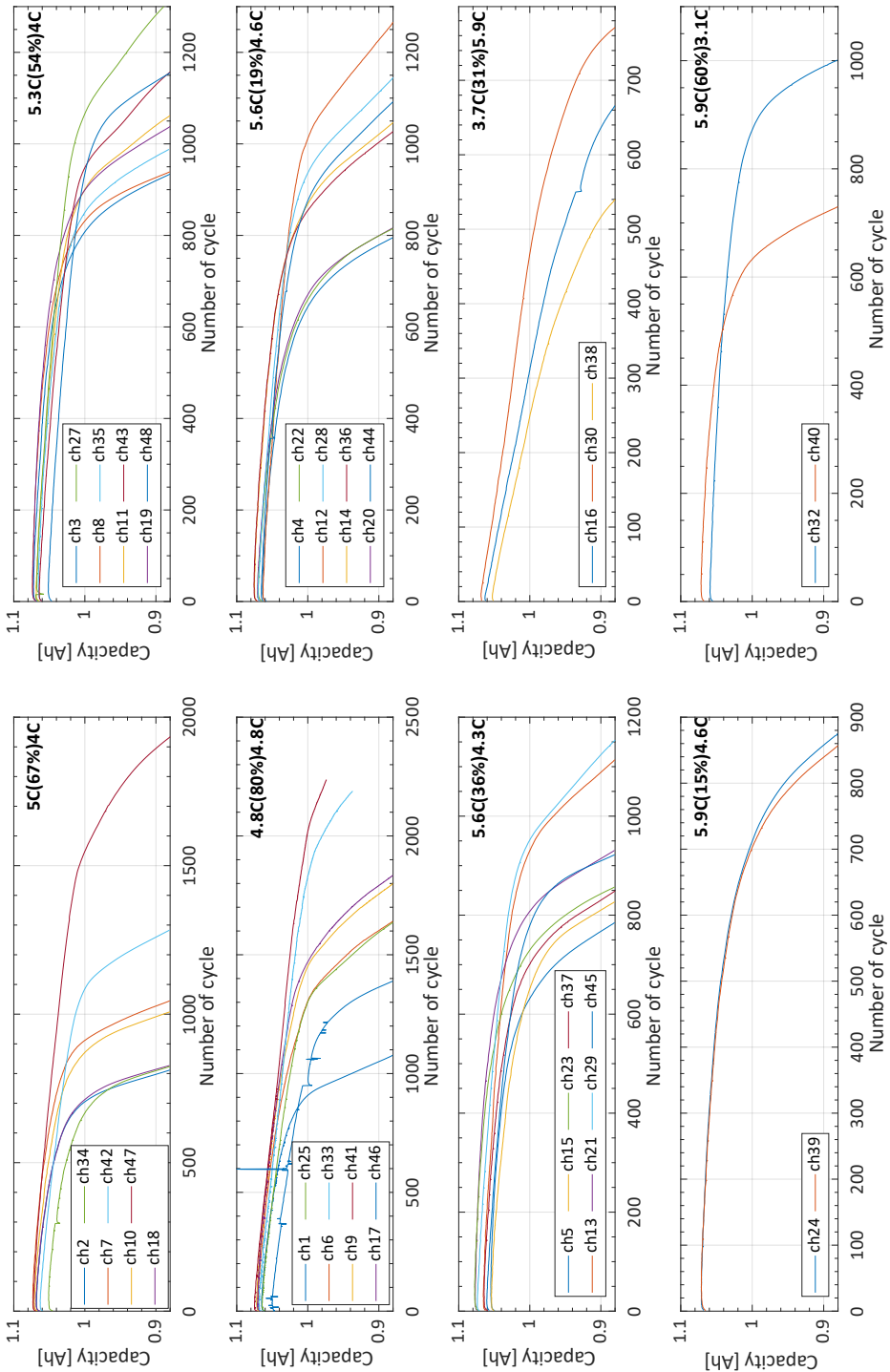
Fig. 8.7. TRI battery dataset. Batch 2018-04-12. Different charging conditions have been grouped together in each subplot. Source of the data: [382].

The batteries have been tested at constant temperature condition of 30 °C inside a controlled temperature chamber and monitored using type T thermocouples.

The TRI dataset has been selected because of the following reasons:

- It is one of the most recent and updated battery datasets for prognostic and health management.
- It is one of the largest datasets including 124 LIBs under test.
- Batteries have been tested under several fast-charging policies, allowing to validate the method under different operating conditions not always considered in literature.
- EOL of batteries under test varies in a wide range between 150 cycles and 2300 cycles, allowing once again to validate the proposed method under several different scenarios.

8.6. Results and Discussion for NASA dataset

In this section the results of the RUL prediction carried out using the proposed procedure on batteries B0005, B0006, B0007 and B018 are presented.

The state space has been estimated according to the Double Exponential model in equations (8.2)-(8.3) and using the Single Exponential model in equations (8.4)-(8.5). The goodness of fit has been evaluated using two measures:

- Coefficient of determination R^2 (R-squared). It represents the proportion of the variance for a dependent variable that is explained by an independent variable or variables in a regression model. The better the regression model, the closer to 1 the R^2 is.
- Root Mean Square Error (RMSE) which is a standard way to measure the error of a model in predicting quantitative data. The better the regression model, the lower the RMSE is.

8.6.1. Implementation of the proposed method

The estimated parameters and the goodness of fit are reported in TABLE VIII.I in case of double exponential model and TABLE VIII.II in case of single exponential model.

TABLE VIII.I

STATE SPACE ESTIMATION ACHIEVED USING CURVE FITTING TOOLBOX FOR BATTERIES
B0005 - B0006 - B0007 - B0018. ESTIMATED PARAMETERS AND GOODNESS OF FIT IN
CASE OF DOUBLE EXPONENTIAL MODEL

BATTERY	k_{pred}	DOUBLE EXPONENTIAL MODEL					
		a	b	c	d	R^2	RMSE
B0005	80	361.6	-0.009979	-359.8	-0.01004	**0.9634**	**0.01637**
	100	2.361	-0.004369	-0.5429	-0.02426	**0.9726**	**0.01953**
	120	2.109	-0.003418	-0.2944	-0.0377	**0.9832**	**0.01896**
B0006	80	-711.2	0.003179	713.2	0.003164	**0.9643**	**0.0319**
	100	2.086	-0.003968	-0.06686	-0.07632	**0.9564**	**0.04037**
B0007	80	-2.66e+05	-0.2192	2.66e+05	-0.2192	**0.9803**	**0.01173**
	100	2.077	-0.002877	-0.2138	-0.04384	**0.9723**	**0.01805**
	120	2.011	-0.002466	-0.15	-0.06315	**0.9799**	**0.01818**
B0018	80	-5.22e-06	0.1182	1.842	-0.002508	**0.9314**	**0.02978**

TABLE VIII.II

STATE SPACE ESTIMATION ACHIEVED USING CURVE FITTING TOOLBOX FOR BATTERIES
B0005 - B0006 - B0007 - B0018. ESTIMATED PARAMETERS AND GOODNESS OF FIT IN
CASE OF SINGLE EXPONENTIAL MODEL

BATTERY	k_{pred}	SINGLE EXPONENTIAL MODEL				
		C_0	a	b	R^2	RMSE
B0005	80	1.8565	-1.118	-111.9	**0.9244**	**0.02324**
	100	1.8565	-1.097	-110.5	**0.961**	**0.02305**
	120	1.8565	-1.133	-112.7	**0.9781**	**0.02144**
B0006	80	2.0353	-1.002	-52.84	**0.9141**	**0.04887**
	100	2.0353	-1.003	-52.79	**0.9384**	**0.04753**
B0007	80	1.8911	-1.043	-110.6	**0.9633**	**0.01581**
	100	1.8911	-0.8971	-101.7	**0.9715**	**0.01814**
	120	1.8911	-0.8717	-99.86	**0.9824**	**0.01687**
B0018	80	1.8550	-0.5238	-35.47	**0.8753**	**0.03962**

Analyzing the goodness of fit in TABLE VIII.I and TABLE VIII.II it is clear that the single exponential model fit extremely well the degradation of the four batteries under test. The results obtained with the single exponential model proposed in this work are comparable with the widely known double exponential model proving that the single exponential model is a valid alternative when a lower number of coefficients is required.

The following steps require the use of the proposed ESN to estimate the battery degradation. TABLE VIII.III summarizes the structure and main parameters of

the proposed DESN (Deep Echo State Network).

ESN LEVELS	3
POPULATION SIZE	100
N	[100, 800]
ELITE COUNT	5
CROSSOVER FRACTION	0.78
α	[0.75,1.4]
ACTIVATION FUNCTION	Tanh
LOSS FUNCTION	MSE
M	15

The network implementation has been realized in python, considering a number of network levels equal to 3, as reported in TABLE VIII.III. The connections between the units in each level of the network has been randomly generated, whereas the number N of units in the reservoir, as well as the spectral radius α, has been selected by applying the GA. The optimization process involving N and α has been performed considering the range [100, 800] and [0.75, 1.4] for the two parameters, respectively. Then, as stopping criterion of the GA, the achievement of the maximum number of generations has been used, here set equal to 15. Moreover, the elite selection process terminates when the best five individuals advance to the next population generation. Differently, the crossover fraction per generation has been set equal to 0.78. It is important to highlight that the number of samples created for each dataset forecast has been properly selected performing random experiment, in order to find the minimum number of samples needed to reach a valuable accuracy prediction. Therefore, the number of training samples varies for each dataset.

Fig. 8.8 highlights the training phase of the proposed method comparing the measured data and the model-based generated dataset considering the RUL prediction of battery B0005 at $k_{pred} = 80\ cycles$ by means of single exponential model. The parameters of the battery's state space used to generate the data are the ones reported in TABLE VIII.II.
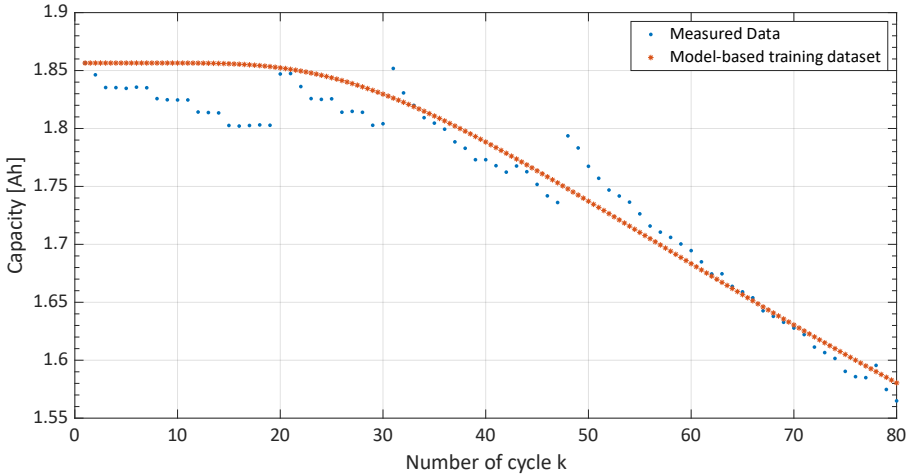
Fig. 8.8. Training of the proposed ESN. The blue dots show the measured data, while the red stars stand for the training dataset generated according to the single exponential model and the state space estimated in TABLE VIII.II (Prediction performed at $k_{pred} = 80\ cycles$.

Fig. 8.9 shows the prediction of the health state performed for battery B0005 using the proposed method at the prediction time $k_{pred} = 100\ cycles$. The measured data are compared with the results of the prediction achieved using the proposed RNN in three different scenarios:

    a.   Network training using the measured data.

    b.   Network training using a large dataset generated according to the state space estimation in TABLE VIII.II and the single exponential model.

    c.   Network training using a large dataset generated according to the state space estimation in TABLE VIII.I and the double exponential model.

Analyzing Fig. 8.9 it is possible to highlight the potentialities of the proposed model. In fact, the capacity predicted considering the scenario a. (training using the measured data) is absolutely not reasonable. The network does not catch the non-linear behavior of the dataset and the battery capacity remains approximately constant without reaching the failure threshold. This is mainly due to the quality of the battery data and the many regeneration phenomena in the considered dataset, while it is not linked to the numerosity of the training dataset. In fact, similar results have been obtained moving the prediction time k_{pred} from 80 cycles up to 150 cycles.
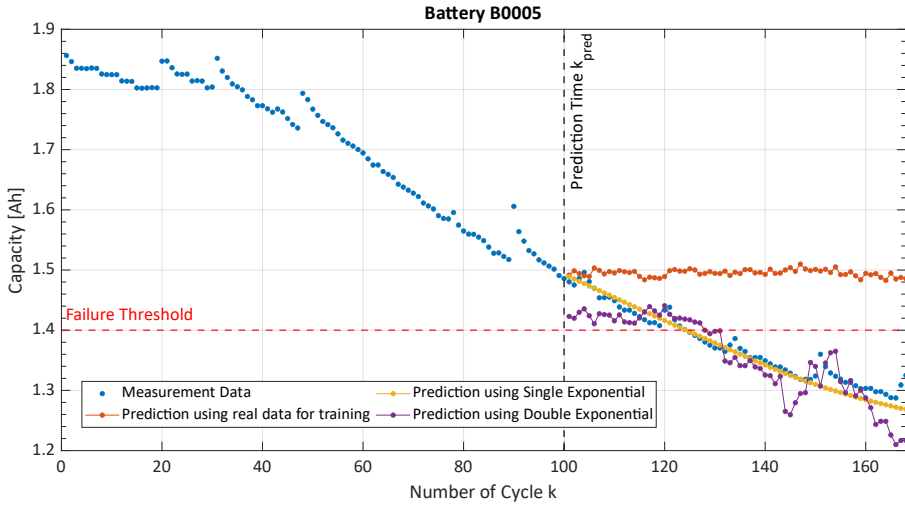
Fig. 8.9. Results of the RUL estimation performed with the proposed approach on the battery B0005 using three different trainings methodology for the developed RNN: training using the measured data (red dots), training using state space estimation and single exponential model (yellow dots), training using state space estimation and double exponential model (purple dots).

Quite the opposite, when the network is trained using the proposed method that integrates the state space estimation and the parameters of TABLE VIII.I and TABLE VIII.II, then the predicted dataset estimates the RUL of the battery with an estimation error of only 3 and 4 cycles (double and single exponential model respectively).

More in detail, the proposed single exponential model follows the measured data almost perfectly, while the double exponential model provides a low estimation error even if the predicted trend does not follow perfectly the measurements. This phenomenon proves the superiority of the proposed single exponential model against the well-established double exponential for this kind of batteries.

Fig. 8.10 compares the capacity prediction for battery B0007 achieved using the single exponential model in three different prediction times: $k_{pred} = 80$ cycles, $k_{pred} = 100$ cycles, and $k_{pred} = 120$ cycles. Considering battery B0007 the proposed single exponential model allows to perfectly follow the trend of the measured data, regardless the time of the estimation k_{pred}.

Obviously, moving forward the prediction time, the predicted capacity approximate the measured data with a lower error.
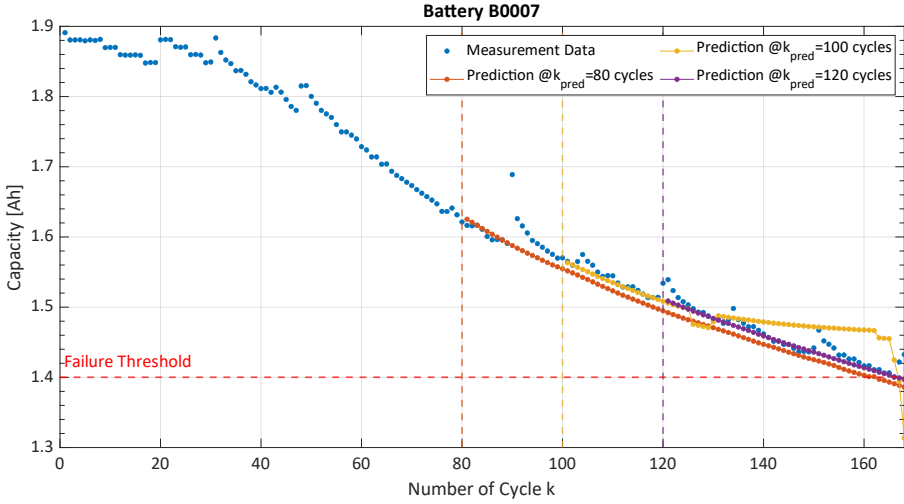
Fig. 8.10. Results of the RUL estimation performed with the proposed approach on the battery B0007 at three different prediction times: 80 cycles (red dots), 100 cycles (yellow dots), 120 cycles (purple dots).

This is due to the fact that a greater prediction times involves a greater measured dataset and therefore a better state space estimation. As a consequence, improving the state space estimation used to train the RNN, also the prediction of the RNN significantly improves providing more accurate predicted Remaining Useful Life RUL_{pred}.

For the sake of brevity, the results of the proposed RUL estimation method are summarized in TABLE VIII.IV in case of both single exponential model and double exponential model.

The goodness of estimation has been analyzed comparing both EE and MSE. The four batteries under test have been analyzed at different prediction times. TABLE VIII.IV reports the results achieved at prediction time $k_{pred} = 80$ cycles, $k_{pred} = 100$ cycles, and $k_{pred} = 120$ cycles.

Focusing on the estimation error, the proposed method ensures a performant estimation with an extremely low absolute error between the measured and the predicted RUL.

Comparing the results achieved using the proposed single exponential model and the well-established double exponential model it is possible to note that the proposed model provides better results for three out of four batteries (B0005, B0006 and B0007). Only battery B0018 favor the double exponential model.

TABLE VIII.IV.

RESULTS OF THE RUL ESTIMATION PERFORMED USING THE PROPOSED METHOD ON THE BATTERIES B0005 - B0006 - B0007 - B0018

BATTERY	MODEL	k_{pred}	RUL_{meas}	RUL_{pred}	EE	MSE
B0005	Single Exp	80	44	45	1	29.3e-3
		100	24	24	0	0.28e-4
		120	4	4	0	0.11e-3
	Double Exp	80	44	50	6	39.7e-3
		100	24	28	4	1.4e-3
		120	4	4	0	1.1e-3
B0006	Single Exp	80	29	29	0	1.5e-3
		100	9	11	2	0.31e-4
	Double Exp	80	29	33	4	2.2e-3
		100	9	7	2	6.7e-3
B0007	Single Exp	80	86	83	3	0.52e-4
		100	66	67	1	0.83e-3
		120	46	46	0	0.14e-3
	Double Exp	80	86	82	4	2.9e-3
		100	66	65	1	2.2e-3
		120	46	46	0	1.8e-3
B0018	Single Exp	80	17	19	2	8.0e-3
	Double Exp	80	17	16	1	5.5e-3

Taking battery B0005 as an example, the estimated RUL_{pred} using the single exponential model decreases from 45 cycle at $k_{pred} = 80\ cycles$ down to 24 cycles at $k_{pred} = 100\ cycles$ and then to only 4 cycles when $k_{pred} = 120\ cycles$. When RUL estimation is performed at $k_{pred} = 120\ cycles$ the proposed approach alerts the maintenance crew that the battery will reach the 30% degradation threshold after only other 4 cycles. Thus, a maintenance task to replace the battery will be planned shortly.

8.6.2. Goodness of estimation

The goodness of the proposed RUL estimation has been studied with two analysis.

Firstly, a comparison between the predicted RUL and the actual RUL of the batteries is presented. Taking battery B0007 as an example, the accuracy of the proposed estimation is shown in Fig. 8.11 considering the single exponential model and varying the prediction time starting from $k_{pred} = 80\ cycles$ up to $k_{pred} = 150\ cycles$.
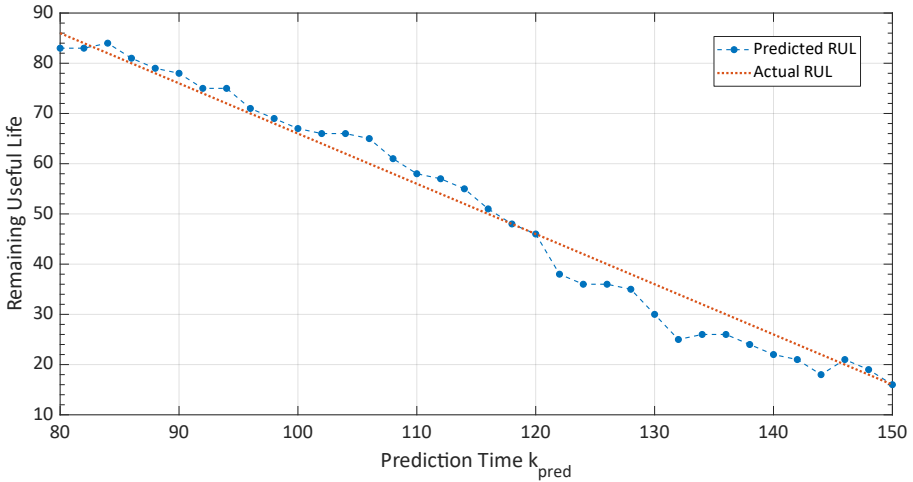
Fig. 8.11. Accuracy estimation of RUL prediction using the single exponential model comparing predicted RUL (blue line) and actual RUL (red line) for battery B0007. The battery End-Of-Life is 166 cycles. Prediction time varies from $k_{pred} = 80\ cycles$ up to $k_{pred} = 150\ cycles$.

Fig. 8.11 highlights the goodness of the proposed method, showing how the predicted RUL trend (blue line) follows accurately the actual RUL (red trend). It can be seen from the figure that many times the prediction ensure a remarkably low absolute error.

To highlight the quality of the prediction, Fig. 8.12 shows the prediction carried out at $k_{pred} = 80\ cycles$ on battery B0007 including the upper and lower 95% confidence bounds (green dashed lines).

Such intervals have been evaluated by means of t-distribution with N-1 degrees of freedom, where N is the number of capacity samples randomly generated by the proposed ESN at the considered cycle k_{pred}.
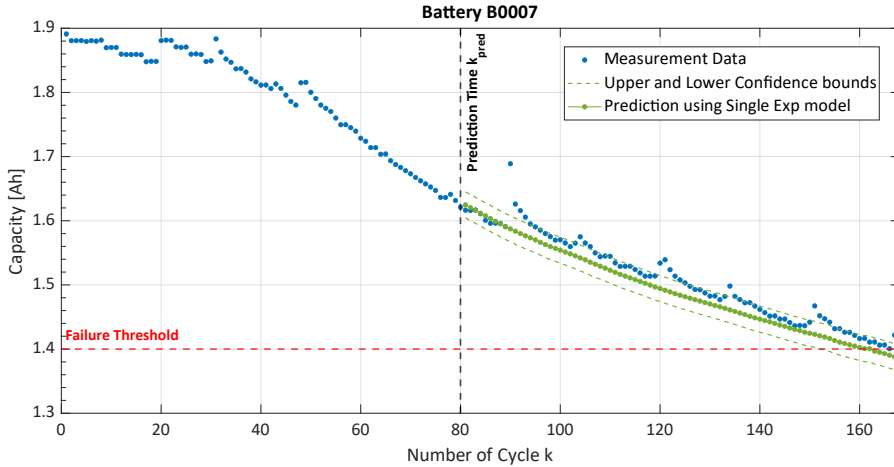
Fig. 8.12. RUL Prediction using the proposed single exponential model in case of battery B0007 (prediction performed at $k_{pred} = 80\ cycles$). The green dashed lines represent the confidence bounds of the proposed prediction.

8.6.3. Comparison with other methods

Finally, the results achieved using the proposed hybrid approach that integrates state space estimation and prediction based on AI have been compared with some of the methods available in literature that provides results applied on the same battery dataset. The comparison reported in TABLE VIII.V includes six different methods:

- A particle filter as in [357]. This comparison is fundamental since the particle filter is one of the widest used approach for RUL estimation of batteries.
- An innovative method also present in [357] based on an improved Long Short-Term Memory Fusion Technique.
- A PF integrated with a nonlinear AR model presented in [360]. This comparison has been chosen since this approach integrates aspect of filtering methods and AI methods similarly to the proposed method.
- An Empirical Mode Decomposition and Autoregressive Integrated Moving Average presented in [359].
- An innovative indirect health indicator based on multiple Gaussian process regression as in [342].
- The Monotonic ESN presented in [367] since it is the same neural network of the proposed approach.

TABLE VIII.V.

COMPARISON BETWEEN RUL ESTIMATION ACHIEVED USING THE PROPOSED METHOD
(BOTH SINGLE AND DOUBLE EXPONENTIAL MODELS) AND USING DIFFERENT APPROACHES
AVAILABLE IN LITERATURE.

Battery	k_{pred}	Proposed method		Literature comparison		
		EE Single Exp	EE Double Exp	Method	EE	Ref.
B0005	80	**1**	6	Particle Filter	8	[357]
B0005	100	**0**	4		6	
B0006	80	**0**	4		7	
B0006	100	**2**	2		3	
B0007	80	**3**	4		8	
B0007	100	**1**	1		7	
B0018	80	**2**	1		7	
B0005	80	**1**	6	Improved Long Short-Term Memory Fusion Technique	3	[357]
B0005	100	**0**	4		2	
B0006	80	**0**	4		2	
B0006	100	**2**	2		1	
B0007	80	**3**	4		3	
B0007	100	**1**	1		2	
B0018	80	**2**	1		1	
B0005	80	**1**	6	Nonlinear AR model and Regularized PF	8	[360]
B0005	100	**0**	4		4	
B0005	100	**0**	4	Empirical Mode Decomposition and AR Integrated Moving Average	4	[359]
B0006	80	**0**	4		3	
B0007	100	**1**	1		2	
B0005	80	**1**	6	Indirect health indicator and multiple Gaussian process regression	6	[342]
B0006	80	**0**	4		3	
B0018	80	**2**	1		5	
B0005	80	**1**	6	Monotonic ESN	6	[367]
B0006	80	**0**	4		3	
B0018	80	**2**	1		1	

The comparison highlights the goodness of estimation provided by the proposed
method. When the single exponential model is taken into account the proposed
approach provides extremely better results of the other methodologies. Instead,
the double exponential model reached worsen results respect to the improved
Long Short-Term Memory Fusion Technique, similar results to the Monotonic
ESN, while overcomes the results of the other approaches included in the
comparison table.

8.7.   Results and Discussion for TRI dataset

This section presents the results of the proposed methodology applied on the TRI battery dataset. Firstly, this section aims at verifying if the proposed single exponential model can be successfully applied to the considered dataset. This step is fundamental to validate the proposed model with a dataset composed by a large number of LIBs. To ensure accurate prognostic and effective RUL estimation the single exponential model must fit properly all the 124 LIBs included in the considered dataset. The estimation of the goodness of fit has been carried out using the coefficient of determination R^2 and the Root Mean Square Error (RMSE). Well-fitting regression models are characterized by values of R2 close to 1 and values of RMSE close to 0. Both goodness of fit measures have been illustrated in the boxplots in Fig. 8.13.

The top subplot shows the results achieved for the three batches in terms of coefficient of determination R2, while the bottom subplot refers to the RMSE. Each boxplot summarizes the goodness of fit of an entire batch of batteries showing its main statistical parameters. This is done to analyze the variability of the parameters and the quality of the fitting. The boxplots in Fig. 8.13 highlight that the single exponential model fit well the degradation mechanisms of the 124 LIBs under test, allowing to extend the application of the proposed procedure to the considered dataset. In fact, the different fast-charging policies barely influence the goodness of fit of the proposed single exponential model.
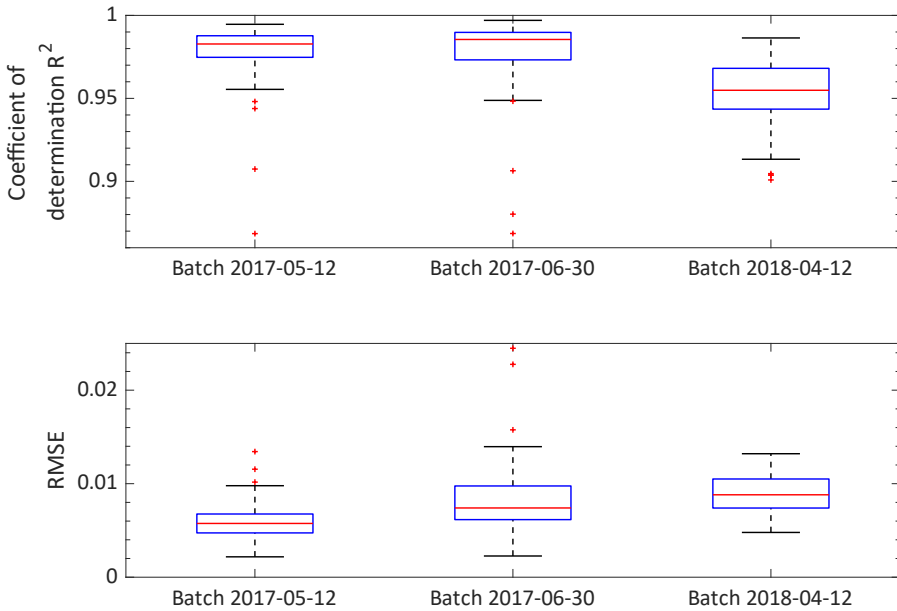
Fig. 8.13. Goodness of fit of the Single exponential model for TRI dataset.

The results of the application of the proposed Deep-ESN are summarized in Fig. 8.14, where the blue trends represent the measurement datasets while the yellow lines stand for the predicted battery capacity datasets. The training phase of the proposed Deep-ESN has been stopped at the 60% of the battery life, while the remaining 40% of the dataset has been used to validate the prediction. Analyzing in detail Fig. 8.14 it is possible to highlight the outstanding performances of the proposed network and validate the application under different fast-charging policies. The most striking results to emerge is that the proposed method is able to effectively predict the future behavior of the batteries regardless the charging policy selected for the specific LIB.

The proposed ESN is able to predict properly the future degradation of the battery capacity under all the 8 considered conditions. More in detail, the prediction errors in terms of absolute RUL error AE and Mean Square Error MSE are shown in TABLE VIII.VI for the different charging conditions. The MSE is the loss function of the proposed network, while the absolute error gives an immediate measure of the prediction quality.

TABLE VIII.VI.

QUALITY OF THE PREDICTION UNDER DIFFERENT CHARGING CONDITIONS. ABSOLUTE ERROR AND MSE ARE USED TO COMPARE THE PREDICTED RUL AND THE MEASURED RUL.

CHARGING POLICY	CHANNEL	AE	MSE
5C(67%)4C	CH 10	3	1.5515e-9
5.3C(54%)4C	CH 43	0	4.2068e-9
4.8C(80%)4.8C	CH 6	0	9.7688e-10
5.6C(19%)4.6C	CH 12	1	1.6169e-7
5.6C(36%)4.3C	CH 45	1	2.5371e-11
3.7C(31%)5.9C	CH 38	0	1.5216e-7
5.9C(15%)4.6C	CH 24	1	3.0841e-8
5.9C(60%)3.1C	CH 40	0	1.2790e-8

To easily understund the quality of the proposed RUL prediction, the analysis of the percentage relative error between predicted capacity and actual measured capacity have been included in TABLE VIII.VII and Fig. 8.15. More in detail, TABLE VIII.VII highlights the maximum percentage error achieved for each one of the 8 fast-charging policies included in "Batch 2018-04-12".
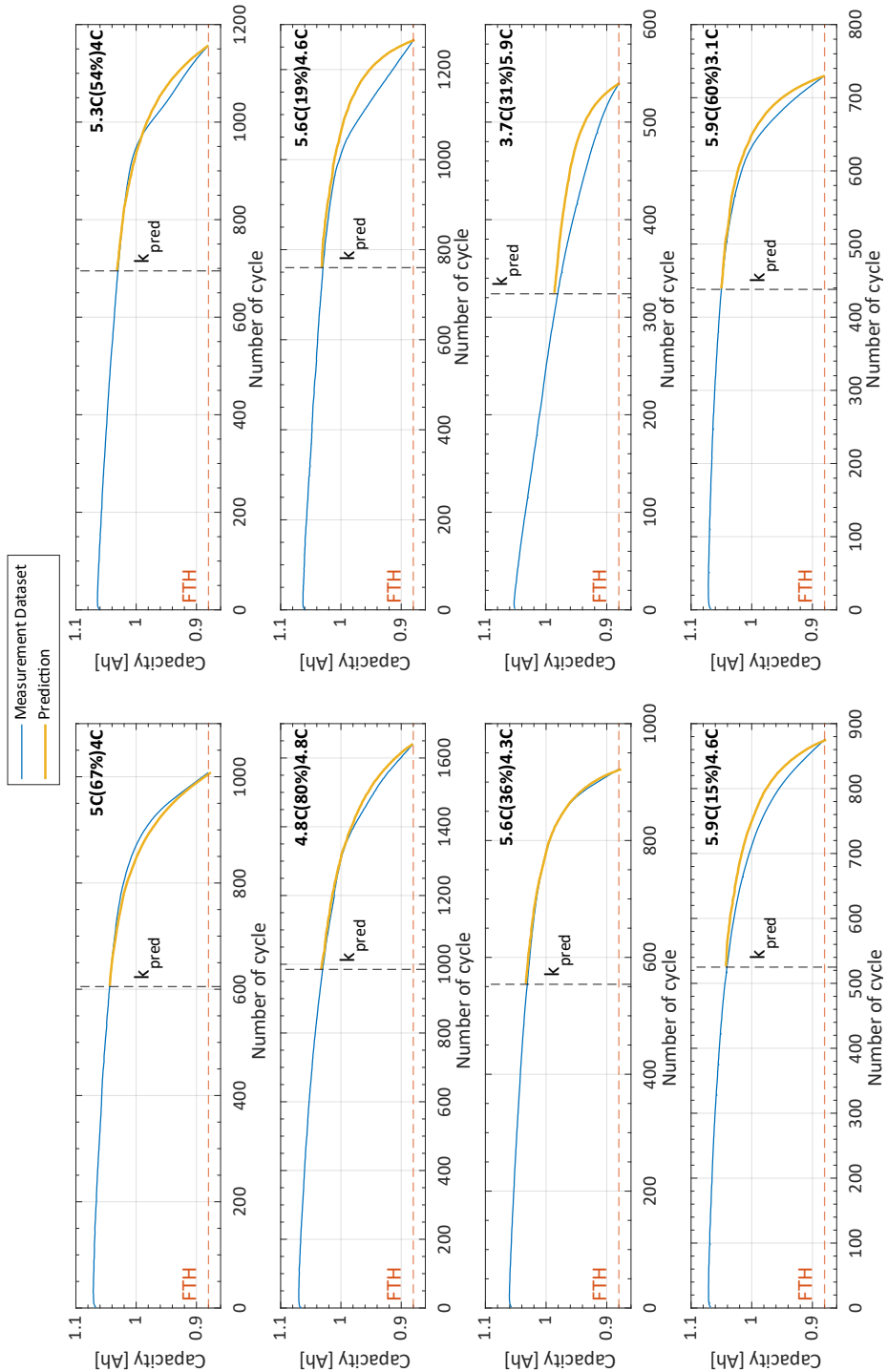
Fig. 8.14. Prediction results performed using the proposed ESN-based procedure on 8 batteries characterized by different fast-charging condition.

TABLE VIII.VII.

MAXIMUM PERCENTAGE ERROR BETWEEN PREDICTED AND MEASURED CAPACITY FOR DIFFERENT CHARGING CONDITIONS.

CHARGING POLICY	CHANNELS	MAX PERCENTAGE ERROR
5C(67%)4C	2 - 7 - 10 - 18 - 42 - 47 - 34	1.1467 %
5.3C(54%)4C	3 - 8 - 11 - 19 - 27 - 35 - 43 - 48	1.9185 %
4.8C(80%)4.8C	1 - 6 - 9 - 17 - 25 - 33 - 41 - 46	1.1817 %
5.6C(19%)4.6C	4 - 12 - 14 - 20 - 22 - 28 - 36 - 44	4.2491 %
5.6C(36%)4.3C	5 - 13 - 15 - 21 - 23 - 29 - 37 - 45	0.7631 %
3.7C(31%)5.9C	16 - 30 - 38	3.1295 %
5.9C(15%)4.6C	24 - 39	2.4023 %
5.9C(60%)3.1C	32 - 40	2.4561 %
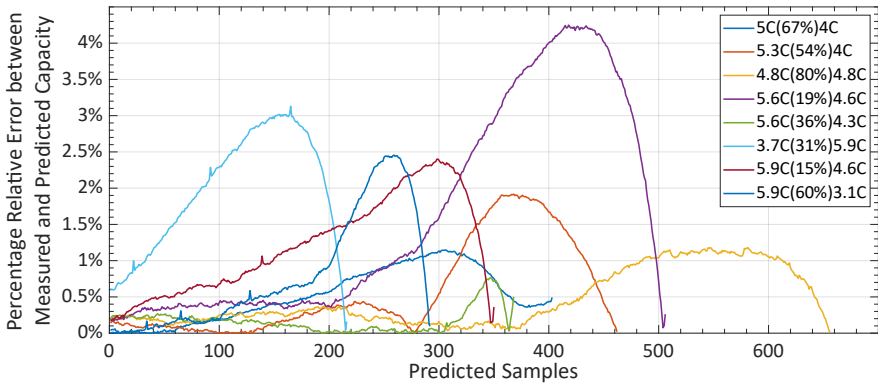
Fig. 8.15. Percentage relative error between predicted and measured capacity. Each trend represents the worst battery of a single charging condition.

The percentage error in each row of the table refers to the worst performed prediction of every charging condition. Such analysis emphasizes that the quality of the prediction decreases when the charging current increases, however the percentage relative error still remains considerably low.

For every one of the worst conditions in TABLE VIII.VII, the complete trend of the prediction error is illustrated in Fig. 8.15, where sample 0 refers to the prediction time k_{pred}. The percentage relative error in Fig. 8.15 is considerably low in the initial phase of the prediction. Then it increases when the capacity

of the LIB is approximately 1 Ah (i.e., $\simeq 90\%$ of rated capacity). After that, thanks to the goodness of the single exponential model, the error decreases reaching values lower than the 0.5% approaching the FTH.

Finally, the quality of the proposed method has been tested in case of a noisy battery dataset. The battery cell in channel 46 of "Batch 2018-04-12" has noisy voltage profiles and thus a noisy discharge capacity profile. According to the authors of the dataset, this could be caused by a problem in one or more electronic connections [382]. The prediction results in case of noisy battery data are illustrated in Fig. 7 varying the time in which the prediction is performed. More in detail, the analysis has been repeated considering as training dataset the 40 %, 50%, 60% and 70% of the battery lifetime. The analysis of Fig. 7 proves the ability of the proposed method to identify the battery degradation behavior also in presence of noisy data, regardless the time in which the prediction is performed.
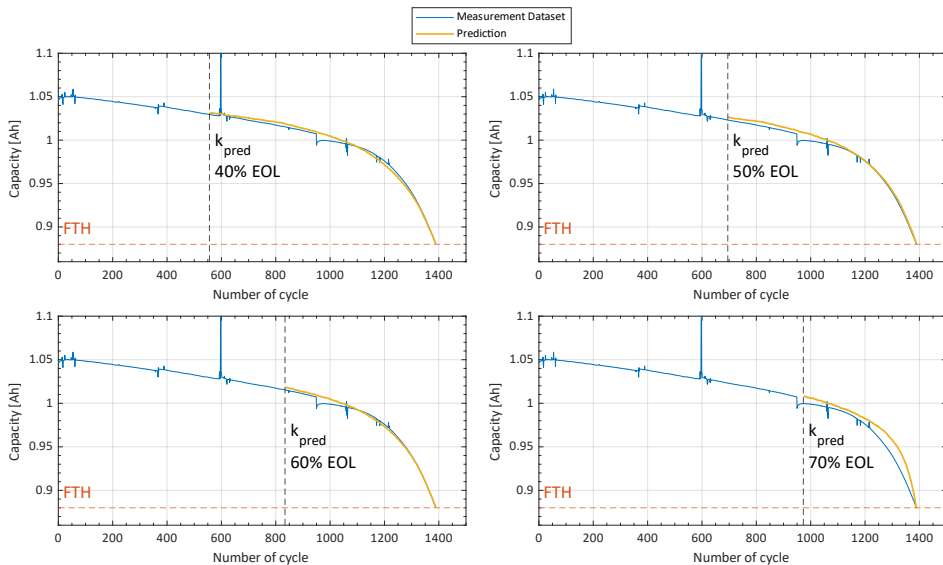
Fig. 8.16. Results of the proposed RUL estimation method in case of noisy dataset. The different predictions in each subplot have been performed at prediction time k_{pred} from 40% to 70% of the actual battery EOL.

Finally, it is important to note that despite the proposed Deep-ESN consists of a deep neural network belonging to the reservoir computing model, there is no large additional computational complexity in the whole learning process in comparison to the conventional ESN. In fact, as detailed in [383], the computational complexity of both the ESN and its deep version results to be

driven by the training process whose complexity is $O(I \cdot D^2)$, in which D is the number of data points in the considered dataset and I is the input length.

8.8. Final remarks

This chapter introduces a hybrid method for Lithium-Ion batteries RUL estimation by means of state space estimation and Recurrent Neural Network. The hybrid approach integrates a condition monitoring unit and a physical degradation model to enhance operation and maintenance. More in detail, the main contributions of this chapter are:

- The introduction of an innovative hybrid approach which integrates CM and physical degradation model to estimate the batteries EOL.
- The integration of an Artificial Intelligence estimation method with a state space estimation which is typical of filtering-based approach. The state space estimation allows to generate a big dataset used for the Network training, ensuring valuable estimation regardless the prediction time.
- Introduction of additional deep layers within the ESN to ensure an accurate estimation of nonlinear trends. This step is essential to guarantee an optimal estimation for Lithium-Ion batteries where the degradation mechanisms are strongly nonlinear.
- Introduction of a single exponential degradation model for Lithium-Ion batteries which is an alternative to the widely known double exponential model. The proposed model provides better results with lower parameters and lower complexity ensuring the same accuracy.

The widely known double exponential model is compared with a proposed single exponential model to estimate the battery degradation by means of the RNN. The training of the neural network has been performed based on a randomly generated dataset according to the state space estimation of the measured data. In other words, the condition monitoring unit provides data regarding the internal capacity of the battery, then the state space is estimated according to the new single exponential model (similarly to the filtering method). These data are used to generate a training dataset for the RNN, which then provides the estimation of the future battery state of charge. The two considered degradation models have different characteristics and different dynamics. However, the

proposed ESN is able to accurately catch the dynamics of both model of all the four datasets, ensuring generalization and robustness of the method.

The analysis of the experimental results performed on two very different battery datasets (i.e., Prognostic Center of Excellence at NASA and Toyota Research Institute - TRI) highlighted the ability of the proposed method to precisely estimate the RUL of several batteries under test. More in detail, the proposed single exponential model provides better results with respect to the well-established double exponential model with a lower complexity and a fewer number of parameters for three out of four batteries. In addition, a comparison with the state of the art proves how the proposed method allows to reach optimal results in terms of RUL estimation error. Furthermore, the experimental results prove the ability of the proposed method to accurately estimate the batteries behavior regardless the selected charging policy.

CHAPTER 9

PROPOSED DATA-DRIVEN RELIABILITY LIFE CYCLE

The aim of this final chapter is to introduce and describe the proposed data-driven reliability life cycle for complex systems. The procedure is presented in this section, paying considerable attention to the relationships between each method and the others included in the whole Reliability Life Cycle. Furthermore, some final remarks about the RAMS methods proposed in the previous chapter have been drawn, with particular attention to the impact of each individual improvements and optimization with respect to the state-of-the-art in the field.

9.1. Introduction

As extensively described in the Introduction section of this work, there are several design for reliability methods available in literature that integrates different reliability tasks. However, all-around Reliability Life Cycle procedures able to consider the complete system life cycle (from design and development to disposal) by a reliability point of view are seldom available.

According to recent literature, different approaches could be used in the different phases of the product life cycle. Depending on the parameters of interest, it is possible to identify different techniques that could be used depending on the specific period of the product life cycle.

For instance, reliability prediction could be used to estimate a component failure rate during the first phase of the design, while life data analysis serves the same purposes when a prototype is ready to be tested.

Another shining example could be found in risk management flow processes. Fault Tree Analysis and Failure Modes and Effects Analysis are both well-established and standardized techniques for risk assessment of complex units. However, they provide different kinds of outcomes about the risk associated to a failure and they are usually implemented alternatively based on the outcome of more interest.

Another fundamental aspect that is barely taken into account in design for reliability methodologies is the key role of diagnostics. Proper and accurate diagnostics and condition monitoring tools should be designed along with the systems that they will have to monitor. Starting from a failure analysis of the system under test, it is essential to introduce adequate sensors and independent elaboration units within the design of the system itself. This will allow to provide data about the health state of the system and consequently to achieve information about the remaining useful life of the product Thus, condition-based maintenance could be plan accordingly, saving a great amount of resources (both money and time) and ensuring adequate level of system availability and productivity. However, this procedure is able to ensure striking and significant results only if it designed and planned during the design phase of the system itself.

In this point of view, this final chapter aims at presents an innovative data-driven reliability life cycle which integrates different RAMS techniques strictly related to each other. A workflow is presented to highlight the relationships between the considered methods and to emphasize how the output of one single approach should be used to improve and optimize the following one.

9.2. Description of the proposed method

This section introduces the proposed Reliability Life Cycle procedure. The complete flowchart of the process is illustrated in Fig. 9.1 where the life cycle of the product is divided into two subsections:

- RAMS methods implemented during design phase with two major purposes:
  - o Evaluate the reliability, availability, maintainability and safety of each component and each subsystem making up the system under analysis.
  - o Carry out a risk assessment procedure in order to find the most critical components by a risk value point of view. This allows to introduce adequate design countermeasures to mitigate such high-risk scenarios.
- Diagnostics and Prognostic approaches carried out after the implementation and installation of the system in the specific field of application.

The above-mentioned subsections are identified using two dashed-line colored squares in Fig. 9.1.

Moving forward to the specific methods taken into consideration, 10 different RAMS methodologies have been included in the proposed data-driven Reliability Life Cycle.

The flowchart in Fig. 9.1 uses different colors of the boxes to identify different areas of application of the techniques. More in detail, the approaches considered as fundamental part of the proposed Reliability Life Cycle are described in the following:

- Reliability Block Diagram (RBD) used to generate a reliability model of the system under test in order to identify and model properly different kind of redundancies.
- Failure Modes, Effects and Criticality Analysis (FMECA) implemented to identify every possible failure of the system and to estimate the risk associated to each critical event.
- Risk Priority Number (RPN) threshold estimation in order to identify a set of critical items and divide it form the negligible components (by a risk-value point of view.
- Reliability Allocation carried out with the aim of estimate the reliability requirements of each individual component and each equivalent subsystem included in the developed device.

- Accelerated Life Test to estimate the failure rate and the reliability parameters of critical components characterized by non-constant failure rate.

- Safety Integrity Level (SIL) evaluation techniques carried our in case the system under analysis is a safety critical unit to be used in s Safety Instrumented System (SIS) or a Safety Related System (SRS).

- Environmental Stress Screening (ESS) test procedure with the aim of identify the weak population and remove it from the strong products. This will allow to avoid infant mortality failures lowering the failure rate values in the first phase of the bathtub curve. Furthermore, ESS procedures can be used to characterize the performances of the developed product in the real scenario in which the system will be installed. This can be characterized by the presence of significant temperature variation, humidity exposure, vibration levels, mechanical shocks and so on.

- Condition Monitoring tools designed during the design phase of the product itself and implemented after the installation of the system on the field in order to achieve information about the health state of the system under analysis.

- Remaining useful Life (RUL) estimation method able to quantify the amount of time from the current moment to the end-of-life of the system starting from condition monitoring data and failure threshold alarms.

- Condition-based maintenance planned properly according to the outcomes of condition monitoring tools and remaining useful life estimation algorithms.

It is important to note that, among all the ten techniques included in this procedure, only two methods have not been discussed in this work: RBD and SIL evaluation. As a matter of fact, the Reliability Block Diagram methodology is a well-defined and well-standardized technique properly described in the international standard IEC 61078 (2016) [197]. By a research point of view, it does not provide any particular starting point since the description of the redundant models is well-defined and accepted in the scientific community. Quite similarly, the SIL evaluation techniques must follow strict and rigorous rules defined and standardized in several international standards, depending on the field of application. Few examples are the IEC 61508 (2011) [384] about the electric and electronic components, or the IEC 61511 about process industry sector [385].
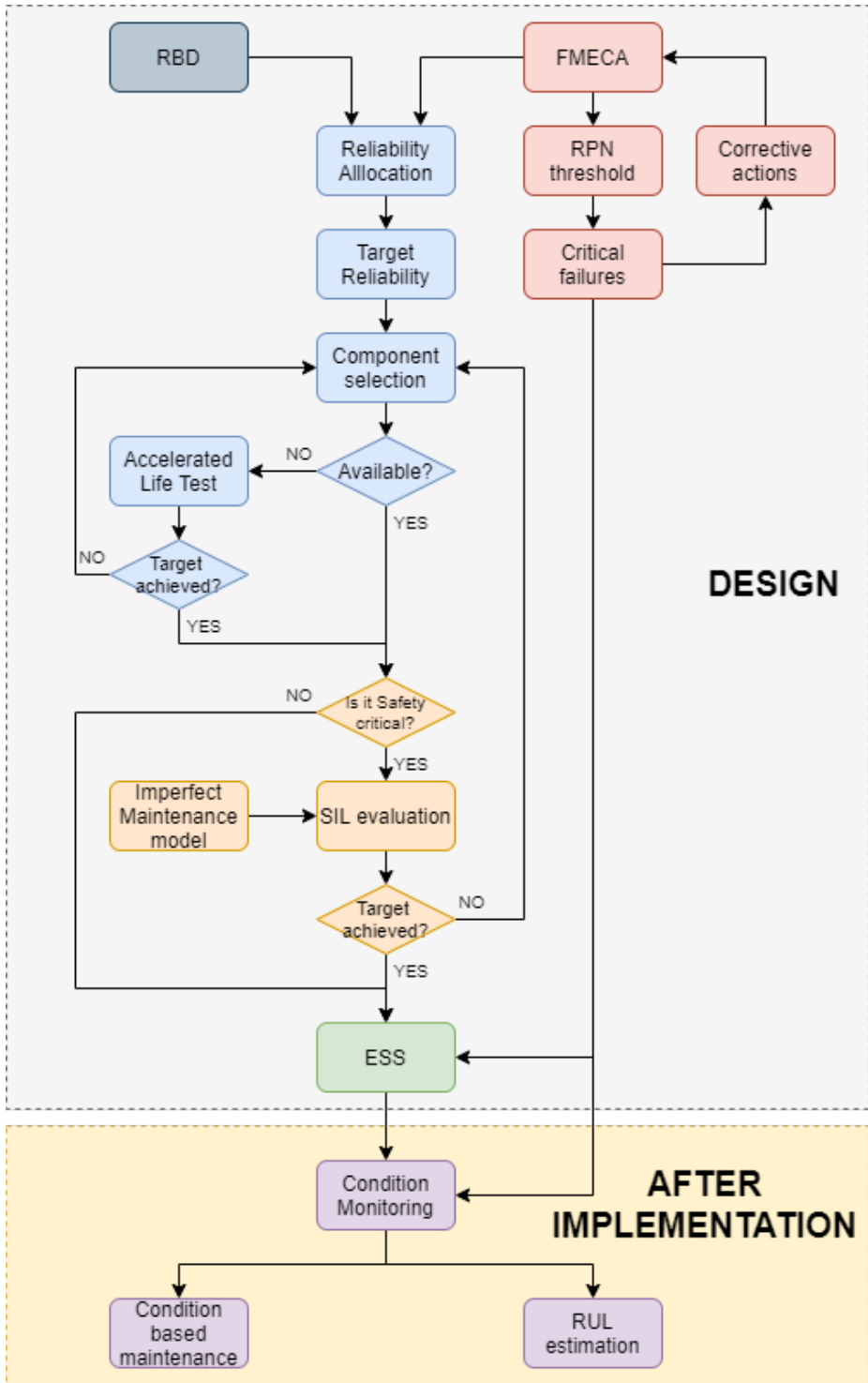
Fig. 9.1. Proposed data-driven reliability life cycle for complex systems.

The proposed procedure illustrated in Fig. 9.1 starts with two approaches carried out simultaneously, a Reliability Block Diagram and a Failure Modes, Effects and Criticality Analysis. While RBD has been considered a single tool, FMECA has been divided into several tasks. Firstly, a classical FMECA should be performed taking into account the considerations about alternative RPNs and scale reductions presented in Section 3. Furthermore, whenever it is possible, the indexes of the FMECA should be assessed quantitatively using the measurements-based procedures presented in the final part of Section 3. After that, a proper clustering of the failure modes between critical, intermediate and negligible modes must be performed according to the proposed Boxplot method for threshold estimation presented in Section 4. This allows to identify the most hazardous conditions and thus implement proper and accurate corrective actions.

After that, RBD and FMECA are used as starting point from the Reliability Allocation procedure. Using the methodology proposed in Section 5 it is possible to evaluate a reliability target for each component and each subunit making up the system. After that, the proper component should be selected on the market. If a device able to ensure the target reliability is available, then it is possible to move forward to the next component. Otherwise, an Accelerated Life Test plan should be used to indirect estimate the reliability parameters of the selected component by means of a Life Data Analysis.

The following step is a SIL evaluation that should pe performed only if the system is a safety-critical unit according to the recommended standards. Imperfect maintenance model should be taken into account in order to ensure a more accurate SIL estimation.

The final step that should be performed before the installation of the system is a screening procedure carried out by means of an ESS test plan. To properly develop an ESS procedure information about failure analysis are required. Then, the test could be used to identify any possible intrinsic malfunction due to the production processes and to characterize the performances of the system in a harsh environment typical of the actual scenarios in which the product will be installed. Two examples of ESS test plans and context-awareness analysis have been presented in Section 6.

After installation and implementation of the considered system, diagnostic and prognostic approaches can be performed. This starts with a Condition Monitoring tool that should be designed and installed along with the system itself. An example of condition monitoring from planning to implementation is presented in Section 7 in case of a wind turbine. Other examples of Condition-based maintenance tasks have also been presented in Section 7. Finally, the

data gather by the condition monitoring tool are used to implement effect Prognostic strategies. An example of prognostic and RUL estimation has been presented in Section 8, where an innovative hybrid method for RUL estimation of Lithium-Ion batteries has been proposed.

9.3. Relationships between the considered techniques

In this section the relationships between the proposed methods are detailed described. Every approach integrated within the proposed Reliability Life Cycle in Fig. 9.1 is related to each other, the output of one technique become the input of the following ones, and vice versa. More in detail:

- The Failure Modes, Effects and Criticality Analysis is essential in order to estimate the most critical items included in the systems and thus to reduce their risk level. This is a cyclic approach which start with a FMECA and continues with an RPN threshold estimation in order to find the most critical units. After that, corrective actions are implemented, and the failure analysis is performed once again. This cycle is continuously improved not only during design phase, but also after installation and implementation of the system.

- FMECA is also used as input of the ESS screening procedure. In order to be effective, an ESS test plan must be designed taking into account the failure modes and failure mechanisms identified during the FMECA. This allows to plan the test bearing in mind what accelerated factors mostly influence the reliability of each component.

- As detailed described in Section 5, the RBD is the standard input of the Reliability Allocation procedure. More in detail, the RBD of the system is essential to identify the different hierarchical levels of the system under test and thus to properly model the redundancies in the proposed allocation methodology.

- Another fundamental input of the Reliability Allocation is the criticality analysis included in the FMECA. Section 5 emphasized how the FMECA report is extremely useful to estimate the influence factor of each component required by the Allocation method.

- Once again, FMECA is strictly linked to another approach which plays a central role in the proposed reliability Life Cycle. In fact, Condition Monitoring data are widely used to improve the assessment of the

Detection rate in the FMECA report, keeping it continuously updated during the entire system life cycle.

- Condition Monitoring data are the starting point for the implementation of Condition-Based Maintenance and prognostic methods such as RUL estimation.
- RBD is not only the input of the Reliability Allocation but also the starting point of the SIL estimation methods according to several international standards.
- Reliability Allocation allows to estimate the reliability requirements of every component and every subsystem included in the design. Thus, it can remarkably simplify the RUL estimation models.

CONCLUSIONS

The work presented in this thesis extends the classical idea of Design for Reliability introducing an innovative data-driven reliability life cycle procedure that integrates different RAMS techniques to optimize the reliability of complex industrial systems during both design and operational phases. Furthermore, the work also presents some improvements and optimizations of the techniques included in the proposed Reliability Life Cycle in order to overcome the major drawbacks highlighted by the literature.

More in detail, Chapter 1 presents an introduction to the work with the aim of emphasize the research questions and the objective of the project. The gaps in the body of knowledge that this research aims to fill are extensively explained, and the problems addressed by this study are properly outlined. Furthermore, Chapter 1 also illustrates the main contributions emphasizing the key element of novelties of this research project. The core of the chapter outlines the importance of the thesis within the context of the RAMS disciplines and more in detail within the topic of Instrumentation and Measurements to Improve Diagnostics, Prognostic and Reliability of complex system. As a matter of fact, the entire work has been developed in order to highlight the fundamental role of metrology within RAMS contexts, paying particular attention to these aspects that are normally neglected during RAMS analysis and simulation approaches.

Chapter 2 provides a brief description of the complex systems taken as case study in the various sections of this work. In particular, six different systems have been used to test the performances of the methodologies introduced in the other chapters and included in the proposed Reliability Life Cycle. More in detail, the chapter starts describing the basic features of an onshore wind turbine, with specific reference to the electrical and electronic units and to the yaw system used to move the turbine toward the wind direction. Other complex systems dealt with in this work are an HVAC (Heating, Ventilation and Air Conditioning) unit installed in high-speed trains and a lubrication system for gas turbines. Furthermore, a general-purpose Inertial Measurement Unit has been presented and described because it is a useful platform in diagnostic and

condition monitoring units. Strictly connected to the latter, lithium-ion batteries and a customized self-made DC-DC converter used to supply WSN-based diagnostic units have also been included because they represent the most critical items in any condition monitoring device.

Chapter 3 illustrates the first technique studied and optimized in this work. The Failure Modes, Effects and Criticality Analysis (FMECA) plays a central role in many Design for Reliability procedure and thus it has been included in the proposed Reliability Life Cycle. Chapter 3 starts illustrating in detail the base theory about FMECA according to the international standard IEC 60812 (last update 2018). An extensive literature review is included in the chapter to emphasize the various different forms of alternative FMECA already published in literature. All the alternative Risk Priority Numbers that do not completely revolutionized the base idea of the IEC 60812 have been taken into account in order to identify the optimal FMECA procedure to be included in the proposed Reliability Life Cycle. The final part of the chapter implements the classical FMECA along with some alternative approaches to the most critical component of an HVAC system for railway applications. A statistical comparison is presented to highlights drawbacks and shortcomings of each method, before introduces some possible approach to reduce subjectivity of FMECA assessment by means of dedicated measurements and sensor technologies.

The following step in the proposed Reliability Life Cycle is the evaluation of an RPN (Risk priority Number) threshold to divide all the identified failure modes in different clusters by a risk value point of view. The review of the state-of-the art pointed out few quantitative methods to carry out this issue, and each one of them suffer many drawbacks.

Trying to fill this need, Chapter 4 proposes a new approach for the Risk Priority Number threshold estimation based on a statistical analysis and compares the proposed method with the other quantitative prioritization techniques found in literature. The goal of the chapter is to introduce an innovative methodology that effectively identify the most critical component of the system under test, which is a fundamental aspect of the proposed Reliability Life Cycle procedure. The proposed approach has been applied to the electrical and electronic components included in a Spanish 2 MW onshore wind turbine. The proposed methodology is an easy, practical and repeatable solution which represents the optimal trade-off between cost of the countermeasures and threshold level (by a risk reduction point of view). The major advantages of the proposed Boxplot procedure are the introduction of the ALARP region in the RPN threshold estimation, the statistical base of the analysis and the ability to solve the subjectivity problem.

Reliability Allocation (RA) is the real core of the whole proposed Reliability Life cycle, and thus Chapter 5 provides an overview of this procedure focusing on some of the most known and widely used techniques available in literature. To the author knowledge, all the RA approaches are based on two assumptions: functional series architecture and exponential failure distribution. Chapter 5 builds upon this issue introducing an innovative iterative approach that allows to overcome both assumptions and thus to apply reliability allocation to any complex system. The validation of the proposed approach has been carried out implementing the method on three different applications: a numerical example, a sensors unit of an HVAC system for high-speed trains and a lube oil console for Oil&Gas applications. The results of the applications prove the effectiveness of the proposed procedure highlighting the advantages of the method and emphasizing how it is possible to overcome the initial hypotheses required by every other allocation method.

The following step of the proposed Reliability Life Cycle is the implementation of a screening procedure by means of ESS (Environmental Stress Screening) test plan in order to identify and remove the defected products.

In this point of view, the first part of Chapter 6 presents the development of a customized test plan and test bed for characterization of Inertial Measurement Units (IMUs)under temperature and vibration stress sources. The reliability and metrological performances of the IMUs have been characterized introducing adequate figures of merits to study the behavior of the devices in time and frequency domains. The second part of Chapter 6 presents a test plan for characterization of DC-DC converters under harsh environment. Also in this case, the reliability and the electrical performances of the device have been investigated using different parameters. The results of both case studies prove how it is possible to integrate an ESS test plan within a Reliability Life Cycle procedure to efficiently and effectively improve the performances of the system through its entire life cycle. Both aims of failure analysis and context-awareness characterization have been properly fulfilled by the proposed test plan. In fact, the experimental analysis allowed to discover defected items and, at the same time, it has been used to characterize the performances of the devices under the actual operating conditions that they will endure.

After the installation and implementation of the system, condition monitoring (CM) starts to play a central role in the proposed Reliability Life Cycle. Thus, Chapter 7 provides an overview of CM techniques taking a wind turbine as an example. An innovative diagnostic-oriented methodology to select the optimal maintenance policy is presented as an alternative to the classical decision-making process. The chapter also presents a new data-driven CM system to

efficiently monitor the health state and detect damages in the wind turbine by means of measurements of critical parameters. Finally, an innovative hybrid-tree Wireless Sensor Network is presented in Chapter 7 in order to effectively and efficiently implement condition monitoring on the whole wind farm.

The data acquired by CM tools con be used for both diagnostic and prognostic purposes. Prognostic and health management represent the final part of the proposed Reliability Life Cycle. In Chapter 8 a hybrid approach based on both Condition Monitoring and physic model is presented to improve the accuracy and precision of prognostic for lithium-ion batteries. An artificial intelligence method is integrated with a state space estimation technique typical of filtering-based approaches. The state space estimation is used to generate a big dataset for the training of a neural network. Some additional deep layers are used to improve the prediction of nonlinear trends (typical of batteries) while the performance optimization of the network is ensured using a genetic algorithm. The proposed method has been applied to a battery degradation dataset from the data repository of Prognostics Center of Excellence at NASA. Two different degradation models are compared, the widely known empirical double exponential model and an innovative single exponential model which allows to ensure optimal performance with fewer parameters required to be estimated.

Finally, Chapter 9 aims at introducing and describing the proposed data-driven reliability life cycle for complex systems. The procedure is presented paying considerable attention to the relationships between each method and the others included in the whole Reliability Life Cycle.

Future development of this work could involve the optimization and improvements for the other methods included in the proposed reliability life cycle that have not been dealt with in this work (i.e. Reliability Block Diagram and SIL evaluation) and the application of the whole Reliability Life Cycle to a single case study, starting from design and development of the system up to installation, operation and maintenance.

Other further improvements could be the extension of the proposed RUL estimation method for battery state of health analysis to other kind of electronic and mechanical components and the implementation of a sensitivity analysis within the context of the proposed Reliability Allocation procedure to quantify the effects of small deviation in the influence factors.

REFERENCES

[1]   R. Reis, G. Wirth, Y. Cao, *Circuit design for reliability*. Springer Science and Media, 2015.

[2]   D. Crowe and F. A., *Design for Reliability*. CRC Press, 2001.

[3]   E. Bradley, *Reliability Engineering: A life Cycle Approach*. CRC Press, 2017.

[4]   G. Yang, *Life CycLe reliability engineering*. John Wiley & Sons, 2007.

[5]   T. Burton, D. Sharpe, N. Jenkins, and E. Bossanyi, *Wind Energy Handbook*. John Wiley & Sons, 2001.

[6]   AEO2019, "Annual Energy Outlook 2019 with projections to 2050." US Energy Information Administration - EIA, 2019.

[7]   C.-L. Nguyen and H.-H. Lee, "Power Management Approach to Minimize Battery Capacity in Wind Energy Conversion Systems," *IEEE Trans. Ind. Appl.*, vol. 53, no. 5, pp. 4843–4854, Sep. 2017.

[8]   WindEurope, "Wind energy in Europe 2020: Statistics and the outlook for 2021-2025." 2021.

[9]   S. R. Brouwer, S. H. S. Al-Jibouri, I. C. Cárdenas, and J. I. M. Halman, "Towards analysing risks to public safety from wind turbines," *Reliab. Eng. Syst. Saf.*, vol. 180, pp. 77–87, 2018.

[10]   I. Munteanu, A. I. Bratcu, N. A. Cutululis, and E. Ceanga, *Optimal Control of WInd ENergy Systems Towards a Global Approach*. Springer, 2008.

[11]   A. González-González, A. Jimenez Cortadi, D. Galar, and L. Ciani, "Condition monitoring of wind turbine pitch controller: A maintenance approach," *Measurement*, vol. 123, no. November 2017, pp. 80–93, Jul. 2018.

[12]   IEC 61400-2, "Wind turbines - Part 2: Small wind turbines." International Electrotechnical Commission, 2015.

[13]   A. Hemami, *Wind Turbine technology*. Cengage Learning, 2012.

[14]   R. Gasch and J. Twele, *Wind Power Plants: Fundamentals, Design, Construction and operation*, Second. Springer-Verlag, 2012.

[15]   M. Catelani, L. Ciani, D. Galar, and G. Patrizi, "Optimizing Maintenance Policies for a Yaw System Using Reliability-Centered Maintenance and Data-Driven Condition Monitoring," *IEEE Trans. Instrum. Meas.*, vol. 69, no. 9, pp. 6241–6249, Sep. 2020.

[16]   Y. Yan, P. B. Luh, and K. R. Pattipati, "Fault Diagnosis of Components and Sensors in HVAC Air Handling Systems With New Types of Faults," *IEEE Access*, vol. 6, pp. 21682–21696, 2018.

[17]   A. Vedavarz, S. Kumar, and M. I. Hussain, *HVAC Handbook of Heating, Ventilation, and*

Air Conditioning for Design & Implementation, Fourth. industrial press inc., 2013.

[18] American Society of Heating Refrigerating and Air-Conditioning Engineers, "Ventilation for acceptable indoor air quality." ANSI/ASHRAE Standard 62.1-2007, 2007.

[19] American Society of Heating Refrigerating and Air-Conditioning Engineers, "Guideline for the Design and Application of Heating, Ventilation and Air Conditioning Equipment for Rail Passenger Vehicles." ASHRAE Guideline 23P, 2014.

[20] S. C. Sugarman, *HVAC fundamentals*, Second. CRC Press: Taylor & Francis Group, 2007.

[21] F. Porges, *HVAC Engineer handbook*, Eleventh. Elsevier Science & Technology Books, 2001.

[22] M. Catelani, L. Ciani, V. Luongo, and R. Singuaroli, "Evaluation of the Safe Failure Fraction for an electromechanical complex system: remarks about the standard IEC61508," in *2010 IEEE Instrumentation & Measurement Technology Conference Proceedings*, 2010, pp. 949–953.

[23] J. Botero-Valencia, D. Marquez-Viloria, L. Castano-Londono, and L. Morantes-Guzmán, "A low-cost platform based on a robotic arm for parameters estimation of Inertial Measurement Units," *Measurement*, vol. 110, pp. 257–262, Nov. 2017.

[24] Q. Chen, X. Niu, J. Kuang, and J. Liu, "IMU Mounting Angle Calibration for Pipeline Surveying Apparatus," *IEEE Trans. Instrum. Meas.*, vol. 69, no. 4, pp. 1765–1774, 2020.

[25] S. O. H. Madgwick, A. J. L. Harrison, and R. Vaidyanathan, "Estimation of IMU and MARG orientation using a gradient descent algorithm," in *2011 IEEE International Conference on Rehabilitation Robotics*, Jun. 2011, pp. 1–7.

[26] H. Fourati, "Heterogeneous Data Fusion Algorithm for Pedestrian Navigation via Foot-Mounted Inertial Measurement Unit and Complementary Filter," *IEEE Trans. Instrum. Meas.*, vol. 64, no. 1, pp. 221–229, Jan. 2015.

[27] P. Mohankumar, J. Ajayan, R. Yasodharan, P. Devendran, and R. Sambasivam, "A review of micromachined sensors for automotive applications," *Measurement*, vol. 140, pp. 305–322, Jul. 2019.

[28] D. Capriglione *et al.*, "Experimental analysis of IMU under vibration," in *16th IMEKO TC10 Conference: "Testing, Diagnostics & Inspection as a comprehensive value chain for Quality & Safety,"* 2019, pp. 26–31.

[29] D. Capriglione *et al.*, "Vibration Step Test for Performance Analysis of Inertial Measurement Unit," in *17th IMEKO TC 10 and EUROLAB Virtual Conference "Global Trends in Testing, Diagnostics & Inspection for 2030,"* 2020, pp. 111–116.

[30] M. Catelani *et al.*, "Design and Experimental analysis of temperature tests for Inertial Measurement Units in Avionic applications," in *2020 IEEE 7th International Workshop on Metrology for AeroSpace (MetroAeroSpace)*, Jun. 2020, pp. 217–221.

[31] G. A. Aydemir and A. Saranlı, "Characterization and calibration of MEMS inertial sensors for state and parameter estimation applications," *Measurement*, vol. 45, no. 5, pp. 1210–1225, Jun. 2012.

[32] B. B. Kocer, V. E. Omurlu, E. Akdogan, and C. S. Tufekci, "Development of a MEMs-based IMU Unit," in *2013 6th International Conference on Recent Advances in Space Technologies (RAST)*, Jun. 2013, pp. 389–393.

[33] G. D'Emilia and E. Natale, "Network of MEMS sensors for condition monitoring of industrial systems: Accuracy assessment of features used for diagnosis," in *17th IMEKO TC 10 and EUROLAB Virtual Conference "Global Trends in Testing, Diagnostics & Inspection for 2030"and EUROLAB Virtual Conference "Global Trends in Testing, Diagnostics and Inspection for 2030,"* 2020, pp. 356–361.

[34] D. Capriglione, M. Carratu, A. Pietrosanto, and P. Sommella, "Online Fault Detection of Rear Stroke Suspension Sensor in Motorcycle," *IEEE Trans. Instrum. Meas.*, vol. 68, no. 5, pp. 1362–1372, May 2019.

[35] D. Capriglione, M. Carratù, A. Pietrosanto, and P. Sommella, "NARX ANN-based instrument fault detection in motorcycle," *Measurement*, vol. 117, pp. 304–311, Mar. 2018.

[36] D. Capriglione, M. Carratù, C. Liguori, V. Paciello, and P. Sommella, "A soft stroke sensor for motorcycle rear suspension," *Measurement*, vol. 106, pp. 46–52, Aug. 2017.

[37] M. Root, *The Tab Battery Book. An in depth guide to contruction, design and use.* Mc Graw Hill Edition, 2011.

[38] H. A. Kiehne, *Battery Technology Handbook- Second Edition.* Expert Verlag Edition, 2003.

[39] L. Ciani, G. Guidi, and G. Patrizi, "Condition-based Maintenance for Oil&Gas system basing on Failure Modes and Effects Analysis," in *2019 IEEE 5th International forum on Research and Technology for Society and Industry (RTSI)*, Sep. 2019, pp. 85–90.

[40] M. Catelani, L. Ciani, G. Guidi, and G. Patrizi, "Reliability Allocation: an iterative approach for complex systems," 2021.

[41] A. Ayachit and M. K. Kazimierczuk, "Averaged Small-Signal Model of PWM DC-DC Converters in CCM Including Switching Power Loss," *IEEE Trans. Circuits Syst. II Express Briefs*, vol. 66, no. 2, pp. 262–266, Feb. 2019.

[42] L. Ciani *et al.*, "Effect of Pulses Distribution in a Buck Converter Controlled with Pulse Skipping Modulation," in *2021 IEEE 15th International Conference on Compatibility, Power Electronics and Power Engineering (CPE-POWERENG)*, Jul. 2021, pp. 1–6.

[43] Mil-Std-1629A, "Military standard procedures for performing a failure mode, effects and criticality analysis." US Department of Defense, Washington DC, 1980.

[44] C. S. Carlson, *Effective FMEAs: Achieving Safe, Reliable, and Economical Products and Processes Using Failure Mode and Effects Analysis.* John Wiley & Sons, 2012.

[45] J. B. Bowles, "The new SAE FMECA standard," in *Annual Reliability and Maintainability Symposium. 1998 Proceedings. International Symposium on Product Quality and Integrity*, 2002, pp. 48–53.

[46] Headquarters Department of the army, "Failure Modes, Effects and Criticality Analysis (Fmeca) for Command, Control, Communications, Computer, Intelligence, Surveillance and Reconnaissance (C4ISR) Facilities," *TM 5-698-4*, 2006.

[47] IEC 60812, "Failure modes and effects analysis (FMEA and FMECA)." International Electrotechnical Commission, 2018.

[48] M. Catelani, L. Ciani, D. Galar, and G. Patrizi, "Risk Assessment of a Wind Turbine: A New FMECA-Based Tool With RPN Threshold Estimation," *IEEE Access*, vol. 8, pp. 20181–20190, 2020.

[49] K. O. Kim and M. J. Zuo, "General model for the risk priority number in failure mode and effects analysis," *Reliab. Eng. Syst. Saf.*, vol. 169, no. September 2017, pp. 321–329, 2018.

[50] M. Catelani, L. Ciani, D. Galar, G. Guidi, S. Matucci, and G. Patrizi, "FMECA Assessment for Railway Safety-Critical Systems Investigating a New Risk Threshold Method," *IEEE Access*, vol. 9, pp. 86243–86253, 2021.

[51] L. Ciani, G. Guidi, and G. Patrizi, "A Critical Comparison of Alternative Risk Priority Numbers in Failure Modes, Effects, and Criticality Analysis," *IEEE Access*, vol. 7, pp. 92398–92409, 2019.

[52] A. Certa, M. Enea, G. M. Galante, and C. M. La Fata, "ELECTRE TRI-based approach to the failure modes classification on the basis of risk parameters: An alternative to the risk priority number," *Comput. Ind. Eng.*, vol. 108, pp. 100–110, Jun. 2017.

[53] S. M. Shrestha *et al.*, "Determination of Dominant Failure Modes Using FMECA on the Field Deployed c-Si Modules Under Hot-Dry Desert Climate," *IEEE J. Photovoltaics*, vol. 5, no. 1, pp. 174–182, Jan. 2015.

[54] A. Mohammadi and M. Tavakolan, "Construction project risk assessment using combined fuzzy and FMEA," in *2013 Joint IFSA World Congress and NAFIPS Annual Meeting (IFSA/NAFIPS)*, Jun. 2013, pp. 232–237.

[55] L. Gan, Y. Pang, Q. Liao, N.-C. Xiao, and H.-Z. Huang, "Fuzzy criticality assessment of FMECA for the SADA based on modified FWGM algorithm & centroid deffuzzification," in *2011 International Conference on Quality, Reliability, Risk, Maintenance, and Safety Engineering*, Jun. 2011, pp. 195–202.

[56] Yu-Mei Niu, Yu-Zhu He, Jian-Hong Li, and Xiao-Jun Zhao, "The optimization of RPN criticality analysis method in FMECA," in *2009 International Conference on Apperceiving Computing and Intelligence Analysis*, Oct. 2009, pp. 166–170.

[57] N. Sellappan and K. Palanikumar, "Modified Prioritization Methodology for Risk Priority Number in Failure Mode and Effects Analysis," *Int. J. Appl. Sci. Technol.*, vol. 03, no. 04, pp. 27–36, 2013.

[58] J. Wu, J. Tian, and T. Zhao, "Failure mode prioritization by improved RPN calculation method," in *2014 Reliability and Maintainability Symposium*, Jan. 2014, pp. 1–6.

[59] J. Braband, "Improving the risk priority number concept," *J. Syst. Saf.*, no. 2, pp. 21–23, 2003.

[60] K.-H. Chang, Y.-C. Chang, and P.-T. Lai, "Applying the concept of exponential approach to enhance the assessment capability of FMEA," *J. Intell. Manuf.*, vol. 25, no. 6, pp. 1413–1427, Dec. 2014.

[61] H. Akbarzade Khorshidi, I. Gunawan, and M. Y. Ibrahim, "Applying UGF Concept to Enhance the Assessment Capability of FMEA," *Qual. Reliab. Eng. Int.*, vol. 32, no. 3, pp. 1085–1093, Apr. 2016.

[62] T.-L. Nguyen, M.-H. Shu, and B.-M. Hsu, "Extended FMEA for Sustainable Manufacturing: An Empirical Study in the Non-Woven Fabrics Industry," *Sustainability*, vol. 8, no. 9, p. 939, Sep. 2016.

[63] G. Carmignani, "An integrated structural framework to cost-based FMECA: The priority-cost FMECA," *Reliab. Eng. Syst. Saf.*, vol. 94, no. 4, pp. 861–871, Apr. 2009.

[64]   F. Rezaei, M. Yarmohammadian, A. Haghshenas, A. Fallah, and M. Ferdosi, "Revised risk priority number in failure mode and effects analysis model from the perspective of healthcare system," *Int. J. Prev. Med.*, vol. 9, no. 1, p. 7, 2018.

[65]   Y. Tang, D. Zhou, and F. T. S. Chan, "AMWRPN: Ambiguity Measure Weighted Risk Priority Number Model for Failure Mode and Effects Analysis," *IEEE Access*, vol. 6, pp. 27103–27110, 2018.

[66]   K.-H. Chang, "Evaluate the orderings of risk for failure problems using a more general RPN methodology," *Microelectron. Reliab.*, vol. 49, no. 12, pp. 1586–1596, Dec. 2009.

[67]   R. Sawhney, K. Subburaman, C. Sonntag, P. Rao Venkateswara Rao, and C. Capizzi, "A modified FMEA approach to enhance reliability of lean systems," *Int. J. Qual. Reliab. Manag.*, vol. 27, no. 7, pp. 832–855, Aug. 2010.

[68]   R. Y. Trianto, M. R. Pahlevi, and B. Z. Bardani, "FMECA development in PLN TRANS-JBTB," in *2017 International Conference on High Voltage Engineering and Power Systems (ICHVEPS)*, Oct. 2017, vol. 2017-Janua, pp. 567–570.

[69]   J. M. Kuitche, R. Pan, and G. TamizhMani, "Investigation of Dominant Failure Mode(s) for Field-Aged Crystalline Silicon PV Modules Under Desert Climatic Conditions," *IEEE J. Photovoltaics*, vol. 4, no. 3, pp. 814–826, May 2014.

[70]   M. Giardina and M. Morale, "Safety study of an LNG regasification plant using an FMECA and HAZOP integrated methodology," *J. Loss Prev. Process Ind.*, vol. 35, pp. 35–45, 2015.

[71]   N. Xiao, H.-Z. Huang, Y. Li, L. He, and T. Jin, "Multiple failure modes analysis and weighted risk priority number evaluation in FMEA," *Eng. Fail. Anal.*, vol. 18, no. 4, pp. 1162–1170, Jun. 2011.

[72]   S. Kabir and Y. Papadopoulos, "A review of applications of fuzzy sets to safety and reliability engineering," *Int. J. Approx. Reason.*, vol. 100, pp. 29–55, Sep. 2018.

[73]   L. A. Zadeh, "Fuzzy sets," *Inf. Control*, vol. 8, no. 3, pp. 338–353, Jun. 1965.

[74]   M. G. Voskoglou, "Fuzzy Logic: History, Methodology and Applications to Education," *Sumerianz J. Educ. Linguist. Lit.*, vol. 1, no. 1, pp. 2617–1732, 2018, [Online]. Available: https://www.sumerianz.com/pdf-files/sjell1(1)10-18.pdf.

[75]   T. J. Ross, *Fuzzy Logic with Engineering Applications*, Third. John Wiley & Sons, 2010.

[76]   K.-Y. Cai, *Introduction to Fuzzy Reliability*. Kluwer Academic Publishers, 1996.

[77]   J. B. Bowles and C. E. Pelaez, "Application of fuzzy logic to reliability engineering," *Proc. IEEE*, vol. 83, no. 3, pp. 435–449, Mar. 1995.

[78]   A. C. F. Guimarães, C. M. F. Lapa, and M. D. L. Moreira, "Fuzzy methodology applied to Probabilistic Safety Assessment for digital system in nuclear power plants," *Nucl. Eng. Des.*, vol. 241, no. 9, pp. 3967–3976, Sep. 2011.

[79]   H. Yang and Z. Bai, "Risk Evaluation of Boiler Tube Using FMEA," in *2009 Sixth International Conference on Fuzzy Systems and Knowledge Discovery*, 2009, vol. 7, pp. 81–85.

[80]   Y.-S. Lee, H.-C. Kim, J.-M. Cha, and J.-O. Kim, "A new method for FMECA using expert system and fuzzy theory," in *2010 9th International Conference on Environment and Electrical Engineering*, 2010, no. 1, pp. 293–296.

[81] A. J. Sang, K. M. Tay, C. P. Lim, and S. Nahavandi, "Application of a Genetic-Fuzzy FMEA to Rainfed Lowland Rice Production in Sarawak: Environmental, Health, and Safety Perspectives," *IEEE Access*, vol. 6, no. iii, pp. 74628–74647, 2018.

[82] V. R. Renjith, M. Jose kalathil, P. H. Kumar, and D. Madhavan, "Fuzzy FMECA (failure mode effect and criticality analysis) of LNG storage facility," *J. Loss Prev. Process Ind.*, vol. 56, no. January, pp. 537–547, Nov. 2018.

[83] M. Hayati and M. Reza Abroshan, "Risk Assessment using Fuzzy FMEA (Case Study: Tehran Subway Tunneling Operations)," *Indian J. Sci. Technol.*, vol. 10, no. 9, pp. 1–9, 2017.

[84] J. B. Bowles and C. E. Peláez, "Fuzzy logic prioritization of failures in a system failure mode, effects and criticality analysis," *Reliab. Eng. Syst. Saf.*, vol. 50, no. 2, pp. 203–213, Jan. 1995.

[85] C. Dağsuyu, E. Göçmen, M. Narlı, and A. Kokangül, "Classical and fuzzy FMEA risk analysis in a sterilization unit," *Comput. Ind. Eng.*, vol. 101, pp. 286–294, Nov. 2016.

[86] L. Liu, S. Ma, Z. Wang, and P. Li, "Use-related risk analysis for medical devices based on improved FMEA," *Work*, vol. 41, pp. 5860–5865, 2012.

[87] M. Braglia, M. Frosolini, and R. Montanari, "Fuzzy criticality assessment model for failure modes and effects analysis," *Int. J. Qual. Reliab. Manag.*, vol. 20, no. 4, pp. 503–524, 2003.

[88] Zaili Yang, S. Bonsall, and Jin Wang, "Fuzzy Rule-Based Bayesian Reasoning Approach for Prioritization of Failures in FMEA," *IEEE Trans. Reliab.*, vol. 57, no. 3, pp. 517–528, 2008.

[89] M. S. Upadhya, "Fuzzy Logic-Based Failure Mode Effect and Criticality Analysis – A Case Study of Water Filters of a Company," *J. Comput. Appl.*, vol. VI, no. 4, pp. 89–93, 2013.

[90] M. Giardina, F. Castiglia, and E. Tomarchio, "Risk assessment of component failure modes and human errors using a new FMECA approach: application in the safety analysis of HDR brachytherapy," *J. Radiol. Prot.*, vol. 34, no. 4, pp. 891–914, Dec. 2014.

[91] T. R. Moss and J. Woodhouse, "Criticality analysis revisited," *Qual. Reliab. Eng. Int.*, vol. 15, no. 2, pp. 117–121, Mar. 1999.

[92] A. Pillay and J. Wang, "Modified failure mode and effects analysis using approximate reasoning," *Reliab. Eng. Syst. Saf.*, vol. 79, no. 1, pp. 69–85, Jan. 2003.

[93] H.-C. Liu, L. Liu, and Q.-L. Lin, "Fuzzy Failure Mode and Effects Analysis Using Fuzzy Evidential Reasoning and Belief Rule-Based Methodology," *IEEE Trans. Reliab.*, vol. 62, no. 1, pp. 23–36, Mar. 2013.

[94] A. C. F. Guimarães and C. M. F. Lapa, "Fuzzy FMEA applied to PWR chemical and volume control system," *Prog. Nucl. Energy*, vol. 44, no. 3, pp. 191–213, Jan. 2004.

[95] A. C. F. Guimarães and C. M. F. Lapa, "Hazard and operability study using approximate reasoning in light-water reactors passive systems," *Nucl. Eng. Des.*, vol. 236, no. 12, pp. 1256–1263, Jun. 2006.

[96] A. C. F. Guimarães and C. M. Franklin Lapa, "Effects analysis fuzzy inference system in nuclear problems using approximate reasoning," *Ann. Nucl. Energy*, vol. 31, no. 1, pp. 107–115, Jan. 2004.

[97] R. K. Sharma, D. Kumar, and P. Kumar, "Systematic failure mode effect analysis (FMEA) using fuzzy linguistic modelling," *Int. J. Qual. Reliab. Manag.*, vol. 22, no. 9, pp. 986–1004,

Dec. 2005.

[98] K. Xu, L. . Tang, M. Xie, S. . Ho, and M. . Zhu, "Fuzzy assessment of FMEA for engine systems," *Reliab. Eng. Syst. Saf.*, vol. 75, no. 1, pp. 17–29, Jan. 2002.

[99] T. L. Jee, K. M. Tay, and C. P. Lim, "A New Two-Stage Fuzzy Inference System-Based Approach to Prioritize Failures in Failure Mode and Effect Analysis," *IEEE Trans. Reliab.*, vol. 64, no. 3, pp. 869–877, Sep. 2015.

[100] E. H. Mamdani and S. Assilian, "An experiment in linguistic synthesis with a fuzzy logic controller," *Int. J. Man. Mach. Stud.*, vol. 7, no. 1, pp. 1–13, Jan. 1975.

[101] M. Sugeno and G. . Kang, "Structure identification of fuzzy model," *Fuzzy Sets Syst.*, vol. 28, no. 1, pp. 15–33, Oct. 1988.

[102] Y. Tsukamoto, "An approach to fuzzy reasoning method," in *Advances in fuzzy set theory and applications*, M. M. Gupta, R. K. Ragade, and R. R. Yager, Eds. Amsterdam: North-Holland Publishing Company, 1979, pp. 137–149.

[103] H. Gargama and S. K. Chaturvedi, "Criticality Assessment Models for Failure Mode Effects and Criticality Analysis Using Fuzzy Logic," *IEEE Trans. Reliab.*, vol. 60, no. 1, pp. 102–110, Mar. 2011.

[104] G. A. Keskin and C. Özkan, "An alternative evaluation of FMEA: Fuzzy ART algorithm," *Qual. Reliab. Eng. Int.*, vol. 25, no. 6, pp. 647–661, Oct. 2009.

[105] Y.-M. Wang, K.-S. Chin, G. K. K. Poon, and J.-B. Yang, "Risk evaluation in failure mode and effects analysis using fuzzy weighted geometric mean," *Expert Syst. Appl.*, vol. 36, no. 2, pp. 1195–1207, Mar. 2009.

[106] Z. Zhang and X. Chu, "Risk prioritization in failure mode and effects analysis under uncertainty," *Expert Syst. Appl.*, vol. 38, no. 1, pp. 206–214, Jan. 2011.

[107] H. Zhang, Y. Dong, I. Palomares-Carrascosa, and H. Zhou, "Failure mode and effect analysis in a linguistic context: A consensus-based multiattribute group decision-making approach," *IEEE Trans. Reliab.*, vol. 68, no. 2, pp. 566–582, 2019.

[108] C.-T. Chen, "Extensions of the TOPSIS for group decision-making under fuzzy environment," *Fuzzy Sets Syst.*, vol. 114, no. 1, pp. 1–9, Aug. 2000.

[109] M. Braglia, M. Frosolini, and R. Montanari, "Fuzzy TOPSIS approach for failure mode, effects and criticality analysis," *Qual. Reliab. Eng. Int.*, vol. 19, no. 5, pp. 425–443, Sep. 2003.

[110] S. Carpitella, A. Certa, J. Izquierdo, and C. M. La Fata, "A combined multi-criteria approach to support FMECA analyses: A real-world case," *Reliab. Eng. Syst. Saf.*, vol. 169, no. June 2016, pp. 394–402, Jan. 2018.

[111] M. Mangeli, A. Shahraki, and F. H. Saljooghi, "Improvement of risk assessment in the FMEA using nonlinear model, revised fuzzy TOPSIS, and support vector machine," *Int. J. Ind. Ergon.*, vol. 69, no. September 2018, pp. 209–216, Jan. 2019.

[112] M. Braglia, "MAFMA: multi-attribute failure mode analysis," *Int. J. Qual. Reliab. Manag.*, vol. 17, no. 9, pp. 1017–1033, Dec. 2000.

[113] A. C. Kutlu and M. Ekmekçioğlu, "Fuzzy failure modes and effects analysis by using fuzzy TOPSIS-based fuzzy AHP," *Expert Syst. Appl.*, vol. 39, no. 1, pp. 61–67, Jan. 2012.

[114] J. Li, H. Fang, and W. Song, "Failure Mode and Effects Analysis Using Variable Precision Rough Set Theory and TODIM Method," *IEEE Trans. Reliab.*, vol. 68, no. 4, pp. 1242–1256, Dec. 2019.

[115] Z. Wang, J.-M. Gao, R.-X. Wang, K. Chen, Z.-Y. Gao, and W. Zheng, "Failure Mode and Effects Analysis by Using the House of Reliability-Based Rough VIKOR Approach," *IEEE Trans. Reliab.*, vol. 67, no. 1, pp. 230–248, Mar. 2018.

[116] H.-C. Liu, Z. Li, W. Song, and Q. Su, "Failure Mode and Effect Analysis Using Cloud Model Theory and PROMETHEE Method," *IEEE Trans. Reliab.*, vol. 66, no. 4, pp. 1058–1072, Dec. 2017.

[117] H.-C. Liu, J.-X. You, P. Li, and Q. Su, "Failure Mode and Effect Analysis Under Uncertainty: An Integrated Multiple Criteria Decision Making Approach," *IEEE Trans. Reliab.*, vol. 65, no. 3, pp. 1380–1392, Sep. 2016.

[118] J. Braband and S. Griebel, "Engineering a Simple, Yet Rigorous, Risk Analysis Method," in *Proceedings of the 22nd International system Safety conference*, 2004, pp. 149–157.

[119] L. Hammadi, A. A. Ouahman, J. E. S. De Cursi, and A. Ibourk, "An approach based on FMECA methodology for a decision support tool for managing risk in Customs supply chain: A case study," in *2015 International Conference on Logistics, Informatics and Service Sciences (LISS)*, Jul. 2015, pp. 1–6.

[120] Y. Chen, L. Du, Y.-F. Li, H.-Z. Huang, and X. Li, "FMECA for aircraft electric system," in *2011 International Conference on Quality, Reliability, Risk, Maintenance, and Safety Engineering*, Jun. 2011, pp. 122–125.

[121] N. J. Lindsey, "An innovative Goddard Space Flight Center methodology for using FMECA as a risk assessment and communication tool," in *2016 Annual Reliability and Maintainability Symposium (RAMS)*, Jan. 2016, vol. 2016-April, pp. 1–9.

[122] IEC 60812, "Analysis techniques for system reliability - Procedure for failure mode and effects analysis (FMEA)." International Electrotechnical Commission, 2006.

[123] IEC 62506, "Methods for product accelerated testing." International Electrotechnical Commission, 2013.

[124] W. B. Nelson, *Accelerated Testing- Statistical Models, Test Plans, and Data Analysis*, Second. John Wiley & Sons, Inc, 2004.

[125] IEC 60749-23, "Semiconductor devices - Mechanical and climatic test methods – Part 23: High temperature operating life." International Electrotechnical Commission, 2004.

[126] D. Capriglione *et al.*, "Characterization of Inertial Measurement Units under Environmental Stress Screening," in *2020 IEEE International Instrumentation and Measurement Technology Conference (I2MTC)*, May 2020, pp. 1–6.

[127] M. Catelani and L. Ciani, "Experimental tests and reliability assessment of electronic ballast system," *Microelectron. Reliab.*, vol. 52, no. 9–10, pp. 1833–1836, Sep. 2012.

[128] JEDEC Solid State Technology, "Failure Mechanisms and Models for Semiconductor Devices." JEP122H, 2016.

[129] M. R. Piña-Monarrez, "Weibull analysis for normal/accelerated and fatigue random vibration test," *Qual. Reliab. Eng. Int.*, vol. 35, no. 7, pp. 2408–2428, Nov. 2019.

[130] IEC 61649, "Weibull analysis." International Electrotechnical Commission, 2008.

[131] L. Ciani and G. Guidi, "Application and analysis of methods for the evaluation of failure rate distribution parameters for avionics components," *Measurement*, vol. 139, pp. 258–269, 2019.

[132] A. Pandey, M. Singh, A. U. Sonawane, and P. S. Rawat, "FMEA Based Risk Assessment of Component Failure Modes in Industrial Radiography," *Int. J. Eng. Trends Technol.*, vol. 39, no. 4, pp. 216–225, Sep. 2016.

[133] S. Broggi *et al.*, "Application of failure mode and effects analysis (FMEA) to pretreatment phases in tomotherapy," *J. Appl. Clin. Med. Phys.*, vol. 14, no. 5, pp. 265–277, Sep. 2013.

[134] A. Jomde *et al.*, "Failure modes effects and criticality analysis of the linear compressor," *Mater. Today Proc.*, vol. 4, no. 9, pp. 10184–10188, 2017.

[135] Z. Bluvband, P. Grabov, and O. Nakar, "Expanded FMEA (EFMEA)," in *Annual Symposium Reliability and Maintainability, 2004 - RAMS*, 2004, pp. 31–36.

[136] Z. Bluvband and P. Grabov, "Failure analysis of FMEA," in *2009 Annual Reliability and Maintainability Symposium*, Jan. 2009, pp. 344–347.

[137] Youhu Zhao, Guicui Fu, Bo Wan, and Chun Pei, "An improved cost-based method of Risk Priority Number," in *Proceedings of the IEEE 2012 Prognostics and System Health Management Conference (PHM-2012 Beijing)*, May 2012, pp. 1–4.

[138] R. E. McDermott, R. J. MIkulak, and M. R. Beauregard, *The basics of FMEA*, Second. CRC Press: Taylor & Francis Group, 2008.

[139] D. Press, *Guidelines for Failure Mode and Effects Analysis (FMEA), for Automotive, Aerospace, and General Manufacturing Industries*. CRC Press, 2003.

[140] J. Sahno, E. Shevtshenko, T. Karaulova, and K. Tahera, "Framework for continuous improvement of production processes," *Eng. Econ.*, vol. 26, no. 2, pp. 169–180, Apr. 2015.

[141] S. Duicu and A.-E. Dumitrascu, "Researches concerning risk assessing using Pareto diagram for design process of technological processes," in *11th WSEAS International conference on Signal processing, computational geometry and artificial vision*, 2011, pp. 189–192.

[142] S. Woo, *Reliability Design of Mechanical Systems*. Cham: Springer International Publishing, 2017.

[143] R. F. Madvari *et al.*, "The Effect of Integrated Management System on Risk Priority Number of Environmental Assessment by FMEA Method in Yazd Persepolis Tile Factory," *J. Disaster Emerg. Res.*, vol. 1, no. 1, pp. 23–28, 2018.

[144] R. Kent, "Design quality management," in *Quality Management in Plastics Processing*, Elsevier, 2016, pp. 227–262.

[145] ISO/IEC 31010, "Risk management - Risk assessment techniques." ISO/TC 262 Risk Management Technical Committee, 2019.

[146] HDBK-217Plus, "Handbook of 217Plus - Reliability Prediction Models." Quanterion Solutions Incorporated, 2015.

[147] Telcordia SR-332, "Reliability Prediction Procedure for Electronic Equipment," no. 4. Telcordia Network Infrastructure Solutions (NIS), 2016.

[148] MIL-HDB-338B, "Electronic Reliability Design Handbook." US Department of Defense,

Washington DC, 1998.

[149] SN 29500, "Failure rates of components." Siemens, 2013.

[150] IEC 61709, "Electric components - Reliability - Reference conditions for failure ratesù and stress models for conversion." International Electrotechnical Commission, 2017.

[151] M. Catelani, L. Ciani, G. Patrizi, and M. Venzi, "Reliability allocation assessment using MEOWA method in complex redundant systems," in *2016 IEEE International Symposium on Systems Engineering (ISSE)*, Oct. 2016, pp. 1–5.

[152] A. Forcina, L. Silvestri, G. Di Bona, and A. Silvestri, "Reliability allocation methods: A systematic literature review," *Qual. Reliab. Eng. Int.*, vol. 36, no. 6, pp. 2085–2107, 2020.

[153] L. Silvestri, D. Falcone, and G. Belfiore, "Guidelines for reliability allocation methods," in *17th International Conference on Modeling and Applied Simulation*, 2018, pp. 191–198.

[154] M. Rausand, A. Barros, and A. Høyland, *System reliability theory. Models, Statistical Methods, and Applications.*, Third. John Wiley & Sons, Inc., 2021.

[155] D. B. Kececioglu, *Reliability Engineering Handbook*, vol. 1. DEStech Publications, 2002.

[156] MIL-HDBK-217F, "Military Handbook - Reliability Prediction of Electronic Equipment." US Department of Defense, Washington DC, 1991.

[157] W. H. Von Alven, *Reliability Engineering, prepared by the engineering and statistical staff of ARINC Research Corporation.* Prentice-Hall,Inc, 1964.

[158] J. M. Bridges, *RELIABILITY OF MILITARY ELECTRONIC EQUIPMENT. Report by Advisory Group on Reliability of Electronic Equipment (AGREE).* Washington, D. C.: Superintendent of documents, U. S. Government Printing Office, 1957.

[159] R. T. Anderson, *Reliability Design Handbook.* Chicago, Illinois: IIT Research Institute, 1976.

[160] V. J. Bracha, "The methods of reliability engineering," *Mach. Des.*, vol. 7, pp. 70–76, 1964.

[161] E. D. Karmiol, *Reliability apportionment. Preliminary Report EIAM 5, Task II.* 1965.

[162] H. E. Kuo, *Reliability assurance: Application for engineering and management*, Second. Chinese Society for Quality, 1999.

[163] R. Fullér and P. Majlender, "On obtaining minimal variability OWA operator weights," *Fuzzy Sets Syst.*, vol. 136, no. 2, pp. 203–215, Jun. 2003.

[164] T. Chen, S. Zheng, H. Liao, and J. Feng, "A Multi-attribute Reliability Allocation Method Considering Uncertain Preferences," *Qual. Reliab. Eng. Int.*, vol. 32, no. 7, pp. 2233–2244, Nov. 2016.

[165] C.-S. Liaw, Y.-C. Chang, K.-H. Chang, and T.-Y. Chang, "ME-OWA based DEMATEL reliability apportionment method," *Expert Syst. Appl.*, vol. 38, no. 8, pp. 9713–9723, 2011.

[166] F. De Felice, G. Di Bona, D. Falcone, and A. Silvestri, "New reliability allocation methodology: The integrated factors method," *Int. J. Oper. Quant. Manag.*, vol. 16, no. 1, pp. 67–85, 2010.

[167] V. Sriramdas, S. K. Chaturvedi, and H. Gargama, "Fuzzy arithmetic based reliability allocation approach during early design and development," *Expert Syst. Appl.*, vol. 41, no. 7, pp. 3444–3449, Jun. 2014.

[168] Z. S. Xu and Q. L. Da, "The ordered weighted geometric averaging operators," *Int. J. Intell. Syst.*, vol. 17, no. 7, pp. 709–716, Jul. 2002.

[169] K.-H. Chang, "A more general reliability allocation method using the hesitant fuzzy linguistic term set and minimal variance OWGA weights," *Appl. Soft Comput.*, vol. 56, pp. 589–596, Jul. 2017.

[170] G. Di Bona, A. Forcina, and A. Silvestri, "Critical Flow Method: A New Reliability Allocation Approach for a Thermonuclear System," *Qual. Reliab. Eng. Int.*, vol. 32, no. 5, pp. 1677–1691, Jul. 2016.

[171] K. O. Kim, Y. Yang, and M. J. Zuo, "A new reliability allocation weight for reducing the occurrence of severe failure effects," *Reliab. Eng. Syst. Saf.*, vol. 117, pp. 81–88, Sep. 2013.

[172] O. P. Yadav and X. Zhuang, "A practical reliability allocation method considering modified criticality factors," *Reliab. Eng. Syst. Saf.*, vol. 129, pp. 57–65, Sep. 2014.

[173] H. Guo, M. Jiang, and W. Wang, "A method for reliability allocation with confidence level," in *2014 Reliability and Maintainability Symposium*, Jan. 2014, no. 5, pp. 1–1.

[174] Z. Guangyan, Q. Tong, S. Yufeng, and H. Weiwei, "The Method of Mission Reliability Allocation for Complex System Based on Simulation," in *CTRQ 2011: The Fourth International Conference on Communication Theory, Reliability, and Quality of Service*, 2011, pp. 122–127.

[175] X. Yu, X. Wang, X. Liu, and Y. Wang, "Reliability reallocation for cost uncertainty of fuel cell vehicles via improved differential evolution algorithm," *Qual. Reliab. Eng. Int.*, vol. 36, no. 1, pp. 303–314, Feb. 2020.

[176] Y. Wang, R. C. M. Yam, M. J. Zuo, and P. Tse, "A comprehensive reliability allocation method for design of CNC lathes," *Reliab. Eng. Syst. Saf.*, vol. 72, no. 3, pp. 247–252, 2001.

[177] H. Yu, G. Zhang, Y. Ran, M. Li, D. Jiang, and Y. Chen, "A Reliability Allocation Method for Mechanical Product Based on Meta-Action," *IEEE Trans. Reliab.*, vol. 69, no. 1, pp. 373–381, Mar. 2020.

[178] Y. Wang, X. Jia, J. Zhao, and Y. Tian, "Improvement of agree allocation method," in *2009 8th International Conference on Reliability, Maintainability and Safety*, 2009, pp. 293–295.

[179] J. Boyd, "Allocation of reliability requirements: a new approach," in *Proceedings annual reliability and maintainability symposium*, 1992, pp. 5–6.

[180] Ronaldo R. Yager, "On Ordered Weighted Averaging Aggregation Operators in Multicriteria Decisionmaking," *IEEE Trans. Syst. Man. Cybern.*, vol. 18, no. 1, pp. 183–190, 1988.

[181] R. Fullér and P. Majlender, "An analytic approach for obtaining maximal entropy OWA operator weights," *Fuzzy Sets Syst.*, vol. 124, no. 1, pp. 53–57, Nov. 2001.

[182] Y.-C. Chang, K.-H. Chang, and C.-S. Liaw, "Innovative reliability allocation using the maximal entropy ordered weighted averaging method," *Comput. Ind. Eng.*, vol. 57, no. 4, pp. 1274–1281, Nov. 2009.

[183] A. Birolini, *Reliability Engineering*. Berlin, Heidelberg: Springer Berlin Heidelberg, 2017.

[184] H. Jia, G. Levitin, Y. Ding, and Y. Song, "Reliability analysis of standby systems with multi - state elements subject to constant transition rates," *Qual. Reliab. Eng. Int.*, vol. 35, pp. 318–328, 2019.

[185] M. Catelani, L. Ciani, A. Bartolini, G. Guidi, and G. Patrizi, "Standby Redundancy for Reliability Improvement of Wireless Sensor Network," in *2019 IEEE 5th International forum on Research and Technology for Society and Industry (RTSI)*, Sep. 2019, pp. 364–369.

[186] M. Venzi, S. Rossin, C. Michelassi, C. Accillaro, M. Catelani, and L. Ciani, "Improved FBD and RBD generation for system reliability assessment," 2013.

[187] M. Catelani, L. Ciani, G. Patrizi, and D. Galar, "Reliability improvement of wind turbine control system based on standby redundancy," 2019.

[188] M. Catelani, L. Ciani, G. Patrizi, and M. Venzi, "Reliability Allocation Procedures in Complex Redundant Systems," *IEEE Syst. J.*, vol. 12, no. 2, pp. 1182–1192, Jun. 2018.

[189] M. J. LuValle, B. G. Lefevre, and S. Kannan, *Design and Analysis of Accelerated Tests for Mission-Critical Reliability*, vol. 47, no. 2. CRC Press LLC, 2004.

[190] M. Catelani, L. Ciani, G. Guidi, and G. Patrizi, "Accelerated Testing and Reliability estimation of electronic boards for automotive applications," in *2021 IEEE International Workshop on Metrology for Automotive (MetroAutomotive)*, Jul. 2021, pp. 199–204.

[191] MIL-HDBK-344A - Notice 2, "Environmental Stress Screening (ESS) of electronic equipment." US Department of Defense, Washington DC, 2012.

[192] IEC 61163-2, "Reliability stress screening - Part 2: Components." International Electrotechnical Commission, 2020.

[193] D. B. Kececioglu and F.-B. Sun, *Environmental stress screening: its quantification, optimization and managementle*. Prentice Hall PTR, 1995.

[194] Thermotron Industries, "The Environmental Stress Screening Handbook." Holland, Michigan, USA, 1988.

[195] B. Peterson, "Environmental Stress Screening Tutorial," *Engineering*. Accolade Engineering Solutions.

[196] S. I. Chan, J. H. Kang, and J. S. Jang, "Reliability improvement of automotive electronics based on environmental stress screen methodology," *Microelectron. Reliab.*, vol. 53, no. 9–11, pp. 1235–1238, Sep. 2013.

[197] IEC 61078, "Reliability block diagram." International Electrotechnical Commission, 2016.

[198] G. D'Emilia, A. Gaspari, and E. Natale, "Sensor fusion for more accurate features in condition monitoring of mechatronic systems," in *2019 IEEE International Instrumentation and Measurement Technology Conference (I2MTC)*, May 2019, pp. 1–6.

[199] G. D'Emilia, A. Gaspari, E. Hohwieler, A. Laghmouchi, and E. Uhlmann, "Improvement of Defect Detectability in Machine Tools Using Sensor-based Condition Monitoring Applications," *Procedia CIRP*, vol. 67, pp. 325–331, 2018.

[200] M. Carratu, M. Ferro, A. Pietrosanto, and V. Paciello, "Smart Power Meter for the IoT," in *2018 IEEE 16th International Conference on Industrial Informatics (INDIN)*, Jul. 2018, pp. 514–519.

[201] D. Capriglione, M. Carratu, A. Pietrosanto, and P. Sommella, "Soft Sensors for Instrument Fault Accommodation in Semiactive Motorcycle Suspension Systems," *IEEE Trans. Instrum. Meas.*, vol. 69, no. 5, pp. 2367–2376, May 2020.

[202] Q. He, C. Zeng, X. He, X. Xu, and Z. Lin, "Calibrating accelerometers for space-stable inertial navigation systems at system level," *Measurement*, vol. 127, pp. 472–480, Oct. 2018.

[203] G. Dissanayake, S. Sukkarieh, E. Nebot, and H. Durrant-Whyte, "The aiding of a low-cost strapdown inertial measurement unit using vehicle model constraints for land vehicle applications," *IEEE Trans. Robot. Autom.*, vol. 17, no. 5, pp. 731–747, 2001.

[204] G. E. Kang and M. M. Gross, "Concurrent validation of magnetic and inertial measurement units in estimating upper body posture during gait," *Measurement*, vol. 82, pp. 240–245, 2016.

[205] S. Zihajehzadeh, Tien Jung Lee, Jung Keun Lee, R. Hoskinson, and E. J. Park, "Integration of MEMS Inertial and Pressure Sensors for Vertical Trajectory Determination," *IEEE Trans. Instrum. Meas.*, vol. 64, no. 3, pp. 804–814, Mar. 2015.

[206] J. Xu, H. He, F. Qin, and L. Chang, "A Novel Autonomous Initial Alignment Method for Strapdown Inertial Navigation System," *IEEE Trans. Instrum. Meas.*, vol. 66, no. 9, pp. 2274–2282, Sep. 2017.

[207] D. Capriglione *et al.*, "Experimental analysis of IMU under vibration," 2019, [Online]. Available: http://www.scopus.com/inward/record.url?eid=2-s2.0-85073277125&partnerID=MN8TOARS.

[208] B. Alandry, L. Latorre, F. Mailly, and P. Nouet, "A CMOS-MEMS Inertial Measurement Unit," in *2010 IEEE Sensors*, 2010, pp. 1033–1036.

[209] S. C. Shen, C. J. Chen, and H. J. Huang, "A new calibration method for MEMS inertial sensor module," in *2010 11th IEEE International Workshop on Advanced Motion Control (AMC)*, Mar. 2010, pp. 106–111.

[210] D. Capriglione *et al.*, "Analysis of MEMS devices under temperature stress test," in *2021 IEEE 8th International Workshop on Metrology for AeroSpace (MetroAeroSpace)*, Jun. 2021, pp. 63–68.

[211] L. Ciani, D. Galar, and G. Patrizi, "Improving context awareness reliability estimation for a wind turbine using an RBD model," in *2019 IEEE International Instrumentation and Measurement Technology Conference (I2MTC)*, May 2019, pp. 1–6.

[212] D. Galar, "Context driven maintenance: an eMaintenance approach," *Manag. Syst. Prod. Eng.*, vol. 3, no. 15, pp. 112–120, 2014.

[213] H. Skima, K. Medjaher, C. Varnier, E. Dedu, and J. Bourgeois, "A hybrid prognostics approach for MEMS: From real measurements to remaining useful life estimation," *Microelectron. Reliab.*, vol. 65, pp. 79–88, Oct. 2016.

[214] D. Capriglione *et al.*, "Development of a test plan and a testbed for performance analysis of MEMS-based IMUs under vibration conditions," *Measurement*, vol. 158, p. 107734, Jul. 2020.

[215] D. Capriglione *et al.*, "Experimental Analysis of Filtering Algorithms for IMU-Based Applications Under Vibrations," *IEEE Trans. Instrum. Meas.*, vol. 70, pp. 1–10, 2021.

[216] A. Ahari, A. Viehl, O. Bringmann, and W. Rosenstiel, "Mission profile-based assessment of semiconductor technologies for automotive applications," *Microelectron. Reliab.*, vol. 91, pp. 129–138, Dec. 2018.

[217] M. Bâzu, L. Gălăţeanu, V. Ilian, J. Loicq, S. Habraken, and J.-P. Collette, "Quantitative

Accelerated Life Testing of MEMS Accelerometers," *Sensors*, vol. 7, no. 11, pp. 2846–2859, Nov. 2007.

[218] M. Tariq Jan, N. Hisham Bin Hamid, M. H. Md Khir, K. Ashraf, and M. Shoaib, "Reliability and Fatigue Analysis in Cantilever-Based MEMS Devices Operating in Harsh Environments," *J. Qual. Reliab. Eng.*, vol. 2014, pp. 1–16, 2014.

[219] J. Iannacci, "Reliability of MEMS: A perspective on failure mechanisms, improvement solutions and best practices at development level," *Displays*, vol. 37, pp. 62–71, Apr. 2015.

[220] W. Merlijn van Spengen, "MEMS reliability from a failure mechanisms perspective," *Microelectron. Reliab.*, vol. 43, no. 7, pp. 1049–1060, Jul. 2003.

[221] Y. Huang, A. Sai Sarathi Vasan, R. Doraiswami, M. Osterman, and M. Pecht, "MEMS Reliability Review," *IEEE Trans. Device Mater. Reliab.*, vol. 12, no. 2, pp. 482–493, 2012.

[222] D. M. Tanner *et al.*, "MEMS Reliability : Infrastructure, Test structures, Experiments and Failure Modes," *Sandia Report*, no. January. Sandia National Laboratories, 2000.

[223] M. Tilli, T. Motooka, V.-M. Airaksinen, S. Franssila, M. Paulasto-Krockel, and V. Lindroos, *Handbook of Silicon Based MEMS Materials and Technologies*, Second. Elsevier, 2015.

[224] A. L. Hartzell, M. G. da Silva, and H. R. Shea, *MEMS Reliability*. Springer US, 2011.

[225] I. Marozau *et al.*, "Reliability assessment and failure mode analysis of MEMS accelerometers for space applications," *Microelectron. Reliab.*, vol. 88–90, no. July, pp. 846–854, Sep. 2018.

[226] L. X. Yu, L. Qin, and A. Da Bao, "Reliability prediction for MEMS accelerometer under random vibration testing," *J. Appl. Sci. Eng.*, vol. 18, no. 1, pp. 41–46, 2015.

[227] B.-J. Lwo, C.-L. Teng, Z.-Y. Huang, K.-H. Tseng, and K.-F. Tseng, "Thermal humidity reliability criterions for a typical TSV device," in *2016 Symposium on Design, Test, Integration and Packaging of MEMS/MOEMS (DTIP)*, May 2016, pp. 1–4.

[228] J.-D. Son, B.-H. Ahn, J.-M. Ha, and B.-K. Choi, "An availability of MEMS-based accelerometers and current sensors in machinery fault diagnosis," *Measurement*, vol. 94, pp. 680–691, Dec. 2016.

[229] G. Rezazadeh, A. Keyvani, and S. Jafarmadar, "On a MEMS based dynamic remote temperature sensor using transverse vibration of a bi-layer micro-cantilever," *Measurement*, vol. 45, no. 3, pp. 580–589, Apr. 2012.

[230] IEC 60068-2-64, "Environmental testing - Part 2: Tests - Test Fh: Vibration, broadband random and guidance." International Electrotechnical Commission, 2008.

[231] MIL-STD-810G, "Environmental Engineering Considerations and Laboratory Tests," no. October. US Department of Defense, Washington DC, 2008.

[232] JEDEC Solid State Technology, "JEDEC STANDARD: Vibration, Variable Frequency." JESD22-B103B.01, 2016.

[233] European Telecommunications Standards Institute, "Environmental Engineering (EE); Environmental conditions and environmental tests for telecommunications equipment; Part 2-5: Specification of environmental tests; Ground vehicle installations." ETSI EN 300 019-2-5, 2002.

[234] ISO 16750-3, "Road vehicles - Environmental conditions and testing for electrical and

electronic equipment - Part 3: Mechanical loads." International Organization for Standardization, 2003.

[235] ANSI C136.31, "American National Standard for Roadway And Area Lighting Equipment — Luminaire Vibration." American National Standards Institute, Inc., 2010.

[236] IEC 60068-2-6, "Environmental testing - Part 2-6: Tests - Test Fc: Vibration (sinusoidal)." International Electrotechnical Commission, 2009.

[237] Automotive Electronics Council, "Failure Mechanism Based Stress Test Qualification for Integrated Circuit." AEC - Q100 - Rev-H, 2014.

[238] IEC 60068-2-80, "Environmental testing Part 2-80: Tests - Test Fi: Vibration-Mixed mode." International Electrotechnical Commission, 2005.

[239] M. Carratù, A. Pietrosanto, P. Sommella, and V. Paciello, "Smart wearable devices for human exposure vibration measurements on two-wheel vehicles," *ACTA IMEKO*, vol. 9, no. 4, p. 121, Dec. 2020.

[240] M. Carratu, A. Pietrosanto, P. Sommella, and V. Paciello, "A wearable low-cost device for measurement of human exposure to transmitted vibration on motorcycle," in *2019 II Workshop on Metrology for Industry 4.0 and IoT (MetroInd4.0&IoT)*, 2019, pp. 329–333.

[241] IEC 60068-2-14, "Environmental testing Part 2-14: tests - Test N: Change of temperature." International Electrotechnical Commission, 2011.

[242] IEC 60068-2-38, "Environmental testing Part 2: Tests - Test Z/AD: Composite temperature/humidity cyclic test." International Electrotechnical Commission, 2021.

[243] JEDEC Solid State Technology, "JEDEC STANDARD: Temperature cycling." JESD22-A104E, 2014.

[244] ISO 16750-4, "Road vehicles - Environmental conditions and testing for electrical and electronic equipment - Part 4: Climatic loads." International Organization for Standardization, 2010.

[245] IEST-RP-PR003.1, "HALT and HASS." Institute of Environmental Sciences and Technology - Product Reliability Division, 2012.

[246] D. Capriglione *et al.*, "Characterization of Inertial measurement units using sine-on-random vibration test," *Meas. Sensors*, vol. 18, p. 100104, Dec. 2021.

[247] D. Capriglione *et al.*, "Performance Analysis of MEMS-based Inertial Measurement Units in terrestrial vehicles," *Measurement*, vol. 186, p. 110237, Oct. 2021.

[248] Hossam-E-Haider, "A low cost MEMS and complementary filter based attitude heading reference system (AHRS) for low speed aircraft," in *3rd International Conference on Electrical Engineering and Information Communication Technology (ICEEICT)*, 2016.

[249] Y. Pititeeraphab, T. Jusing, P. Chotikunnan, N. Thongpance, W. Lekdee, and A. Teerasoradech, "The effect of average filter for complementary filter and Kalman filter based on measurement angle," in *2016 9th Biomedical Engineering International Conference (BMEiCON)*, Dec. 2016, pp. 1–4.

[250] D. Tomaszewski, J. Rapiński, and R. Pelc-Mieczkowska, "Concept of AHRS Algorithm Designed for Platform Independent Imu Attitude Alignment," *Reports Geod. Geoinformatics*, vol. 104, no. 1, pp. 33–47, Dec. 2017.

[251] L. Huchel, T. C. Krause, T. Lugowski, S. B. Leeb, and J. Helsen, "Chasing the Cut: A Measurement Approach for Machine Tool Condition Monitoring," *IEEE Trans. Instrum. Meas.*, vol. 70, pp. 1–10, 2021.

[252] L. Lu, Y. He, Y. Ruan, and W. Yuan, "Wind Turbine Planetary Gearbox Condition Monitoring Method Based on Wireless Sensor and Deep Learning Approach," *IEEE Trans. Instrum. Meas.*, vol. 70, pp. 1–16, 2021.

[253] M. A. Hmida and A. Braham, "An On-Line Condition Monitoring System for Incipient Fault Detection in Double-Cage Induction Motor," *IEEE Trans. Instrum. Meas.*, vol. 67, no. 8, pp. 1850–1858, Aug. 2018.

[254] H. M. Hashemian, "State-of-the-Art Predictive Maintenance Techniques," *IEEE Trans. Instrum. Meas.*, vol. 60, no. 1, pp. 226–236, Jan. 2011.

[255] H. Tarzamni, E. Babaei, F. P. Esmaeelnia, P. Dehghanian, S. Tohidi, and M. B. B. Sharifian, "Analysis and Reliability Evaluation of a High Step-Up Soft Switching Push–Pull DC–DC Converter," *IEEE Trans. Reliab.*, vol. 69, no. 4, pp. 1376–1386, Dec. 2020.

[256] D. Newell and M. Duffy, "Review of Power Conversion and Energy Management for Low-Power, Low-Voltage Energy Harvesting Powered Wireless Sensors," *IEEE Trans. Power Electron.*, vol. 34, no. 10, pp. 9794–9805, Oct. 2019.

[257] F. Corti, A. Reatti, G. Patrizi, L. Ciani, M. Catelani, and M. K. Kazimierczuk, "Probabilistic evaluation of power converters as support in their design," *IET Power Electron.*, vol. 13, no. 19, pp. 4542–4550, Dec. 2020.

[258] S. Saponara and G. Ciarpi, "Electrical, Electromagnetic, and Thermal Measurements of 2-D and 3-D Integrated DC/DC Converters," *IEEE Trans. Instrum. Meas.*, vol. 67, no. 5, pp. 1078–1090, May 2018.

[259] S.-Y. Kim *et al.*, "Design of a High Efficiency DC–DC Buck Converter With Two-Step Digital PWM and Low Power Self-Tracking Zero Current Detector for IoT Applications," *IEEE Trans. Power Electron.*, vol. 33, no. 2, pp. 1428–1439, Feb. 2018.

[260] G. Ortiz, M. G. Leibl, J. E. Huber, and J. W. Kolar, "Design and Experimental Testing of a Resonant DC–DC Converter for Solid-State Transformers," *IEEE Trans. Power Electron.*, vol. 32, no. 10, pp. 7534–7542, Oct. 2017.

[261] R. A. Mastromauro, M. C. Poliseno, S. Pugliese, F. Cupertino, and S. Stasi, "SiC MOSFET Dual Active Bridge converter for harsh environment applications in a more-electric-aircraft," in *2015 International Conference on Electrical Systems for Aircraft, Railway, Ship Propulsion and Road Vehicles (ESARS)*, Mar. 2015, vol. 2015-May, pp. 1–6.

[262] S. Saponara and G. Ciarpi, "IC Design and Measurement of an Inductorless 48 V DC/DC Converter in Low-Cost CMOS Technology Facing Harsh Environments," *IEEE Trans. Circuits Syst. I Regul. Pap.*, vol. 65, no. 1, pp. 380–393, Jan. 2018.

[263] W. Van De Sande, S. Ravyts, O. Alavi, P. Nivelle, J. Driesen, and M. Daenen, "The Sensitivity of an Electro-Thermal Photovoltaic DC–DC Converter Model to the Temperature Dependence of the Electrical Variables for Reliability Analyses," *Energies*, vol. 13, no. 11, p. 2865, Jun. 2020.

[264] R. Wang *et al.*, "A High-Temperature SiC Three-Phase AC–DC Converter Design for >$100 ^{\circ}$C Ambient Temperature," *IEEE Trans. Power Electron.*, vol. 28, no. 1, pp. 555–572, Jan. 2013.

[265] Y. Bin, C. Hui, X. Qingzhong, and L. Xiaowei, "Study of highly accelerated thermal cycling test for DC/DC converter," in *2015 16th International Conference on Electronic Packaging Technology (ICEPT)*, Aug. 2015, pp. 1070–1074.

[266] L. Ciani, M. Catelani, A. Bartolini, G. Guidi, and G. Patrizi, "Influence of Raised Ambient Temperature on a Sensor Node Using Step-Stress Test," *IEEE Trans. Instrum. Meas.*, vol. 69, no. 12, pp. 9549–9556, Dec. 2020.

[267] H. Kosai, J. Scofield, S. McNeal, B. Jordan, and B. Ray, "Design and Performance Evaluation of a 200 °C Interleaved Boost Converter," *IEEE Trans. Power Electron.*, vol. 28, no. 4, pp. 1691–1699, Apr. 2013.

[268] B. S. Moss, R. R. Boudreaux, and R. M. Nelms, "Low temperature operation of a boost converter [for space power]," in *IECEC 96. Proceedings of the 31st Intersociety Energy Conversion Engineering Conference*, 1985, vol. 1, no. March, pp. 599–604.

[269] IEST-RP-PR001.2, "Management and Technical Guidelines for the Environmental Stress Screening (ESS) Process." Institute of Environmental Sciences and Technology - Product Reliability Division, 2016.

[270] H. Mou, W. Hu, Y. Sun, and G. Zhao, "A comparison and case studies of electronic product reliability prediction methods based on handbooks," in *2013 International Conference on Quality, Reliability, Risk, Maintenance, and Safety Engineering (QR2MSE)*, 2013, pp. 112–115.

[271] G. Graditi, G. Adinolfi, V. Palladino, and M. Valenti, "Reliability assessment of Modular Multilevel Converters by industrial and military prediction models," in *2019 8th International Conference on Renewable Energy Research and Applications (ICRERA)*, 2019, pp. 780–785.

[272] JEDEC Solid State Technology, "JEDEC STANDARD: Cycled Temperature-Humidity-Bias Life Test." JESD22-A100C, 2007, [Online]. Available: http://www.jedec.org/sites/default/files/docs/22a100c.pdf.

[273] MIL-STD-883L, "Test method Standard: Environmental Test methods for Microcircuits." US Department of Defense, 2019.

[274] IEC 60068-2-39, "Environmental testing - Part 2-39: Tests - Tests and guidance: Combined temperature or temperature and humidity with low air pressure tests." International Electrotechnical Commission, 2015.

[275] G. Kohlrusz, K. Enisz, B. Csomós, and D. Fodor, "Electric energy converter development and diagnostics in mixed-signal simulation environment," *ACTA IMEKO*, vol. 7, no. 1, p. 20, Apr. 2018.

[276] I. Bodini, M. Lancini, S. Pasinetti, and D. Vetturi, "Techniques for on-board vibrational passenger comfort monitoring in public transport," *ACTA IMEKO*, vol. 3, no. 4, p. 32, 2014.

[277] A. Reatti, M. K. Kazimierczuk, M. Catelani, and L. Ciani, "Monitoring and field data acquisition system for hybrid static concentrator plant," *Measurement*, vol. 98, pp. 384–392, Feb. 2017.

[278] P. Gangsar and R. Tiwari, "A support vector machine based fault diagnostics of Induction motors for practical situation of multi-sensor limited data case," *Measurement*, vol. 135, pp. 694–711, Mar. 2019.

[279] V. De Vita, G. D. L. Di Leo, G. Fabbrocini, C. Liguori, A. Paolillo, and P. Sommella,

"Statistical Techniques Applied to the Automatic Diagnosis of Dermoscopic Images," *ACTA IMEKO*, vol. 1, no. 1, p. 7, Jul. 2012.

[280] E. Petritoli, F. Leccese, M. Botticelli, S. Pizzuti, and F. Pieroni, "A RAMS analysis for a precision scale-up configuration of "Smart Street" pilot site: an Industry 4.0 Case Study," *ACTA IMEKO*, vol. 8, no. 2, p. 3, Jun. 2019.

[281] A. Ayachit, A. Reatti, and M. K. Kazimierczuk, "Small-signal modeling of PWM dual-SEPIC dc-dc converter by circuit averaging technique," in *IECON 2016 - 42nd Annual Conference of the IEEE Industrial Electronics Society*, Oct. 2016, pp. 3606–3611.

[282] F. Corti, F. Grasso, A. Reatti, A. Ayachit, D. K. Saini, and M. K. Kazimierczuk, "Design of class-E ZVS inverter with loosely-coupled transformer at fixed coupling coefficient," in *IECON 2016 - 42nd Annual Conference of the IEEE Industrial Electronics Society*, Oct. 2016, pp. 5627–5632.

[283] Y. Wang, Z. Zhu, H. Song, and K. Shi, "Wind turbine gearbox condition monitoring based on extreme gradient boosting," in *IECON 2017 - 43rd Annual Conference of the IEEE Industrial Electronics Society*, Oct. 2017, vol. 2017-Janua, pp. 6017–6023.

[284] K. Singh, H. Malik, and R. Sharma, "Condition monitoring of wind turbine gearbox using electrical signatures," in *2017 International conference on Microelectronic Devices, Circuits and Systems (ICMDCS)*, Aug. 2017, vol. 2017-Janua, pp. 1–6.

[285] J. Moubray, *Reliability Centered Maintenance*, Second. Butterworth-Heinemann, 1997.

[286] N. B. Bloom, *Reliability Centered Maintenance: Implementation made simple.* McGraw-Hill Companies, 2006.

[287] NASA Headquarters, "Reliability Centered Maintenance guide for facilities and collateral equipment." 2000.

[288] IEC 60300-3-11, "Dependability management – Part 3-11 - Application guide – Reliability centred maintenance." International Electrotechnical Commission, 2009.

[289] M. C. Magro, P. Pinceti, M. Antonelli, E. De Paola, P. Firpo, and E. Marino, "CBM for a fleet of railway vehicles: Infrastructure and algorithms," *ACTA IMEKO*, vol. 5, no. 4, pp. 56–63, 2016.

[290] D. Seneviratne, L. Ciani, M. Catelani, and D. Galar, "Smart maintenance and inspection of linear assets: An Industry 4.0 approach," *ACTA IMEKO*, vol. 7, no. 1, p. 50, Apr. 2018.

[291] E. De Francesco, E. De Francesco, R. De Francesco, F. Leccese, and M. Cagnetti, "A proposal to update LSA databases for an operational availability based on autonomic logistic," in *2015 IEEE Metrology for Aerospace (MetroAeroSpace)*, Jun. 2015, pp. 38–43.

[292] E. De Francesco, R. De Francesco, F. Leccese, and M. Cagnetti, "A proposal to improve the system life cycle support of composites structures mapping zonal testing data on LSA Databases," in *2016 IEEE Metrology for Aerospace (MetroAeroSpace)*, 2016, pp. 151–155.

[293] H. Soltanali, A. Rohani, M. H. Abbaspour-Fard, A. Parida, and J. T. Farinha, "Development of a risk-based maintenance decision making approach for automotive production line," *Int. J. Syst. Assur. Eng. Manag.*, no. December, Dec. 2019.

[294] K. Fischer, F. Besnard, and L. Bertling, "Reliability-Centered Maintenance for Wind Turbines Based on Statistical Analysis and Practical Experience," *IEEE Trans. Energy*

Convers., vol. 27, no. 1, pp. 184–195, Mar. 2012.

[295] A. Pandey and P. M. Sonwane, "Implementation of Reliability Centred Maintenance for transformer," in *2016 International Conference on Automatic Control and Dynamic Optimization Techniques (ICACDOT)*, Sep. 2016, pp. 578–581.

[296] M. Rafiei, M.-H. Khooban, M. A. Igder, and J. Boudjadar, "A Novel Approach to Overcome the Limitations of Reliability Centered Maintenance Implementation on the Smart Grid Distance Protection System," *IEEE Trans. Circuits Syst. II Express Briefs*, vol. 67, no. 2, pp. 320–324, Feb. 2020.

[297] K. Tirapong and S. Titti, "Reliability improvement of distribution system using Reliability Centered Maintenance," in *2014 IEEE PES T&D Conference and Exposition*, 2014, pp. 1–5.

[298] H. A. Khorshidi, I. Gunawan, and M. Y. Ibrahim, "Reliability centered maintenance using system dynamics approach," in *2015 IEEE International Conference on Industrial Technology (ICIT)*, Mar. 2015, vol. 2015-June, no. June, pp. 1932–1936.

[299] Z. Chen *et al.*, "Mission Reliability-Oriented Selective Maintenance Optimization for Intelligent Multistate Manufacturing Systems With Uncertain Maintenance Quality," *IEEE Access*, vol. 7, pp. 109804–109816, 2019.

[300] J. T. Selvik and T. Aven, "A framework for reliability and risk centered maintenance," *Reliab. Eng. Syst. Saf.*, vol. 96, no. 2, pp. 324–331, Feb. 2011.

[301] K. Zakikhani, F. Nasiri, and T. Zayed, "Availability-based reliability-centered maintenance planning for gas transmission pipelines," *Int. J. Press. Vessel. Pip.*, vol. 183, no. October 2019, p. 104105, Jun. 2020.

[302] B. Yssaad and A. Abene, "Rational Reliability Centered Maintenance Optimization for power distribution systems," *Int. J. Electr. Power Energy Syst.*, vol. 73, pp. 350–360, Dec. 2015.

[303] D. He, X. Zhang, C. Ge, and E. Chen, "A Novel Reliability-Centred Opportunistic Maintenance Strategy for Metro Train Complex System," *IEEE Intell. Transp. Syst. Mag.*, no. September 2020, pp. 0–0, 2020.

[304] P. Afzali, F. Keynia, and M. Rashidinejad, "A new model for reliability-centered maintenance prioritisation of distribution feeders," *Energy*, vol. 171, pp. 701–709, Mar. 2019.

[305] S. H. A. Rahmati, A. Ahmadi, and B. Karimi, "Multi-objective evolutionary simulation based optimization mechanism for a novel stochastic reliability centered maintenance problem," *Swarm Evol. Comput.*, vol. 40, no. May 2017, pp. 255–271, Jun. 2018.

[306] D. Piasson, A. A. P. Bíscaro, F. B. Leão, and J. R. S. Mantovani, "A new approach for reliability-centered maintenance programs in electric power distribution systems based on a multiobjective genetic algorithm," *Electr. Power Syst. Res.*, vol. 137, pp. 41–50, Aug. 2016.

[307] J.-H. Heo *et al.*, "A Reliability-Centered Approach to an Optimal Maintenance Strategy in Transmission Systems Using a Genetic Algorithm," *IEEE Trans. Power Deliv.*, vol. 26, no. 4, pp. 2171–2179, Oct. 2011.

[308] M. Caciotta *et al.*, "A first study on prognostic system for electric engines based on Envelope Analysis," in *2014 IEEE Metrology for Aerospace (MetroAeroSpace)*, 2014, pp. 362–366.

[309] F. Besnard and L. Bertling, "An Approach for Condition-Based Maintenance Optimization Applied to Wind Turbine Blades," *IEEE Trans. Sustain. Energy*, vol. 1, no. 2, pp. 77–83,

Jul. 2010.

[310] ISO 14224, "Petroleum, petrochemical and natural gas industries — Collection and exchange of reliability and maintenance data for equipment." International Organization for Standardization, 2016.

[311] M. Catelani, L. Ciani, G. Patrizi, and D. Galar, "Reliability improvement of wind turbine control system based on standby redundancy," in *2019 International Symposium on Systems Engineering (ISSE)*, Oct. 2019, pp. 1–5.

[312] L. Ciani, D. Galar, and G. Patrizi, "Improving context awareness reliability estimation for a wind turbine using an RBD model," in *2019 IEEE International Instrumentation and Measurement Technology Conference (I2MTC)*, May 2019, pp. 1–6.

[313] M. Modarres, M. Amiri, and C. Jackson, "Overview of Probabilistic Physics-of-Failure Approach to Reliability," in *Probabilistic Physics of Failure Approach to Reliability*, Second., Hoboken, NJ, USA: John Wiley & Sons, Inc., 2017, pp. 1–11.

[314] Y. Huang and C. Gühmann, "Wireless Sensor Network for Temperatures Estimation in an Asynchronous Machine Using a Kalman Filter," *ACTA IMEKO*, vol. 7, no. 1, p. 5, 2018.

[315] L. D'Alvia, E. Palermo, S. Rossi, and Z. Del Prete, "Validation of a low-cost wireless sensors node for museum environmental monitoring," *ACTA IMEKO*, vol. 6, no. 3, p. 45, Sep. 2017.

[316] Karthika K.C, "Wireless mesh network: A survey," in *2016 International Conference on Wireless Communications, Signal Processing and Networking (WiSPNET)*, Mar. 2016, pp. 1966–1970.

[317] A. Hać, *Wireless Sensor Network Designs*. Chichester, UK: John Wiley & Sons, Ltd, 2003.

[318] Y. Zhang, L. Jijun, and H. Hu, *Wireless Mesh Networking: Architectures, Protocols and Standards*. Tailor & Francis Group, 2007.

[319] V. Pasquali, G. D'Alessandro, R. Gualtieri, and F. Leccese, "A new data logger based on Raspberry-Pi for Arctic Notostraca locomotion investigations," *Measurement*, vol. 110, pp. 249–256, Nov. 2017.

[320] V. Pasquali *et al.*, "Monitoring and Analyzing of Circadian and Ultradian Locomotor Activity Based on Raspberry-Pi," *Electronics*, vol. 5, no. 4, p. 58, Sep. 2016.

[321] L. Ciani, A. Bartolini, G. Guidi, and G. Patrizi, "Condition monitoring of wind farm based on wireless mesh network," 2019.

[322] M. Catelani, L. Ciani, A. Bartolini, G. Guidi, and G. Patrizi, "Standby redundancy for reliability improvement of wireless sensor network," 2019.

[323] V. J. Hodge, S. O'Keefe, M. Weeks, and A. Moulds, "Wireless Sensor Networks for Condition Monitoring in the Railway Industry: A Survey," *IEEE Trans. Intell. Transp. Syst.*, vol. 16, no. 3, pp. 1088–1106, Jun. 2015.

[324] J. Guo, Z. Li, and M. Li, "A Review on Prognostics Methods for Engineering Systems," *IEEE Trans. Reliab.*, vol. 69, no. 3, pp. 1110–1129, Sep. 2020.

[325] A. Diez-Olivan, J. Del Ser, D. Galar, and B. Sierra, "Data fusion and machine learning for industrial prognosis: Trends and perspectives towards Industry 4.0," *Inf. Fusion*, vol. 50, no. October 2018, pp. 92–111, Oct. 2019.

[326] M. Baur, P. Albertelli, and M. Monno, "A review of prognostics and health management of machine tools," *Int. J. Adv. Manuf. Technol.*, vol. 107, no. 5–6, pp. 2843–2863, Mar. 2020.

[327] G. D'Emilia, A. Gaspari, D. Lancione, and E. Natale, "Prediction of the remaining useful life of mechatronic systems, using internal sensors," in *2020 IEEE International Workshop on Metrology for Industry 4.0 & IoT*, Jun. 2020, pp. 75–79.

[328] M. Rezamand, M. Kordestani, R. Carriveau, D. S. K. Ting, M. E. Orchard, and M. Saif, "Critical Wind Turbine Components Prognostics: A Comprehensive Review," *IEEE Trans. Instrum. Meas.*, vol. 69, no. 12, pp. 9306–9328, Dec. 2020.

[329] H. Hanachi, C. Mechefske, J. Liu, A. Banerjee, and Y. Chen, "Performance-Based Gas Turbine Health Monitoring, Diagnostics, and Prognostics: A Survey," *IEEE Trans. Reliab.*, vol. 67, no. 3, pp. 1340–1363, Sep. 2018.

[330] V. Atamuradov, K. Medjaher, F. Camci, P. Dersin, and N. Zerhouni, "Railway Point Machine Prognostics Based on Feature Fusion and Health State Assessment," *IEEE Trans. Instrum. Meas.*, vol. 68, no. 8, pp. 2691–2704, Aug. 2019.

[331] C. Bhargava *et al.*, "Review of Health Prognostics and Condition Monitoring of Electronic Components," *IEEE Access*, vol. 8, pp. 75163–75183, 2020.

[332] S. Kumar *et al.*, "A Comprehensive Review of Condition Based Prognostic Maintenance (CBPM) for Induction Motor," *IEEE Access*, vol. 7, pp. 90690–90704, 2019.

[333] W. Mao, J. He, and M. J. Zuo, "Predicting Remaining Useful Life of Rolling Bearings Based on Deep Feature Representation and Transfer Learning," *IEEE Trans. Instrum. Meas.*, vol. 69, no. 4, pp. 1594–1608, Apr. 2020.

[334] H. Meng and Y.-F. Li, "A review on prognostics and health management (PHM) methods of lithium-ion batteries," *Renew. Sustain. Energy Rev.*, vol. 116, no. September, p. 109405, 2019.

[335] I. Sanz-Gorrachategui *et al.*, "Remaining Useful Life Estimation for LFP Cells in Second-Life Applications," *IEEE Trans. Instrum. Meas.*, vol. 70, pp. 1–10, 2021.

[336] X. Hu, L. Xu, X. Lin, and M. Pecht, "Battery Lifetime Prognostics," *Joule*, vol. 4, no. 2, pp. 310–346, Feb. 2020.

[337] A. Guha and A. Patra, "Online Estimation of the Electrochemical Impedance Spectrum and Remaining Useful Life of Lithium-Ion Batteries," *IEEE Trans. Instrum. Meas.*, vol. 67, no. 8, pp. 1836–1849, Aug. 2018.

[338] C. Okoh, R. Roy, J. Mehnen, and L. Redding, "Overview of Remaining Useful Life Prediction Techniques in Through-life Engineering Services," *Procedia CIRP*, vol. 16, pp. 158–163, 2014.

[339] X.-S. Si, W. Wang, C.-H. Hu, and D.-H. Zhou, "Remaining useful life estimation – A review on the statistical data driven approaches," *Eur. J. Oper. Res.*, vol. 213, no. 1, pp. 1–14, 2011.

[340] L. Wu, X. Fu, and Y. Guan, "Review of the Remaining Useful Life Prognostics of Vehicle Lithium-Ion Batteries Using Data-Driven Methodologies," *Appl. Sci.*, vol. 6, no. 6, p. 166, 2016.

[341] D. Liu, J. Pang, J. Zhou, Y. Peng, and M. Pecht, "Prognostics for state of health estimation of lithium-ion batteries based on combination Gaussian process functional regression," *Microelectron. Reliab.*, vol. 53, no. 6, pp. 832–839, Jun. 2013.

[342] J. Liu and Z. Chen, "Remaining Useful Life Prediction of Lithium-Ion Batteries Based on

Health Indicator and Gaussian Process Regression Model," *IEEE Access*, vol. 7, pp. 39474–39484, 2019.

[343] T. Li, H. Pei, Z. Pang, X. Si, and J. Zheng, "A Sequential Bayesian Updated Wiener Process Model for Remaining Useful Life Prediction," *IEEE Access*, vol. 8, pp. 5471–5480, 2020.

[344] X. Xu, S. Tang, C. Yu, J. Xie, X. Han, and M. Ouyang, "Remaining Useful Life Prediction of Lithium-ion Batteries Based on Wiener Process Under Time-Varying Temperature Condition," *Reliab. Eng. Syst. Saf.*, p. 107675, Apr. 2021.

[345] S. Wang, L. Shang, Z. Li, H. Deng, and Y. Ma, "Lithium-ion battery security guaranteeing method study based on the state of charge estimation," *Int. J. Electrochem. Sci.*, vol. 10, pp. 5130–5151, 2015.

[346] Z. He, Z. Yang, X. Cui, and E. Li, "A Method of State-of-Charge Estimation for EV Power Lithium-Ion Battery Using a Novel Adaptive Extended Kalman Filter," *IEEE Trans. Veh. Technol.*, vol. 69, no. 12, pp. 14618–14630, Dec. 2020.

[347] L. He and D. Guo, "A Threshold Extend Kalman Filter Algorithm for State of Charge Estimation of Lithium-Ion Batteries in Electric Vehicles," *IEEE J. Emerg. Sel. Top. Ind. Electron.*, vol. 9735, no. c, pp. 1–1, 2020.

[348] J. Meng, G. Luo, and F. Gao, "Lithium Polymer Battery State-of-Charge Estimation Based on Adaptive Unscented Kalman Filter and Support Vector Machine," *IEEE Trans. Power Electron.*, vol. 31, no. 3, pp. 2226–2238, Mar. 2016.

[349] X. Li, L. Peng, L. Gao, D. Bi, X. Xie, and Y. Xie, "A Robust Hybrid Filtering Method for Accurate Battery Remaining Useful Life Prediction," *IEEE Access*, vol. 7, pp. 57843–57856, 2019.

[350] M. Ahwiadi and W. Wang, "An Enhanced Mutated Particle Filter Technique for System State Estimation and Battery Life Prediction," *IEEE Trans. Instrum. Meas.*, vol. 68, no. 3, pp. 923–935, Mar. 2019.

[351] Z. Liu, G. Sun, S. Bu, J. Han, X. Tang, and M. Pecht, "Particle Learning Framework for Estimating the Remaining Useful Life of Lithium-Ion Batteries," *IEEE Trans. Instrum. Meas.*, vol. 66, no. 2, pp. 280–293, Feb. 2017.

[352] D. Liu, X. Yin, Y. Song, W. Liu, and Y. Peng, "An On-Line State of Health Estimation of Lithium-Ion Battery Using Unscented Particle Filter," *IEEE Access*, vol. 6, pp. 40990–41001, 2018.

[353] X. Cong, C. Zhang, J. Jiang, W. Zhang, Y. Jiang, and X. Jia, "An Improved Unscented Particle Filter Method for Remaining Useful Life Prognostic of Lithium-ion Batteries With Li(NiMnCo)O 2 Cathode With Capacity Diving," *IEEE Access*, vol. 8, pp. 58717–58729, 2020.

[354] R. Wang and H. Feng, "Lithium-ion batteries remaining useful life prediction using Wiener process and unscented particle filter," *J. Power Electron.*, vol. 20, no. 1, pp. 270–278, 2020.

[355] F. Li and J. Xu, "A new prognostics method for state of health estimation of lithium-ion batteries based on a mixture of Gaussian process models and particle filter," *Microelectron. Reliab.*, vol. 55, no. 7, pp. 1035–1045, Jun. 2015.

[356] L. Chen, J. An, H. Wang, M. Zhang, and H. Pan, "Remaining useful life prediction for lithium-ion battery by combining an improved particle filter with sliding-window gray

model," *Energy Reports*, vol. 6, pp. 2086–2093, Nov. 2020.

[357] X. Hu, X. Yang, F. Feng, K. Liu, and X. Lin, "A Particle Filter and Long Short-Term Memory Fusion Technique for Lithium-Ion Battery Remaining Useful Life Prediction," *J. Dyn. Syst. Meas. Control*, vol. 143, no. 6, pp. 1–13, Jun. 2021.

[358] L. Chen *et al.*, "Remaining Useful Life Prediction of Battery Using a Novel Indicator and Framework With Fractional Grey Model and Unscented Particle Filter," *IEEE Trans. Power Electron.*, vol. 35, no. 6, pp. 5850–5859, Jun. 2020.

[359] Y. Zhou and M. Huang, "Lithium-ion batteries remaining useful life prediction based on a mixture of empirical mode decomposition and ARIMA model," *Microelectron. Reliab.*, vol. 65, pp. 265–273, Oct. 2016.

[360] D. Liu, Y. Luo, J. Liu, Y. Peng, L. Guo, and M. Pecht, "Lithium-ion battery remaining useful life estimation based on fusion nonlinear degradation AR model and RPF algorithm," *Neural Comput. Appl.*, vol. 25, no. 3–4, pp. 557–572, Sep. 2014.

[361] S. Wang, L. Zhao, X. Su, and P. Ma, "Prognostics of Lithium-Ion Batteries Based on Battery Performance Analysis and Flexible Support Vector Regression," *Energies*, vol. 7, pp. 6492–6508, Oct. 2014.

[362] H. Dong, X. Jin, Y. Lou, and C. Wang, "Lithium-ion battery state of health monitoring and remaining useful life prediction based on support vector regression-particle filter," *J. Power Sources*, vol. 271, pp. 114–123, Dec. 2014.

[363] J. Zhou, D. Liu, Y. Peng, and X. Peng, "An optimized Relevance Vector Machine with incremental learning strategy for lithium-ion battery remaining useful life estimation," in *2013 IEEE International Instrumentation and Measurement Technology Conference (I2MTC)*, May 2013, vol. 63, no. 1, pp. 561–565.

[364] Y. Yan, H. Fang, and Z. Li, "Lithium-ion Battery Remaining Useful Life Prediction Based on an Integrated Method," in *2019 IEEE 8th Data Driven Control and Learning Systems Conference (DDCLS)*, May 2019, pp. 592–597.

[365] L. Ren, L. Zhao, S. Hong, S. Zhao, H. Wang, and L. Zhang, "Remaining Useful Life Prediction for Lithium-Ion Battery: A Deep Learning Approach," *IEEE Access*, vol. 6, pp. 50587–50598, 2018.

[366] J. Qu, F. Liu, Y. Ma, and J. Fan, "A Neural-Network-Based Method for RUL Prediction and SOH Monitoring of Lithium-Ion Battery," *IEEE Access*, vol. 7, pp. 87178–87191, 2019.

[367] Datong Liu, Wei Xie, Haitao Liao, and Yu Peng, "An Integrated Probabilistic Approach to Lithium-Ion Battery Remaining Useful Life Estimation," *IEEE Trans. Instrum. Meas.*, vol. 64, no. 3, pp. 660–670, Mar. 2015.

[368] Dan Xu, Qidong Wei, Yunxia Chen, and Rui Kang, "Reliability Prediction Using Physics–Statistics-Based Degradation Model," *IEEE Trans. Components, Packag. Manuf. Technol.*, vol. 5, no. 11, pp. 1573–1581, Nov. 2015.

[369] P. L. T. Duong and N. Raghavan, "Heuristic Kalman optimized particle filter for remaining useful life prediction of lithium-ion battery," *Microelectron. Reliab.*, vol. 81, no. December 2017, pp. 232–243, Feb. 2018.

[370] Y. Wu, W. Li, Y. Wang, and K. Zhang, "Remaining Useful Life Prediction of Lithium-Ion Batteries Using Neural Network and Bat-Based Particle Filter," *IEEE Access*, vol. 7, pp.

54843–54854, 2019.

[371] B. Duan, Q. Zhang, F. Geng, and C. Zhang, "Remaining useful life prediction of lithium-ion battery based on extended Kalman particle filter," *Int. J. Energy Res.*, vol. 44, no. 3, pp. 1724–1734, Mar. 2020.

[372] L. Li, A. A. F. Saldivar, Y. Bai, and Y. Li, "Battery Remaining Useful Life Prediction with Inheritance Particle Filtering," *Energies*, vol. 12, no. 14, p. 2784, Jul. 2019.

[373] C. Sun, M. Song, S. Hong, and H. Li, "A Review of Designs and Applications of Echo State Networks," Dec. 2020, [Online]. Available: http://arxiv.org/abs/2012.02974.

[374] M. Chen, U. Challita, W. Saad, C. Yin, and M. Debbah, "Artificial Neural Networks-Based Machine Learning for Wireless Networks: A Tutorial," *IEEE Commun. Surv. Tutorials*, vol. 21, no. 4, pp. 3039–3071, 2019.

[375] H. Peng, C. Chen, C.-C. Lai, L.-C. Wang, and Z. Han, "A Predictive On-Demand Placement of UAV Base Stations Using Echo State Network," in *2019 IEEE/CIC International Conference on Communications in China (ICCC)*, Aug. 2019, pp. 36–41.

[376] Q. Luo, J. Zhou, Y. Sun, and O. Simpson, "Jointly optimized echo state network for short-term channel state information prediction of fading channel," in *2020 International Wireless Communications and Mobile Computing (IWCMC)*, Jun. 2020, pp. 1480–1484.

[377] A. A. Ferreira and T. B. Ludermir, "Genetic algorithm for reservoir computing optimization," in *2009 International Joint Conference on Neural Networks*, Jun. 2009, pp. 811–815.

[378] T. Back, *Evolutionary Algorithms in Theory and Practice.* New York: Oxford University Press, 1996.

[379] S. A. Hasib *et al.*, "A Comprehensive Review of Available Battery Datasets, RUL Prediction Approaches, and Advanced Battery Management," *IEEE Access*, vol. 9, pp. 86166–86193, 2021.

[380] G. dos Reis, C. Strange, M. Yadav, and S. Li, "Lithium-ion battery data and where to find it," *Energy AI*, vol. 5, p. 100081, Sep. 2021.

[381] B. Saha and K. Goebel, "Battery Data Set," *NASA Ames Prognostics Data Repository.* NASA Ames Research Center, Moffett Field, CA, 2007, [Online]. Available: http://ti.arc.nasa.gov/project/prognostic-data-repository.

[382] K. A. Severson *et al.*, "Data-driven prediction of battery cycle life before capacity degradation," *Nat. Energy*, vol. 4, no. 5, pp. 383–391, May 2019.

[383] Q. Ma, L. Shen, and G. W. Cottrell, "Deep-ESN: A Multiple Projection-encoding Hierarchical Reservoir Computing Framework," Nov. 2017, [Online]. Available: http://arxiv.org/abs/1711.05255.

[384] IEC 61508, "Functional safety of electrical/electronic/programmable electronic safety-related systems. Part 1 - 7." 2010.

[385] IEC 61511, "Functional safety - Safety instrumented systems for the process industry sector. Part 1 - 4." International Electrotechnical Commission, 2016.

LIST OF ORIGINAL PUBLICATION

The research activity of the author has led to several publications in international journals and conferences. These are summarized below.

BIBLIOMETRIC INDICES

The author's bibliometric indices are the following:

H-index = 9,

total number of citations = 217 by 131 documents

source: SCOPUS database on March 16, 2022

INTERNATIONAL JOURNALS

1. M. Catelani, L. Ciani, G. Patrizi, and M. Venzi, "Reliability Allocation Procedures in Complex Redundant Systems," **IEEE Syst. J.**, vol. 12, no. 2, pp. 1182–1192, Jun. 2018.

2. L. Ciani, G. Guidi, and G. Patrizi, "A Critical Comparison of Alternative Risk Priority Numbers in Failure Modes, Effects, and Criticality Analysis," **IEEE Access**, vol. 7, pp. 92398–92409, 2019.

3. M. Catelani, L. Ciani, D. Galar, and G. Patrizi, "Risk Assessment of a Wind Turbine: A New FMECA-Based Tool With RPN Threshold Estimation," **IEEE Access**, vol. 8, pp. 20181–20190, 2020.

4. M. Catelani, L. Ciani, G. Guidi, and G. Patrizi, "Maintainability improvement using allocation methods for railway systems," **ACTA IMEKO**, vol. 9, no. 1, pp. 10–17, 2020.

5. L. Ciani, A. Bartolini, G. Guidi, and G. Patrizi, "A hybrid tree sensor network for a condition monitoring system to optimise maintenance policy," **ACTA IMEKO**, vol. 9, no. 1, pp. 3–9, 2020.

6. V. Pazzi et al., "Analysis of the Influence of the GPS Errors Occurred While Collecting Electrode Coordinates on the Electrical Resistivity of Tumuli," **Sensors**, vol. 20, no. 10, p. 2966, May 2020.

7. D. Capriglione et al., "Development of a test plan and a testbed for performance analysis of MEMS-based IMUs under vibration conditions," **Measurement**, vol. 158, p. 107734, Jul. 2020.

8. M. Catelani, L. Ciani, D. Galar, and G. Patrizi, "Optimizing Maintenance Policies for a Yaw System Using Reliability-Centered Maintenance and Data-Driven Condition Monitoring," **IEEE Trans. Instrum. Meas.**, vol. 69, no. 9, pp. 6241–6249, Sep. 2020.

9. L. Ciani, M. Catelani, A. Bartolini, G. Guidi, and G. Patrizi, "Influence of Raised Ambient Temperature on a Sensor Node Using Step-Stress Test," **IEEE Trans. Instrum. Meas.**, vol. 69, no. 12, pp. 9549–9556, Dec. 2020.

10. F. Corti, A. Reatti, G. Patrizi, L. Ciani, M. Catelani, and M. K. Kazimierczuk, "Probabilistic evaluation of power converters as support in their design," **IET Power Electron.**, vol. 13, no. 19, pp. 4542–4550, Dec. 2020.

11. L. Ciani et al., "Comparing the Effects of GPS Error on Different Electrical Resistivity Tomography Arrays for Archeological Investigations," **IEEE Trans. Instrum. Meas.**, vol. 70, Article No. 1001612, 2021.

12. D. Capriglione et al., "Experimental Analysis of Filtering Algorithms for IMU-Based Applications Under Vibrations," **IEEE Trans. Instrum. Meas.**, vol. 70, Article No. 3507410, 2021.

13. M. Hämäläinen et al., "Ultra-Wideband Radar-Based Indoor Activity Monitoring for Elderly Care," **Sensors**, vol. 21, no. 9, p. 3158, May 2021.

14. L. Ciani, G. Guidi, G. Patrizi, and D. Galar, "Condition-Based Maintenance of HVAC on a High-Speed Train for Fault Detection," **Electronics**, vol. 10, no. 12, p. 1418, Jun. 2021.

15. M. Catelani, L. Ciani, D. Galar, G. Guidi, S. Matucci, and G. Patrizi, "FMECA Assessment for Railway Safety-Critical Systems Investigating a New Risk Threshold Method," **IEEE Access**, vol. 9, pp. 86243–86253, 2021.

16. M. Catelani, L. Ciani, G. Guidi, and G. Patrizi, "An enhanced SHERPA (E-SHERPA) method for human reliability analysis in railway engineering," **Reliab. Eng. Syst. Saf.**, vol. 215, no. February, Article No. 107866, Nov. 2021.

17. L. Ciani, M. Catelani, A. Bartolini, G. Guidi, and G. Patrizi, "Design optimisation of a wireless sensor node using a temperature-based test plan," **ACTA IMEKO**, vol. 10, no. 2, pp. 37–45, 2021.

18. M. Catelani, L. Ciani, R. Fantacci, G. Patrizi, and B. Picano, "Remaining Useful Life Estimation for Prognostics of Lithium-Ion Batteries Based on Recurrent

Neural Network," **IEEE Trans. Instrum. Meas.**, vol. 70, Article No. 3524611, 2021.

19. L. Ciani, G. Guidi, G. Patrizi, and D. Galar, "Improving Human Reliability Analysis for Railway Systems Using Fuzzy Logic," **IEEE Access**, vol. 9, pp. 128648–128662, 2021.

20. M. Catelani, L. Ciani, G. Guidi, G. Patrizi, and D. Galar, "Estimate the useful life for a heating, ventilation, and air conditioning system on a high-speed train using failure models," **ACTA IMEKO**, vol. 10, no. 3, pp. 100–107, 2021.

21. D. Capriglione et al., "Performance Analysis of MEMS-based Inertial Measurement Units in terrestrial vehicles", **Measurement**, Vol. 186, Article No. 1102337, 2021.

22. L. Ciani, G. Guidi, and G. Patrizi, "Fuzzy-based approach to solve classical RPN drawbacks for railway signaling systems," **IEEE Intelligent Transportation System Magazine**, Article in Press, 2021.

23. M. Catelani, L. Ciani, A. Bartolini, C. Del Rio, G. Guidi, G. Patrizi, "Reliability analysis of wireless sensor network for smart farming applications", **Sensors**, vol. 21, no. 22, Article number 7683, 2021.

24. M. Catelani, L. Ciani, and G. Patrizi, "Logic Solver Diagnostics in Safety Instrumented Systems for Oil and Gas Applications," **Safety**, vol. 8, no. 1, p. 15, 2022.

25. G. Patrizi et al., "Electrical Characterization under Harsh Environment of DC-DC Converters used in Diagnostic Systems", **IEEE Trans. Instrum. Meas.**, Vol. 71, Article No. 3504811, 2022.

26. L. Ciani, G. Guidi and G. Patrizi, "Human reliability in railway engineering: Literature review and bibliometric analysis of the last two decades", **Safety Science**, Article in Press, 2022.

INTERNATIONAL CONFERENCES AND WORKSHOPS

1. M. Catelani, L. Ciani, G. Patrizi, and M. Venzi, "Reliability allocation assessment using MEOWA method in complex redundant systems," in **2016 IEEE International Symposium on Systems Engineering (ISSE)**, Oct. 2016.

2. L. Ciani, G. Guidi, G. Patrizi, and M. Venzi, "System Maintainability Improvement using Allocation Procedures," in **2018 IEEE International Systems Engineering Symposium (ISSE)**, Oct. 2018.

3. D. Capriglione et al., "Experimental analysis of IMU under vibration," in **16th IMEKO TC10 Conference**: "Testing, Diagnostics & Inspection as a comprehensive value chain for Quality & Safety," 2019, pp. 26–31.

4. L. Ciani, A. Bartolini, G. Guidi, and G. Patrizi, "Condition Monitoring of Wind Farm based on Wireless Mesh Network," in **16th IMEKO TC10 Conference**: "Testing, Diagnostics & Inspection as a comprehensive value chain for Quality & Safety," 2019, pp. 39–44.

5. V. Pazzi et al., "ERT investigation of tumuli: does the errors in locating electrodes influence the resistivity?," in **2019 IMEKO TC-4 International Conference on Metrology for Archaeology and Cultural Heritage**, 2019, pp. 527–532.

6. L. Ciani, D. Galar, and G. Patrizi, "Improving context awareness reliability estimation for a wind turbine using an RBD model," in **2019 IEEE International Instrumentation and Measurement Technology Conference (I2MTC)**, May 2019, pp. 1–6.

7. M. Catelani, L. Ciani, A. Bartolini, G. Guidi, and G. Patrizi, "Standby Redundancy for Reliability Improvement of Wireless Sensor Network," in **2019 IEEE 5th International forum on Research and Technology for Society and Industry (RTSI)**, Sep. 2019, pp. 364–369.

8. L. Ciani, G. Guidi, and G. Patrizi, "Condition-based Maintenance for Oil&Gas system basing on Failure Modes and Effects Analysis," in **2019 IEEE 5th International forum on Research and Technology for Society and Industry (RTSI)**, Sep. 2019, pp. 85–90.

9. M. Catelani, L. Ciani, G. Patrizi, and D. Galar, "Reliability improvement of wind turbine control system based on standby redundancy," in **2019 International Symposium on Systems Engineering (ISSE)**, Oct. 2019, pp. 1–5.

10. L. Ciani, M. Catelani, A. Bartolini, G. Guidi, and G. Patrizi, "Electrical characterization of a monitoring system for precision farming under temperature stress," in **24th IMEKO TC4 International Symposium and 22nd International Workshop on ADC and DAC Modelling and Testing**, 2020, pp. 270–275.

11. D. Capriglione et al., "Vibration Step Test for Performance Analysis of Inertial Measurement Unit," in **17th IMEKO TC 10** and EUROLAB Virtual Conference "Global Trends in Testing, Diagnostics & Inspection for 2030," 2020, pp. 111–116.

12. V. Pazzi et al., "Evaluation of the GPS errors influence on the resistivity in ERT investigation of funeral mounds," in **EGU General Assembly**, 2020

13. M. Catelani, L. Ciani, A. Bartolini, G. Guidi, and G. Patrizi, "Characterization of a low-cost and low-power environmental monitoring system," in **2020 IEEE International Instrumentation and Measurement Technology Conference (I2MTC)**, May 2020, pp. 1–6.

14. D. Capriglione et al., "Characterization of Inertial Measurement Units under Environmental Stress Screening," in **2020 IEEE International Instrumentation and Measurement Technology Conference (I2MTC)**, May 2020, pp. 1–6.

15. M. Catelani et al., "Design and Experimental analysis of temperature tests for Inertial Measurement Units in Avionic applications," in **2020 IEEE 7th International Workshop on Metrology for AeroSpace (MetroAeroSpace)**, Jun. 2020, pp. 217–221.

16. M. Catelani et al., "Reliability and Functional Analysis of IMU systems under temperature-based stress tests," in **2021 IEEE International Instrumentation and Measurement Technology Conference (I2MTC)**, May 2021.

17. M. Catelani et al., "Effects of inaccurate electrode positioning in subsurface resistivity measurements for archeological purposes," in **2021 IEEE International Instrumentation and Measurement Technology Conference (I2MTC)**, May 2021.

18. D. Capriglione et al., "Analysis of MEMS devices under temperature stress test," in **2021 IEEE 8th International Workshop on Metrology for AeroSpace (MetroAeroSpace)**, Jun. 2021, pp. 63–68.

19. M. Catelani, L. Ciani, G. Guidi, and G. Patrizi, "Accelerated Testing and Reliability estimation of electronic boards for automotive applications," in **2021 IEEE International Workshop on Metrology for Automotive (MetroAutomotive)**, Jul. 2021, pp. 199–204.

20. L. Ciani et al., "Effect of Pulses Distribution in a Buck Converter Controlled with Pulse Skipping Modulation," in **2021 IEEE 15th International Conference on Compatibility, Power Electronics and Power Engineering (CPE-POWERENG)**, Jul. 2021, pp. 1–6.

21. M. Catelani, L. Ciani, G. Guidi, and G. Patrizi, "Human error probability estimation for safety and diagnostic systems in railway engineering," **Meas. Sensors, Proc. Of the IMEKO XXIII World congress (IMEKO2021)**, Vol. 18, p. 100105, Dec. 2021.

22. D. Capriglione et al., "Characterization of Inertial measurement units using sine-on-random vibration test," **Meas. Sensors, Proc. Of the IMEKO XXIII World congress (IMEKO2021)**, vol. 18, p. 100104, Dec. 2021.

23. M. Catelani, L. Ciani, G. Guidi, and G. Patrizi, "Reliability Analysis of Diagnostic System for Condition Monitoring of Industrial Plant", **2021 IEEE 6th International Forum on Research and Technology for Society and Industry (RTSI)**, September 6-9, 2021

24. M. Catelani, L. Ciani, G. Guidi, and G. Patrizi, "Reliability Allocation: an iterative approach for complex systems", **2021 IEEE International Symposium on Systems Engineering (ISSE)**, September 2021

NATIONAL JOURNALS

1. M. Catelani, L. Ciani, G. Guidi, G. Patrizi, "Introduzione alla logica Fuzzy nell'analisi FMECA", **Tutto_Misure**, anno XXII, N. 01, 2020.

2. M. Catelani, L. Ciani, G. Guidi, G. Patrizi, "Applicazione della logica Fuzzy all'analisi FMECA", **Tutto_Misure**, anno XXII, N. 02, 2020.

3. M. Catelani, L. Ciani, L. Cristaldi, G. Patrizi, "La logica Fuzzy a supporto degli strumenti utilizzati nell'analisi della sicurezza dei sistemi industriali", **Tutto_Misure**, anno XXIV, N. 01, 2022.

NATIONAL CONFERENCES

1. M. Catelani, L. Ciani, G. Patrizi, "Analisi degli effetti delle condizioni ambientali sull'affidabilità del sistema di controllo di una turbina eolica", Atti del **XXXVI Congresso nazionale di misure elettriche ed elettroniche GMEE**, 12-14 Settembre 2019, Perugia, Italia.

2. M. Catelani et al., "Performance Analysis of MEMS-based IMUs under vibration stress", Atti del **XXXVII Congresso nazionale di misure elettriche ed elettroniche GMEE**, 10-12 Settembre 2020.

3. M. Catelani, L. Ciani, A. Bartolini, G. Guidi, G. Patrizi, "Analisi in temperatura di un nodo sensore mediante test stress a gradino", Atti del **XXXVII Congresso nazionale di misure elettriche ed elettroniche GMEE**, 10-12 Settembre 2020.

4. M. Catelani et al., "Effetti dell'errato posizionamento degli elettrodi nelle misure di resistività del terreno per la ricerca di tumuli etruschi", Atti del **XXXVII Congresso nazionale di misure elettriche ed elettroniche GMEE**, 10-12 Settembre 2020.

5. M. Catelani, L. Ciani, A. Bartolini, G. Patrizi, "Confronto metodi di pilotaggio di un convertitore Buck per applicazione agricola", Atti del **XXXVIII Congresso nazionale di misure elettriche ed elettroniche GMEE**, 16-18 Settembre 2021.

6. D. Capriglione et al., "Functional analysis of inertial measurement units for automotive field", Atti del **XXXVIII Congresso nazionale di misure elettriche ed elettroniche GMEE**, 16-18 Settembre 2021.

7. M. Catelani et al. "Influenza della qualità dei dati di tomografia elettrica sui risultati d'inversione della resistività per applicazioni archeologiche", Atti del **XXXVIII Congresso nazionale di misure elettriche ed elettroniche GMEE**, 16-18 Settembre 2021.